

ISSN:1305-130X

e-ISSN:1305-1385

# CELAL BAYAR UNIVERSITY JOURNAL OF SCIENCE



Manisa Celal Bayar Üniversitesi  
Fen Bilimleri Dergisi

2024

VOLUME:20

ISSUE:4



# Journal of Science

Volume: 20, Issue: 4, Year: 2024

## Contact

Manisa Celal Bayar University

The Graduate School

Campus of Şehit Prof Dr İlhan Varank 45140 Yunusemre – MANİSA, TÜRKİYE

Tel: (00 90) 236 201 27 05

Fax: (00 90) 236 241 21 49

E-mail: [lee.fendergi@cbu.edu.tr](mailto:lee.fendergi@cbu.edu.tr)

Web: <https://dergipark.org.tr/tr/pub/cbayarfbe>

“CBU Journal of Science is indexed by ULAKBIM-TUBITAK TR-DIZIN”



ISSN 1305-130X

E-ISSN 1305-1385

CBUJOS is published quarterly at The Graduate School of Manisa Celal Bayar University

“CBU Journal of Science is a refereed scientific journal”



## Celal Bayar University Journal of Science

**Owner:** Manisa Celal Bayar University, The Graduate School

**Editor in Chief:** Prof. Dr. Kamil ŞİRİN

**Editor:** Assoc. Prof. Dr. İlker Çetin KESKİN

**Layout Editor & Secretary**

Res. Assist. Musa OVALI

Res. Assist. Gencay TEPE

**Subject Editors**

Prof. Dr. Ali KONURALP, Manisa Celal Bayar University, Mathematics

Prof. Dr. Sezai TAŞKIN, Manisa Celal Bayar University, Electrical and Electronics Engineering

Prof. Dr. Kamuran AKTAŞ, Manisa Celal Bayar University, Biology

Prof. Dr. Tuğma ÖZACAR ÖZTÜRK, Manisa Celal Bayar University, Computer Engineering

Assoc. Prof. Dr. Bora CANBULA, Manisa Celal Bayar University, Computer Engineering

Assoc. Prof. Dr. Emriye AY, Manisa Celal Bayar University, Chemical

Assoc. Prof. Dr. Etem KÖSE, Manisa Celal Bayar University, Physics

Assoc. Prof. Dr. İbrahim Fadıl SOYKÖK, Manisa Celal Bayar University, Mechatronics Engineering

Assoc. Prof. Dr. Serhat ARAS, University of Health Science, Medical Physics

**International Scientific Advisory Board**

Prof. Dr. Arianit REKA; State University of Tetova, Macedonia

Prof. Dr. Tomasz NIEMIEC; Warsaw University of Life Sciences, Poland

Prof. Dr. Alyani ISMAIL; Universiti Putra, Malaysia

Prof. Dr. Iuliana APRODU; Dunarea de Jos University, Romania

Assoc. Prof. Can BAYRAM; University of Illinois, USA

Assoc. Prof. Dr. Johanan Christian PRASANN; Madras Christian College, South India

Assoc. Prof. Dr. Nouredine ISSAOUI ; Université de Monastir, Tunisie.

Assoc. Dr. Edward Albert UECKERMANN; North-West University, South Africa

Assoc. Dr. Zhi-Qiang ZHANG; The University of Auckland, Holland

Assist. Prof. Dr. Young Ki KIM; Pohang University of Science and Technology, South Korea

Assist. Prof. Dr. Mona MIRHEYDARI; Rutgers University, USA

Assist. Prof. Dr. Donatella ALBANESE; Università Degli Studi Di Salerno, Italy

Assist. Prof. Dr. Jinghua JIANG; The University of Memphis, USA

Assist. Prof. Dr. Jens OLDELAND; University of Hamburg, Germany

Dr. Cheng CHENG; Apple Inc., USA

Dr. Sajedah AFGHAH; Microsoft Corporation, USA

Dr. Jinghua JIANG; The University of Memphis

**National Scientific Advisory Board**

Prof. Dr. Mustafa Ersöz; Selçuk University

Prof. Dr. Oğuz Gürsoy; Mehmet Akif University

Prof. Dr. Mehmet Çevik; İzmir Katip Çelebi University

Prof. Dr. Sezgin Çelik; Yıldız Teknik University

Prof. Dr. Osman Dayan; Çanakkale Onsekiz Mart University

Prof. Dr. Serdar İplikçi; Pamukkale University

Prof. Dr. Yasin Üst; Yıldız Teknik University

Prof. Dr. Mahmut Kuş; Konya Teknik University

Prof. Dr. Ertunç Gündüz; Hacettepe University

Prof. Dr. Tülin Aydemir; Manisa Celal Bayar University

Prof. Dr. Sezai Taşkın; Manisa Celal Bayar University

Prof. Dr. Fatma Şaşmaz Ören; Manisa Celal Bayar University

Prof. Dr. Fatih Selimefendigil; Manisa Celal Bayar University

Prof. Dr. Osman Çulha; Manisa Celal Bayar University

Prof. Dr. Ali Konuralp; Manisa Celal Bayar University

Prof. Dr. Erol Akpınar; Abant İzzet Baysal University

Prof. Dr. Ali Demir; Manisa Celal Bayar University

Prof. Dr. Serap Derman; Yıldız Teknik University

Prof. Dr. Özlem Çağındı; Manisa Celal Bayar University

Assoc. Prof. Dr. Fatih Doğan; Çanakkale Onsekiz Mart University

Assoc. Prof. Dr. Yeliz Yıldırım; Ege University

Assoc. Prof. Dr. Hayati Mamur; Manisa Celal Bayar University

Assoc. Prof. Dr. Mehmet Söylemez; Adıyaman University

Assoc. Prof. Dr. Nil Mansuroğlu; Ahi Evran University

Assist. Prof. Dr. Zeynep Çipiloğlu Yıldız; Manisa Celal Bayar University



---

## **CBU Journal of Science**

Celal Bayar University Journal of Science (CBUJOS) covers scientific studies in the fields of Engineering and Science and publishes accounts of original research articles concerned with all aspects of experimental and theoretical studies. CBU Journal of Science is a refereed scientific journal published four times annually (March, June, September and December) by The Graduate School of Manisa Celal Bayar University. CBU Journal of Science considers the original research articles written in English for evaluation.

CBU Journal of Science is indexed by TUBİTAK ULAKBİM TR-DİZİN, and also is included in DOAJ, Cite Factor, Journal TOCS, Advanced Science Index and OAJI databases. Digital Object Identifier (DOI) number will be assigned for all the articles being published in CBU Journal of Science.

Instructions for Authors and Article Template can be found on the page of Celal Bayar University Journal of Science DergiPark (<https://dergipark.org.tr/tr/pub/cbayarfb>)







**Vol: 20, Issue: 4, Year: 2024**

**Contents**

<b><u>Research Article</u></b>	<b><u>Pages</u></b>
<b>1. Application of LoRa Technology in Monitoring Solution for Photovoltaic Systems</b> DOI: 10.18466/cbayarfbe.1526601 Ercan Aykut*, Safaa Hawas	1-11
<b>2. A new method proposal to enhance foreground images against noisy backgrounds: Haytham Thresholding</b> DOI:10.18466/cbayarfbe.1485592 Esin Mutlu, Serkan Dereli*	12-19
<b>3. Nascency of Physiopathological Activation by The Effect of Genomic Single Nucleotide Exchange Factor in The PNPLA3 rs738409 Genotype of Patients with Hepatocellular Carcinoma</b> DOI:10.18466/cbayarfbe.1437557 Anıl Delik*, Yakup Ülger	20-27
<b>4. Detection of Atrial Fibrillation with Custom Designed Wavelet-based Convolutional Autoencoder</b> DOI: 10.18466/cbayarfbe.1508153 Öykü Eravcı, Nalan Özkurt*, Özlem Memiş, Evrim Şimşek	28-39
<b>5. The Effect of Substrate Dielectric Constant and Thickness on Millimeter Wave Band Patch Antenna Performance</b> DOI:10.18466/cbayarfbe.1514216 Seda Ermis*	40-59
<b>6. Use of Active Carbon Produced by Hydrothermal Method from Agricultural Waste in Methylene Blue Removal</b> DOI: 10.18466/cbayarfbe.1517079 Mustafa Boyrazlı , Elif Arancı Öztürk*, Emrah Çelik , Mehmet Ali Yashı	60-66
<b>7. The Concept of Parafree Zinbiel Algebras</b> DOI: 10.18466/cbayarfbe.1455387 Zekiye Çiloğlu Şahin*	67-71
<b>8. Thermal Performance Analysis of a Liquid Cooling Plate for Power Electronics</b> DOI: 10.18466/cbayarfbe.1528939 M. Bahattin Akgül*, Furkan Sinan Erçel	72-81
<b>9. Using Deep Learning Architectures For Skin Cancer Classification</b> DOI: 10.18466/cbayarfbe.1513945 Bafreen Mohammed*, Özkan İnik	82-91
<b>10. A study on chaotic dynamics of deep artificial neural network activated by biological neuron model</b> DOI: 10.18466/cbayarfbe.1538362 Erdem Erkan*	92-100
<b>11. Synthesis and Characterization of Schiff Base Compounds Containing Mono and Disulfonic Groups</b> DOI: 10.18466/cbayarfbe.1529884 İsmet Kaya*, Feyza Kolcu, Sude Süel	101-106
<b>12. Unveiling the antioxidant secrets: Phytochemical profiling and bioactive potential of water extracts from Muğla propolis samples</b> DOI: 10.18466/cbayarfbe.1566363 Cengiz Sarıkürkcü*	107-115
<b>13. The Determination of Molecular Electrostatic Potential and Anticancer Properties of Eugenol: A Theoretical Study</b> DOI: 10.18466/cbayarfbe.1490879 Bilge Bıçak*	116-122
<b>14. Correction / Erratum Article</b> DOI: 10.18466/cbayarfbe.1609273 Vedia Nüket Tirtom*, Fatma Özkafalı	123-123

# Application of LoRa Technology in Monitoring Solution for Photovoltaic Systems

Ercan AYKUT<sup>1\*</sup> , Safaa Thamer HAWAS<sup>2</sup> 

<sup>1</sup> İstanbul Gelişim University, Electrical Electronics Engineering, Avcılar, İstanbul, Türkiye

<sup>2</sup> İstanbul Gelişim University, Electrical Electronics Engineering, Avcılar, İstanbul, Türkiye

\*[eykut@gelisim.edu.tr](mailto:eykut@gelisim.edu.tr)

\* Orcid No: 0000-0001-8639-8408

Received: 1 August 2024

Accepted: 10 September 2024

DOI: 10.18466/cbayarfbe.1526601

## Abstract

Solar array systems with photovoltaic (PV) modules are extensively utilized in remote fields, agriculture, military, and various other sections. However, the challenge lies in the long distances between these installations and end-users, necessitating remote monitoring systems. In this study, we leverage Long Range (LoRa) wireless communication technology due to its extended range, cost-effectiveness, and user-friendly nature. The study focuses on the design and implementation of a Monitoring System (MS) tailored for PV applications, utilizing LoRa technology. The primary objective is to enhance the efficiency, reliability, and maintenance of PV installations by continuously monitoring system health and performance. The MS encompasses sensors, microcontrollers, and processors to collect and process data on PV, battery banks, load, and grid parameters, including voltage, current, temperature, and state of charge (SoC). Processed data is transmitted via LoRa to a centralized control station for analysis and decision-making. LoRa's attributes, such as long-range coverage, low power consumption, and obstacle penetration, make it particularly suitable for remote PV installations. We provide a detailed overview of the system architecture, components, communication protocols, as well as data processing algorithms and battery health estimation techniques. Experimental evaluation conducted on a test PV setup demonstrates the MS's effectiveness in monitoring battery health, anomaly detection, and facilitating remote maintenance in the normal and up-normal conditions and modes. Simulation on the MATLAB/Simulink platform validates the system's functionality under various operating conditions, ensuring robust performance.

**Keywords:** Renewable Energy, Solar Array, PV, Monitoring System, Lora, Battery, Operating Conditions and Modes.

## 1. Introduction

The Internet of Things (IoT) denotes a system where physical devices, appliances, vehicles, and other objects are interconnected through sensors, software, and internet connectivity. This network enables the collection and exchange of data over the internet, allowing for remote monitoring and control. IoT enables seamless integration between the physical world and computer systems, facilitating data gathering, analysis, and automation to improve efficiency and decision-making processes, ultimately enhancing quality of life. IoT signifies a significant advancement in comparison to the existing Internet infrastructure[1], [2], [3]. The primary objective of the IoT is to enhance operational efficiency and facilitate adaptation. The spread of smart objects and

devices within the IoT has experienced a substantial growth. This phenomenon facilitates the manifestation of intelligent behavior in a diverse range of devices. IoT-enabled items have been equipped with intelligent functionalities, including sensors, RFID technology, and other forms of embedded computing. The notion of a globally networked future is no longer confined to futuristic technology significant of science fiction. The various devices and objects in our surroundings are interconnected inside a network commonly referred to as the IoT[4], [5].

Consequently, a universally accepted definition of the IoT is lacking, leading to a lack of clarity regarding its implications. Numerous acronyms and abbreviations have been devised to denote the concept of the IoT,

including M2M (Machine to Machine), WoT (Web of Things), CoT (Cloud of Things), and IoE (Internet of Everything). While there are writers who contend that the two expressions possess identical meanings, there are others that establish evident differentiations between them. The IoT is a complex network that has the potential to introduce numerous innovative concepts and societal conventions[6], [7], [8], [9]. The primary objective of IoT innovations is to streamline operations across diverse sectors, enhancing system efficacy, and ultimately elevating the overall quality of life. This ambitious goal encompasses a multitude of applications, permeating virtually every facet of modern existence[10], [11].

Similarly, the incorporation of IoT technologies into industrial processes reshapes manufacturing paradigms, fostering enhanced production processes and seamless communication between human operators and machinery[12]. This comprehensive monitoring extends across the production chain, from quality control to logistics and distribution, ensuring operational efficiency and minimizing losses to bolster market competitiveness. In a groundbreaking advancement, a Monitoring System (MS) that leverages LoRa and IoT technologies in rural areas underscores the transformative potential of wireless sensor networks (WSNs)[9]. LoRa, short for Long Range, is a Low-Power Wide-Area Network (LPWAN) protocol that enables long-distance communication between devices with minimal energy consumption. It operates on unlicensed frequency bands, making it suitable for applications in remote and rural areas. LoRa technology is closely intertwined with the IoT, a network of interconnected devices capable of exchanging data over the internet. In the context of the MS mentioned, IoT facilitates the collection, transmission, and analysis of data from sensors deployed in rural environments[13]. By integrating LoRa with IoT, the MS enables efficient and cost-effective monitoring of various parameters, such as environmental conditions or photovoltaic system performance, over large geographical areas[14].

Despite challenges like node vulnerability to damage and extreme weather events in photovoltaic systems, innovative solutions such as subterranean sensor networks ensure continuous real-time data acquisition. These networks, enabled by LoRa and IoT technologies, enhance the resilience and reliability of monitoring systems in remote locations. Moreover, wireless sensor networks (WSNs) equipped with LoRa technology have become indispensable across diverse sectors, including industry, healthcare, and precision agriculture. They offer versatile monitoring capabilities, allowing for the collection of data in various environmental conditions. LoRa technology is suitable for a wide range of applications, including smart cities, agriculture, and industrial monitoring[15], [16]. This underscores the significance of LoRa-enabled IoT solutions in addressing monitoring and communication challenges across

different domains. Additionally, the segment evaluates communication protocols to tackle challenges in contemporary IoT platforms serving photovoltaic batteries[17]. This highlights the importance of selecting appropriate communication protocols, such as LoRa, to optimize data transmission and enhance the efficiency of IoT-enabled monitoring systems in specific applications like photovoltaic systems. In order to furnish a thorough comparison of different LPWAN technologies, encompassing LoRa, Sigfox, NB-IoT, and Zigbee, all of which emerge as potential contenders for expansive IoT implementations[18], the authors precisely analyze the technical attributes of these technologies and evaluate their applicability across diverse IoT scenarios.

In the study, the authors use LoRa technology to design and implement a battery monitoring system for PV applications. LoRa technology was first and has since gained popularity due to its ability to provide long-range communication at a low power consumption. In a paper[19], the authors discuss the advantages of LoRa technology, including its long-range communication capability (up to 10 km in rural areas), low power consumption (up to 10 years' battery life), and high interference immunity.

Several studies have proposed the use of LoRa technology for monitoring systems (MS) in PV applications. Peruzzi and Pozzebon studied a monitoring system based on LoRa technology, designed and implemented for a 24V battery bank in a PV system. The MS was able to monitor the voltage, current, and temperature of the battery bank and transmit the data wirelessly to a remote monitoring station over a distance of 3 km. The system was also able to send alerts to the monitoring station in case of battery overcharge or discharge[19].

In another study, Gupta and Gupta proposed a MS based on LoRa technology for a 12V battery bank in a PV system. The BMS was able to monitor the SoC, SoH, and SoF of the battery bank and transmit the data wirelessly to a remote monitoring station over a distance of 2 km. The system was also able to send alerts to the monitoring station in case of battery overcharge or discharge[20]. Cabello et al., designed a battery monitoring system (BMS) based on LoRa technology and implemented for a 48V battery bank in a PV system. The BMS was able to monitor the voltage, current, temperature, and SoC of the battery bank and transmit the data wirelessly to a remote monitoring station over a distance of 1 km. The system was also able to send alerts to the monitoring station in case of battery overcharge or discharge[21]. Talib et al., focuses on developing a PV monitoring system that can help ensure the efficient operation of photovoltaic (PV) systems. The study begins by highlighting the importance of battery monitoring in PV

systems, particularly in remote areas where power supply is unreliable[22].

Raza et al., emphasize that a reliable battery monitoring system can help prevent downtime, reduce maintenance costs, and prolong the lifespan of the batteries. They argue that a low-power, wide-area network (LPWAN) technology like LoRa can be used to design a cost-effective and efficient battery monitoring system[23].

Khalifeh et al., designed a system consisting of a microcontroller unit (MCU), a LoRa module, a battery voltage and current sensor, and a temperature sensor. The MCU is responsible for collecting data from the sensors and transmitting it wirelessly to a base station via LoRa technology. The authors explain that LoRa technology is particularly suitable for battery monitoring systems because it provides a long-range communication capability, low power consumption, and high interference immunity [24].

Kutluay et al., present the results of their experiments to evaluate the performance of the proposed system. They conducted tests on a 12 V lead-acid battery that was charged and discharged at different rates. The results showed that the battery monitoring system was able to accurately measure the battery voltage, current, and temperature, and transmit the data wirelessly to the base station. The authors also noted that the system had a low power consumption and could operate for a long time on a single battery[25].

Despite its advantages, LoRa technology also has some limitations. In a study Raza et al., identify several limitations of LoRa technology, including its limited data rate (up to 50 kbps), susceptibility to interference from other LoRa networks, and the need for a clear line-of-sight for long-range communication. The authors suggest that LoRa technology may not be suitable for applications that require high data rates or are located in areas with high levels of interference[23].

Traditional wireless communication technologies used in battery monitoring systems, such as Wi-Fi and Bluetooth, may not provide sufficient coverage in remote areas or may consume excessive power, leading to inefficiencies and increased maintenance costs. The implementation of a battery monitoring system for photovoltaic applications based on LoRa technology can potentially overcome these challenges. LoRa offers long-range and low-power capabilities that are well-suited for monitoring and managing battery systems in remote and off-grid locations. The key problem to address is how to design and implement a reliable, energy-efficient, and scalable battery monitoring system using LoRa technology, which can cater to different battery types and photovoltaic system setups while ensuring data security and real-time monitoring and control.

In this study a LoRa Based battery monitoring system for PV applications has been designed and simulated by MATLAB/Simulink. The study shows that instead of other wireless connections such as Wifi and Bluetooth, LoRa can also be used for monitoring battery. Different from other studies, this study investigates the LoRa for longer distance of 5 km. Also the design of the PV system is wider and more comprehensive. Moreover, maximum power point tracking (MPPT) and voltage control modes are applied.

## 2. Materials and Methods

The suggested system consists of two components, of which the first is the PV solar system comprising a solar cell arrays, MPPT, boost converter, battery bank, bidirectional converter, load, and controller. The study comprises the LoRa communication and monitoring MATLAB simulation which are employed for transmitting and receiving significant system parameters, like voltages, current, power, and some other parameters.

### 2.1. PV System

Figure 1 depicts the PV system with monitoring system, which consists of boost controller, the PV array, MPPT controller and the load.

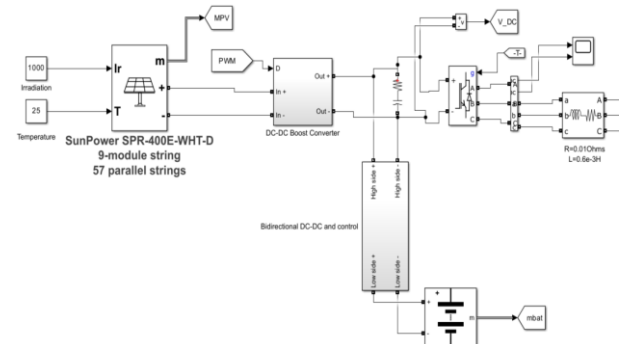


Figure 1. PV system

The proposed system outlines the configuration of complete grid connected photovoltaic three-phase AC power system with battery backup, facilitating the following objectives:

- Determine the required battery ranking depended on the connected load profile and the obtainable solar energy.
  - Establish the optimal arrangement of panels, considering the number of connected series and parallel strings panels.
  - Design a constant voltage three-phase AC supply.
  - Choose appropriate values for the proportional gain and of the PI controller and the phase-lead time constant.
- Both the solar PV and battery storage components are capable of supporting grid-connected three-phase loads, with the load connected to a constant voltage three-phase AC supply. The solar PV system operates in two modes:

maximum power point tracking (MPPT) and de-rated voltage control modes, employing a battery management system equipped with bi-directional DC-DC converters. For MPPT of the solar PV system, the system utilizes the Perturbation and Observation (P&O) technique as one of the available MPPT techniques.

Various parameters can be specified within the system, including the average daily connected load profile, the daily available average solar energy in the region (measured in kWh), operating temperature of the solar PV system, day of autonomy, battery recharge time, output DC voltage, and specifications of the solar panels used. The determination of the number of PV panels required to meet the specified generation capability relies on data provided by the manufacturer of the solar panels. PI controller of the form is chosen to control the solar PV and battery management system.

## 2.2. LoRa Model

A MATLAB file code used to simulate LoRa transceiver to calculate BER and required transmission power and SNR. LoRa simulation based on the MATLAB code published by [26]. The published code is used to simulate LoRa communication system for “Multiple-Frequency-Shift-Keying (MFSK)” modulation in both coherent and none-coherent techniques, and also the system simulated for two types of noise.

The solar plant voltage, current, irradiance and power are transmitted over LoRa communication system and monitored in the remote-control room. The proposed system simulated for all possible operating cases. The flow chart of the system is shown in figure 2.

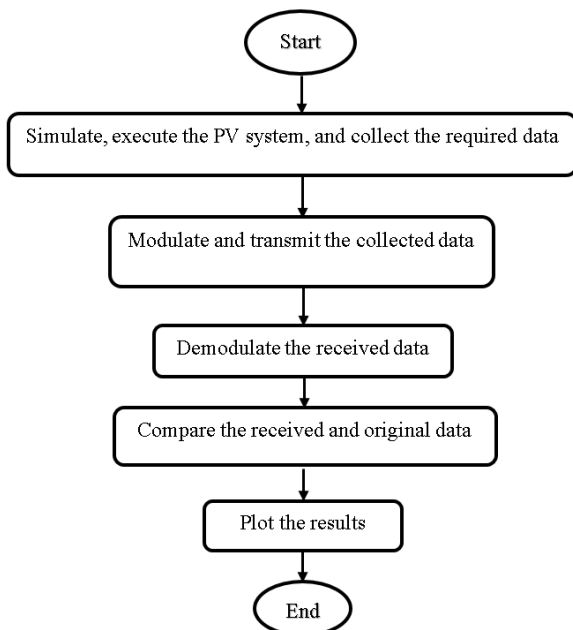


**Figure 2.** Flowchart of the system

## 2.3. LoRa Protocols

In the context of a battery monitoring system, LoRa technology can be used to implement the Medium Access Layer (MAC) protocol for wireless communication. The MAC layer is responsible for managing the transmission of data between devices in a network, and Lora technology provides a reliable and efficient method for wireless communication between battery monitoring devices. In the context of a battery monitoring system using Lora technology, the MAC layer can be implemented using the following steps:

- Establishing a Network: The first step in implementing the MAC layer is to establish a network. This involves setting up a Lora gateway, which serves as the central communication hub for the battery monitoring devices. The gateway is responsible for receiving data from the battery monitoring devices and forwarding it to the appropriate destination.

- Defining Communication Channels: Once the network is established, communication channels need to be defined. Lora technology uses a spread spectrum modulation technique to transmit data over multiple frequency channels. By defining communication channels, the battery monitoring devices can communicate with the gateway without interfering with each other.

- Implementing the MAC Protocol: With the network and communication channels defined, the MAC protocol can be implemented. The MAC protocol manages the transmission of data between the battery monitoring devices and the gateway. It defines the rules for accessing the communication channels, handling collisions, and ensuring reliable communication.

- Transmitting and Receiving Data: Once the MAC protocol is implemented, data can be transmitted and received between the battery monitoring devices and the gateway. The battery monitoring devices collect data on the battery voltage, current, and temperature, and transmit it wirelessly to the gateway using LoRa technology. The gateway receives the data and forwards it to a central database or user interface for analysis.

Figure 3 illustrates a simplified LoRa frame, featuring the addition of a LoRa protocol header. This LoRa header is crucial for transmission and consequently prolongs the transmission time, despite the number of useful bits remaining unchanged. As a result, the effective transmission throughput is reduced.



**Figure 3.** LoRa technology MAC frame



In the context of utilizing the LoRa protocol, various protocol layers have been introduced. Each layer provides specific services, with the upper layers being closer to the user, while the lower layers pertain to the transmission medium. As illustrated in Figure 4, the LoRaWAN protocol consists of two main layers: the application layer and the Medium Access Control (MAC) layer. These layers form the basis of the LoRaWAN protocol, which facilitates transmission over the internet via gateways. As the frame passes through the gateway, a different header is appended to the frame to enable transmission over the internet. This new header, known as the IP header, allows the frame to be transmitted over the internet while preserving the content of the original LoRaWAN frame. Thus, the content of the LoRaWAN frame remains intact throughout the transmission process.

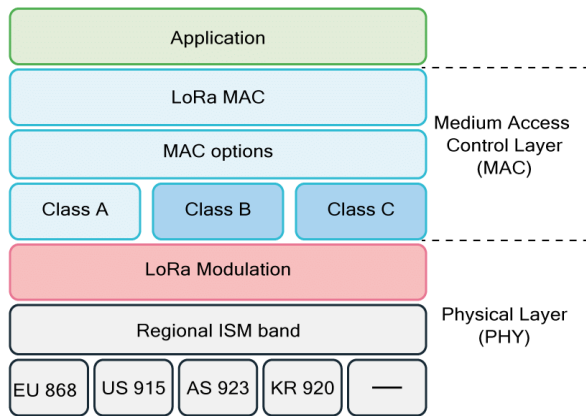


**Figure 4.** LoRa MAC protocol layers for the design of EMS[27]

In the utilization of the LoRa protocol, additional protocol layers have been incorporated, with each layer providing specific services. As the data is transmitted through the frame, it undergoes encapsulation in each lower layer, effectively adding details to the transmission process. The composition of the entire LoRa frame, including the information encapsulated at each layer, is illustrated in Figure 5, where the LoRa spreading frame is as depicted in Figure 6.

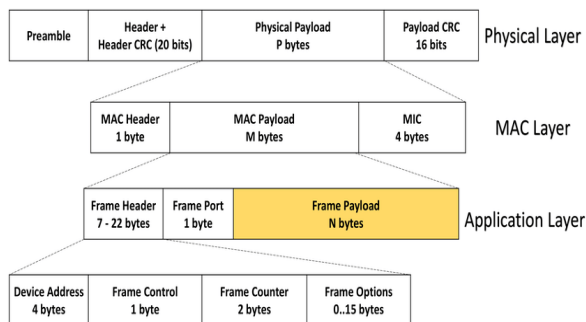


**Figure 5.** Frame of the LoRa different layers[28]

Before encapsulating user data in the Application layer, they undergo encryption using the Application Session Key (AppSKey) to ensure the security of the transaction.

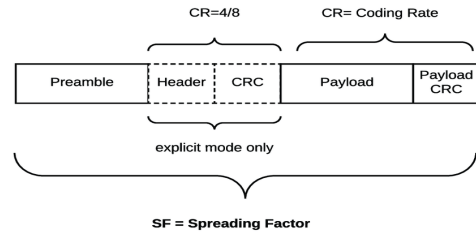


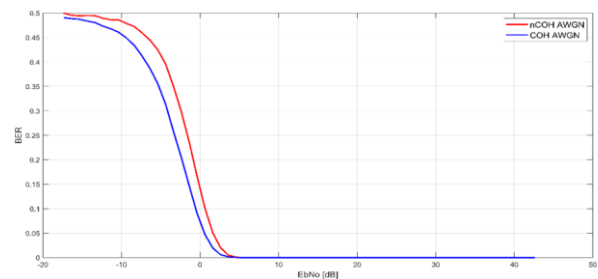
**Figure 6.** Spreading factor LoRa frame for EMS PV application[28]

### 3. Discussion

#### 3.1. LoRa Simulation

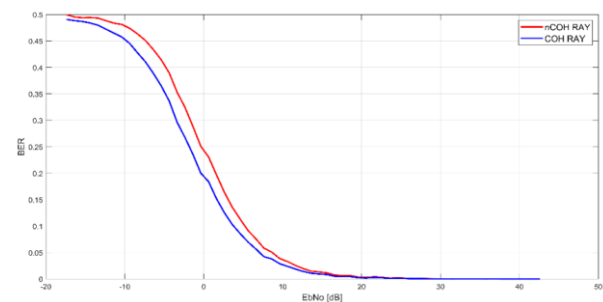
In this work the communication system simulated in specific conditions to check its performance. In LoRa technology a distance of 5km has been considered. Voltage, current, SoC, load and power has been examined.

Figure 7 shows the BER for coherent and non-coherent FSK modulation and noises with respect to the SNR, the simulation outcomes compared for AWGN noise.



**Figure 7.** BER for LoRa in coherent and non-coherent FSK for AWGN noise effect

While the system response in case of Rayleigh noise is shown in figure 8.



**Figure 8.** BER for LoRa in coherent and non-coherent FSK for Rayleigh noise effect

The power/frequency curve is shown in figure 9.

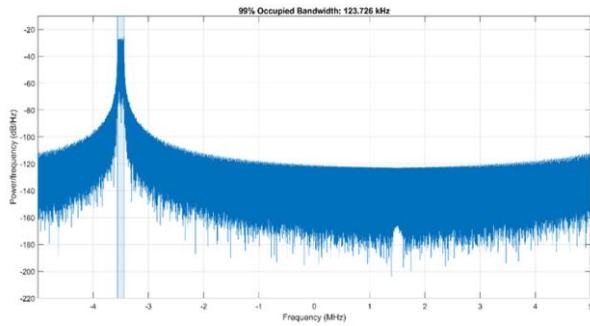


Figure 9. Occupied bandwidth

While figure 10 is showing the spectrum density for the LoRa communication system

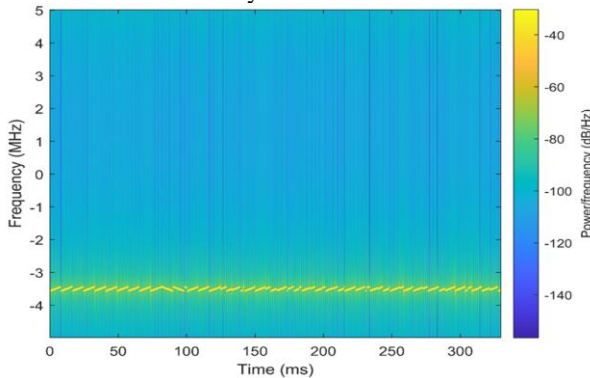


Figure 10. Spectrogram for LoRa communication system

### 3.2. PV System

The PV solar system is simulated for all expected operating conditions (solar irradiance level, loading, MMPT, Constant voltage). The following sets are used and the results are generated by using the values in Table 1.

Table 1. Parameters of the system used in the simulation

Parameters	Value
Required PV Power rating	200 kW
Minimum number of panels required per string	8 pcs
Maximum number of panels connected per string without reaching maximum voltage	10 pcs
Minimum power rating of the solar PV plant	1,80 kW
Maximum power possible per string without reaching maximum DC voltage	400 W
Actual number of panels per string	9 pcs
Number of strings connected in parallel	57 pcs
Actual solar PV plant power	200 kW
Rated Ah of the battery	400 Ah
Battery nominal voltage	400 V
Fully charged voltage	465 V

Reference battery charging current	45,24 A
Nominal (Average) discharge current	43,48 A
Maximum battery discharging current	43,47 A
Initial state-of-charge (%)	70%
Maximum battery charging Power	~18 kW
Maximum battery discharging Power	~16 kW

The battery discharge parameters can be concluded with the figure 11.

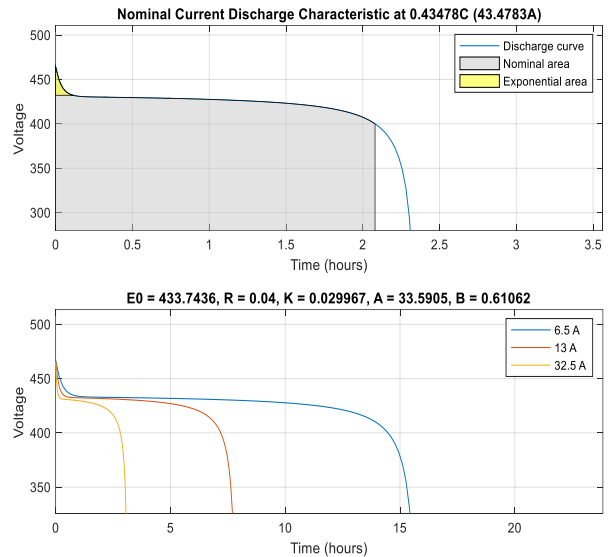


Figure 11. Battery discharging parameters (voltage, current, time)

To understand the system behavior with the monitoring, it can take the normal operating case with irradiance of  $G=1000W/m^2$  and STC temperature with  $T=25C^{\circ}$ . The PV voltage ( $V_{PV}$ ), current ( $I_{PV}$ ), and the power ( $P_{PV}$ ) are shown in the figure 12.

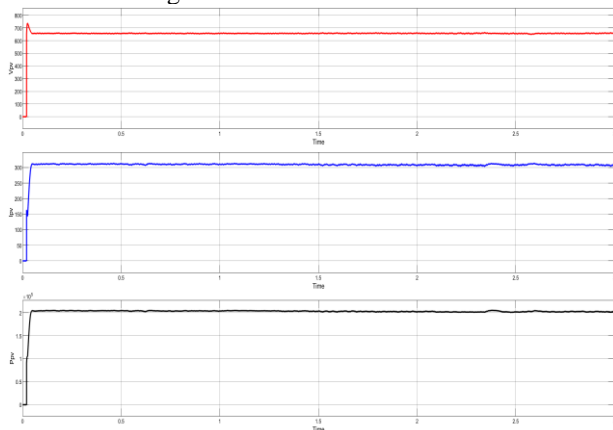
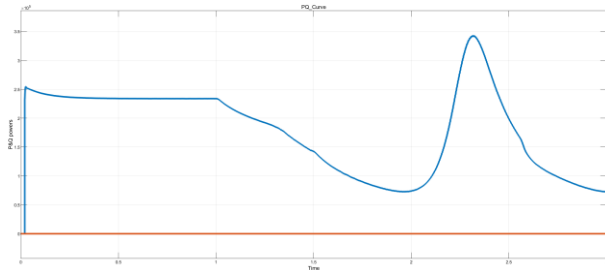


Figure 12. PV voltage, current, and power under a  $1000W/m^2$  results

As the irradiance is constant along the whole period, so the PV voltage, current, and power are of fixed values that are related to our system configuration. Also for continuous controlling the system, it is clear from figure 13 that the real power (P) is varied according to the



control state and the reactive power (Q) is always zero to keep the unity power factor for the PV system.



**Figure 13.** The real power (P) and the reactive power (Q) for the PV part

As illustrated in figure 14, the three phases voltage ( $V_{abc}$ ) and current ( $I_{abc}$ ) that are supplied to the P<sub>CC</sub> and hence to the load or the grid are pure sine waves and with appropriate values.

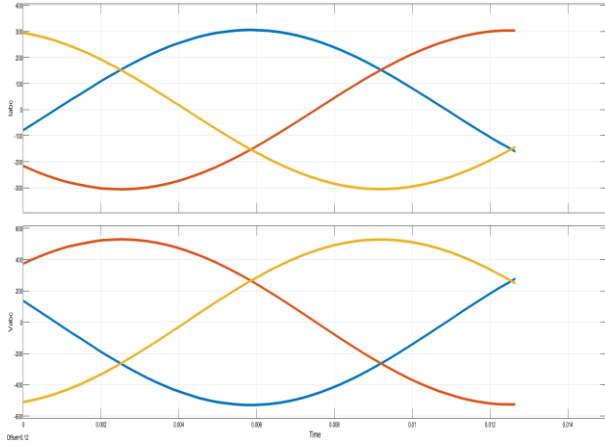


**Figure 14.** The three phases voltage ( $V_{abc}$ ) and current ( $I_{abc}$ )

The load types in the reality system are inductive load type, so there are generated real power ( $P_L$ ) and reactive power ( $Q_L$ ) that are both greater than zero. Figure 15 depicts the load powers.

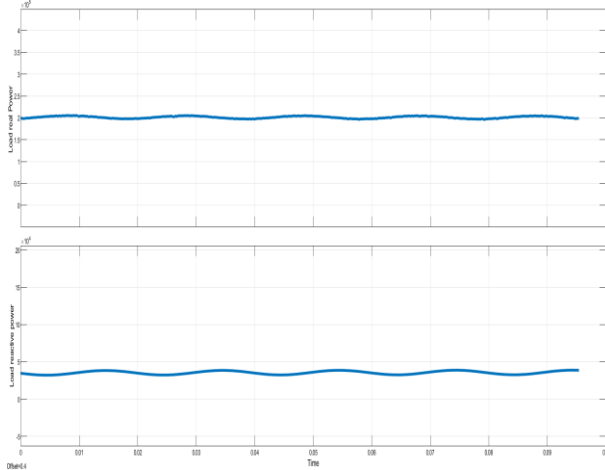


**Figure 15.** Real power ( $P_L$ ) and reactive power ( $Q_L$ )

The load demand ( $P_L$ ) is varied during the period, as a result the battery and grid powers ( $P_{bat}$  &  $P_G$ ) are varied also depending on the load variation. Figure 16 explains the load variation effect on system performance.

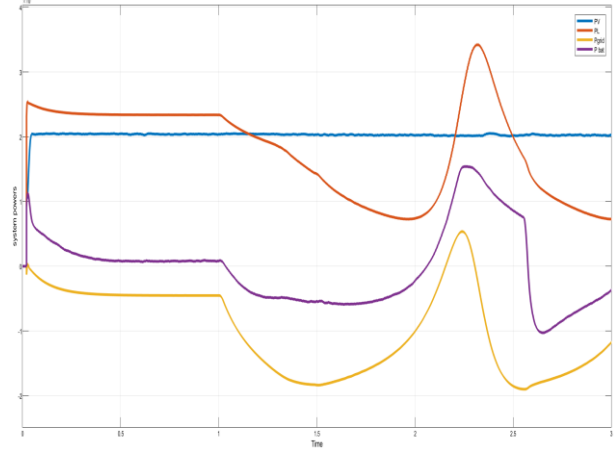


**Figure 16.** Load variation effect on system performance for 1000W/m<sup>2</sup>

It can divide and test the validity of the proposed PV system during its operations periods as:

From (0-1) sec, the  $P_L$  is greater than  $P_{PV}$ , so the battery can compensate the difference and the  $P_G$  is near to zero.

From (1.1-2.2) sec, the  $P_L$  is lower than  $P_{PV}$ , so the battery can be in idle state and the difference between  $P_{PV}$  and  $P_L$  is transferred to the grid as a  $P_G$ .

From (2.2-2.5) sec, the  $P_L$  is overstated to high power value and the  $P_{PV}$  with the  $P_L$  can't provide the load demand requirement, as a result the grid power  $P_G$  can compensate the system by the required power.

From (2.5-3) sec, again the  $P_L$  is lower than  $P_{PV}$ , the battery is of good charging level, the difference between  $P_{PV}$  and  $P_L$  is transferred to the grid as a  $P_G$ .

The state of the battery operation under the case study is as shown in figure 17.

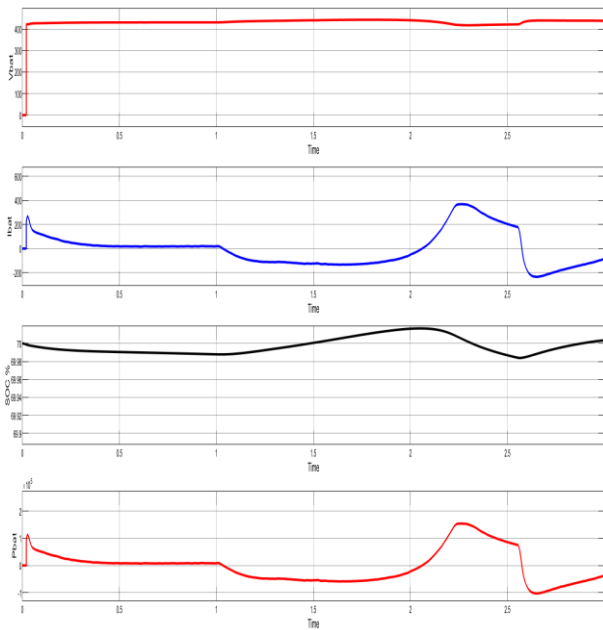


**Figure 17.** The battery voltage, current, SoC and power curves for 1000W/m<sup>2</sup>

It is clear the battery state curves that the battery voltage  $V_{bat}$  can keep its value with constant along the whole period, while the battery current  $I_{bat}$  and power  $P_{bat}$  is varied depending to the system working and with three levels: high to charge the battery, low when discharging the battery, and constant when no needing to the battery power. The state of charge (SoC) is varied according to battery operating modes, however, in the case under study the SoC is near to nominal setting value which is 70%.

In our research, we aim to develop a comprehensive monitoring and data acquisition system for a photovoltaic (PV) solar power system integrated with battery storage, load, and grid connection. The primary objective is to ensure efficient operation and management of the system by continuously monitoring key parameters such as PV voltage, current, and power; battery voltage, current, power, and State of Charge (SoC); load voltage, current, and power; as well as grid voltage, current, and power.

In our operational modes and throughout the entire duration, we continuously monitor previous states and values by displaying results using MATLAB/Simulink interfaces. For each parameter, we transmit four values: the maximum (max.), minimum (min.), mean, and variance. The max. value signifies the highest recorded value, while the min. value indicates the lowest. The mean value represents the average, and the variance reflects the deviation from the mean, representing the standard deviation. These measurements are taken for significant parameters including:

- Photovoltaic (PV): Voltage ( $V_{PV}$ ), current ( $I_{PV}$ ), and power ( $P_{PV}$ ).

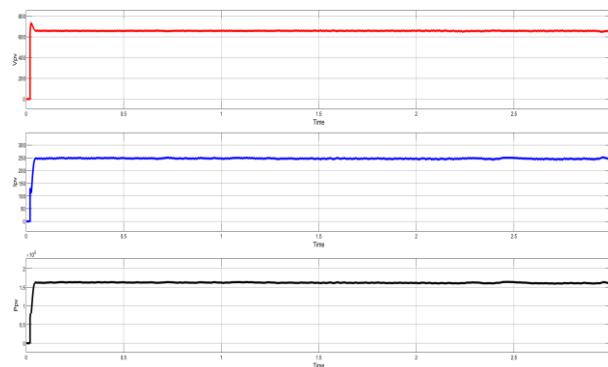
- Battery: Voltage ( $V_{bat}$ ), current ( $I_{bat}$ ), power ( $P_{bat}$ ), and State of Charge (SoC).
  - Load: Voltage ( $V_L$ ), current ( $I_L$ ), and power ( $P_L$ ).
  - Grid: Voltage ( $V_G$ ), current ( $I_G$ ), and power ( $P_G$ ).
- Subsequently, LoRa technology is utilized to continuously transmit and receive the aforementioned values, saving them as a worksheet or Excel file for further analysis.

By continuously monitoring these parameters, we can assess the performance of each component within the system and identify any anomalies or deviations from expected values. This real-time monitoring capability enables us to optimize system operation, detect and diagnose faults or failures promptly, and make informed decisions regarding system maintenance and performance improvement.

Furthermore, by transmitting the monitored data using LoRa communication technology, we can remotely access and analyze the system's performance data in real-time. This remote monitoring capability is particularly valuable for off-grid or remote solar power installations, where on-site inspection and maintenance may be challenging or impractical.

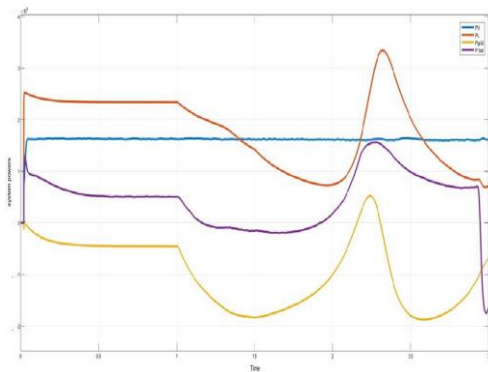
Overall, our goal is to develop a robust and reliable monitoring system that provides valuable insights into the performance and operation of PV solar power systems, facilitating efficient management and optimization of renewable energy resources.

Now, if the radiation is 800 W/m<sup>2</sup> and STC temperature with  $T=25C^\circ$ , the PV voltage ( $V_{PV}$ ), current ( $I_{PV}$ ), and the power ( $P_{PV}$ ) are shown in the figure 18.



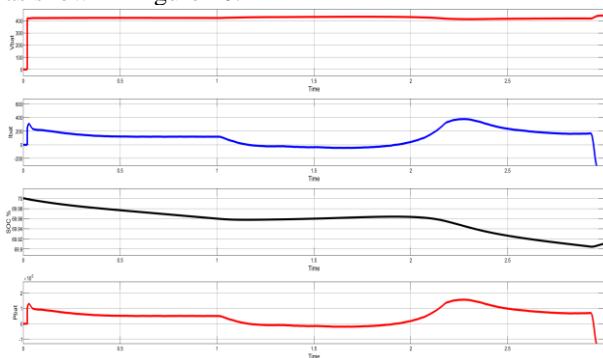
**Figure 18.** PV voltage, current, and power under 800W/m<sup>2</sup> results

Figure 19 explains the load variation effect on system performance.



**Figure 19.** Load variation effect on system performance for  $800\text{W}/\text{m}^2$

The state of the battery operation under the case study is as shown in figure 20.



**Figure 20.** The battery voltage, current, SoC and power curves for  $800\text{W}/\text{m}^2$

#### 4. Conclusion

PV solar array systems are widely used in many applications and always installed in far places, therefore such systems need remote monitoring process with suitable communication tool that can easily transceiver the commands and data. In this work, an IOT application for remote monitoring of grid-off /grid-connected solar PV array systems supplied with variable load is installed. The communication system used for data transmission is LoRa based. The solar power system works in two modes depending on the connected load, MPPT mode and constant voltage mode.

Data collection and processing play a critical role in monitoring systems tailored for Photovoltaic (PV) applications. It outlines the types of data collected by the system, encompassing various parameters such as PV performance metrics, battery status indicators, load characteristics, and grid-related parameters. To facilitate efficient transmission, this data will be transmitted using LoRa technology, ensuring secure communication channels while integrating robust security measures to safeguard the integrity of the transmitted data.

Solar power system simulated using MATLAB/Simulink software for all expected operating cases such as solar irradiance variation and load variation. LoRa communication system also simulated using MATLAB software for many types of modulation and SNR.

The system readings (voltages, currents, and powers) are transmitted and received in the remote monitoring room. The transmitted and received data are compared to show the system performance. For all simulated cases the data accuracy is very high.

The PV system operates in different modes, which are influenced by factors such as solar irradiance, generated solar power, connected load, battery state of charge (SoC), and maximum battery charging/discharging current limits. To optimize the system's performance and track the maximum power point (MPP) of the solar PV, two maximum power point tracking (MPPT) techniques can be employed: Incremental Conductance (INC) or Perturbation and Observation (P&O).

Several parameters need to be specified, including the average daily connected load profile, the region's daily available average solar energy (kWhr), solar PV system operating temperature, day of autonomy, battery recharge time, AC supply availability, and solar panel specifications. The determination of the number of PV panels required to meet the specified generation capability is based on data provided by the solar panel manufacturer.

Among numerous variables, the DC bus voltage level ( $V_{dc}$ ), solar irradiance ( $G_{rad}$ ), and battery state of charge (SoC) are crucial in determining the appropriate operating mode through supervisory control.

For future work, the studied system can be implemented using physical components that can verify the system performance from networking site of view. Also the examined system can be instantiated using real time components like microcontrollers, networking adaptor and attachable devices. Moreover, a double control room system may be a good solution for both communication loss or to overcome the local controller failure, to make the system more stable.

Lastly, in a viability of Wi-Fi system, it can depend on more accurate and friendly communication protocol like the ThinkSpeak environment protocol.

#### Author's Contributions

**Ercan Aykut:** Supervising, writing, editing, evaluating.

**Safaa Thamer Hawas:** Data collection, simulation, writing.

## Ethics

There are no ethical issues after the publication of this manuscript.

## References

- [1]. O. Bello and S. Zeadally, "Intelligent Device-to-Device Communication in the Internet of Things," *IEEE Systems Journal*, vol. 10, no. 3, pp. 1172–1182, Sep. 2016, doi: 10.1109/JSYST.2014.2298837.
- [2]. J. Mineraud, O. Mazhelis, X. Su, and S. Tarkoma, "A gap analysis of Internet-of-Things platforms," *Computer Communications*, vol. 89–90, pp. 5–16, Sep. 2016, doi: 10.1016/j.comcom.2016.03.015.
- [3]. D. Sehrawat and N. S. Gill, "Smart Sensors: Analysis of Different Types of IoT Sensors," in *2019 3rd International Conference on Trends in Electronics and Informatics (ICOEI)*, Tirunelveli, India: IEEE, Apr. 2019, pp. 523–528. doi: 10.1109/ICOEI.2019.8862778.
- [4]. A. J. Jara, P. Lopez, D. Fernandez, J. F. Castillo, M. A. Zamora, and A. F. Skarmeta, "Mobile digcovery: discovering and interacting with the world through the Internet of things," *Pers Ubiquit Comput*, vol. 18, no. 2, pp. 323–338, Feb. 2014, doi: 10.1007/s00779-013-0648-0.
- [5]. A. Čolaković and M. Hadžialić, "Internet of Things (IoT): A review of enabling technologies, challenges, and open research issues," *Computer Networks*, vol. 144, pp. 17–39, Oct. 2018, doi: 10.1016/j.comnet.2018.07.017.
- [6]. R. H. Weber and E. Studer, "Cybersecurity in the Internet of Things: Legal aspects," *Computer Law & Security Review*, vol. 32, no. 5, pp. 715–728, Oct. 2016, doi: 10.1016/j.clsr.2016.07.002.
- [7]. S. Madakam, R. Ramaswamy, and S. Tripathi, "Internet of Things (IoT): A Literature Review," *JCC*, vol. 03, no. 05, pp. 164–173, 2015, doi: 10.4236/jcc.2015.35021.
- [8]. P. Sethi and S. R. Sarangi, "Internet of Things: Architectures, Protocols, and Applications," *Journal of Electrical and Computer Engineering*, vol. 2017, pp. 1–25, 2017, doi: 10.1155/2017/9324035.
- [9]. Z. Ez Dallalbashi, S. Alhayalir, M. Jabbar Mnati, and A. Abdaljabar Alhayali, "Low-cost battery monitoring circuit for a photovoltaic system based on LoRa/LoRaWAN network," *IJECS*, vol. 29, no. 2, p. 669, Feb. 2023, doi: 10.11591/ijeecs.v29.i2.pp669-677.
- [10]. S. Nižetić, P. Šolić, D. López-de-Ipiña González-de-Artaza, and L. Patrono, "Internet of Things (IoT): Opportunities, issues and challenges towards a smart and sustainable future," *Journal of Cleaner Production*, vol. 274, p. 122877, Nov. 2020, doi: 10.1016/j.jclepro.2020.122877.
- [11]. T. M. Ghazal *et al.*, "IoT for Smart Cities: Machine Learning Approaches in Smart Healthcare—A Review," *Future Internet*, vol. 13, no. 8, p. 218, Aug. 2021, doi: 10.3390/fi13080218.
- [12]. M. Javaid, A. Haleem, R. P. Singh, R. Suman, and E. S. Gonzalez, "Understanding the adoption of Industry 4.0 technologies in improving environmental sustainability," *Sustainable Operations and Computers*, vol. 3, pp. 203–217, 2022, doi: 10.1016/j.susoc.2022.01.008.
- [13]. A. Ma, J. C. Tonday Rodriguez, and M. Sha, "Enabling Reliable Environmental Sensing with LoRa, Energy Harvesting, and Domain Adaptation," in *2024 33rd International Conference on Computer Communications and Networks (ICCCN)*, Kailua-Kona, HI, USA: IEEE, Jul. 2024, pp. 1–9. doi: 10.1109/ICCCN61486.2024.10637563.
- [14]. O. Chidolue and T. Iqbal, "Real-time monitoring and data acquisition using LoRa for a remote solar powered oil well," *IJAPE*, vol. 13, no. 1, p. 201, Mar. 2024, doi: 10.11591/ijape.v13.i1.pp201-212.
- [15]. R. Prodanović *et al.*, "Wireless Sensor Network in Agriculture: Model of Cyber Security," *Sensors*, vol. 20, no. 23, p. 6747, Nov. 2020, doi: 10.3390/s20236747.
- [16]. F. B. G. Pratama, F. Hidayatullah, E. L. I. P. Sari, I. K. A. Enriko, F. N. Gustiyana, and A. Luthfi, "Solar-Powered LoRa Wireless Water Quality Monitoring for Saline Tilapia Aquaculture," in *2024 International Conference on Green Energy, Computing and Sustainable Technology (GECOST)*, Miri Sarawak, Malaysia: IEEE, Jan. 2024, pp. 72–76. doi: 10.1109/GECOST60902.2024.10474710.
- [17]. S. Al-Sarawi, M. Anbar, K. Alieyan, and M. Alzubaidi, "Internet of Things (IoT) communication protocols: Review," in *2017 8th International Conference on Information Technology (ICIT)*, Amman, Jordan: IEEE, May 2017, pp. 685–690. doi: 10.1109/ICITECH.2017.8079928.
- [18]. A. Khalifeh, K. A. Aldahdouh, K. A. Darabkh, and W. Al-Sit, "A Survey of 5G Emerging Wireless Technologies Featuring LoRaWAN, Sigfox, NB-IoT and LTE-M," in *2019 International Conference on Wireless Communications Signal Processing and Networking (WiSPNET)*, Chennai, India: IEEE, Mar. 2019, pp. 561–566. doi: 10.1109/WiSPNET45539.2019.9032817.
- [19]. G. Peruzzi and A. Pozzebon, "A Review of Energy Harvesting Techniques for Low Power Wide Area Networks (LPWANs)," *Energies*, vol. 13, no. 13, p. 3433, Jul. 2020, doi: 10.3390/en13133433.
- [20]. S. Gupta and S. Gupta, "Energy Efficiency in IoT Based on Sensor Node Deployment Pattern," *RACS*, vol. 15, no. 6, p. e310322196674, Jul. 2022, doi: 10.2174/2666255814666210920160947.
- [21]. G. M. Cabello, S. J. Navas, I. M. Vázquez, A. Iranzo, and F. J. Pino, "Renewable medium-small projects in Spain: Past and present of microgrid development," *Renewable and Sustainable Energy Reviews*, vol. 165, p. 112622, Sep. 2022, doi: 10.1016/j.rser.2022.112622.
- [22]. A. N. Talib, K. Hafeez, M. J. Mnati, and S. A. Khan, "Design and Implementation of New Battery Monitoring System for Photovoltaic Application," in *2022 4th Global Power, Energy and Communication Conference (GPECOM)*, Nevsehir, Turkey: IEEE, Jun. 2022, pp. 1–7. doi: 10.1109/GPECOM55404.2022.9815759.
- [23]. U. Raza, P. Kulkarni, and M. Sooriyabandara, "Low Power Wide Area Networks: An Overview," *IEEE Commun. Surv. Tutorials*, vol. 19, no. 2, pp. 855–873, 2017, doi: 10.1109/COMST.2017.2652320.
- [24]. A. Khalifeh, F. Mazunga, A. Nechibvute, and B. M. Nyambo, "Microcontroller Unit-Based Wireless Sensor Network Nodes: A Review," *Sensors*, vol. 22, no. 22, p. 8937, Nov. 2022, doi: 10.3390/s22228937.



- [25]. K. Kutluay, Y. Cadirci, Y. S. Ozkazanc, and I. Cadirci, "A New Online State-of-Charge Estimation and Monitoring System for Sealed Lead–Acid Batteries in Telecommunication Power Supplies," *IEEE Trans. Ind. Electron.*, vol. 52, no. 5, pp. 1315–1327, Oct. 2005, doi: 10.1109/TIE.2005.855671.
- [26]. B. Al Homssi, K. Dakic, S. Maselli, H. Wolf, S. Kandeepan, and A. Al-Hourani, "IoT Network Design Using Open-Source LoRa Coverage Emulator," *IEEE Access*, vol. 9, pp. 53636–53646, 2021, doi: 10.1109/ACCESS.2021.3070976.
- [27]. D.-H. Kim, E.-K. Lee, and J. Kim, "Experiencing LoRa Network Establishment on a Smart Energy Campus Testbed," *Sustainability*, vol. 11, no. 7, p. 1917, Mar. 2019, doi: 10.3390/su11071917.
- [28]. A. Sales Mendes, D. M. Jiménez-Bravo, M. Navarro-Cáceres, V. Reis Quietinho Leithardt, and G. Villarrubia González, "Multi-Agent Approach Using LoRaWAN Devices: An Airport Case Study," *Electronics*, vol. 9, no. 9, p. 1430, Sep. 2020, doi: 10.3390/electronics9091430.

# A new method proposal to enhance foreground images against noisy backgrounds: Haytham Thresholding

Esin Mutlu<sup>1</sup> , Serkan Dereli<sup>2\*</sup> 

<sup>1</sup> Department of Electrical-Electronic Engineering, Faculty of Technology, Sakarya University of Applied Sciences, Sakarya, Türkiye

<sup>2</sup> Department of Electrical-Electronic Engineering, Faculty of Technology, Sakarya University of Applied Sciences, Sakarya, Türkiye

\* [dereli@subu.edu.tr](mailto:dereli@subu.edu.tr)

\* Orcid No: 0000-0002-1856-6083

Received: 17 May 2024

Accepted: 30 September 2024

DOI: 10.18466/cbayarfbe.1485592

## Abstract

Since only pixel intensities are taken into account in the binarization of gray images during the thresholding stage, it brings with it a significant problem. Because, since the relationship between pixels in the image is neglected, it is seen that noises are sometimes defined as an object, sometimes plays a role in changing the detected object, especially in noisy images where illumination is not uniform. In this study, a locally adaptive thresholding algorithm called Haytham Thresholding is proposed in order to eliminate these limitations of global thresholding algorithms and to eliminate noise caused by lighting during the binarization of the image. Especially in the literature, it is seen that noise is high in methods performed by taking the standard deviation into account when the image has a gradient feature. To prevent this, pixel values were normalized by taking into account the weights of the pixels in the window region instead of their standard deviation. These normalized values were added to the matrix values obtained by the average filter and then subtracted from the original image matrix. In the experiments, the proposed method was compared with Otsu and three different local thresholding algorithms by using four different image types also used in the literature. The comparison of the methods was made both visually and with image quality metrics such as PSNR and SSIM. As a result, it has been observed that the proposed method produces successful results compared to both global thresholding and local thresholding algorithms frequently used in the literature.

**Keywords:** Binarization, Image Segmentation, Image Enhancement, Image Processing, Local Thresholding

## 1. Introduction

The scientific world has spent the last half century in the fields of artificial intelligence, computer vision and image processing [1]. Especially with Industry 4.0 and digitalization, these areas continue to increase their popularity with the spread of self-learning devices and systems [2]. Although these expressions seem to be intertwined, according to the generally accepted opinion, image processing is among the sub-branches of computer vision and computer vision is among the sub-branches of artificial intelligence [3].

While image processing is used to prepare the resulting images for processing such as noise removal and image

transformation, computer vision is used to produce meaningful data from images such as object recognition,

feature extraction and classification [4]. In other words, while image processing is used for operations with images as inputs and outputs in the literature, operations whose input is image, but output is meaningful data are considered as computer vision [5].

Figure 1 shows the flowchart mostly used in the field of computer vision. Pre-processing in this diagram and Binarization, which is the subject of this study, are the stages used in image processing. As can be seen from this figure, Binarization is the last step in image processing [6] and in a sense, it is extremely important for the segmentation and following other operations to be performed correctly [7]. Because if an object on the



image cannot be detected correctly, neither the classification of this object nor its features can be extracted in the next stages. This shows that both preprocessing and binarization stages are very important [8]. Binarization is the process of distinguishing whether pixels belong to the background or foreground object according to a certain threshold value from the two-dimensional gray image [9]. Considering the importance of the subject, it is seen that the studies focus on obtaining the threshold value used to determine whether the pixel belongs to the background or the object. For this purpose, many algorithms and techniques, which are grouped as local, global and adaptive, have been proposed in the literature [10].

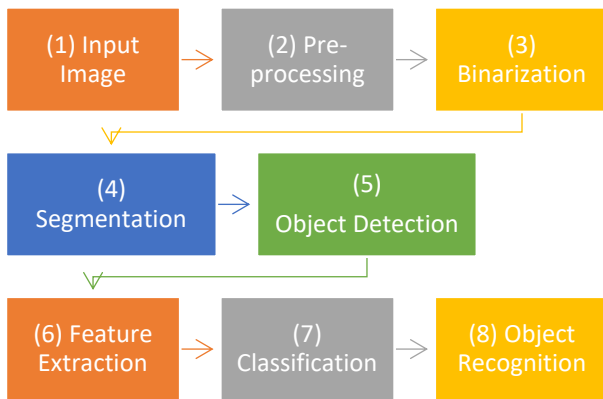


**Figure 1.** Flow diagram of computer vision

The techniques used and suggested in the literature for binarization consisting of 0 and 1 values are known as thresholding. As seen in Figure-2, thresholding is also one of the simplest image segmentation techniques known, which is the separation of each object in that image [11]. Yanowitz and Bruckstein proposed a segmentation technique based on adaptive thresholding for situations where it is difficult to separate the object from the background in images where the illumination is not uniform [12]. They used double thresholding method to perform segmentation of white blood cell from acute lymphoblastic leukemia images. They applied the thresholding method to the gray format of the image and the HSV format separately and continued the flow by obtaining a binary image from the intersection of both outputs [13]. They proposed a dynamic thresholding algorithm for the segmentation and classification of colored skin images. They drew attention to two important problems in studies that normally use fixed thresholding values: First, there are pixels that are classified as skin even though there is no skin. The other is with pixels that are treated as background even though they are skin [14]. First, they identified the most important weakness of the Otsu global thresholding algorithm as follows: If the difference between the background and foreground in the image does not change significantly, that is, if there is no contrast between these two situations, then Otsu

cannot provide accurate thresholding. In order to avoid this negative situation, they proposed the gray stretching method, which reveals the wavelet transform-based class variance change [15]. They proposed a new local thresholding algorithm to solve the time-consuming problems of traditional local thresholding algorithms. For this purpose, instead of the standard deviation used in traditional methods, they used an integral image to obtain the mean process at the local level in a shorter time [16]. They identified a shortcoming in the study of Otsu, the most well-known global thresholding algorithm, and made a new proposal to improve it. They argued that Otsu thresholding algorithm produces the threshold value closer to the class with high variance value if the difference in variance within the class is high in the image, and they presented a proposal that adjusts the threshold value to adjust for this deficiency [17]. They proposed an algorithm that works adaptively in the local structure to determine the threshold value in gradient images where the illumination is variable. Because they claimed that global thresholding algorithms are insufficient to process such images correctly, instead local algorithms produce more appropriate threshold values [18]. Similarly, they proposed a new method based on average filters and gradients to determine the correct threshold value for images with variable illumination and contrast. The averaging filter is used to normalize the noisy background [19]. Inspired by nature, they proposed a much more interesting neutrosophic-based thresholding algorithm. Because the neutrosophic has a natural ability to obtain uncertain data. With the Neutrosophic technique, the values of the noise-based uncertain pixels in the image can be obtained [20].

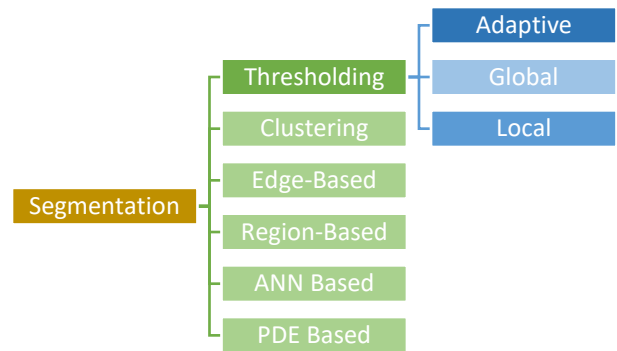


**Figure 2.** Methods of image segmentation

As a result, the following conclusions can be drawn from the literature review:

- If the image does not have a lighting problem and the background has a uniform distribution, then global thresholding algorithms produce effective results.
- If the color contrast between the background and foreground of the image is high, then global thresholding techniques will give successful results.



- Adaptive local thresholding algorithms give better results in images with lighting problems and close contrast between background and foreground objects.
- Thresholding algorithms are still widely used in image segmentation.

In the method emphasized in this study, a new matrix is created using the pixel weights of local regions. This matrix, which normalizes pixel values according to neighboring pixel values, is used in the final stage to reveal the background in the image. Thus, each pixel plays a role in separating the ground in its own region from the foreground.

The following sections of the study are organized as follows: First, the method proposed in the study is explained comprehensively with examples at the algorithmic level. Then, experiments are performed and analyzes are made on test images frequently used in these areas in the literature. In the last stage, the findings are expressed as a result.

## 2. Materials and Methods

Binarization is known as taking the values of 1 and 0 according to a certain threshold value so that the pixels on the image can be processed more easily [21]. In fact, the main purpose of the process is to divide the image into two separate parts, the background and the foreground [22]. Thresholding techniques, which are one of the most important subjects of image processing and generally divided into two as local and global in the literature, are used for this process [23]. However, in this study, the adaptive method, which is one of the popular thresholding techniques of recent times, was preferred. Because mostly the images obtained are exposed to different noises, especially regionally, it becomes difficult to detect the objects in these images. Adaptive methods improve binary conversion by using different thresholding values in different regions on the same image [24].

In this study, a binarization method is proposed to accurately convert images with non-uniform illumination into binary images. The basic idea behind the proposed method is to create a second copy of the original image, which is weaker in terms of pixels, and to subtract this copy image from the original image. Thus, in the final image, the background pixels are represented with a truly zero value, while the foreground pixels are represented with higher pixel values. Therefore, the minimum contrast value required to separate the background from the foreground can be reduced to only 1 pixel. In fact, in Figure 3, this situation is expressed as the separation of pixels with a value of zero as background in the binarization stage.

The step-by-step process flow chart of the proposed method is shown in Figure 3. In addition, since the proposed method performs local thresholding, it was applied by scanning the original image with a window of a certain size, as in the literature. As seen in the figure, the process starts by taking a new frame from the image. Average filter, normalization, subtraction, binarization and morphological decomposition operations are applied sequentially to each frame. The stage that distinguishes the study from the literature is the normalization stage, in which the coefficient is used in the extraction stage is obtained. Because the aim at this stage is to strengthen the background region of the image or the pixel values close to the background region and mark them as the background region in the difference process. This situation is clearly seen in the 5th image in the images given in Figure 7, where the difference process is performed, and the pixels are brought very close to the background region. Therefore, in the last stage, the pixel values that do not have a zero value (or have a value  $\geq 1$ ) are marked as part of the foreground.

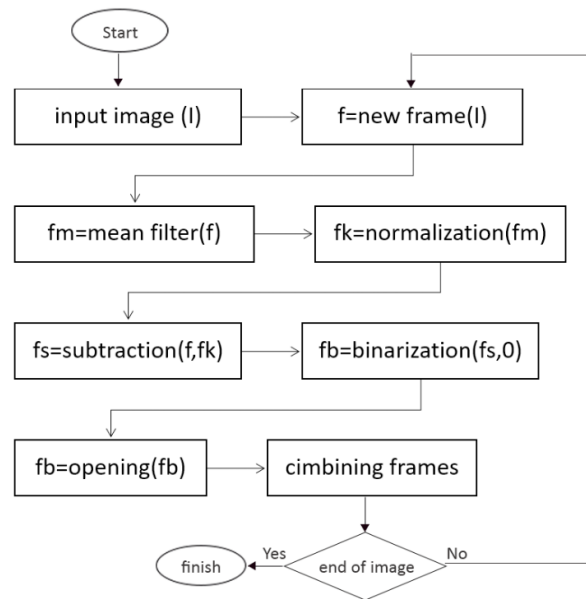


**Figure 3.** The flow chart of the proposed method

According to Figure 4, in the next step, high value pixels are reduced by applying the Mean filter to the image converted to gray. As it is known, this filter changes the value of the pixel according to the average of the pixels in the determined group [25]. After applying the mean filter, a formula is proposed in this study to make the background and foreground distinction clear, and this stage is named Normalization in Figure 3.

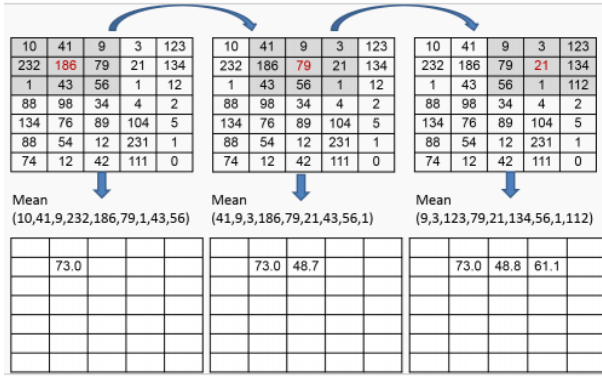


**Figure 4.** Step-by-step mean filter representation

The calculation used in the local thresholding algorithm proposed in this study is performed by taking the difference of the input image matrix from the normalization matrix, as given in Equation-3.1. In this equation,  $f$  refers to the next frame matrix obtained from the input image and  $fk$  refers to the normalization matrix. The step of obtaining the normalization matrix in this equation is given in Equation-3.2. In this equation, the image softened by the average filter is expanded by adding it with the  $k$  coefficient expressed in Equation-3.3. This value, which is unique to this study and produced dynamically with this equation in each image frame, is actually included in the process as a constant value in the traditional local thresholding algorithm. The aim here is to minimize the noise that is likely to remain in the image.  $n$  is the digital conversion resolution value of the processed image. Since 8-bit images were used in this study, the calculation was made as  $n = 8$ . Each equation is repeated for the pixel values of all frames obtained from the input image.

$$fs(x, y) = f(x, y) - fk(x, y) \quad (3.1)$$

$$fk(x, y) = fm(x, y) + k \quad (3.2)$$

$$k = \frac{2^n}{mean(f)} \quad (3.3)$$

In the subtraction step, the normalized matrix value is subtracted from the frame matrix, which is converted to gray. In fact, with this subtraction, the image background is set to zero, which is the lowest pixel value. The changes in the pixel values in the image matrix from the beginning to the end of the proposed method in the study are illustrated in Figure 5. In this figure, the "a" matrix part belongs to the original gray image, the "b" matrix part belongs to the normalization process, and the "c" matrix part belongs to the difference matrix. In this process, zero values seen in the "c" matrix are determined as background, while other values are interpreted as belonging to the foreground object.

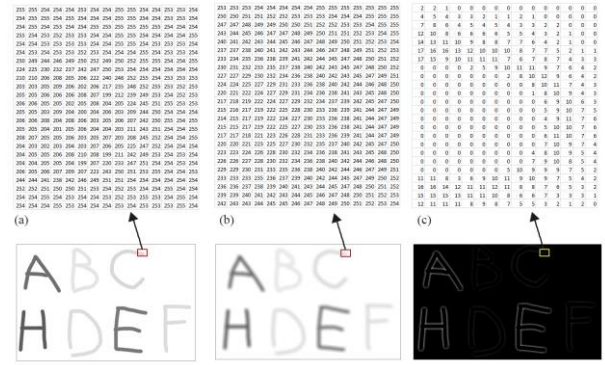


**Figure 5.** Image pixel values resulting from different algorithm steps (a: input matrix; b: normalization matrix; c: subtraction matrix)

The effect of the normalization process proposed in this study on the output image and its contribution to the study are depicted in Figure-5. If thresholding had been done without normalization, the output image shown as (a) in Figure 6, which was quite noisy, would have been obtained. However, as a result of the normalization process, these noises were eliminated and the image (b) in Figure 6 was obtained.



**Figure 6.** Difference of mean filter and normalization stages in the output matrix (a: mean filter matrix; b: normalization matrix)

During the binarization phase, the "c" matrix seen in Figure 5 is converted to binary format by taking the zero value as a reference. Therefore, pixels with a value of "0" are decomposed as background, and pixels with a value greater than "0" are decomposed as foreground.

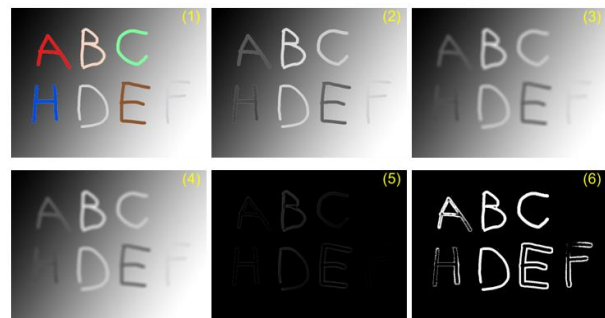


**Figure 7.** Illustrated explanation of the stages of the proposed method

Figure 7 shows the effects of all the steps performed in the proposed method on the images separately. These images show the following operations in order:

- (1): Input image
- (2): Gray conversion of input image
- (3): Image with mean filter
- (4): Normalized image with Equation 3.2 and 3.3
- (5): Arithmetic subtraction of Image-4 from Image-2 using Equation 3.1
- (6): Binary image obtained from image 5 with 0 value pixels as background and other pixels as foreground

### 3. Findings and Discussion

This study presents a proposal to optimally obtain the threshold value of images with gradient colour distribution, where global thresholding algorithms are quite unsuccessful. For this, the mean filtered image was subjected to normalization with the process seen in Equation-1, and thus the background values of the image were brought very close to the 0 value. In order to demonstrate the success of the proposed method, some images used in the literature have also been tested in this method.

Figure 8 shows the test images used in this study. When selecting test images, the fact that they were used in the literature was the reason for preference. In addition, for the success of the proposed method, it was preferred that both the background and foreground have a gradient image feature.

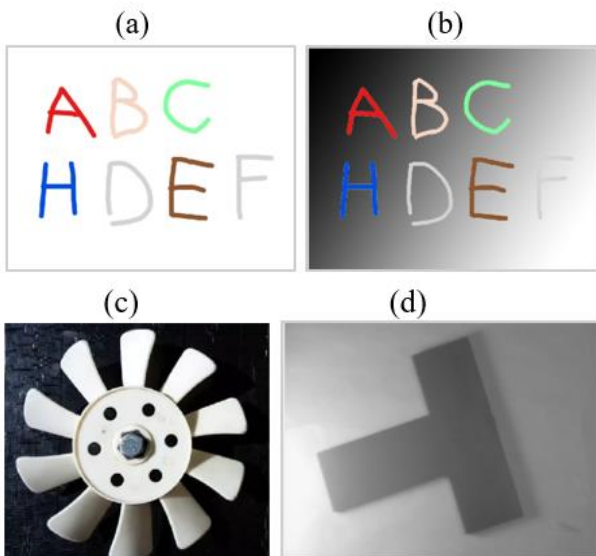


**Figure 8.** Test images used in the study

In Figure 9, the threshold value obtained by the Otsu Algorithm is used for binary image conversion. These results show that the success of global thresholding algorithms is very poor in cases where the color distributions in the image are opposite. Because, as it is known, global thresholding algorithms use the same

threshold value in the entire image. Therefore, when the color intensity of the background changes or the color intensity of the objects qualified as foreground differs, the result is quite unsuccessful. Figure 10 illustrates examples of thresholding operations performed with the method proposed in this study. When the samples are examined in detail, it is seen that the method is very successful especially in images with gradient colour density.

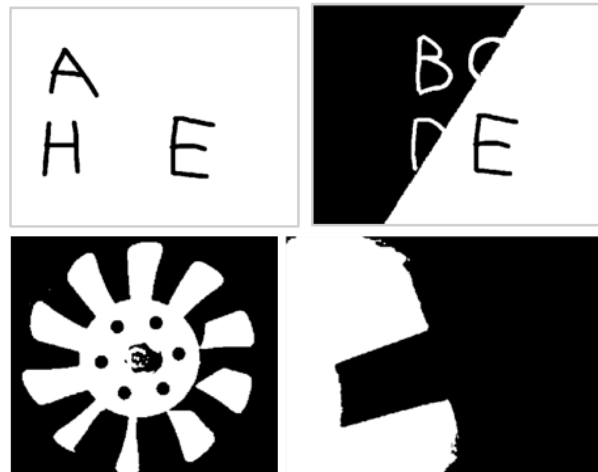


**Figure 9.** Test results with global thresholding algorithm (Otsu)

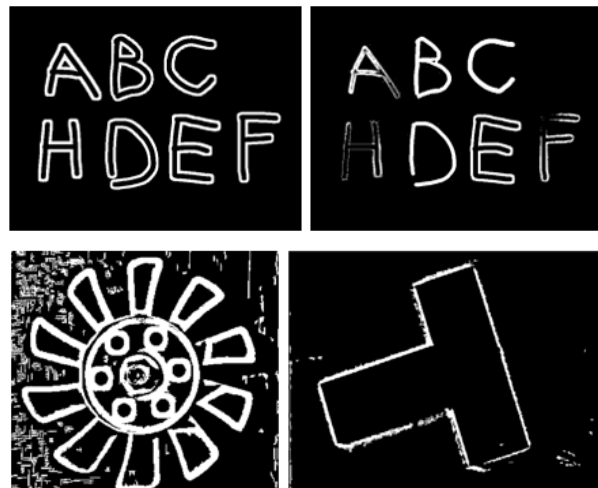


**Figure 10.** The results obtained with the local adaptive thresholding method proposed in this study

In many projects based on image processing or computer vision, maximum system success can be achieved by creating special areas at the point of getting the most ideal image. However, nowadays, since such projects are spread over the general and open area, it can be checked whether the image is obtained in the most ideal way after the image is taken. In this case, the field of machine learning comes into play, as whether



the images obtained are unavoidably appropriate or not depends on the learning of the system. Here, the method proposed in this study will be an indispensable part of such a system. Because the images are directly proportional to the light intensity and in many cases it becomes difficult for the light to affect each part of the image at the same rate. Therefore, sometimes the resulting image may have a gradient colour feature. The detection of objects in such an image will be possible with the methods proposed in this study.

Finally, the contribution of the normalization stage to the output image, which makes this study stand out in the literature, is clearly seen in Figure-11. In this figure, (a) and (d) show the input test image, (b) and (e) show the binary image formed with the average filter, and (c) and (f) show the binary image formed with the normalization process. It has produced very successful results, especially in converting images with gradient background illumination into binary images (see e and

f). If the images are to be interpreted, it appears that the normalization stage has eliminated any possible noise in the image.

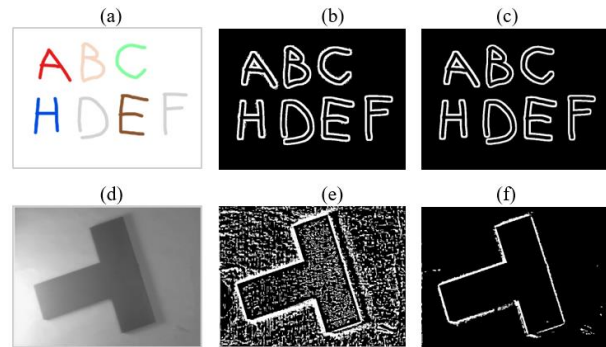


**Figure 11.** Contribution of the normalization stage to the quality of the output image

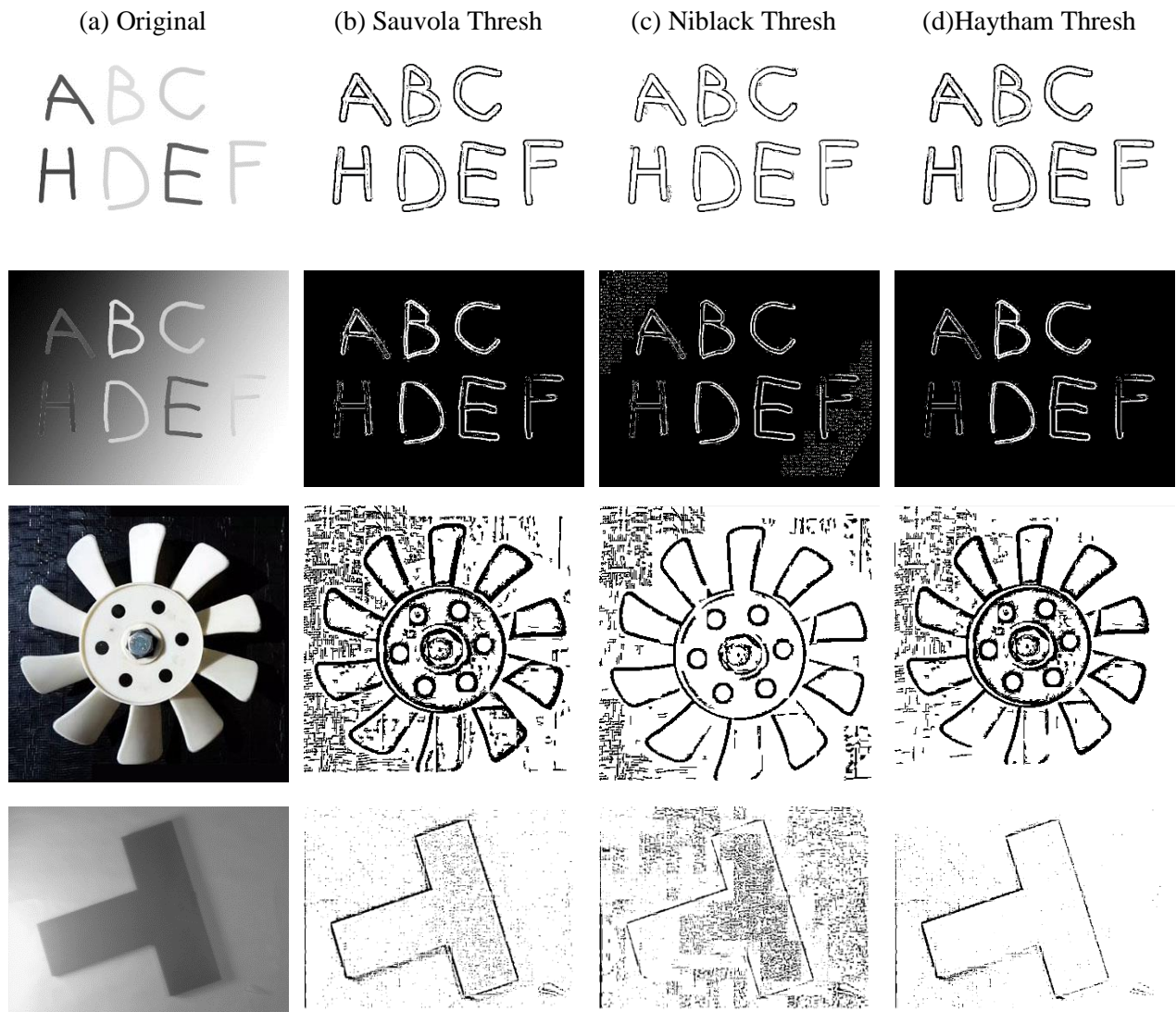


**Figure 12.** Comparison with some local thresholding methods in the literature

Figure 12 contains a visual comparison of three local thresholding techniques frequently used in the literature and the technique proposed in this study. In the experiments, images with only a gradient background were not preferred. It was also preferred in images where the contrast between the foreground and background was low. It is seen that the proposed technique has a clear advantage over other methods in both high contrast and gradient background samples.

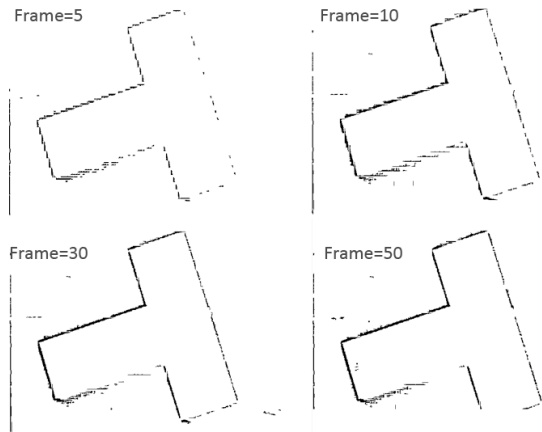


**Figure 13.** Effects of frame size on the success of the method in local scanning

Figure 13 illustrates the effects of the frame sizes used by the proposed method during image scanning on the success of the method. It is observed that as the frame gets smaller, the number of lost pixels increases, while as the frame gets larger, the number of false pixels thought to belong to the object increases.

Table 1 gives a quantitative comparison of the proposed method with important local thresholding techniques frequently used in the literature, in terms of measurement with image quality metrics. As can be seen from this table, the proposed method could not achieve the best result only in test image number 3. The reason for this is that the contrast between the background and foreground in the test image is high and it can be easily segmented with the global thresholding method. However, it is clearly seen that the proposed method has better image quality metrics than the other two methods. Other than that, in all test images, the methods in the literature fell behind the proposed method.

**Table 1.** Measuring test results with image quality metrics

Image	Sauvola		Niblack		Bernsen		Haytham	
	PSNR	SSIM	PSNR	SSIM	PSNR	SSIM	PSNR	SSIM
Test image 1 (Fig 10.a)	36.61	0.795	37.45	0.804	33.78	0.749	38.05	0.815
Test image 2 (Fig 10.b)	34.36	0.698	31.38	0.556	29.65	0.488	36.25	0.758
Test image 3 (Fig 10.c)	27.36	0.336	29.43	0.441	30.74	0.535	29.74	0.491
Test image 4 (Fig 10.d)	37.41	0.4994	31.44	0.347	31.47	0.323	40.54	0.665

Table 2 shows the calculation times used by the method used in the literature and proposed in this study during the binarization process of the test images. As can be clearly seen from this table, the method proposed in this study performs similar results to other methods in terms of running time. Therefore, this technique can be easily used instead of other techniques in the detection and segmentation stages of images.

**Table 2.** Measuring test results in terms of computation time

Image	Computation Time			
	Sauvola	Niblack	Bernsen	Haytham
Test image 1 (Fig 10.a)	0.414	0.371	0.793	0.401
Test image 2 (Fig 10.b)	0.373	0.384	0.812	0.379
Test image 3 (Fig 10.c)	0.174	0.182	0.511	0.175
Test image 4 (Fig 10.d)	0.294	0.316	0.565	0.305

#### 4. Conclusion

In this study, the problem of obtaining threshold values of images with gradient colour density in thresholding, which is one of the most critical stages of image processing, has been solved. For this purpose, a new normalization matrix was created using the weights of the relevant pixel region and the output image was created with this matrix. To demonstrate the success of the proposed method, it was compared with both global and local thresholding algorithms frequently used in the literature. In the comparison, images with gradient background and gradient foreground features were preferred, along with images in which the contrast between the background and foreground was minimal. The success of the proposed method is clearly evident in the visual outputs and is also demonstrated qualitatively by PSNR and SSIM image quality metrics. Therefore, the method proposed in this study can be easily used both in cases where general thresholding is required and in situations where illumination is problematic. When

evaluated in terms of future projection of the study, the expectations are as follows: Since the success of the proposed method is directly related to the normalization matrix created, the success of the method can be further increased by developing this matrix with different techniques in the literature or by combining it with other local thresholding techniques.

### Acknowledgement

This work was supported by the Office of Scientific Research Projects Coordination at Sakarya University of Applied Sciences. Project number: 122-2023.

### Author's Contributions

**Esin Mutlu:** Performing experiments, comparisons with scientific metrics and helped in manuscript preparation.

**Serkan Dereli:** Created the algorithm, coded it in Matlab and result interpretation.

### Ethics

There are no ethical issues after the publication of this manuscript.

### References

- [1]. Aslam, Y, Santhi, N. 2020. A comprehensive survey on optimization techniques in image processing. *Materials Today: Proceedings*, vol. 24:1758-1765.
- [2]. Dargan, S, Kumar, M, Ayyagari, M, Kumar, G. 2020. A survey of deep learning and its applications: a new paradigm to machine learning. *Archives of Computational Methods in Engineering*, vol. 27(4):1071-1092.
- [3]. Viejo, C, G, Torrico, D, Dunshea, F, Fuentes, S. 2019. Emerging technologies based on artificial intelligence to assess the quality and consumer preference of beverages. *Beverages*, 5(62):1-25.
- [4]. Hamuda, E, Glavin, M, Jones, E. 2016. A survey of image processing techniques for plant extraction and segmentation in the field. *Computers and Electronics in Agriculture*, 125:184-199.
- [5]. Wiley, V, Lucas, T. 2018. Computer vision and image processing: a paper review. *International Journal of Artificial Intelligence Research*, 2:29-36.
- [6]. Dereli, S. 2020. True-Random Number Generator Based on Image Histogram. *Academic Perspective Procedia*, 3(1):301-307.
- [7]. Chaubey, A. 2016. Comparison of the local and global thresholding methods in image segmentation. *World Journal of Research and Review*, 2:1-4.
- [8]. Aqeel, E. 2015. The Use of Threshold Technique in image segmentation. *Journal of the College of Basic Education*, 21:797-806.
- [9]. Xiong, W., Zhou, L., Yue, L., Li, L., Wang, S. 2021. An enhanced binarization framework for degraded historical document images. *EURASIP Journal on Image and Video Processing*, 2021(1): 13.
- [10]. Guruprasad, P. Overview of different thresholding methods in image processing, in 3rd National Conference on ETACC, 2020.
- [11]. Kaur, D, Kaur, Y. 2014. Various image segmentation techniques: a review. *International Journal of Computer Science and Mobile Computing*, 3(5):809-814.
- [12]. Kang, S., Iwana, B. K., Uchida, S. 2021. Complex image processing with less data—Document image binarization by integrating multiple pre-trained U-Net modules. *Pattern Recognition*, 109: 107577.
- [13]. Li, Y, Zhu, R, Mi, L, Cao, Y, Yao, D. 2016. Segmentation of white blood cell from acute lymphoblastic leukemia images using dual-threshold method. *Computational and mathematical methods in medicine*, 2016:1-12.
- [14]. Khairnar, S., Thepade, S. D., Gite, S. 2021. Effect of image binarization thresholds on breast cancer identification in mammography images using OTSU, Niblack, Burnsen, Thepade's SBTC. *Intelligent Systems with Applications*, 10: 200046.
- [15]. Liu, L, Yang, N, Lan, Y, Li, J. 2015. Image segmentation based on gray stretch and threshold algorithm. *Optik*, 126:626-629.
- [16]. Xiang, F, Jian, Z, Wei, W, Licheng, H. 2015. A new local threshold segmentation algorithm. *Computer Applications and Software*, 32:195-197.
- [17]. Yang, P, Song, W, Zhao, X, Zheng, R, Qingge, L. 2020. An improved Otsu threshold segmentation algorithm. *International Journal of Computational Science and Engineering*, 22:146-153.
- [18]. Mehta, N., Braun, P. X., Gendelman, I., Alibhai, A. Y., Arya, M., Duker, J. S., Waheed, N. K. 2020. Repeatability of binarization thresholding methods for optical coherence tomography angiography image quantification. *Scientific Reports*, 10(1): 15368.
- [19]. Mustafa, W, Yazid, H. 2016. Background correction using average filtering and gradient based thresholding. *Journal of Telecommunication, Electronic and Computer Engineering (JTEC)*, 8:81-88.
- [20]. Guo, Y, Y. 2014. A novel image thresholding algorithm based on neutrosophic similarity score. *Measurement*, 58:175-186.
- [21]. Su, B, Lu, S, Tan, C. 2012. Robust document image binarization technique for degraded document images. *EEE transactions on image processing*, 22:1408-1417.
- [22]. Lin, M., Ji, R., Xu, Z., Zhang, B., Chao, F., Lin, C. W., Shao, L. 2022. Siman: Sign-to-magnitude network binarization. *IEEE Transactions on Pattern Analysis and Machine Intelligence*, 45(5): 6277-6288.
- [23]. Wunnava, A, Naik, M, Panda, R, Jena, B, Abraham, A. 2020. A novel interdependence based multilevel thresholding technique using adaptive equilibrium optimizer. *Engineering Applications of Artificial Intelligence*, 94:1-19.
- [24]. Saputra, M, Santosa, P. Obstacle Avoidance for Visually Impaired Using Auto-Adaptive Thresholding on Kinect's Depth Image. in IEEE 14th Intl Conf on Scalable Computing and Communications and Its Associated Workshops, 2014.
- [25]. Kandemir, C, Kalyoncu, C, Toygar, Ö. 2015. A weighted mean filter with spatial-bias elimination for impulse noise removal. *Digital Signal Processing*, 46:164-174.

# Nascency of Physiopathological Activation by The Effect of Genomic Single Nucleotide Exchange Factor in The *PNPLA3* rs738409 Genotype of Patients with Hepatocellular Carcinoma

Anıl Delik<sup>1\*</sup> , Yakup Ülger<sup>2</sup> 

<sup>1</sup> Cukurova University, Faculty of Science and Literature, Department of Biology, Adana, Türkiye

<sup>2</sup> Cukurova University, Faculty of Medicine, Department of Gastroenterology, Adana, Türkiye

\*[anildelik@gmail.com](mailto:anildelik@gmail.com)

\* Orcid No: 0000-0002-6443-9392

Received: 16 April 2024

Accepted: 4 October 2024

DOI: 10.18466/cbayarfbe.1437557

## Abstract

Background Patatin-like Phospholipase Domain-Containing 3 (*PNPLA3*) rs738409 is a genetic variant that is associated with an increased risk of developing hepatocellular carcinoma (HCC) in patients with chronic liver disease. This functional mechanism may cause liver cancer by altering protein function without affecting gene expression. Our aim in this study is to investigate the potential effect of *PNPLA3* polymorphism on HCC development and to report its results. Material and Methodology A case-control study was designed involving 224 diagnosed and pathologically confirmed patients with HCC. Four groups were formed as ([HBV] n = 110, [HCV] n = 38, [other etiologies] n = 76) and 62 healthy controls. *PNPLA3* genotyping in patients diagnosed with HCC was concluded by DNA isolation from blood samples. *PNPLA3* rs738409 variant was genotyped in RT PCR device with Taq Man allelic separation test designed by the manufacturers according to protocols. The C nucleotide and G nucleotide were detected in VIC; FAM hydrolysis probes were used for genotyping and binding. SPSS program was used for statistical analysis. Results The *PNPLA3* genotypes were determined for the groups of HBV-related HCC, HCV-related HCC, other etiologies-related HCC, and control. The HBV-related HCC group had CC (n = 58), CG (n = 36), and GG (n = 16) genotypes. The HCV-related HCC group had CC (n = 22), CG (n = 9), and GG (n = 7) genotypes. The other etiologies-related HCC group had CC (n = 35), CG (n = 26), and GG (n = 15) genotypes. The control group had CC (n = 36), CG (n = 13), and GG (n = 13) genotypes. Conclusions *PNPLA3* rs738409 is an inherited risk factor for HCC development in chronic liver disease. Our study found that the GG genotype can directly activate liver cancer in other etiology groups. According to our findings, we think that *PNPLA3* polymorphism can be used as a biomarker in the development of HCC due to other etiologies group.

**Keywords:** Adiponutrin, Chronic Liver Disease, Cirrhosis, Genetic, Genotyping

## 1. Introduction

Hepatocellular carcinoma (HCC) is the most lethal cancer of the liver and ranks among the top causes of cancer-related deaths worldwide. [1]. According to the data in 2015, it was reported that there were 900,000 liver carcinogenesis cases worldwide [2,3]. Liver cancer, with a death / incidence rate of 0.95, constitutes one of the deadliest cancers in general. The etiology of HCC is well defined by studies [4], with the most important risk factors being chronic hepatitis B virus (HBV), nonalcoholic fatty liver disease (NAFLD), chronic hepatitis C virus (HCV), metabolic syndromes and alcohol intake. The association between HCC

genetic susceptibility and higher risk of HCC in HBV and HCV-infected patients in several studies conducted in Asia, supports the role of genetic susceptibility in liver cancer [5,6]. In addition to environmental factors, the functions of genetic and epigenetic mechanisms are inevitable in the development of liver cancer, which has very high mortality rates [7] and can provide important information in explaining the variations observed in individuals susceptible to HCC development among high-risk populations. The link between various genome studies performed in HCC patients and HCC-*PNPLA3* is noted in studies [8].

Protein 3 (adiponutrin), which contains the patatin-like phospholipase domain, is a protein of 481 amino acids



that is most highly expressed in hepatocytes [9]. This SNP triggers increased hepatocellular triglyceride accumulation and is associated with the development of HCC [10]. *PNPLA3* increases hepatocellular lipid accumulation to higher levels by affecting the enzymatic hydrolysis of triglycerides. Due to the chemical structure of methionine, its long side chain greatly reduces the catalytic activity of the enzyme despite the functional catalytic couple [11]. The damaged *PNPLA3* protein accumulates on hepatic lipid droplets and paves the way for the development of HCC due to its decreased lipolytic activity [12]. In a genetic study conducted in a population of 2503 patients with HCC development on a cirrhotic basis, it was revealed that the *PNPLA3* variant is a very important risk factor. [13]. In studies conducted, the emergence of HCC proliferation in the development of HCV-related cirrhosis is associated with the *PNPLA3* variant [14]. Therefore, we hypothesize that the *PNPLA3* genetic variation (rs738409: C>G) can be a pre-diagnosis non-invasive biomarker for liver cancer.

## 2. Materials and Methods

### 2.1. Study Design

A total of 224 patients with HCC who applied to the Department of Gastroenterology and 62 controls were included in this study. Ethics committee approval was obtained for the study and informed consent forms were obtained from all patients. HCV, HBV infective, other etiologies (such as, alcohol intake, NAFLD, metabolic disease) and control group. Control group was formed from the population without liver disease, over 18 years old, no smoking, no alcohol, normal liver enzyme levels. Ultrasonography and liver function tests of healthy controls were determined as normal values. Diagnosis of HCC patients was made using ultrasonography, computed tomography, and tumor biopsy. The category of other etiologies included autoimmune liver disease, steatohepatitis (alcoholic, NASH), cryptogenic cirrhosis, Budd Chiari syndrome, Wilson's disease and hereditary tyrosinemia.

### 2.2. Determination of *PNPLA3* Single Nucleotide Polymorphism (SNP)

Primers specially designed for this study were used for *PNPLA3* rs738409 (to provide amplification). One of the probes is attached to the C nucleotide and the other to the G nucleotide. RT-PCR endpoint analysis was used to detect mutant variants.

### 2.3. Genotyping

For our study, genomic DNA was obtained and isolation from whole blood was provided using a DNA isolation kit (DNA kit, Germany, Hidden, QIAGEN). *PNPLA3* rs738409 variant was genotyped in RT PCR device with

Taq Man allelic separation test designed by the manufacturers according to protocols. The amplification primers used in our study were synthesized by Thermo Fischer using standard phosphoramidite chemistry and fluorescent dye (victoria green fluorescent [VIC]), and 6-carboxyfluorescein (fluorescein amidites [FAM]) labeled probes were purified by reverse-phase high-performance liquid chromatography (HPLC). The primer sequences used for the *PNPLA3* rs738409 polymorphism were designed as Forward primer: 5'-GAGGGTGTATGTTAGTTCCTCCCGT-3', Reverse primer: 5'-AGCACACTTCAGAGGCCCC-3'. The C nucleotide and G nucleotide were detected in VIC; FAM hydrolysis probes were used for genotyping and binding. One of the probes binds to the C nucleotide, while the other binds to the G nucleotide. Endpoint analysis uses this difference to distinguish between wild-type and mutant types.

### 3.4. Statistical analysis

Statistical Package Software for Social Science, version 21 SPSS program was used for statistical analysis. Kolmogorov-Smirnov's test was used for normal distribution. Chi-square test, Student's t-test, Mann-Whitney U test, ANOVA and Kruskal-Wallis tests were used to analyze the data obtained in our study.

## 3. Results and Discussion

### 3.1. Demographic, laboratory data and genetic polymorphism

The main draft of the study is the relationship and comparison between *PNPLA3* genotype and HCC (HBV, HCV and other etiologies). Patients with HCC (n = 224) a mean age of 62.4 years old, with 78.6% of male; the main etiologies of underlying liver disease were HBV (n = 110), HCV (n = 38), other etiologies (n = 76) and 88.8% of the patients had cirrhosis. HBV related (CC = 58, 53.3%, CG = 36, 32.7%, GG = 16, 14%), HCV related (CC = 22, 57.9%, CG = 9, 23.7%, GG = 7, 18.4%), Others etiologies (CC = 35, 46.1%, CG = 26, 34.2%, GG = 15, 19.7%), control (CC = 36, 58%, CG = 13, 21.3%, GG = 13, 21.3%) respectively, (p = 0.49) (Table 1).

Laboratory results were examined according to the etiology distribution and parameters with significant differences were specified; Mean and standard deviation for total cholesterol HCC (143 ± 47), HBV related (154.3 ± 43), HCV related (109.8 ± 28), other etiologies (141.4 ± 58) (p = 0.008). Glucose for HCC (119 ± 64), HBV related (110 ± 40), HCV related (162 ± 114), other etiologies (107 ± 41) respectively (p = 0.006). All other results and p values are shown in Table 2. AFP <400 ng/ml overall HCC (n = 132, 69.5%), HBV related (n = 74, 70.5%), HCV related (n = 23, 67.6%), other etiologies (n = 35, 68.6%), AFP > 400 ng/ml overall

HCC (n = 58, 30.5 %), HBV related (n = 31, 29.5%), HCV related (n = 11, 32.4%), other etiologies (n = 16, 31.4%), respectively (p = 0.94). Cirrhosis according to *PNPLA3* genotypes in HCC, with cirrhosis patients CC genotype (n = 90, 54.5%), CG genotype (n = 52, 31.5%), GG genotype (n = 23, 13.9%), without cirrhosis patients CC genotype (n = 7, 35%), CG genotype (n = 7, 35%), GG genotype (n = 6, 30%), (p = 0.11) (Table 3). The G allele of rs738409 was significantly associated with increased HCC susceptibility (odds ratio [OR] = 1.25, 95% confidence interval [CI] = 1.04–1.50, p = 0.018). GG genotype of rs738409 was also associated with higher HCC risk (OR = 1.59, 95% CI = 1.06–2.39, p = 0.024). CG genotype of rs738409 showed a trend

toward increased HCC risk (OR = 1.016, 95% CI = 0.99–1.03, p = 0.11). GG genotype of rs738409 was associated with elevated HCC susceptibility (OR = 1.018, 95% CI = 1.00–1.03, p = 0.03). The CG+GG genotypes of rs738409 were significantly linked to HCC risk (OR = 1.021, 95% CI = 1.00–1.03, p = 0.01). CC+GG genotypes of rs738409 were associated with increased HCC susceptibility (OR = 1.003, 95% CI = 0.98–1.01, p = 0.03). *PNPLA3* rs738409 variant appears to play a role in HCC susceptibility. These findings contribute to our understanding of genetic factors influencing liver cancer risk (Table 4).

**Table 1.** Patatin like phospholipase domain containing 3 (*PNPLA3*) genotype rates in hepatocellular carcinoma (HCC) patients according to etiological distribution

Characteristics	CC Genotype	CG Genotype	GG Genotype	P value
HBV, (n,%)	58 (53.3)	36 (32.7)	16 (14)	0.49
HCV (n,%)	22 (57.9)	9 (23.7)	7 (18.4)	
Other Etiology (n,%)	35 (46.1)	26 (34.2)	15 (19.7)	
Control (n,%)	36 (58)	13 (21)	13 (21)	
Overall (n,%)	151 (52.8)	84 (29.3)	51 (17.9)	

HBV: Hepatitis B, HCV: Hepatitis C

**Table 2.** Initial presentation clinical outcome 224 patients with hepatocellular carcinoma (HCC) according to etiologies.

Characteristics	Overall HCC (n= 224)	HBV (n=110)	HCV (n= 38)	Other Etiologies (n=76)	P value
Age (years), mean ± SD	62.4 ± 11	61 ± 10.5	67.1 ± 7.5	62 ± 1.9	0.01
Gender					0.31
Female (n,%)	48 (21.4)	19 (17.3)	9 (23.7)	20 (26.3)	
Male (n,%)	176 (78.6)	91 (87.7)	29 (76.3)	56 (73.7)	
HBG (kg/m <sup>2</sup> ), mean ± SD	12.1 ± 2.1	12.2 ± 1.9	11.4 ± 1.8	12.2 ± 2.6	0.3
TC (mg/dl), mean ± SD	143 ± 47	154.3 ± 43	109.8 ± 28	141.4 ± 58	0.008
LDL (mg/dL), mean±SD	87.1 ± 41	94.2. ± 40	64.3 ± 23.5	89.3 ± 51.5	0.06
TG (mg/dL), mean ± SD	102 ± 58.5	110.7 ± 64	83.5 ± 64	95.6 ± 55.1	0.28
HDL (mg/dL),mean ±SD	35.2 ± 19.6	38..2 ± 24	28.7 ± 9.8	33.8 ± 11.5	0.28
HCT mean ± SD	34.9 ± 6.1	35.12 ± 6.7	33.74 ± 4.5	35.5 ± 6	0.41
PLT x1000/m <sup>3</sup> , mean ± SD	145.4 ± 95	138.7 ± 79	132.5 ± 86	167.4 ± 123	0.13
Ferritin (U/L), mean ± SD	376 ± 458	388 ± 480	353 ± 363	365 ± 484	0.93
Glucose mean ± SD	119 ± 64	110 ± 40	162 ± 114	107 ± 41	0.006
Creatinin, mean ± SD	0.96 ± 0.4	0.95 ± 0.46	1.1 ± 0.6	0.81 ± 0.3	0.45
HbA1c, mean ± SD	6.25 ± 1.4	6 ± 1.1	6.8 ± 2.2	N.A.	0.39
TP, mean ± SD	6.9 ± 1.1	7 ± 0.7	7.2 ± 0.5	6.1 ± 2.3	0.13
Albumin gr/dl, mean ± SD	3.03 ± 0.6	3.01 ± 0.6	3.02 ± 0.6	3.07 ± 0.5	0.87
PT, mean ± SD	16.1 ± 5.5	16.1 ± 6	16.4 ± 4.6	16 ± 4.8	0.93
Smoking					0.10
Yes (n,%)	94 (47.7)	57 (51.8)	12 (33.3)	25 (47.2)	
No (n,%)	104 (52.3)	53 (48.2)	23 (63.7)	28 (52.8)	
INR, mean ± SD	1.33 ± 0.2	1.32 ± 0.2	1.35 ± 0.2	1.34 ± 0.3	0.80
CRP, mean ± SD	27.8 ± 40	30.9 ± 43	17.4 ± 24	28.4 ± 41.1	0.30

AFP (n=190)					0.94
<400 ng/ml, (n,%)	132 (69.5)	74 (70.5)	23 (67.6)	35 (68.6)	
>400 ng/ml, (n,%)	58 (30.5)	31 (29.5)	11 (32.4)	16 (31.4)	
MELD, mean ± SD	12.65 ± 4.9	12.86 ± 5.4	12.64 ± 4.5	12.14 ± 4.2	0.80
Tümör diameter	6.22 ± 4	5.6 ± 3.2	7 ± 5.9	6.7 ± 3	0.13
Cirrhosis					0.24
Yes, (n,%)	167 (88.8)	89 (86.4)	32 (97)	46 (88.5)	
No, (n,%)	21 (11.2)	14 (13.6)	1 (3)	6 (11.5)	
Vascular invasion					0.96
Yes, (n,%)	62 (34.4)	33 (34)	11 (33.3)	18 (36)	
No, (n,%)	118 (65.6)	64 (66)	22 (67.7)	32 (64)	

HGM, hemoglobin, LDL: Light dansite lipoprotein, TG: Trigiliserit, HDL: High dansite lipoprotein, GGT: Gama glutamil transpherase, TC: Total colesterol, T.B: Total bilirubin, PLT: platelet, CRP: Creaktive protein, AFP: alfa feto protein, MELD: Model for end stage Liver disease, SD: Standart devialation, PT; protrombin, N.A.: not available

**Table 3.** Distrubition of *PNPLA3* polymorphism (CC, CG, GG) in hepatocellular carcinoma (HCC)

Characteristics	CC Genotype (n=115)	CG Genotype (n=71)	GG Genotype (n=37)	P value
Age (years), mean ± SD	62.1 ± 11	63.1 ± 9.1	61.9 ± 12.4	0.82
Gender				0.44
Female (n,%)	26 (54.2)	17 (35.4)	5 (10.4)	
Male (n,%)	88 (51.2)	53 (30.8)	31 (18)	
HBG (kg/m <sup>2</sup> ), mean ± SD	12.3 ± 2.1	11.8 ± 2.3	12.5 ± 1.9	0.46
TC (mg/dl), mean ± SD	151.4 ± 49	137.5 ± 49	129.1 ± 37	0.30
LDL (mg/dL), mean±SD	94.5 ± 46	80.9 ± 39	79.6 ± 33.5	0.39
TG (mg/dL), mean ± SD	101.4 ± 50	114.1 ± 75	80.2 ± 31	0.25
HDL (mg/dL), mean ±SD	35.4 ± 26	35.6 ± 15	34.5 ± 9.5	0.98
HCT mean ± SD	35.8 ± 5.8	33.4 ± 6.9	35.7 ± 5.3	0.04
PLT x1000/m <sup>3</sup> , mean ± SD	147.7 ± 94	151.2 ± 97	124 ± 97	0.43
Ferritin (U/L), mean ± SD	356.5 ± 473	411 ± 446	374 ± 461	0.84
Glucose mean ± SD	116.8 ± 45	109.5 ± 38.5	151.7 ± 129	0.11
Creatinin, mean ± SD	0.79 ± 0.18	0.95 ± 0.25	1.21 ± 0.8	0.03
HbA1c, mean ± SD	6.03 ± 0.65	6.9 ± 1.7	4.47 ± 0.18	0.06
TP, mean ± SD	6.92 ± 0.71	6.91 ± 1.72	4.47 ± 0.18	0.99
Albumin gr/dl, mean ± SD	3.08 ± 0.64	3.04 ± 0.71	2.88 ± 0.50	0.39
PT, mean ± SD	15.59 ± 4.53	17.14 ± 7.3	15.4 ± 2.7	0.19
Smoking				0.61
Yes (n,%)	53 (57.6)	25 (27.2)	14 (15.2)	
No (n,%)	49 (48)	34 (33.3)	19 (18.6)	
INR, mean ± SD	1.3 ± 0.3	1.36 ± 0.2	1.31 ± 0.2	0.53
CRP, mean ± SD	23.9 ± 33	33.4 ± 51	25.7 ± 34	0.43
AFP (n=190)				0.014
<400 ng/ml, (n,%)	72 (55.8)	42 (32.6)	15 (11.6)	
>400 ng/ml, (n,%)	28 (49.1)	16 (28.1)	13(22.8)	
MELD, mean ± SD	12.54 ± 5.2	12.6 ± 45	12 ± 4.7	0.89
Tümör diameter, mean ± SD	6.57 ± 4.24	5.73 ± 3.75	6.06 ± 4.09	0.45
Cirrhosis				0.11
Yes, (n,%)	90 (54.5)	52 (31.5)	23 (13.9)	
No, (n,%)	7 (35)	7 (35)	6 (30)	

Vascular invasion				0.70
Yes, (n,%)	31 (51.7)	21 (35)	8 (13.3)	
No, (n,%)	62 (53)	35 (29.9)	20 (17.1)	

LDL: Light Dansite lipoprotein, TG: Trigiliserit, HDL: High dansite lipoprotein,TC: Total colesterol, T.B Total bilirubin, GGT: Gama glutamil transpherase, TC: Total colesterol, PLT: platelet, CRP: Creactive protein, AFP: alfa feto protein, MELD: Model for end stage Liver disease, SD: Standart devialation,HGM, hemoglubin, PT; protrombin

**Table 4.** The *PNPLA3* genotypes and allele frequencies in HCC and control group

<i>PNPLA3</i> alleles	HCC n=76 (%)	Control n=62 (%)	P value	OR (%95 CI)
Allel				
C	96 (63,1)	83 (66,9)		1.00 (reference)
G	56 (36,9)	41 (33,1)	0.018	1.25 (0.04-1,50)
Codominant				
CC	35 (46)	34 (54,8)		1.00 (reference)
CG	26 (34,2)	15 (24,2)	0.11	1.016 (0.99-1.03)
GG	15 (19,8)	13 (21)	0.024	1.59 (1.06-2,39)
Dominat				
GG	15 (19,7)	13 (21)	0.03	1.018 (1.00-1.03)
CC+CG	61 (80,3)	49 (79)		1.00 (reference)
Recessive				
CC	35 (46)	34 (54,8)		1.00 (reference)
CG+GG	41 (54)	28 (45,1)	0.01	1.021 (1.00-1.03)
Overdominant				
CC+GG	50 (65,8)	47 (75,8)		1.00 (reference)
CG	26 (34,2)	15 (24,2)	0.03	1.003 (0.98-1.01)

HCC: hepatocellular carcinoma

There are not enough studies to define the effective role of *PNPLA3* in the development of HCC in cancer development. However, we can think of *PNPLA3*'s genetic susceptibility for HCC development as a natural extension of the relationship between NAFLD and *PNPLA3* genetic variation. Similarly, this is common in patients with other HCC risk factors, including fatty liver disease, HCV infection [15], diabetes mellitus, obesity [16] and alcohol use [17]. Alcohol lubrication and NAFLD create a similar pathological condition

[18,19]. The rs738409 (G) variant of the *PNPLA3* gene is a major genetic factor that contributes to steatosis and fibrosis progression in various liver diseases, according to independent studies [20-23].

The prognosis of HCC patients with the GG genotype of the *PNPLA3* variant was worse than those with the CC or CG genotype. The GG genotype has a distinct prognostic impact on HCC survival compared with the main survival predictors. Patients with the *PNPLA3* GG genotype may have a higher risk of vascular invasion,

poor tumor differentiation, lymph node involvement, or other clinical factors that affect HCC prognosis, although this hypothesis lacks definitive evidence. Hassan et al. proposed that cirrhosis symptoms, such as bleeding, fluid accumulation in the abdomen, and low platelet count, make the clinical management of HCC more challenging and often force oncologists to lower the optimal dose of intensive chemotherapy or restrict surgical removal [24]. This could reduce the patients' survival by impairing their response to treatment and narrowing their effective treatment options. It is hard to assess the relationship between *PNPLA3* genotypes and the response to different treatment types separately, because of the variety of treatment methods used. In our study, the relationship between HCC *PNPLA3* was examined and CC genotype was found as 52.8%, CG genotype 29.3%, GG genotype 17.9% in all HCC patients and *PNPLA3* relation was found to be more significant in other etiology group patients including alcoholic, NAFLD group. CC genotype is 46.1%, CG genotype is 34.2%, GG genotype is 19.7%, respectively in other etiology group. The survival curve of the *PNPLA3* other etiologies group shows that patients with the GG genotype have a lower survival rate ( $p = 0.65$ ). Our study is consistent with the results of Hassan et al. The relationship between *PNPLA3* and HCC was first reported to increase the prevalence of liver cancer in patients with rs738409 (GG) homozygous HCV-associated liver disease [25]. This research involved a small subset of patients in a case-control study [26]. Chronic inflammation caused by the complex interplay of oxidative stress, liver fat accumulation, and insulin resistance is a hallmark of liver diseases related to HCV. This inflammation creates a pro-oncogenic microenvironment that favors tumor growth. These traits are intrinsically connected, and they mutually enhance each other in the process of alcoholic carcinogenesis [27]. In addition, it has been reported that some HCV-dependent protein is directly linked to tumorigenesis and accelerates carcinogenic processes [28]. This report suggests that *PNPLA3* has a weaker effect on HCC risk in patients with HCV-associated cirrhosis compared with alcoholics. In our study, CC genotype 57.9%, CG genotype 23.7%, GG genotype 18.4% were found in the relationship between *PNPLA3*-HCV. It was determined as the lowest group as the GG genotype ratio. In our study, it was determined that the *PNPLA3* gene rs738409 C > G polymorphism increased the risk of HCC development due to other etiology (NASH) and the GG genotype increased OR:1.59 (1.00-1.04) times more risk and was statistically significant ( $p = 0.024$ ) (Table 4). Studies have shown that *PNPLA3* polymorphism is an independent factor associated with serum AFP. Moritou et al. investigated the patient characteristics related to the *PNPLA3* 148 M genotype [29]. In our study, serum AFP level was the factor that we found significantly related to *PNPLA3* genotype ( $p = 0.014$ ). Although it was stated in some studies that AFP level could be a significant biomarker for the

diagnosis of HCC patients, Caviglia et al. reported that they could not reach this result stated in their study. According to our result, we think that the effective use of AFP level with other serum biomarkers may create a useful result for the diagnosis of liver cancer. In a case-control study involving 200 patient populations, it was reported that the combination of AFP level and exosomal hnRNPH1 mRNA markers increased the diagnostic value for liver cancer by 0.891 (95% CI = 0.873-0.939,  $p = 0.005$ ). The sensitivity of the study was 87.5% and the specificity was 84.8% [13,24]. In our study, the AUC value was determined as 0.51 without combining AFP with other biomarkers (95% CI = 0.407-0.618,  $p = 0.82$ ). The *PNPLA3* variant causes an increase in triglyceride accumulation in liver cells, and together it causes non-activation of the protein hydrolase enzyme and activation of hepatic stellate cells, triggering the development of liver cancer [30].

#### 4. Conclusion

In conclusion, limitations of our study include that it was conducted in a single center, did not include patients from different geographical regions and ethnic groups, and long-term follow-up data are incomplete, making it difficult to assess the long-term effects of the *PNPLA3* rs738409 genotype. Despite these limitations, our study contains important genetic data that may be needed in the diagnosis of HCC. A strong diagnostic marker can be created by integrating the *PNPLA3* polymorphism CG and GG genotype with other serum non-invasive biomarkers in patients with chronic liver HCC due to NAFLD and alcohol etiology.

#### Author Contributions

Concept – A.D., Y.Ü.; Design – A.D., Y.Ü.; Supervision – A.D., Y.Ü.; Resources – A.D., Y.Ü.; Materials – A.D., Y.Ü.; Data Collection and/or Processing – A.D., Y.Ü.; Analysis and/or Interpretation – A.D.; Literature Search – A.D.; Writing Manuscript – A.D.; Critical Review – Y.Ü.; Other – Y.Ü.

#### Ethics

Ethics Committee approval was received at the Local Ethics Committee, Cukurova University Balcalı Hospital Faculty of Medicine Ethics Committee, dated 08.03.2024, code of ethics committee: 33, meeting number: 142

#### References

- [1]. Chen B., et al., *Harnessing big “omics” data and AI for drug discovery in hepatocellular carcinoma*. Nat Rev Gastroenterol Hepatol. 2020;17:238-51.
- [2]. Bray F., et al., *Global Cancer Statistics GLOBOCAN estimates of incidence and mortality*



- worldwide for 36 cancers in 185 countries. *CA Cancer J. Clin.* 2018;68, 394–424.
- [3]. Global Burden of Disease Liver Cancer Collaboration et al. *The burden of primary liver cancer and underlying etiologies from 1990 to 2015 at the global, regional, and national level: results from the global burden of disease study 2015.* *JAMA Oncol.* 2017;3, 1683–1691.
- [4]. Ryerson AB., et al., *Annual report to the nation on the status of cancer, 1975-2012, featuring the increasing incidence of liver cancer.* *Cancer.* 2016;122, 1312–1337.
- [5]. Njei B., et al., *Emerging trends in hepatocellular carcinoma incidence and mortality.* *Hepatology.* 2015;61:191–199.
- [6]. Forner A., Reig M. and Bruix J., *Hepatocellular carcinoma.* *Lancet* 2018;391:1301-14.
- [7]. Yang J., et al., *PNPLA3 and TM6SF2 Variants as Risk Factors of Hepatocellular Carcinoma Across Various Etiologies and Severity of Underlying Liver Diseases.* *Int J Cancer* 2018; 144; 533-544.
- [8]. Brownin JD. and Horton JD. *Molecular mediators of hepatic steatosis and liver injury.* *J Clin Invest.* 2004;114:147-152.
- [9]. Naik A., Košir R. and Rozman D. *Genomic aspects of NAFLD pathogenesis.* *Genomics.* 2013; 102: 84-95.
- [10]. Hori M., et al., *Association between combination of glutathione-S-transferase M1, T1 and P1 genotypes and non-alcoholic fatty liver disease.* *Liver Int.* 2009;29:164-8.
- [11]. Xin YN., et al., *Molecular dynamics simulation of PNPLA3 I148M polymorphism reveals reduced substrate access to the catalytic cavity.* *Proteins* 2013; 81: 406-414.
- [12]. Pirazzi C., et al., *Patatinlike phospholipase domain-containing 3 (PNPLA3) I148M (rs738409) affects hepatic VLDL secretion in humans and in vitro.* *J Hepatol* 2012; 57: 1276-1282.
- [13]. Browning JD., et al., *Prevalence of hepatic steatosis in an urban population in the United States: Impact of ethnicity.* *Hepatology.* 2004; 40: 1387– 1395.
- [14]. Czaja AJ., et al., *Host- and disease-specific factors affecting steatosis in chronic hepatitis C.* *J Hepatol.* 1998; 29: 198– 206.
- [15]. Stickel F., et al., *Genetic variation in the PNPLA3 gene is associated with alcoholic liver injury in Caucasians.* *Hepatology.* 2011;53:86-95.
- [16]. Trepo E., et al., *Common polymorphism in the PNPLA3/adiponutrin gene confers higher risk of cirrhosis and liver damage in alcoholic liver disease.* *J Hepatol,* 2011;55:906-912.
- [17]. Valenti L., et al., *Patatin-like phospholipase domain-containing 3 I148M polymorphism, steatosis, and liver damage in chronic hepatitis C.* *Hepatology.* 2011;53:791-799
- [18]. E. Trepo, et al. *Impact of patatin-like phospholipase-3 (rs738409 C>G) polymorphism on fibrosis progression and steatosis in chronic hepatitis C.* *Hepatology.* 2011;54:60-69.
- [19]. H.D. Nischalke, C. et al., *The PNPLA3 rs738409 148 M/M genotype is a risk factor for liver cancer in alcoholic cirrhosis but shows no or weak association in hepatitis C cirrhosis.* *PLoS One.* 2011;6:27087.
- [20]. H.K. Seitz and F. Stickel. *Molecular mechanisms of alcohol-mediated carcinogenesis.* *Nat Rev Cancer.* 2007;7: 599-612.
- [21]. D.R. McGivern and S.M. Lemon. *Virus-specific mechanisms of carcinogenesis in hepatitis C virus associated liver cancer.* *Oncogene.* 2011;30:1969-1983.
- [22]. Liu YL., et al., *Carriage of the PNPLA3 rs738409 C >G polymorphism confers an increased risk of non-alcoholic fatty liver disease associated hepatocellular carcinoma.* *J Hepatol.* 2014; 61: 75– 81.
- [23]. Xu H., et al., *Serum exosomal hnRNPH1 mRNA as a novel marker for hepatocellular carcinoma.* *Clin Chem Lab Med.* 2017;56:479–484
- [24]. Hassan MM et al., *Genetic variation in the PNPLA3 gene and hepatocellular carcinoma in USA: risk and prognosis prediction.* *Mol Carcinog.* 2013;52 Suppl 1:E139-47.
- [25]. Caviglia GP, et al., *Highly sensitive alpha-fetoprotein, lens culinaris agglutinin-reactive fraction of alpha-fetoprotein and des-gamma-carboxyprothrombin for hepatocellular carcinoma detection.* *Hepatol Res* 2016;46:E130–E135
- [26]. He S., et al., *A sequence variation (I148M) in PNPLA3 associated with nonalcoholic fatty liver disease disrupts triglyceride hydrolysis.* *J Biol Chem.* 2010; 285: 6706– 15.

- [27]. Pirazzi C., et al., *Patatin-like phospholipase domain-containing 3 (PNPLA3) I148M (rs738409) affects hepatic VLDL secretion in humans and in vitro*. J Hepatol. 2012; 57: 1276– 82.
- [28]. Min HK., et al., *Metabolic profiling reveals that PNPLA3 induces widespread effects on metabolism beyond triacylglycerol remodeling in Huh-7 hepatoma cells*. Am J Physiol Gastrointest Liver Physiol. 2014; 307: G66– 76.
- [29]. Pirazzi C., et al., *PNPLA3 has retinyl-palmitate lipase activity in human hepatic stellate cells*. Hum Mol Genet. 2014; 23: 4077– 85.
- [30]. Moritou Y., et al., *Predictive Impact of Polymorphism of PNPLA3 on HCC Development After Interferon Therapy in Japanese Patients With Chronic Hepatitis C*. Springerplus. 2013; 2: 251.



# Detection of Atrial Fibrillation with Custom Designed Wavelet-based Convolutional Autoencoder

Öykü Eravcı<sup>1</sup> , Nalan Özkurt<sup>2\*</sup> , Özlem Memiş<sup>3</sup> , Evrim Şimşek<sup>3</sup> 

<sup>1</sup> Graduate School, Yaşar University, Izmir, Türkiye

<sup>2</sup> Dept. of Electrical Electronics Engineering, Yaşar University, Izmir, Türkiye

<sup>3</sup> Dept. of Cardiology Ege University, Izmir, Türkiye

\* [nalan.ozkurt@yasar.edu.tr](mailto:nalan.ozkurt@yasar.edu.tr)

\* Orcid No: 0000-0002-7970-198X

Received: 1 July 2024

Accepted: 9 October 2024

DOI: 10.18466/cbayarfbe.1508153

## Abstract

Remote monitoring of patients is of great importance in terms of early diagnosis of diseases and improving people's quality of life. With the rapid development of deep learning techniques, wearable health technologies have leaped forward. This has made the automatic diagnosis even more important. In this study, we provide a deep learning approach for classifying Atrial Fibrillation (AF) arrhythmia that uses a customized wavelet-based convolutional autoencoder (WCAE) model. WCAE is employed as an anomaly detector, which combines the time-frequency domain examination ability of wavelet and the data-driven feature learning capability of convolutional autoencoders. The proposed approach received average scores of 95.45%, 99.99%, 90.90%, and 95.23% for accuracy, precision, recall, and F1, respectively, on a large selection of publicly available datasets. The outcomes of the experiments demonstrate the significance of using deep learning-based models in diagnosing AF. Moreover, it is observed that utilization of wavelet methods along with autoencoder model has a great potential for biomedical signal processing systems.

**Keywords:** Atrial fibrillation detection, ECG, Autoencoder, Deep learning, Discrete wavelet transform

## 1. Introduction

In the last century, Atrial Fibrillation (AF) has been the most extensively studied heart rhythm disorder, yielding valuable findings [1]. Atrial Fibrillation (AF) is an irregular and rapid atrial rhythm that can occur at a rate of 300-500 beats per minute. In Normal Sinus Rhythm (NSR), the atria conduct electrical impulses smoothly and regularly, initiated by the sinoatrial node. However, AF occurs when there are abnormalities in the generation of impulses or structural abnormalities in the cellular connections, resulting in irregular and chaotic impulses [2]. Clinical practice most commonly manages atrial fibrillation (AF), which is associated with a higher risk of death, stroke, and peripheral embolism, and the incidence of this condition rises with age [1]. According to a 2023 guideline for the diagnosis and management of atrial fibrillation by the American College of Cardiology (ACC) and American Heart Association (AHA), the number of patients with AF in 2010 was estimated that 5.2 million, that is expected to rise to 12.1 million by the year 2030. The number of new AF patients added each

year was 1.2 million in 2010, and it is expected that this number will increase to 2.6 million per year by 2030 [2]. The electrocardiogram (ECG) has been a widely used tool in clinical medicine by both cardiologists and non-cardiologists for many years. It is a fast, simple, and inexpensive test available even in settings with limited resources. The test provides insights into the physiological and structural state of the heart and can also provide important diagnostic information for systemic conditions [3]. The condition known as AF is identified by irregular activation of the atrium, which results in reduced heart muscle function. AF can be easily identified on a surface electrocardiogram by the absence of atrial depolarization, represented by a P-wave, and instead showing a quivering isoelectric line. This irregular activation also leads to irregular ventricular activation, which QRS complexes represent, and ultimately impaired muscle contraction [4].

The usual way of diagnosis of arrhythmias is to consider standard electrocardiograms (ECGs), event recorders recordings. This method has limited monitoring periods and occasionally miss intermittent arrhythmic events

among patients who use them. In case of one-day-long ECG recordings of Holter devices, the manual interpretation of ECG data can be time-consuming and subject to human error, leading to potential misdiagnoses [5]. In recent years, extensive work has been carried out to determine the fundamental cellular, molecular, and electrophysiological modifications that make patients more susceptible to the initiation and persistence of AF [6]. With the advent of deep learning methods, studies are focused on automatic detection techniques that can be integrated into wearable devices. Despite advances in cardiovascular disease detection methods, accurately classifying AF is still challenging since the condition can present with varying patterns of arrhythmia, subtle variations in ECG signals, and overlaps with other types of arrhythmias, making it difficult to distinguish using traditional techniques. This makes customized treatment plans and reliable prognostication difficult.

Overall, the literature review demonstrates the advancements in cardiac arrhythmia classification, focusing on the accuracy and scores of recent methods, including deep learning models, autoencoders, and CNN. These studies provide valuable insights into the potential of these techniques for improving ECG arrhythmia detection and classification accuracy, although further improvements are still necessary. Therefore, this study aims to establish a custom-designed Wavelet-based Convolutional Autoencoder (WCAE) structure and propose a successful and efficient arrhythmia detection system with machine learning methods. The contributions of this study can be summarized as

- Improving the AF detector performance due to learning the signal pattern with convolution filters of the convolutional autoencoder using only one channel of ECG signal.
- Combining wavelets' multiresolution signal analysis ability with a deep learning algorithm by proposing a WCAE structure.
- Handling the data imbalance problem by training the network with only one type of signal utilizing anomaly detection

Thus, instead of simply categorizing rhythms, this model focuses on spotting abnormalities, offering a fresh perspective on AF detection. Additionally, testing the model on different datasets reveals its flexibility and reliability in various situations. These unique features distinguish this study from others, providing a more thorough approach to AF detection.

## 2. Literature Review

Recent studies have focused on the accuracy of various atrial fibrillation (AF) classification methods, including autoencoders, convolutional neural networks (CNN), and other deep learning models. Hu et al. [7] proposed a novel frequency-domain feature, specifically the frequency corresponding to the maximum amplitude in the spectrum, to improve atrial fibrillation (AF) detection.

By applying a decision tree algorithm to data from the MIT-BIH database, their approach achieved high accuracy (98.9%), sensitivity (97.93%), and specificity (99.63%), highlighting the effectiveness of this method in distinguishing AF signals. Chen et al. [8] proposed a feedforward neural network model for AF detection, achieving an accuracy of 84.00%, sensitivity of 84.26%, specificity of 93.23%, and an area under the receiver operating characteristic curve of 89.40%. Furthermore, Cheng et al. [9] developed a method for AF detection directly from compressed ECG, achieving a varying accuracy with from 91.63% to 98.40% for the signals of 10 seconds. Other studies focusing on deep learning approaches have also shown significant potential in predicting AF accurately. For instance, Wei et al. [10] developed a deep-learning algorithm for atrial fibrillation detection, achieving an F-1 score of 88.2% and accuracy of 97.3%. They utilized spectrograms of pre-processed ECG signals and a fine-tuned EfficientNet B0 model, demonstrating the effectiveness of transfer learning in AF classification. Similarly, Faust et al. achieved an accuracy of 99.09% for AF detection using long short-term memory networks with RR interval signals by only considering the RR irregularity and uses long records to capture 100 RR intervals [11]. Rasmussen et al. [12] proposed a semi-supervised setup using an unsupervised variational autoencoder combined with a supervised classifier to distinguish between AF and non-AF using ECG records, indicating the potential of autoencoders in AF classification with an accuracy of 98.7%. Despite obtaining high accuracy values in these studies, the experiments have been conducted within a limited dataset and focused on lengthy samples. Hence, further development is still required for their applicability in real-life scenarios. To address these limitations, techniques like autoencoders, which are neural networks designed to encode input data into a compressed representation and then decode it back to closely match the original input, offer promising potential for enhancing the robustness and generalizability of these models [13]. The autoencoder is a self-supervised learning system and it aims to minimize the reconstruction error between the input and the output during training [14]. The autoencoder is also employed as a feature extraction as in [15]. The study utilizes an auto-encoder convolutional network (ACN) model based on one-dimensional convolutional neural networks (1D-CNN). These obtained features are then fed into a support vector machine (SVM) classifier, which achieves an overall accuracy of 98.84% in classifying arrhythmia using the MIT-BIH arrhythmia database [15]. Another instance of AE study, Choi et al. [16] proposed an atrial fibrillation (AF) diagnosis system using unsupervised learning with an LSTM-based autoencoder for anomaly detection in ECG segments (PreQ, QRS, and PostS). Their approach, which distinguished between normal and AF segments with AUROC scores up to 0.96, was further validated with an XG-Boosted model, achieving an area under ROC curve score of 0.98 and an F1 score of 0.94.

This method addresses the limitations of supervised learning by providing significant evidence for AF detection based on anomaly scores.

Our previous study proposes an efficient wavelet-based convolutional autoencoder model for the feature extraction of the five arrhythmia types, such as normal sinus rhythm (NSR), right bundle branch block (RBBB), left bundle branch block (LBBB), premature ventricular contractions (PVC), atrial premature contractions (APC) [17]. The study mentioned above used Wavelet-based Convolutional Autoencoder as a feature extractor to classify heartbeats with a Multilayer Perceptron (MLP). The wavelets' success in grasping the time-frequency domain distribution of the signals was integrated into the learning capability of autoencoders. As a result of the analysis with different wavelet families, the Bior 3.5 wavelet produced superior performance compared to the

previous studies. The quality and quantity of data is an essential issue in biomedical detection studies. Most of the deep learning models need a vast amount of data that represents the underlying phenomenon. Furthermore, each class should have sufficient data to train the network. In one of the previous studies, the Synthetic Minority Oversampling Technique (SMOTE) was employed to integrate the ECG arrhythmia detection model with the emergent IoT healthcare devices [18]. Then, the performance with different classifiers was compared for two classes, such as cardiovascular disease or not. Another study concentrates on generating synthetic samples for ECG signals [19]. They illustrated that the proposed model with a Generative Adversarial Network improves the classification accuracy compared to the ResNet34-LSTM3 model.

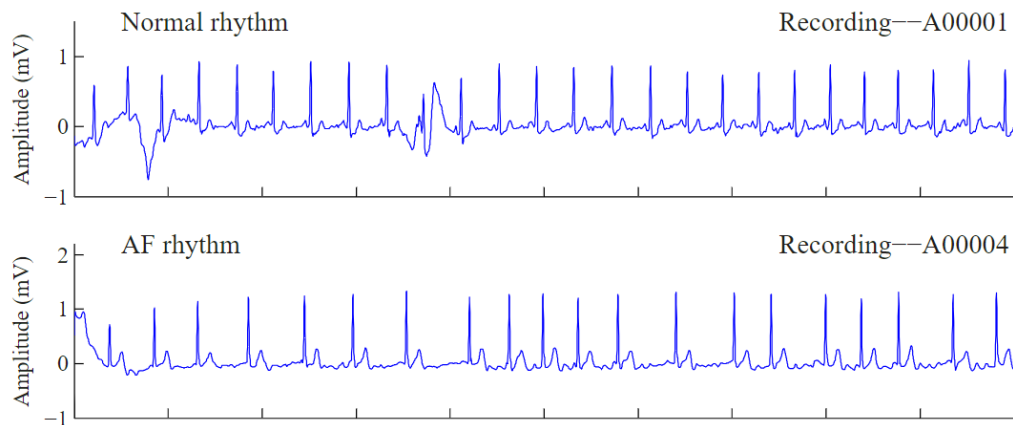


**Figure 1.** (top) Normal Sinus Rhythm and (bottom) Atrial Fibrillation ECG recordings [22].

### 3. Background

#### 3.1 ECG and Atrial Fibrillation

Electrocardiography (ECG) is a technique that records the electrical activity of the heart by detecting and amplifying the small electrical impulses generated by cardiac muscle depolarization and repolarization. This process is depicted as waves and intervals on the ECG tracing, including the P-wave, QRS complex, and T-wave, each representing specific electrical events in the cardiac cycle. By carefully interpreting these waveform characteristics, clinicians can assess rhythm regularity, identify conduction abnormalities, and recognize signs of ischemia or infarction. This diagnostic tool is commonly used for its rapidity, simplicity, and cost-effectiveness, making it indispensable even in resource-constrained settings. ECG plays a crucial role in diagnosing various cardiac and systemic conditions with its ability to provide insights into the physiological and structural status of the heart. Typically, ECG recordings are made for a few seconds to get a quick idea of the heart's rhythm. Holter ECG monitoring detects arrhythmic conditions that

cannot be captured during a standard ECG. Continuously recording heart activity over an extended period, such as 24 hours, provides crucial information for diagnosing and managing heart conditions.

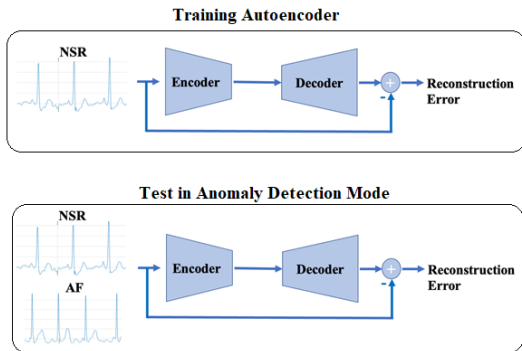
Atrial fibrillation is a commonly encountered arrhythmia that can lead to stroke, embolism, or even death when diagnosed late. The most used method for timely detection of this severe condition is the examination of ECG records. In ECG recordings, three specific signs of atrial fibrillation are mainly considered: the absence of the P wave, irregular RR intervals, and fibrillation on the baseline.

Figure 1 illustrates examples of ECG recordings of normal sinus rhythm and atrial fibrillation. As can be observed from the upper graph, P waves, QRS complexes, and T waves can be easily identified for each beat. The distance between R peaks is regular. However, in the second graph, beats are observed in irregular time instants. Furthermore, P peaks are absent, and a quivering isoelectric line is shown at the TQ interval.

### 3.2 Autoencoders and Anomaly Detection

Autoencoders (AEs) are a type of neural network extensively researched in deep learning. They are mainly used for unsupervised learning tasks such as dimensionality reduction, data compression, and feature extraction. The basic idea of an autoencoder is to learn a compressed representation of input data, encode it into a lower-dimensional latent space, and then decode it back to its original form [13]. The autoencoder's working process involves using two networks: an encoder and a decoder. The encoder takes the input data and creates a compressed representation, then fed to the decoder. The decoder then reconstructs the original input data from the compressed representation.

This study used an autoencoder in anomaly detection mode. NSR ECG signals constructs the normal class where AF signals were treated as abnormal beats. Thus, the autoencoder was trained with only NSR signals as represented in Figure 2. In the testing phase, both NSR and AF signals are applied to the autoencoder, and the reconstruction error is calculated, as seen in Figure 2. This approach allowed for the evaluation of how well the autoencoder could reconstruct both NSR and AF signals, providing insights into its performance in distinguishing between the two rhythm types. If the error is less than the given threshold value, it is labeled as NSR; if it is greater than the given threshold value, it is labeled AF.



**Figure 2.** Training and testing autoencoder for the classification of NSR and AF heart rhythms in anomaly detection mode.

The critical issue in anomaly detection is to select the threshold. In this study, the following steps are applied to obtain an acceptable threshold value that leads to successful detection:

1. Calculate reconstruction loss on normal data using the model.
2. Calculate reconstruction loss on anomalous data using the model.
3. Generate a range of threshold values between the minimum and maximum reconstruction loss values observed in the normal data.

- Iterate over different threshold values to find the best F1 score. For each threshold value, compute the precision, recall, and F1 scores.
  - Update the best F1 score and corresponding threshold if the current F1 score exceeds the previous one.
4. Return the best threshold and corresponding F1 score as the optimal threshold.

The identified optimal threshold is applied to the mixed test data, consisting of normal and atrial fibrillation samples. The performance of the selected threshold is evaluated based on various metrics, such as Precision, Recall, and F1 score, to assess the effectiveness of the anomaly detection system.

### 3.3 Wavelet Transform

The Continuous Wavelet Transform (CWT) operates by sliding a scaled wavelet function along the time axis of a signal, adjusting its magnitude through scaling and its position through translation [24]. Functions meeting specific mathematical criteria can be named wavelets, with common examples including Gaussian, Mexican Hat (the second derivative of a Gaussian), Haar, and Morlet functions [24]. In mathematical terms, convolving a signal  $x(t)$  with a wavelet function  $\psi(t)$ , yields the wavelet transform of  $x(t)$ . Using two parameters, translation  $b$  and dilation  $a$ , the Continuous Wavelet Transform (CWT) is defined as:

$$T(a, b) = \frac{1}{\sqrt{a}} \int_{-\infty}^{\infty} x(t) \psi^* \left( \frac{t-b}{a} \right) dt \quad (1)$$

Here, '\*' denotes the complex conjugate of the wavelet function. Parameter  $b$  indicates location in time axis, while  $a$  signifies the scale of the wavelet. The scaled and translated wavelet is defined as

$$\psi_{a,b}(t) = \frac{1}{\sqrt{a}} \psi \left( \frac{t-b}{a} \right) \quad (2)$$

The closer the wavelet matches the characteristics of the signal, the more detailed information can be extracted from the signal. The Discrete Wavelet Transform (DWT) applies an orthogonal wavelet basis to a continuous signal in discrete steps. It employs discrete values of parameters  $a$  and  $b$  moving in each  $b$  position with discrete steps proportional to  $a$ , establishing a connection between  $a$  and  $b$ . This relationship is encapsulated in a wavelet form expressed as

$$\psi_{a,b}(t) = \frac{1}{\sqrt{a_0^m}} \psi \left( \frac{t - nb_0 a_0^m}{a_0^m} \right) \quad (3)$$

The most typical values of dilation and translation steps are  $a_0 = 2$  and  $b_0 = 1$ , that is called as dyadic grid. The dyadic wavelet equation can be mathematically expressed as

$$\psi_{m,n}(t) = \frac{1}{\sqrt{2^m}} \psi\left(\frac{t-2^m}{2^m}\right) \quad (4)$$

where the scale index is  $m$ . The scaling function is denoted by

$$\phi_{m,n}(t) = \frac{1}{\sqrt{2^m}} \phi\left(\frac{t-n}{2^m}\right) \quad (5)$$

Here,  $\phi_{m,n}(t)$  represents the scaling function derived from the shift value  $n$  on the time axis for the  $m^{\text{th}}$  index of the scaling function. As a result of the convolution of the scaling function and the signal yields  $S_{m,n}$ , the approximation coefficient.

$$S_{m,n} = \int_{-\infty}^{\infty} x(t) \phi_{m,n}(t) dt \quad (6)$$

If the input signal is finite and bounded by certain integers it can be obtained as

$$S_{m+1,n} = \frac{1}{\sqrt{2}} \sum_k c_{k-2n} S_{m,k} \quad (7)$$

The  $c_k$  are the scaling coefficients. Multiplying  $c_k$  by  $1/\sqrt{2}$  yields the high-pass filter vector [24]. Similarly, utilizing the approximation coefficients in terms of  $b_k$ , detail coefficients can be computed.

$$T_{m+1,n} = \frac{1}{\sqrt{2}} \sum_k b_{k-2n} S_{m,k} \quad (8)$$

Here,  $b_k$  represents the reconfigured scaling coefficients of  $c_k$ . Multiplying  $b_k$  by  $1/\sqrt{2}$  yields the low-pass filter vector. The reconstruction low-pass and high-pass filter coefficients wavelets are obtained by time-reversal of analysis filter coefficients. The following steps are followed to calculate the wavelet coefficients [24]:

1. Take a signal  $S$  with length  $N$ , assume that  $S_{0,k} = x_k$
2. Select a discrete wavelet suitable for signal  $S$ .
3. Use the high-pass and low-pass filter coefficients of the selected wavelet.
4. Convolve signal  $S$  with the low-pass filter coefficients obtained from the corresponding wavelet, essentially containing a sequence of  $(1/\sqrt{2})c_k$  values.
5. Apply the same process as in step 4 with the high-pass filter coefficients, essentially containing a sequence of  $(1/\sqrt{2})b_k$  values.
6. Down-sample the results of the high-pass and low-pass filtering by selecting every  $(2n+1)$ th value along the length of the vector.
7. Obtain detail coefficients after high-pass filtering and down-sampling.

8. Obtain approximation coefficients after low-pass filtering and down-sampling and repeat the algorithm from step 1 using the result of this step.

This process achieves the atomic decomposition of the signal through filtering, as depicted schematically in Figure 3.

**Table 1.** Description of the databases.

Data	Subject	Lead	Duration of recordings	Sampling frequency
NSRDB	18	2	24 hours	128 Hz
AFDB	25	2	10 hours	250 Hz
AFPC	771	1	10-60 seconds	300 Hz

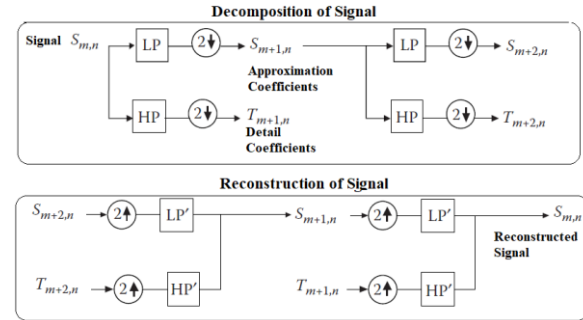


**Figure 3.** Two-level signal decomposition and reconstruction using wavelet coefficients [24].

## 4. Materials and Methods

### 4.1. Dataset

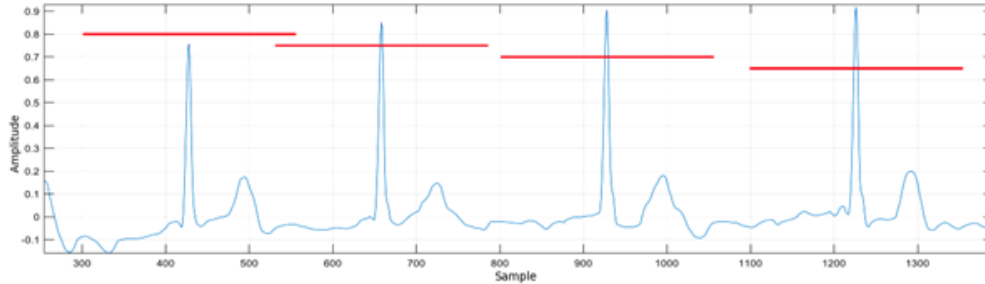
Autoencoder studies were carried out using publicly available ECG databases. NSR data “MIT-BIH Sinus Rhythm Database” (NSRDB) [20] and Atrial Fibrillation data “MIT-BIH Atrial Fibrillation Database (AFDB)” [21], “The PhysioNet/Computing in Cardiology Challenge 2017” (AFPC) [22] taken from databases. The features of the entire database are listed in Table 1.

Table 1 shows that NSRDB includes 24-hour data from 18 healthy individuals. The AFDB database recordings were obtained with ECG recorders with a frequency bandwidth of approximately 0.1 Hz to 40 Hz with a sampling frequency of 250Hz [21]. AFDB consist of records that obtained from 25 different patients. Each records have 10 hours duration and labelled as AF and other type of rhythms. The single-channel ECG recordings from AFDB was used in the competition held by Physionet in 2017. Only the AF labelled beats of the Physionet competition data was included in this study. The locations and beat labels of the QRS complexes of ECG signals in the NSRDB and AFDB databases are



available. AFPC recordings were taken with the AliveCor device, and the sampling frequency is 300Hz [22]. The AFPC training set includes 8528 records which have the time duration from 10 to 60 seconds. These records labelled as normal, AF, noisy and other rhythms. AF signals in the AFPC database were separated with the

Pan Tompkins algorithm and labeled by expert authors of this study. The sampling frequency was converted to 250 Hz for data at different sampling frequencies, thus same window length can be used for experiments. Before the data was applied to the autoencoder, signal is divided into 256 samples windows as illustrated in Figure 4.



**Figure 4.** Illustration of ECG Signal Windowing, red lines represent signal windows.

The located R peaks are aligned in the middle of each window. In Figure 4, each red line shows the interval of a signal window. The number of data windows resulting from the process is listed in Table 2.

**Table 2.** Number of Data Windows Used in Training and Testing

<i>Data</i>	<i>NSRDB</i>	<i>AFDB</i>	<i>AFPC</i>
<i>Number of frames used for training</i>	800,000	-	-
<i>Number of frames used testing (Test 1)</i>	395,455	395,455	-
<i>Number of frames used testing (Test 2)</i>	32,010	-	32,010

#### 4.1 Wavelet Based Convolutional Autoencoder Design

A Wavelet-based Convolutional AutoEncoder (WCAE) structure, that was proposed in our previous study [16], was employed in anomaly detection mode in this study. In the literature, wavelet transform is commonly employed as a preprocessing method, where wavelet coefficients or signals filtered by wavelet filters are used as inputs to deep learning architectures for training. In our proposed approach, a wavelet layer is integrated as a layer into a convolutional autoencoder structure. The custom-designed EncoderMiniBlock and DecoderMiniBlock are optimized during training to

effectively model the signal. When considering the feature space, the likelihood of overfitting increases with the complexity of the model during training. In this study, a simple architecture was preferred to avoid overfitting and simultaneously reduce computational complexity. The proposed model is given in Figure 5.

The best model was discovered through experimenting with different models, changing architectures, layer counts, and other configurations. We found that the proposed model performed the best after trying various options. As seen in Figure 5, three EncoderMiniBlocks containing 128, 64 and 32-dimensional filters are used in the encoder. Similarly, in the decoding section, 32, 64, 128 dimensional decoding MiniBlocks are included. The last layer contains a single-unit Fully Connected Layer (Dense layer) and Rectified Linear Unit (ReLU). Within the EncoderMiniBlock, there are convolutional layer or 1D convolution layer, Discrete Wavelet Transform (ADD) layer, batch normalization layer and dropout layer, respectively. WaveTF library was used for wavelet function implementation [23].

WaveTF is a TensorFlow library that implements 1D and 2D wavelet transforms and exposes them as Keras layers, so they can be easily added to machine learning workflows. The library implements the most used Haar and DB2 wavelet kernels. To handle boundary effects, anti-symmetric reflection filling is applied, which broadens the signal while preserving its first-order finite difference at the boundary. WaveTF transparently supports both 32- and 64-bit floating point at runtime.

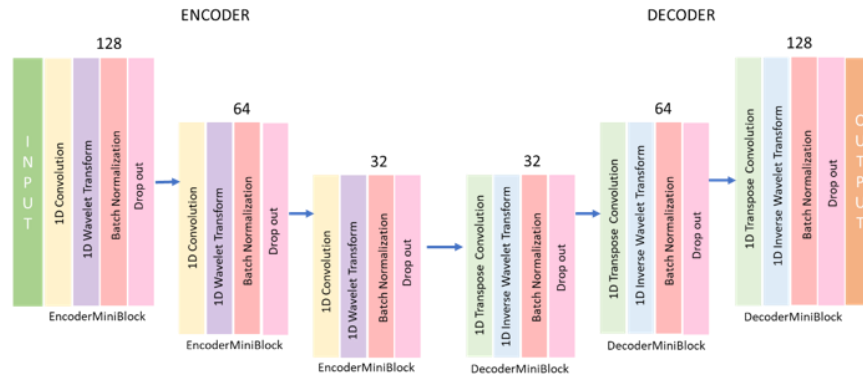


**Figure 5.** Proposed Wavelet-Based Convolutional Autoencoder Model

**Table 3.** Reconstruction low pass filter coefficients of the wavelet functions used in this study

	DB 2	DB3	DB 4	SYM 4	COIF 2	BIOR 3.5
$g_0[0]$	0.48296	0.03223	-0.230378	0.032223	0.016387	0.0
$g_0[1]$	0.836516	0.08544	0.714847	-0.012604	-0.041465	0.0
$g_0[2]$	0.2241439	-0.13501	0.630881	-0.099219	-0.067373	0.0
$g_0[3]$	-0.1294095	-0.45988	-0.027984	0.2978578	0.3861101	0.0
$g_0[4]$		0.80689	0.187035	0.8037388	0.8127236	0.1767767
$g_0[5]$		-0.33267	0.0308414	0.4976187	0.417005	0.5303301
$g_0[6]$			-0.0328830	-0.029636	-0.0764886	0.5303301
$g_0[7]$			-0.010597	-0.075766	-0.0594344	0.1767767
$g_0[8]$					0.02368017	0.0
$g_0[9]$					0.00561144	0.0
$g_0[10]$					-0.0018232	0.0
$g_0[11]$					-0.0007206	0.0

If wavelet transformation is active in the EncoderMiniBlock, the transformation function is defined for the selected wavelet. In the original version of the library, only Haar and Daubhecies 2 wavelets are defined. However, we observed from our studies and from the literature reviews that when the signal shape resembles the analyzed signal the wavelet transform analysis extracts more meaningful information from the signal. Thus in this study, wavelets, which were successfully used in ECG classification and AF detection in literature, were also adapted to the library. The DecoderMiniBlock contains a 1D transpose convolution layer, Inverse Wavelet Transform (IDWT) layer, batch normalization layer and dropout layer, respectively. In this study, autoencoder experiments were conducted with Haar and DB2 wavelets as well as wavelets that generally give successful results in biomedical signal classification. By entering low-pass reconstruction filter coefficients, new wavelets can be implemented in WaveTF library. The wavelet coefficients used are listed in Table 3.

## 5. Results and Discussions

This study aims to train the wavelet-based convolutional autoencoder with a single class of data, optimize it according to this signal, and obtain an efficient system separating the signal type from others in the testing phase. Model in Figure 5 was trained with NSR data from the NSRDB database. At the end of the training, the tests were performed with data from the NSRDB database, which the model did not see in training, and data taken from two different databases, AFDB and AFPC. Experiments were conducted in the TensorFlow 2 environment in Python 3 of Google Colaboratory. If there is no improvement in the validation error for ten epochs, early stopping is applied to prevent overfitting. Adagrad optimization algorithm was used with 128-dimensional batches. The initial learning rate was chosen as 10-3. The training is set to continue for a maximum of 50 epochs. In Test 1, 395,455 entries from the NSRDB database and 395,455 from the AFDB database were used.

In Test 2, 32,010 entries from the NSRDB database and 32,010 from the AFPC database were used. The model was trained with 800,000 NSR entries from the NSRDB database for both tests. The data is divided into separate sets for training and testing purposes. During the training phase, the model learns to reconstruct the input data without exposure to the data of the patients in the test set. This ensures that the test set consists of unseen examples, allowing for a rigorous evaluation of the model's generalization performance. Therefore, when training an autoencoder, the test data remains entirely independent, ensuring an unbiased assessment of the model's ability to reconstruct unseen instances.

### 5.1 Experiment 1: Effect of Wavelet Family on Performance

This experiment assesses how different wavelet families impact the performance of convolutional autoencoder models in anomaly detection tasks using ECG signals. By training multiple models with various wavelet families (e.g., Daubechies, Symlet, Coiflet), the study aims to identify the optimal wavelet family that enhances the model's ability to extract relevant features and accurately detect anomalies.

The WCAE Model (Figure 5) structure was established without a wavelet layer and also with the various wavelets. The system was optimized, and the loss function MAE, which gave the best results, was selected. The results of the experiments are listed in Table 4. In Figure 6 (a) and (b), separate performance graphs for both experiments are given according to wavelet type.

**Table 4.** Experiment 1 Results: Analysis and Findings.

Wavelet		Accuracy	Precision	Recall	F1
		%	%	%	%
No Wavelet	Test 1	57.09	78.62	55.02	64.74
	Test 2	50.14	99.37	50.07	66.58
Haar	Test 1	91.44	94.61	87.92	91.14
	Test 2	94.03	99.98	88.09	93.66
Db2	Test 1	91.79	94.41	88.88	91.56
	Test 2	93.94	99.96	87.92	93.55
Db3	Test 1	92.21	98.48	85.77	91.69
	Test 2	94.23	99.99	88.46	93.88
Db4	Test 1	84.23	85.32	82.77	84.02
	Test 2	91.44	100.00	82.89	90.64
Sym4	Test 1	92.96	94.95	90.77	92.81
	Test 2	95.44	99.99	90.90	95.23
Coif2	Test 1	76.70	72.87	85.22	78.56
	Test 2	92.68	99.96	85.39	92.10
Bior3.5	Test 1	86.98	87.89	85.85	86.86
	Test 2	93.02	99.99	86.05	92.50

When Table 4 and Figure 6 are examined, it is observed that the addition of a wavelet layer improves the classification performance noticeably. Among all wavelet families, Symlet 4 produced the best accuracy, and all the scores are balanced for this wavelet. In Test 2, all wavelets achieved better results compared to Test 1. The downloaded site provided the labels of the AFDB database used in Test 1. However, upon visual inspection by the experts, it was determined that the labeling was done in blocks, and some AF beats had more normal sinus rhythm characteristics than AF. Our cardiologist authors relabeled all the beats in AFPC dataset, and all the beats used in Test 2 were correctly identified. This may explain the difference between the classification performance. Symlet 4 wavelet is evenly ahead in all performance scores for both sets.

### 5.2 Experiment 2: Effect of Input Window Size on Performance

This experiment focuses on the influence of input window size variations on the performance of anomaly detection models trained on ECG signals. By varying the window size and evaluating model performance metrics, the experiment aims to determine the optimal window size for effectively capturing temporal dependencies and detecting anomalies in ECG data. The Sym4 wavelet and AFPC database were used in the tests. The results are given in Table 5 and Figure 7. The highest success was achieved for length 256.

**Table 5.** The effect of different window size on the performance metrics

Window Size	Accuracy %	Precision %	Recall %	F1 %
256	<b>95.44</b>	<b>99.99</b>	90.9	<b>95.23</b>
512	92.35	91.44	<b>93.13</b>	92.28
1024	90.36	96.36	86.03	90.90

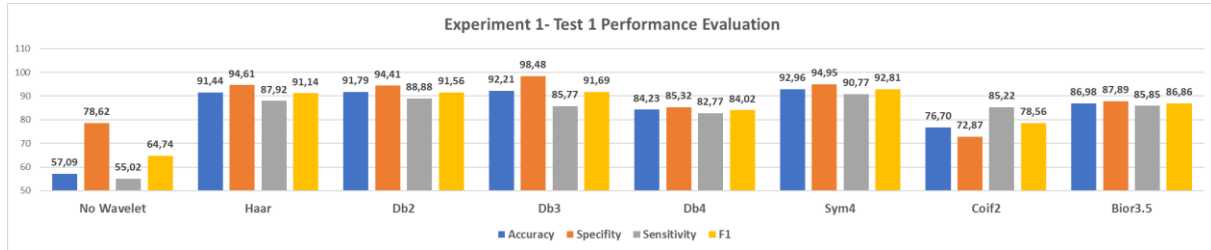
### 5.3 Discussion

This study proposes a new custom-designed autoencoder model for detecting atrial fibrillation. The integration of the wavelet layer into autoencoder architecture is investigated, and the network's performance is tested under different conditions. In an unbalanced dataset, even good accuracies are obtained with most of the deep learning algorithms, and either the precision or recall values will be lower according to the type of data insufficiency. When the number of data given in Table 2 is considered, the data is unbalanced in favor of NSR beats in our study, as in real-world cases. The proposed model consists of 514,113 trainable parameters. While practical guidelines often recommend having at least ten times the number of samples as trainable parameters,

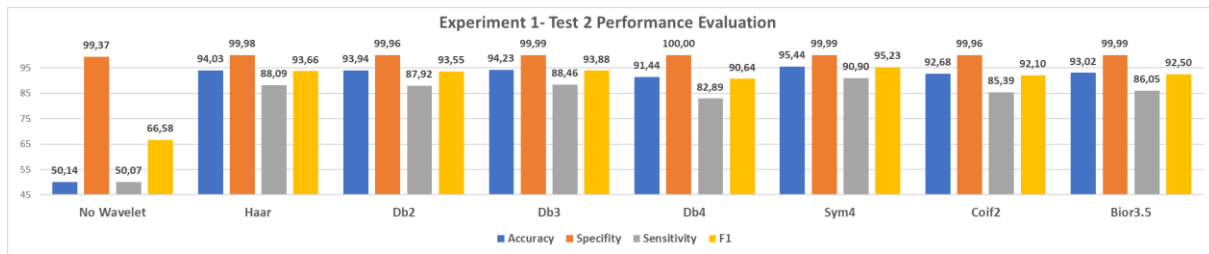
which would amount to roughly 5 million samples, the common QRS pattern in ECG data allowed for sufficient training with 800,000 NSR entries from the NSRDB database.

wavelet analysis is extensively used for noise reduction and compression tasks, the wavelet-based autoencoder is a new approach to arrhythmia detection.

Another contribution of this study is integrating the wavelet layer into the autoencoder model. Although



(a)



(b)

**Figure 6.** Mother Wavelet Performance Comparison of WCAE (a) Test 1 results with AFDB dataset (b) Test 2 results with AFPC dataset.

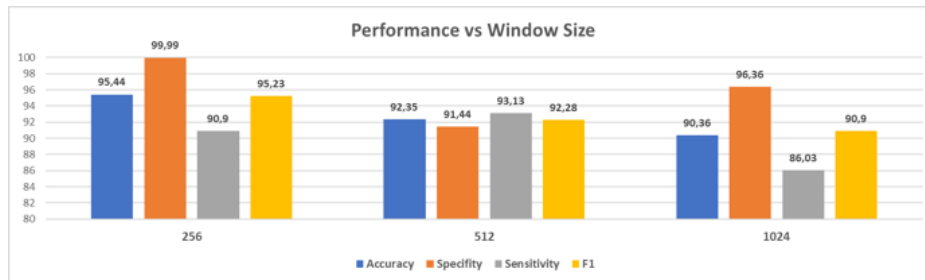


**Figure 7.** Impact of Window Size on Performance Metrics

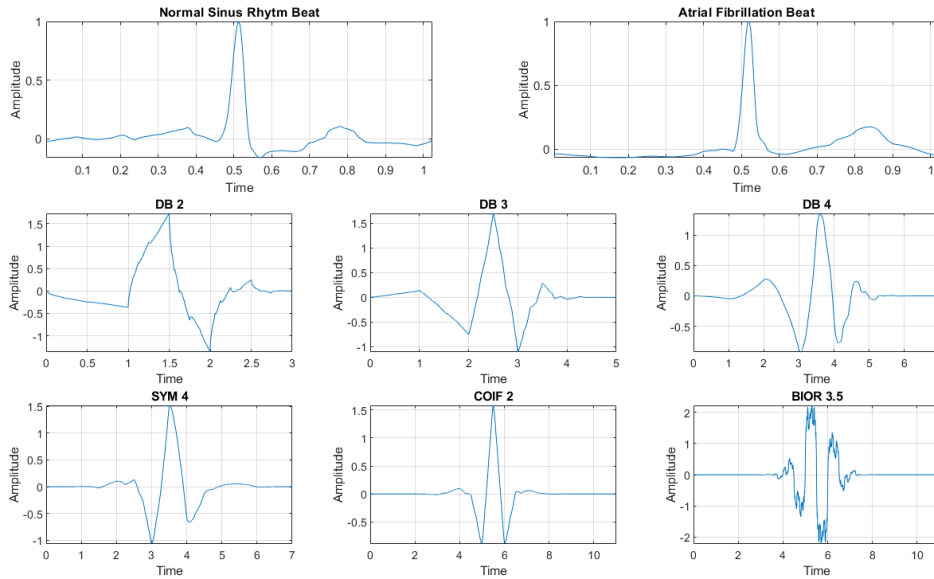


**Figure 8.** Samples of NSR and AF beats compared to mother wavelet morphology.

In experiment 1, different wavelet families are tested. We observed that with the addition of wavelet layer, a notable enhancement in the detection performance was obtained. Furthermore, it is observed that the Symlet 4 wavelet produces the best results. The results validate our intuition that the wave closely resembling the analyzed normal sinus rhythm waveform will be deemed successful. In Figure 8, the graph of normal sinus rhythm and atrial fibrillation beat samples are introduced to compare with the mother wavelets used in this paper. As can be observed from the figure, the Symlet 4 wavelet is the most similar wavelet morphologically. During the model design phase, the impact of altering the structures by varying the number and positions of the layers were conducted. Our findings revealed that the proposed model, as depicted in Fig. 5, outperforms the other models tested, thus other models were not included in the paper.

As another experiment, the input window size of the system is changed for the proposed model with Sym4 wavelet. The window size 256 is observed to perform better in accuracy, precision, and F1 scores. The AF detection performance of the state-of-the-art machine learning models in the literature is also considered. In [8], a feedforward neural network is trained and tested with PhysioNet Computing in Cardiology Challenge 2017, MIT-BIH arrhythmia, and 84% accuracy is obtained. Cheng et al. [9] classified 10s duration ECG signals into two classes, AF and non-AF, using a one-dimensional convolutional neural network and considering the effect of compression. According to the compression ratio, the accuracies vary from 91.63% to 98.40%. In [10], a pre-trained model, EfficientNet, is used for spectrogram images of ECG signals. The best accuracy is obtained as 97.3% with an F1 score of 88.24% for 9 to 61 seconds samples from PhysioNet Computing in Cardiology Challenge 2017. An LSTM model is trained with RR

interval signals from the MIT-BIH Atrial Fibrillation Database and achieved 98.51% accuracy [11]. Unlike our study, only RR interval irregularities are considered, and data blocks of 100 RR intervals are needed for testing. The final accuracy of the model is 98.51%. Rasmussen et al. [12] consider semi supervised learning with the Variational Autoencoder model. They used 10-second samples from the MIT-BIH

Atrial Fibrillation Database, and encoded data is classified with a fully connected model. 111,894 segments and 12,434 segments were used for training and testing, respectively. The testing accuracy varies between 94% and 98.8% for different amounts of labeled data proportion. Among the literature studies, the most significant data size collected from different datasets is considered in our study. A promising accuracy values and F1 scores were achieved with a short window of approximately 1 second. Our manuscript introduces a novel wavelet-based convolutional autoencoder for detecting AF beats, where the integration of a wavelet layer significantly enhances anomaly detection performance. This approach leverages the inherent ability of wavelets to capture both time and frequency information, providing a more robust feature representation compared to traditional convolutional autoencoders. As a result, our model outperforms state-of-the-art methods by improving detection accuracy and reducing false positives in AF beat identification.

The computational complexity of our proposed model was rigorously assessed, taking into account both its resource demands and its effectiveness in real-time applications. Comprising 514,113 trainable parameters and 384 fixed wavelet transform parameters, the model operates with an average of 17.1 GB of system memory, 17.4 GB of GPU memory, and 27 GB of disk space during training. Extensive measurements of processing



times for both training and testing reveal that our model achieves a computational complexity of approximately  $O(n)$ , with processing times scaling linearly with data size. This linear scalability, as detailed in Table 6, underscores the model's efficiency and suitability for real-world deployment.

**Table 6.** Train and test processing times

<i>Experiment</i>	<i>Processing Time (Seconds)</i>
<i>Train</i>	4097
<i>Test 1</i>	267
<i>Test 2</i>	92

To experimentally determine the processing complexity, processing time was measured for different data sizes. When the data size increases 10 times, the processing time also increases approximately 10 times. This means that the processing complexity is approximately  $O(n)$ .

## 6. Conclusions

In this study, we developed a robust autoencoder structure based on wavelets, which proved highly effective even for a short window of approximately 1 seconds. We conducted various tests using different basic wavelets and analyzed key performance metrics such as accuracy, sensitivity, precision, and F1 score. These evaluations helped us to compare the effectiveness of different wavelets. We also examined factors like input length and loss function across various models. Among the tested methodologies, the Sym4 wavelet emerged as the most promising and successful.

The wavelet layer is shown to improve the performance of the autoencoder structure in anomaly detection mode. Thus, the proposed model can be employed in different signal-processing applications, even for unbalanced datasets. The selection of wavelets plays an essential role in the network performance.

The proposed model can be used to detect abnormal heart rhythms in Holter recordings or within wearable health monitoring systems. Once the system is trained and optimized with data collected from the new system, its short testing time will enable near real-time applications. However, there are two main limitations to the study. In this study, the selection of the wavelet family was heuristic which directly determines the system performance. We are planning to propose a signal-specific wavelet construction procedure to improve the classification performance. Furthermore, the deep learning techniques, especially the autoencoder is

characterized by a sophisticated architecture, leading to significant computational demands. Future research also includes efforts to reduce the process complexity.

## Acknowledgement

This study has been supported by the The Scientific and Technological Research Council of Türkiye TÜBİTAK 1001-121E119 Research Project.

## Author's Contributions

**Öykü Eravcı:** Design, data collection and processing, analysis, literature review, writing.

**Nalan Özkurt:** Conception, design, interpretation, supervision, writing, critical review

**Özlem Memiş:** Data collection, analysis and interpretation, writing.

**Evrım Şimşek:** Conception, design, interpretation, supervision, critical review

## Ethics

There are no ethical issues for the publication of this manuscript.

## References

- [1]. Sagris, M., Vardas, E. P., Theofilis, P., Antonopoulos, A. S., Oikonomou, E., & Tousoulis, D. (2021). Atrial fibrillation: pathogenesis, predisposing factors, and genetics. *International journal of molecular sciences*, 23(1), 6.
- [2]. Clinical Practice Guidelines 2023 ACC/AHA/ACCP/HRS Guideline for the Diagnosis and Management of Atrial Fibrillation: A Report of the American College of Cardiology/ American Heart Association Joint Committee on Clinical Practice Guidelines Developed in Collaboration With and Endorsed by the American College of Clinical Pharmacy and the Heart Rhythm Society, PMID: 38153996 DOI: [10.1161/CIR.0000000000001207](https://doi.org/10.1161/CIR.0000000000001207)
- [3]. Siontis, K.C., Noseworthy, P.A., Attia, Z.I. *et al.* Artificial intelligence-enhanced electrocardiography in cardiovascular disease management. *Nat Rev Cardiol* **18**, 465–478 (2021). <https://doi.org/10.1038/s41569-020-00503-2>
- [4]. Filos, D., Tachmatzidis, D., Maglaveras, N., Vassilikos, V., & Chouvarda, I. (2019). Understanding the beat-to-beat variations of P-waves morphologies in AF patients during sinus rhythm: a scoping review of the atrial simulation studies. *Frontiers in Physiology*, 10, 742.
- [5]. Chung, E. K. (2013). *Ambulatory electrocardiography: holter monitor electrocardiography*. Springer Science & Business Media.
- [6]. Wijesurendra, R. S., & Casadei, B. (2019). Mechanisms of atrial fibrillation. *Heart*, 105(24), 1860-1867.
- [7]. Hu, Y., Zhao, Y., Liu, J., Pang, J., Zhang, C., & Li, P. (2020). An effective frequency-domain feature of atrial fibrillation based on time-frequency analysis. *BMC Medical Informatics and Decision Making*, 20, 1-11.

- [8]. Chen, Y., Zhang, C., Liu, C., Wang, Y., & Wan, X. (2022). Atrial fibrillation detection using a feedforward neural network. *Journal of Medical and Biological Engineering*, 42(1), 63-73.
- [9]. Cheng, Y., Hu, Y., Hou, M., Pan, T., He, W., & Ye, Y. (2020). Atrial fibrillation detection directly from compressed ECG with the prior of measurement matrix. *Information*, 11(9), 436.
- [10]. Wei, T. R., Lu, S., & Yan, Y. (2022). Automated atrial fibrillation detection with ECG. *Bioengineering*, 9(10), 523.
- [11]. Faust, O., Shenfield, A., Kareem, M., San, T. R., Fujita, H., & Acharya, U. R. (2018). Automated detection of atrial fibrillation using long short-term memory network with RR interval signals. *Computers in biology and medicine*, 102, 327-335.
- [12]. Rasmussen, S. M., Jensen, M. E., Meyhoff, C. S., Aasvang, E. K., & Sørensen, H. B. (2021, November). Semi-supervised analysis of the electrocardiogram using deep generative models. In *2021 43rd Annual International Conference of the IEEE Engineering in Medicine & Biology Society (EMBC)* (pp. 1124-1127). IEEE.
- [13]. Bank, D., Koenigstein, N., & Giryas, R. (2023). Autoencoders. *Machine learning for data science handbook: data mining and knowledge discovery handbook*, 353-374.
- [14]. Singh, A., & Ogunfunmi, T. (2021). An overview of variational autoencoders for source separation, finance, and bio-signal applications. *Entropy*, 24(1), 55.
- [15]. Ojha, M. K., Wadhvani, S., Wadhvani, A. K., & Shukla, A. (2022). Automatic detection of arrhythmias from an ECG signal using an auto-encoder and SVM classifier. *Physical and engineering sciences in medicine*, 45(2), 665-674.
- [16]. Choi, S., Choi, K., Yun, H. K., Kim, S. H., Choi, H. H., Park, Y. S., & Joo, S. (2024). Diagnosis of atrial fibrillation based on AI-detected anomalies of ECG segments. *Heliyon*, 10(1).
- [17]. Eravcı, Ö., Özkurt, N., "Arrhythmia Detection with Custom Designed Wavelet-based Convolutional Autoencoder," 2023 International Conference on Innovations in Intelligent Systems and Applications (INISTA'2023), Hammamet, Tunisia, 2023, pp. 1-5, <https://doi.org/10.1109/INISTA59065.2023.10310328>
- [18]. Isabels, K.R., Devi, K.M., Anand, R., Athe, R., Chowdhury, S.S., Pund, S.S., "An Intellectual Fusion Classification Prototypical for an Imbalanced Electrocardiogram Data", SN Computer Science (2023) 4:721, <https://doi.org/10.1007/s42979-023-02120-5>
- [19]. Shaik, J., Bhavanam, S.N, "Arrhythmia Detection Using ECG-Based Classification with Prioritized Feature Subset Vector-Associated Generative Adversarial Network", SN Computer Science (2023) 4:519, <https://doi.org/10.1007/s42979-023-01970-3>
- [20]. A.L. Goldberger, L.A.N. Amaral, L. Glass, et al., PhysioBank, PhysioToolkit, and PhysioNet: components of a new research resource for complex physiologic signals [J], *Circulation* 101 (23) (2000) e215–e220, <https://doi.org/10.1161/01.cir.101.23.e215>
- [21]. G. Moody, A new method for detecting atrial fibrillation using RR intervals[J], *Comput. Cardiol.* (1983) 227–230.
- [22]. Clifford, G. D., Liu, C., Moody, B., Li-wei, H. L., Silva, I., Li, Q., & Mark, R. G. (2017, September). AF classification from a short single lead ECG recording: The PhysioNet/computing in cardiology challenge 2017. In *2017 Computing in Cardiology (CinC)* (pp. 1-4). IEEE.
- [23]. Versaci, F. (2020). WaveTF: A Fast 2D Wavelet Transform for Machine Learning in Keras. *ICPR Workshops*.
- [24]. Addison, P.S., *The Illustrated Wavelet Transform Handbook: Introductory Theory and Applications in Science, Engineering, Medicine and Finance*, CRC Press, 2002

# The Effect of Substrate Dielectric Constant and Thickness on Millimeter Wave Band Patch Antenna Performance

Seda Ermis<sup>1\*</sup> 

<sup>1</sup>Osmaniye Korkut Ata University, Electrical and Electronics Engineering Department, Osmaniye, Türkiye

\*[sedaermis@osmaniye.edu.tr](mailto:sedaermis@osmaniye.edu.tr)

\* Orcid No: 0000-0002-3105-7080

Received: 10 July 2024

Accepted: 10 October 2024

DOI: 10.18466/cbayarfbe.1514216

## Abstract

In last decade, the fifth generation of telecom network (5G) has been a new era as a result of fast-growing mobile industry. Unlike its predecessors, 5G will not only provide faster, better mobile broadband experience, but also broaden communication network with new services such as device-to-device communications or connecting IoT devices and users. For this purpose, 5G aims to achieve massive network capacity, ultra-low latency, higher data speed and greater network reliability. According to the report of ITU World Radiocommunication Conference 2019 (WRC-19), several new frequency bands between 20-70 GHz, were announced for allocation of 5G. Frequencies in the Ka-band (27-40 GHz) are particularly attractive due to their low atmospheric attenuation. At the specified frequency range i.e., millimeter wave band, antenna design for 5G applications is very crucial to provide high gain and efficiency as well as broadband communication which is indispensable for high-speed data traffic. At this point, Microstrip patch antennas, stand out amongst others because of their numerous attractive features. In this work, the effect of substrate dielectric constant and thickness to the Rectangular Microstrip Antenna (RMA) performance is examined for high frequency 5G applications. The RMA is designed to operate at 38 GHz and antenna performance has been analyzed according to various dielectric substrates, such as RT5880, RO3003, FR4, RT6006 and RT6010, considering different dielectric constants, thicknesses, and tangential losses. All designs and analyses have been accomplished by using ANSYS HFSS (High-Frequency Structure Simulator) and comparative results of the work are presented.

**Keywords:** 5G, 38 GHz, RMA, Substrate Dielectric Constant, Substrate Thickness

## 1. Introduction

In 2011, the evolution of 4G/LTE wireless technology has been pivotal to offer much higher data rate and reduced latency for mission critical applications, thereby expanding wireless network capacity with more advanced multimedia services. Following the global deployment of 4G/LTE networks, the increasing number of mobile phone users and multimedia applications led to a significant rise in mobile traffic. According to Cisco, mobile traffic experienced approximately 70% growth in 2014 and 63% growth in 2016. [1-3].

As the upcoming generation over 4G, The Fifth Generation of Mobile Technology, or 5G, aimed not only provide a peer-to-peer mobile communication but also a connection between users and IoT devices which means massive growth of mobile data in its various forms. For

this purpose, major requirements for 5G were defined as follows [3,4]:

- Ten times higher data rate (1~10 Gbps) from traditional 4G/LTE network's peak data rate of 150 Mbps
  - Around 1 ms round trip latency which indicates almost ten times reduced latency from 4G's 10 ms round trip time
  - Wide bandwidth to enable many linked devices to use for longer periods of time in one location
  - Offer connectivity to thousands of devices in order to realize the IoT goal
  - 99.999% Perceived availability and guarantee full coverage regardless of users' location
  - Long battery life and decrease in energy consumption
- To meet these requirements, 4G wireless communications spectrum which is between 300 MHz and 3 GHz band was expanded with high frequency

millimeter wave (mm-wave) band, ranging from 3~300 GHz. Thus, even a small fraction of the available mm-wave spectrum has the potential to provide data rates and capacity that are hundreds of times higher than those offered by the existing cellular spectrum [5].

5G was defined in 2018 by the 3rd Generation Partnership Project (3GPP). In addition to frequencies below 6 GHz (3.3-3.8 GHz), which are similar to existing 4G frequencies in the transition from 4G LTE to 5G, an additional spectrum area, called the millimeter band, has been opened in the 20-70 GHz range [4-6]. Frequencies within the Ka-band (27-40 GHz) are particularly noteworthy due to their low atmospheric attenuation. Despite these advancements, 5G technology has not yet been fully deployed, and ongoing research efforts aim to further its development [7-11].

Although 5G features such as high data rate and minimum latency can be achieved relatively easily, signal path loss, multipath effect, connection losses, short-scale signal attenuation and narrow network coverage are still problems for this communication technology. Ongoing studies to improve 5G system performance includes creating radiation in the desired form, improving antenna impedance bandwidth, using narrow beam width and high gain antenna, small cell technology and MIMO (Multiple Input Multiple Output) antenna with high beam directing feature and low scanning loss etc. To overcome these problems and improve 5G network performance develop an efficient antenna design has great importance [12-13].

For a reliable signal transmission in mobile communication, it is desired to use a small size, high gain, low loss, high performance broadband antenna. Traditionally, Microstrip Patch Antennas are the most popular candidate for 5G applications, which are frequently preferred by many researchers because of low cost, light weight, ease of manufacture and installation, durability, and easy integration into microwave circuits. However, besides these advantages, microstrip antennas also have narrow bandwidth, limited gain and low efficiency. To address these issues, researchers have explored various techniques to enhance the gain and bandwidth of patch antennas and improve their performance. Some of the widely recognized and frequently utilized methods are adding parasitic patch element to the antenna structure, slotting on the patch surface, defecting ground surface (DGS), the increment of substrate thickness, use of coupling type of feeding and the design of array configurations. These methods are well-documented in the literature [5,14-24].

For instance, Demirci employed non-contacting insert feeding and proximity coupling feeding techniques to design both single and array-type rectangular microstrip antennas that resonate at 28 GHz, in 2020 [5].

Additionally, the introduction of slits on the surface of the upper patch enabled dual-band operation at 28 GHz and 38 GHz [15]. Furthermore, it was reported that the antenna gain increased with the use of 2-element and 4-element Rectangular Microstrip Antenna (RMA) array designs. Also, the bandwidth of the antenna improved through the use of defected ground structures or by incorporating parasitic patch into the design [22].

In 2020, Sharaf et al. introduced a compact dual-frequency microstrip patch antenna designed for dual-band 5G applications operating at 38 and 60 GHz. The proposed antenna consisted of two electromagnetically coupled patches printed on the Rogers RO3003 substrate with the dielectric constant ( $\epsilon_r$ ) of 3, a loss tangent ( $\delta$ ) of 0.001 and a thickness (h) of 0.25 mm. Experimental results revealed that the impedance matching bandwidths (for  $|S_{11}| < -10dB$ ) and gains were approximately 2 GHz and 6.5 dBi for the 38 GHz band, and 3.2GHz and 5.5 dBi for the 60 GHz band, respectively [14].

In 2020, Haneef et al. conducted a performance analysis of a rectangular microstrip antenna operating at 28 GHz using various dielectric substrates. In their study, the substrate thickness was maintained at 1.6 mm, and the evaluation focused exclusively on antenna gain. However, for 5G applications, wide bandwidth is a crucial parameter for enabling higher data transfer rate, which was not considered in the analysis. The study identified RT-Duroid 6010 as the most suitable substrate for 5G applications, featuring a thickness of 1.6 mm, a loss tangent of 0.0023, and a dielectric constant of 10.2. Besides the limitation of very narrow bandwidth, another drawback of this study was that the use of a thick substrate with a high dielectric constant increases surface current, which can lead to higher-order wave modes, high degree of side/back lobe level and multiple resonance frequencies. These issues are particularly significant for MIMO antenna arrays, as it may result in mutual coupling, electromagnetic interference, and crosstalk effects [16].

Similarly, in 2020, Ramli et al. presented an analysis of a 3.5 GHz microstrip patch antenna design utilizing three different substrate materials: FR-4, RT-5880, and TLC-30, with respective thicknesses of 1.6 mm, 1.575 mm, and 1.58 mm. The reported gains for the antenna were 3.338 dB for FR-4, 4.660 dB for RT-5880, and 5.083 dB for TLC-30. Additionally, the bandwidths observed for these substrates were 247.1 MHz for FR-4, 129.7 MHz for RT-5880, and 177.2 MHz for TLC-30 [17].

Sree et al., in 2021, designed and fabricated a microstrip patch antenna for sub-6 GHz band 5G applications. The proposed antenna was based on Rogers RO5880 substrate with a dielectric constant of 2.2 and a thickness of 1.6 mm. To achieve dual-band operation, the Defected Ground Structure (DGS) technique was applied to the patch layer. Experimental results demonstrated overall



gains of 5 dB and 4.57 dB at 4.53 GHz and 4.97 GHz, respectively. However, the study did not investigate the effect of varying substrate thickness on antenna performance. It is generally understood that reducing the substrate thickness can enhance gain due to lower associated losses [19].

In 2023, Kumar et al. proposed a compact, tri-band, slotted monopole antenna with a hexagonal shape patch for sub-6 GHz of 5G applications such as Wi-Fi, WLAN or WiMAX. In the designed and manufactured antenna, 1.6 mm thick FR-4 substrate was used and DGS technique was applied to increase bandwidth. The measured peak gains were 1.35 dB at 2.45 GHz, 2.55 dB at 3.65 GHz and 3.8 dB at 5.5 GHz. Also, measured bandwidths were reported as 112 MHz, 700 MHz and 1359 MHz at 2.45 GHz, 3.65GHz and 5.5 GHz respectively [23].

Numerous examples of microstrip patch antenna designs are documented in the literature, encompassing a wide range of frequency bands, patch geometries, substrate types, and thicknesses. Additionally, various performance enhancement techniques have been applied to these antennas, and this review could be expanded to include these examples. Regardless of the method employed, researchers generally begin by defining the antenna geometry, operating frequency, substrate permittivity, and thickness as the initial steps in their design process. Due to the absence of analytical methods for calculating the propagation characteristics of microstrip antennas with arbitrarily shaped patches, the desired operational frequency range is typically determined through parametric studies and optimization of antenna dimensions, with the aid of specialized software. When selecting the dielectric constant and thickness of the substrate, antenna engineers must thoroughly understand and assess their impact on antenna performance within the specific frequency band of interest. Such an understanding will facilitate more accurate predictions for complex antenna design studies and lead to more successful outcomes through appropriate substrate selection. Furthermore, the literature indicates a gap in comprehensive evaluations, particularly concerning how substrate characteristics affect antenna performance in the millimeter-wave band, highlighting an area that merits further investigation.

For these reasons, in this study, the effect of substrate dielectric constant and thickness to the Rectangular Microstrip Antenna (RMA) performance is examined for high frequency 5G applications. The RMA is designed to operate at 38 GHz due to low atmospheric attenuation at Ka-band. Then, antenna performance has been analyzed according to various dielectric substrates, such as RT5880, RO3003, FR4, RT6006 and RT6010 as well as dielectric constants, thicknesses and tangential loss. All designs and analyses have been accomplished by using

ANSYS HFSS (High-Frequency Structure Simulator) and comparative results of the work are presented.

## 2. Materials and Methods

The most commonly used microstrip antennas have shape of rectangular. The basic form of a Rectangular Microstrip Antenna (RMA) consists of a ground plane, a dielectric substrate and a patch with feed line. As seen from the Fig.1, width and length of the radiating patch are  $W_p$  and  $L_p$ , whereas  $W_g$  and  $L_g$  are width and length of the ground plane,  $\epsilon_r$  is the dielectric constant of the substrate,  $h$  and  $t$  are thicknesses of the dielectric and patch, respectively.

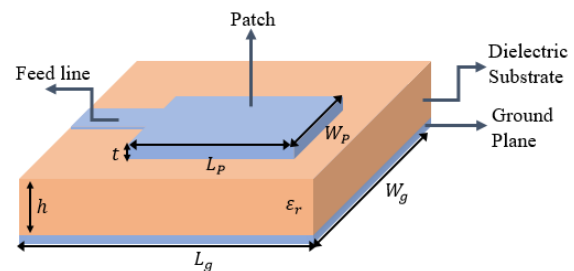


**Figure 1.** Geometry of the RMA

Many different dielectric materials can be used in design microstrip antennas and generally, their dielectric constants are in the range of  $2.2 \leq \epsilon_r \leq 12$  with the thickness  $h \ll \lambda_0$  ( $\lambda_0$  is the free space wavelength). For enhanced antenna efficiency, wider bandwidth, and a more loosely bound radiation field, thick substrates with lower dielectric constants are generally preferred. However, this approach results in increased antenna size and can lead to less stable radiation patterns. Conversely, thin substrates with high dielectric constants are favored for microstrip antennas integrated into microwave circuits. Such substrates confine the radiation more effectively to the substrate, leading to more stable radiation and minimizing unwanted radiation areas. Nevertheless, this choice tends to increase loss and reduce bandwidth [25].

The dimensions of a rectangular patch antenna can be mathematically calculated using straightforward formulas derived from the transmission line model or cavity model. These approaches offer designers a simple and efficient means to estimate the antenna dimensions required for a specific resonance frequency and they are most accurate for thin substrates at lower frequencies. In the transmission line model, the design procedure begins by determining the substrate dielectric constant ( $\epsilon_r$ ), substrate thickness ( $h$ ) and resonance frequency ( $f_r$ ). For an efficient radiator, a practical patch width  $W_p$  that leads to good radiation efficiencies is

$$W_p = \frac{1}{2f_r \sqrt{\mu_0 \epsilon_0}} \sqrt{\frac{2}{\epsilon_r + 1}} = \frac{\vartheta_0}{2f_r} \sqrt{\frac{2}{\epsilon_r + 1}} \quad (1)$$



where  $\vartheta_o = c = 3 \times 10^8 \text{ m/sn}$ ,  $\mu_o = 4\pi \times 10^{-7} \text{ H/m}$ ,  $\varepsilon_o = 8.85 \times 10^{-12} \text{ F/m}$  are speed of light, magnetic permeability and dielectric constant in free space respectively. Due to the finite dimension of the patch, radiation occurs at the edges of the patch and it can be represented by two radiating slots along the length. Although electric field lines mostly concentrate in the substrate, some part of it is placed in the air due to the fringing effect [25]. Therefore, nonhomogeneous line of two dielectrics is taken into account by calculation of the effective dielectric constant which is given as,

$$\varepsilon_{\text{reff}} = \frac{\varepsilon_r + 1}{2} + \frac{\varepsilon_r - 1}{2} \left[ 1 + 12 \frac{h}{W_p} \right]^{-\frac{1}{2}} \quad (2)$$

where  $\frac{W_p}{h} > 1$

At lower frequencies the  $\varepsilon_{\text{reff}}$  remains relatively constant, often referred to as a static value. However, as the operating frequency increases, particularly in the millimeter wave band,  $\varepsilon_{\text{reff}}$  approaches the dielectric constant of the substrate. Therefore,  $\varepsilon_{\text{reff}}$  is, in fact, a frequency-dependent parameter [25]. On the other hand, due to the fringing effect, the patch looks greater electrically than its physical dimension. and so, the increment in length  $\Delta L$  and the effective length of the patch are calculated as;

$$\Delta L = \frac{0.412h(\varepsilon_{\text{reff}} + 0.3) \left( \frac{W_p}{h} + 0.264 \right)}{(\varepsilon_{\text{reff}} - 0.258) \left( \frac{W_p}{h} + 0.8 \right)} \quad (3)$$

$$L_{\text{eff}} = \frac{1}{2f_r \sqrt{\varepsilon_{\text{reff}}} \sqrt{\mu_o \varepsilon_o}} \quad (4)$$

Therefore, the actual length of the patch,  $L_p$ , is

$$L_p = L_{\text{eff}} - 2\Delta L = \frac{1}{2f_r \sqrt{\varepsilon_{\text{reff}}} \sqrt{\mu_o \varepsilon_o}} - 2\Delta L \quad (5)$$

The theoretical calculations for antenna and microstrip line impedances are detailed in Ref. [25]. While the transmission line model is effective for practical calculations of rectangular patch dimensions at lower frequencies for thin substrates, it has limitations. To address these limitations and achieve more accurate results, particularly for designs beyond these constraints, it is necessary to employ simulation software to optimize antenna dimensions and obtain precise performance predictions.

In this study, single RMA is designed to operate 38 GHz and antenna performance has been analyzed according to various dielectric substrates and thicknesses using ANSYS HFSS software, as explained in the following section.

## 2.1 38 GHz Single RMA Design and Analyses

A single RMA operates at 38 GHz was designed by HFSS simulation environment. The antenna structure comprises a concentric upper patch, a bottom patch (ground plane) and a substrate, with the center of the antenna structure aligned at the origin. Antenna is fed by 50Ω non-contact inset-feed to enhance key performance parameters such as gain, bandwidth, efficiency, return loss and directivity. The dimensions of both antenna and feed line were optimized for impedance matching and maximum power transfer. Fig. 2 illustrates the top view of the RMA geometry and in Fig.3, its simulated 3D model in the HFSS software is depicted.

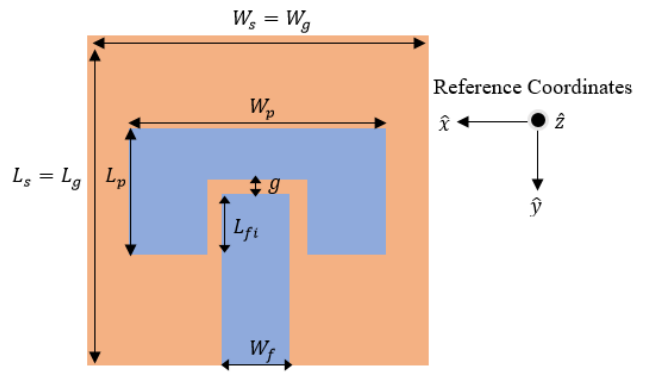


**Figure 2.** Top view of the designed RMA geometry

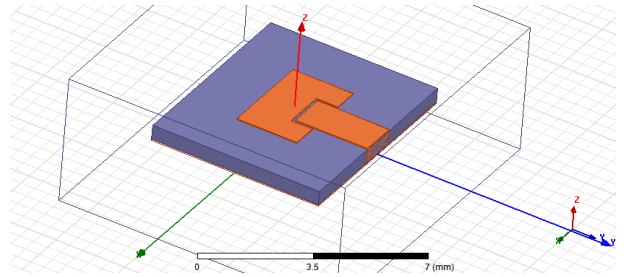


**Figure 3.** Constructed 3D RMA geometry in the simulation environment

Due to gap ( $g$ ) between patch and feed line, energy is provided by coupling effect and this feeding technique allows to optimize patch and feed line separately. Hence, the gap ( $g$ ) between patch and feed line, as well as dimensions of the patch ( $L_p, W_p$ ), feed line ( $L_{fi}, W_f$ ) and ground ( $L_g = L_s, W_g = W_s$ ) are all optimized by using Sequential Quadratic Programming (SQP) algorithm which is one of the most successful method for nonlinear constrained optimization problems. Definition of all design parameters are given in Table 1. Since the aim of the study is to examine performance of the RMA at mm-wave band for various dielectric substrates and thicknesses, the most commonly used 5 dielectric materials are chosen for analysis and their specifications are summarized in Table 2.

**Table 1.** Design parameters of the RMA

Parameter	Definition
$L_s = L_g$	Substrate and ground patch length
$W_s = W_g$	Substrate and ground patch width
$L_p$	Upper patch length
$W_p$	Upper patch width
$L_{fi}$	Embedding distance of the inset feed
$W_f$	Width of the feed line
$g$	Gap between feed line and patch
$h$	Substrate thickness
$t$	Upper and ground patch thickness

**Table 2.** Specifications of dielectric materials used in analyses

Dielectric Substrate	Dielectric Constant	Tangent Factor
Rogers RT5880	2.2	0.0009
Rogers RO3003	3	0.0013
FR4 epoxy	4.4	0.02
Rogers RT6006	6.15	0.0019
Rogers RT6010	10.2	0.0023

To evaluate the impact of the substrate permittivity five test groups are established for dielectric materials listed in Table 2. Then, for each test group, multiple substrate thicknesses—specifically, 1.57 mm, 0.787 mm, 0.508 mm, 0.256 mm, and 0.125 mm—are utilized and analyzed in the test cases. This approach provides valuable insights into the effects of substrate height and permittivity on key antenna performance parameters, such as resonance frequency ( $f_r$ ), return loss ( $S_{11}$ ), gain ( $G$ ), bandwidth ( $BW$ ) and directivity by interpreting the results of the analyses.

The bandwidths ( $BW$ ) of the designed antennas are calculated by the difference between the lower ( $f_{c1}$ ) and upper ( $f_{c2}$ ) cutoff frequencies, which correspond to a -10 dB return loss, within a continuous frequency spectrum. This criterion is widely recognized in mobile communication and, as such, is considered appropriate for practical applications. Additionally, in HFSS simulations, antenna gain is presented in decibels (dB) rather than decibels relative to an isotropic radiator (dBi). It is crucial to note that HFSS inherently normalizes all gain values in reference to an isotropic antenna. Therefore, the gain values expressed in dB in HFSS simulations can be directly interpreted as dBi.

In the Test Group#1, Rogers RT5880 material with a dielectric constant of  $\epsilon_r=2.2$  and a loss tangent of  $\tan\delta=0.0009$  is employed as the substrate. Test Cases 1.1 through 1.5 examine range of substrate thicknesses, specifically 1.57 mm, 0.787 mm, 0.508 mm, 0.256 mm, and 0.125 mm. The patch and feed line dimensions are optimized to achieve minimal return loss, alongside maximum gain and bandwidth at the 38 GHz resonance frequency. A comprehensive summary of all design and performance parameters for the simulated antennas is

provided in Table 3. Additionally, comparative return loss graphs for each substrate thickness are presented in Fig. 4. The far-field gain and 3D directivity patterns for this test group are visually represented in the supplementary document, Appendix 1, Fig. A1 (a) through (e), corresponding to the different substrate thicknesses: 1.57 mm, 0.787 mm, 0.508 mm, 0.256 mm, and 0.125 mm. In the gain patterns,  $\phi = 0^\circ$  and  $\phi = 90^\circ$  represents E and H-planes, with the indicated markers representing the main lobe magnitude at 38 GHz.

Similarly, in Test Group#2, all design cases are constructed by using substrate material Rogers RO3003 with a dielectric constant of  $\epsilon_r=3$  and a loss tangent of  $\tan\delta=0.0013$ . After optimization and analyses are performed, Table 4 provides a comprehensive summary of all design and performance parameters for this test group. For visual representation of the performance parameters given in the table, far-field gain and 3D directivity patterns are represented in Fig. A2 (a) through (e), for substrate thicknesses defined previously. Also, comparative evaluation of return losses for each substrate thickness is given in Fig. A3. Both Fig. A2 and A3 can be found in the supplementary document, Appendix 1.

In Test Group#3, all design cases utilize FR4 epoxy substrate, characterized by a dielectric constant of  $\epsilon_r=4.4$  and a loss tangent of  $\tan\delta=0.02$ . Following optimization and analysis, Table 5 presents a comprehensive summary of all design and performance parameters for this group. For visual representation of the analyses results given in the table, far-field gain and 3D directivity patterns are presented in Fig. A4, panels (a) through (e), corresponding to the previously defined substrate thicknesses. Fig. A5 provides a comparative evaluation of return losses for each substrate thickness. Both Fig. A4 and A5 can be found in the supplementary document, Appendix 1.

In Test Group#4, all design cases employ Rogers RT6006 substrate, which has a dielectric constant of  $\epsilon_r=6.15$  and a loss tangent of  $\tan\delta=0.0019$ . Following optimization and analysis, Table 6 presents a comprehensive summary of all design and performance parameters for this test group. For visual representation of the analyses results given in the table, far-field gain and 3D directivity plots are shown in Fig. A6, (a) through (e), corresponding to the substrate thicknesses. Fig. A7 presents a comparative evaluation of return losses for each substrate thickness. Both Fig. A6 and A7 can be found in the supplementary document, Appendix 1.

Finally, In Test Group#5, Rogers RT6010 dielectric material characterized by a dielectric constant of  $\epsilon_r=10.2$  and a loss tangent of  $\tan\delta=0.0023$  has been used as substrate for all design cases. Following optimization and analysis, Table 7 offers a comprehensive summary of all design and performance parameters for this test group. For visual representation of the analyses results

given in the table, far-field gain and 3D directivity patterns are presented in Fig. A8, from (a) to (e), corresponding to the substrate thicknesses. Fig. A9 provides a comparative evaluation of return losses for each substrate thickness. Both Fig. A8 and A9 can be found in the supplementary document, Appendix 1.

### 3. Results and Discussion

To assess the impact of substrate dielectric constant and thickness on antenna performance for the simulated design cases, the performance parameters are presented in Fig.4, Fig. A1 through A9 (see supplementary document, Appendix 1) and summarized in Tables 3 through 7 are compared. In Fig. 5. directivities, in Fig. 6 gains and in Fig. 7 band widths of designed antennas are plotted across various substrate thicknesses. In these figures, each colored line represents a test group with a specific dielectric constant. Finally, the key findings of this study are summarized as follows;

- First of all, the optimal thickness of the substrate is typically determined based on the wavelength within the dielectric material to facilitate ease of calculation and to prevent convergence issues in numerical simulations. For an operation frequency of 38 GHz, the wavelength in the free space is approximately 7.89 mm. The wavelength within the dielectric is estimated by dividing this value by the square root of the dielectric constant, resulting a wavelength of approximately 2.47 mm for the highest dielectric constant ( $\epsilon_r=10.2$ ) and 5.32 mm for the lowest dielectric constant ( $\epsilon_r=2.2$ ). In test case involving a very thick substrate with a thickness of  $h=1.57$  mm, the ratio of the thickness to the wavelength within the dielectric material is around 0.635 for the  $\epsilon_r=10.2$ . For high computational accuracy, this ratio is recommended to be below 0.1 [26]. As a result, to ensure convergence in the solution process, the number of iterations must be increased, which in turn leads to longer computational times especially for the thick substrate with high dielectric constant.
- One of the most well-known features of microstrip antennas is thick substrates with low dielectric constant provides wider bandwidth, and more loosely bound radiation field which increase antenna efficiency with the expanse of larger antenna size. Conversely, thin substrates with high permittivity confine the radiation mostly in the substrate, leading to more stable radiation due to tightly bounded fields which results in narrow bandwidth. These makes them less efficient but the advent of smaller antenna size. Similarly, general evolution of the study shows that decreasing substrate thicknesses also decrease bandwidth, for all test groups. The widest bandwidth which is 18.87 GHz was provided by the first test group with the dielectric constant of 2.2 and substrate thickness of 1.57 mm. However, except the
- first test group, the widest bandwidth achieved for the thickness of 0.787 mm for all others (see Fig. 7). That means for most of the designs the optimum thickness for widest bandwidth should be around 0.787 mm. Although, the bandwidth of the antenna mainly depends on the dielectric constant, thickness and frequency, studies shows that dielectric losses also effective on the cut of frequencies and so the bandwidths [26]. On the other hand, the narrowest bandwidth values are provided by the simulations with thinner substrates (i.e.  $h=0.127$  or  $0.254$  mm) and higher dielectric constant (i.e.  $\epsilon_r=6.15$  or  $10.2$ ), as expected.
- For the test groups utilizing substrates with higher dielectric constants (i.e.  $\epsilon_r=6.15$  or  $10.2$ ), the return loss graphs (see supplementary document, Appendix1, Fig. A7 and A9) reveal the occurrence of multiple resonance frequencies within the 25–50 GHz range. Additionally, these groups exhibit a significant limitation in terms of extremely narrow bandwidth. A very high dielectric constant substrate tightly confines the electromagnetic field within the material, leading to the excitation of multiple wave modes within a narrow frequency band, which results in multiple resonance peaks. Furthermore, substrates with high dielectric constants increase surface current, which enhances the interaction between radiating waves and surface waves, further contributing to the excitation of multiple resonant frequencies. These challenges are particularly critical for MIMO antenna arrays, as they may lead to mutual coupling, electromagnetic interference, and crosstalk effects.
- For the test groups using substrates with relatively low dielectric constants (i.e.  $\epsilon_r=2.2, 3$  or  $4$ ), thinner substrates result in higher gain, as seen from Fig. 6. This is because, for a thinner substrate where  $L_p/h \gg 1$  or  $W_p/h \gg 1$ , the fringing field effect is reduced, indicating fewer losses. However, for these test groups, the optimal substrate thickness for maximizing gain is approximately 0.254 mm, which is not the minimum thickness used in analyses. When the substrate becomes excessively thin, the proximity of the patch to the ground plane increases the impact of conduction and dielectric losses. These losses cause energy dissipation within the substrate rather than allowing it to radiate effectively, leading to a decrease in overall antenna efficiency and gain. Therefore, while thinner substrates initially enhance gain by reducing losses and improving radiation efficiency, making the substrate excessively thin results in diminished radiation and increased losses, ultimately reducing the gain.
- In controversially, for the test group using substrates with the highest dielectric constants ( $\epsilon_r=10.2$ ), thinner substrates result in reduce gain (see Fig. 6).

The radiation mechanism in microstrip antennas controlled fringing fields at the edges of the patch. In high dielectric constant materials, fringing fields are weak and so, most of the electromagnetic energy is confined within the substrate material rather than radiated. As the substrate thickness decreases, the concentration of the electromagnetic field within the material increases, leading to greater energy absorption and consequently, lower radiation efficiency and reduced gain. This reduction in radiated energy also accounts for the very narrow bandwidths observed in this test group.

- Far-field gain and directivity patterns indicate that test groups utilizing thin substrates with relatively low dielectric constants (i.e.  $\epsilon_r=2.2, 3$  or  $4$ ) exhibit a significant concentration of radiated power directed almost perpendicularly to the antenna surface, with a very low tilt angle (see supplementary document, Appendix 1, from (a) through (e) in Fig. A1, A2 and A4). Additionally, for these test groups, the main lobe level is enhanced, while the back lobe level is diminished as the substrate thickness decreases. Conversely, test groups employing thin substrates with high dielectric constants (i.e.  $\epsilon_r=6.15$  or  $10.2$ ) demonstrate an almost bidirectional far-field radiation pattern (see supplementary document, Appendix 1, from (a) through (e) in Fig. A6 and A8).
- Among all test cases, the highest gain and directivity ( $\sim 8.67$  dB) is achieved by using the substrate RT5880 ( $\epsilon_r=2.2$ ) and a thickness of  $h=0.254$  mm. However, the bandwidth for this test case is very narrow, approximately 0.7 GHz. On the other hand, the highest bandwidth ( $\sim 18.8$  GHz) across all test cases is achieved with the design using the substrate RT5880 ( $\epsilon_r=2.2$ ) and a thickness of  $h=1.57$  mm. For this test case gain and directivity is around 5.9 dB (see Table 3 and Fig.5-7.)
- The test case with a substrate dielectric constant of  $\epsilon_r=3$  and a thickness of  $h=0.787$  mm is particularly noteworthy due to its very wide bandwidth of approximately 17.6 GHz (46% of operation frequency) and relatively higher gain and directivity of around 7 dB, as given in Table 4. and Fig.5-7. This combination makes it a suitable choice for wide band antenna design with high efficiency.
- In contrast, for the test group utilizing a substrate with a very high dielectric constant ( $\epsilon_r=10.2$ ), the highest gain (7.9 dB) and directivity (8.3 dB) are achieved with thickest substrate (i.e.  $h=1.57$ mm). However, despite the high values of gain and directivity, bandwidth remains exceptionally narrow, ranging from 0.3 to 2.6 GHz across all substrate thicknesses (see Table 7 and Fig. 5–7). The use of a high-dielectric-constant substrate induces the excitation of multiple wave modes within a

narrow frequency band and increases surface waves, which enhances the interaction between radiating waves and surface waves. This interaction reduces antenna efficiency and is particularly problematic for closely spacing array designs due to mutual coupling and crosstalk effects.

#### 4. Conclusion

The objective of this study was to investigate the impact of key substrate properties on the performance of rectangular microstrip antennas (RMA), which is the most fundamental forms of microstrip antennas. The RMA was designed to operate at 38 GHz, targeting high-frequency 5G applications due to the low atmospheric attenuation in the Ka-band and simulations conducted over the frequency range of 25–50 GHz. To perform analyses, five test groups were established using well-known dielectric substrates, including RT5880, RO3003, FR4, RT6006, and RT6010. For each test group multiple substrate thicknesses (1.57 mm, 0.787 mm, 0.508 mm, 0.256 mm, and 0.125 mm) were utilized and analyzed in the design test cases to examine the effect of these variations on key antenna performance metrics, including resonance frequency ( $f_r$ ), return loss ( $S_{11}$ ), gain ( $G$ ), bandwidth ( $BW$ ) and directivity.

The findings of this study effectively demonstrate the relationship between substrate characteristics and antenna performance. The results indicate that selecting a substrate material with a lower dielectric constant (e.g.,  $\epsilon_r=2.2, 3$  or  $4$ ) is critical for efficient millimeter-wave band RMA designs. Notably, the test case with a substrate dielectric constant of  $\epsilon_r=3$  and a thickness of  $h=0.787$  mm stands out due to its exceptionally wide bandwidth of approximately 17.6 GHz (46% of the operating frequency) and relatively high gain and directivity, both around 7 dB. This combination makes it an ideal candidate for wideband antenna design with high efficiency in the millimeter-wave band.

In general, for low dielectric substrates, a trade-off between wider bandwidth and lower gain can be achieved by adjusting the substrate thickness and optimizing the antenna's size parameters. This flexibility allows the design to be tailored to specific applications, depending on the primary performance requirements. Conversely, substrates with very high dielectric constants (e.g.,  $\epsilon_r=10.2$ ) leading to increased surface wave propagation, multiple resonant frequencies, and higher dielectric losses. These challenges are particularly significant for MIMO antenna arrays, where they can contribute to mutual coupling and crosstalk effects.

Overall, the results of this study provide valuable insights into the influence of substrate properties on RMA performance, offering guidance that can inform more advanced antenna design studies, particularly in the context of high-frequency 5G applications.



**Table 3.** Summary of all design and performance parameters for test cases in Test Group#1

TEST GROUP #1 Dielectric Substrate: Rogers RT/duroid 5880 ( $\epsilon_r = 2.2, \tan\delta = 0.0009$ )							
	Parameter	Unit	Test Case 1.1	Test Case 1.2	Test Case 1.3	Test Case 1.4	Test Case 1.5
Design Parameters	$h$	mm	1.57	0.787	0.508	0.254	0.127
	$L_s = L_g$	mm	8	7	6	6	6
	$W_s = W_g$		6	6	7	8	9
	$L_p$		2.2978	1.835	2.157	2.4063	2.583
	$W_p$		3.852	3.913	3.33	3.336	2.9879
	$L_{fi}$		0.507	0.826	0.673	0.671	0.7534
	$W_f$		2.679	1.284	1.306	1.243	1.370
$g$	0.199		0.1699	0.1048	0.116	0.1199	
Performance Parameters	$f_r$	GHz	37.98	38.02	38.12	38.1	38.00
	$S_{11}$	dB	-27.52	-30.36	-30.92	-37.33	-45.75
	$f_{c1} - f_{c2}$	GHz	25.54- 44.6	34.45-41.83	36.44-39.56	37.24-38.78	37.60-38.32
	$BW$	GHz	18.87	7.38	3.12	1.54	0.72
	$G$	dB	5.87	7.61	8.26	8.67	8.59
	Directivity	dB	5.89	7.53	8.23	8.67	8.67

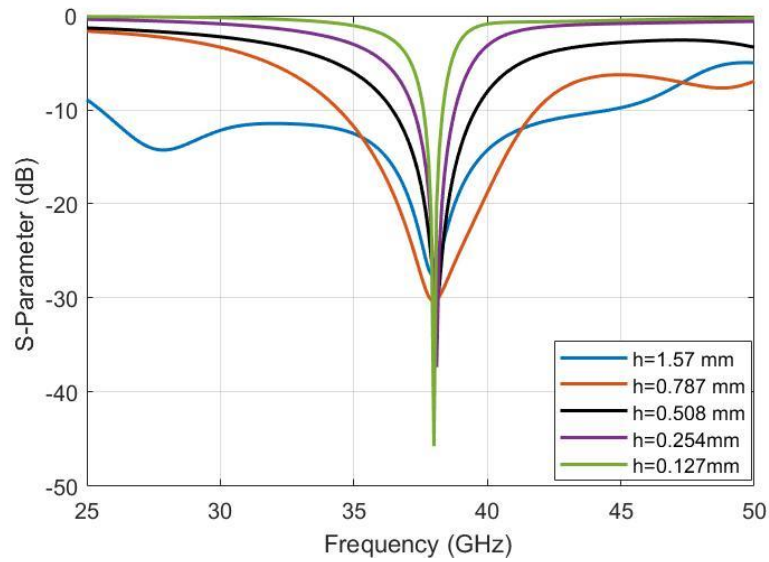


**Figure 4.** Comparison of Return loss ( $S_{11}$ ) graphs for Test Group#1 ( $\epsilon_r = 2.2$ ) across various thicknesses



**Table 4.** Summary of all design and performance parameters for test cases in Test Group#2

TEST GROUP #2 Dielectric Substrate: Rogers RO3003 ( $\epsilon_r = 3, \tan\delta = 0.0013$ )							
	Parameter	Unit	Test Case 2.1	Test Case 2.2	Test Case 2.3	Test Case 2.4	Test Case 2.5
Design Parameters	$h$	mm	1.57	0.787	0.508	0.254	0.127
	$L_s = L_g$	mm	6	6	6	6	6
	$W_s = W_g$		5.22	5.5	7	8	9
	$L_p$		1.218	1.535	1.832	2.2	2.321
	$W_p$		3.626	3.5	3.474	3.03	3
	$L_{fi}$		0.2925	0.28	0.388	0.302	0.5164
	$W_f$		1.942	1.76	1.693	1.913	1.694
$g$	0.1		0.1	0.116	0.171	0.13	
Performance Parameters	$f_r$	GHz	38.02	38.04	38.0	37.9	37.9
	S11	dB	-39.76	-43.91	-37.89	-43.78	-27.27
	$f_{c1} - f_{c2}$	GHz	28.26-39.63	34.23-51.87	36.12-39.56	36.82-38.72	37.57-38.18
	BW	GHz	11.37	17.64	3.44	1.9	0.6
	G	dB	5.84	7.11	7.62	8.16	7.81
	Directivity	dB	5.83	7.09	7.60	8.18	8.00

**Table 5.** Summary of all design and performance parameters for test cases in Test Group#3

TEST GROUP #3 Dielectric Substrate: FR4_epoxy ( $\epsilon_r = 4.4, \tan\delta = 0.02$ )							
	Parameter	Unit	Test Case 3.1	Test Case 3.2	Test Case 3.3	Test Case 3.4	Test Case 3.5
Design Parameters	$h$	mm	1.57	0.787	0.508	0.254	0.127
	$L_s = L_g$	mm	5.32	5	4	4.5	5
	$W_s = W_g$		3.56	4	5	6	7
	$L_p$		1.215	1.22	1.437	1.6849	1.9598
	$W_p$		3.23	2.92	3.0537	3.157	2.6728
	$L_{fi}$		0.27	0.25	0.25	0.2987	0.294
	$W_f$		1.87	1.5	1.2752	1.442	1.85
$g$	0.1		0.1	0.05	0.078	0.086	
Performance Parameters	$f_r$	GHz	38.0	38.08	37.92	38.14	38.0
	S11	dB	-40.46	-43.05	-35.80	-40.40	-43.05
	$f_{c1} - f_{c2}$	GHz	34.23-40.91	33.84-47.35	35.25-40.71	36.81-39.35	37.26-38.91
	BW	GHz	6.68	13.51	5.46	2.54	1.64
	G	dB	4.38	5.12	6.58	6.59	5.93
	Directivity	dB	5.08	5.64	7.15	6.59	7.96

**Table 6.** Summary of all design and performance parameters for test cases in Test Group#4

TEST GROUP #4 Dielectric Substrate: Rogers RT/duroid 6006 ( $\epsilon_r = 6.15, \tan\delta = 0.0019$ )							
	Parameter	Unit	Test Case 4.1	Test Case 4.2	Test Case 4.3	Test Case 4.4	Test Case 4.5
Design Parameters	$h$	mm	1.57	0.787	0.508	0.254	0.127
	$L_s = L_g$	mm	7.55	7	7.6	7	7
	$W_s = W_g$		5	5	5	5	5
	$L_p$		2.997	2.6954	2.74	3.043	3.1825
	$W_p$		3	2.114	3.43	2.6	2.107
	$L_{fi}$		0.5	0.3118	0.5	0.2634	0.3936
	$W_f$		1.877	1.275	1.4	1.0505	0.5
$g$	0.1		0.0781	0.1	0.05	0.05	
Performance Parameters	$f_r$	GHz	38.00	38.04	37.9	38.0	38.02
	S11	dB	-24.33	-31.47	-37.84	-29.23	-17.13
	$f_{c1} - f_{c2}$	GHz	37.45-38.55	35.39-40.07	37.23-38.52	37.78-38.24	37.93-38.11
	BW	GHz	1.1	4.68	1.29	0.46	0.18
	G	dB	6.16	6.12	6.31	6.40	6.00
	Directivity	dB	6.37	6.16	6.47	6.74	6.84

**Table 7.** Summary of all design and performance parameters for test cases in Test Group#5

TEST GRUP #5 Dielectric Substrate: Rogers RT/duroid 6010 ( $\epsilon_r = 10.2, \tan\delta = 0.0023$ )							
	Parameter	Unit	Test Case 5.1	Test Case 5.2	Test Case 5.3	Test Case 5.4	Test Case 5.5
Design Parameters	$h$	mm	1.57	0.787	0.508	0.254	0.127
	$L_s = L_g$	mm	8	6.5	7	7	7
	$W_s = W_g$		5.3	5.5	5.5	8	8
	$L_p$		2.5737	3.99	2.271	2.3172	2.01
	$W_p$		4.127	3.5	3.54	3.93542	4.4556
	$L_{fi}$		0.8975	1.096	0.8481	0.8051	1.2498
	$W_f$		1.7441	1.9928	1.2862	1.0157	1.9501
$g$	0.126		0.083	0.06437	0.0903	0.0587	
Performance Parameters	$f_r$	GHz	38.0	38.06	37.96	38.04	38.0
	$S_{11}$	dB	-43.89	-22.96	-36.62	-24.09	-24.7
	$f_{c1} - f_{c2}$	GHz	37.61-39.06	36.85-39.46	37.34-38.59	37.87-38.20	37.83-38.26
	$BW$	GHz	1.45	2.61	1.25	0.33	0.43
	$G$	dB	7.95	7.72	7.11	6.99	5.88
	Directivity	dB	8.35	7.86	7.30	7.67	6.92

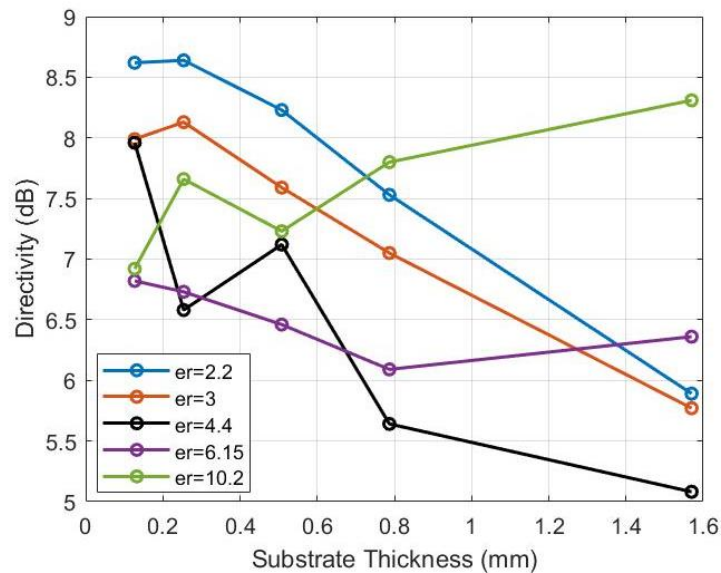


**Figure 5.** Comparison of directivities of designed antennas across various substrate thicknesses (each colored line represents a test group with a specific dielectric constant as indicated in the label)

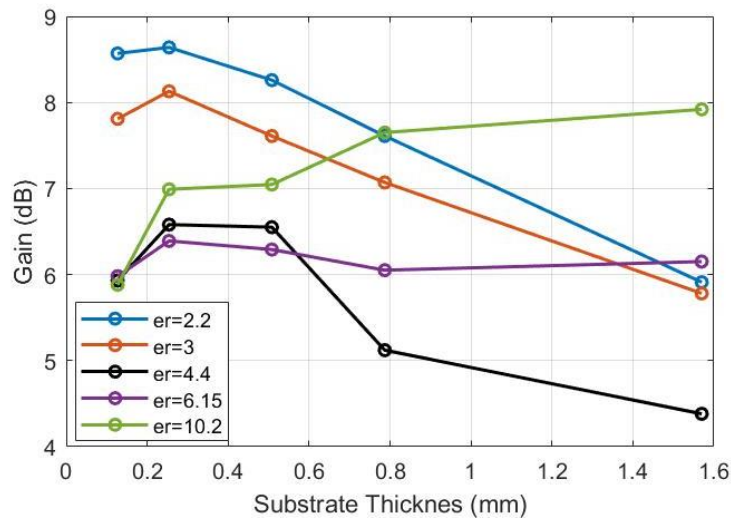


**Figure 6.** Comparison of gains of designed antennas across various substrate thicknesses (each colored line represents a test group with a specific dielectric constant as indicated in the label)

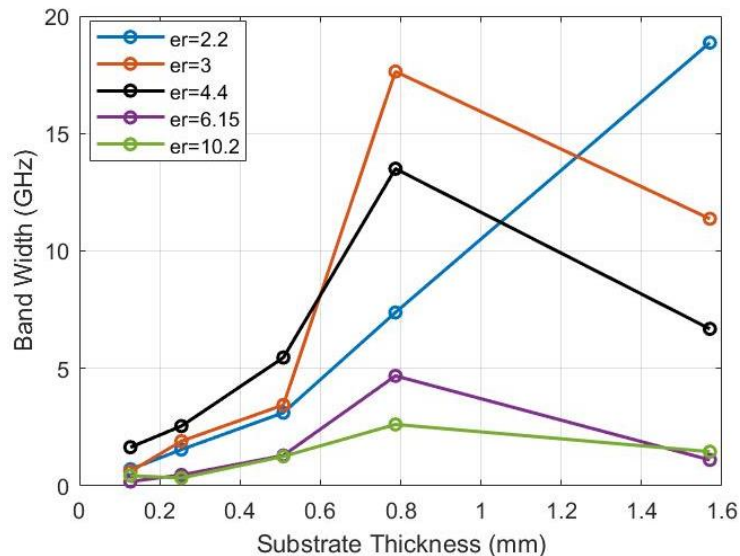


**Figure 7.** Comparison of band widths of designed antennas across various substrate thicknesses (each colored line represents a test group with a specific dielectric constant as indicated in the label)

## References

[1]. Internet: Cisco “Visual Networking Index: Global Mobile Data Traffic Forecast Update, 2014–2019”, 2015. Available: [www.Cisco.com](http://www.Cisco.com).

[2]. Internet: Cisco, “Global 2016 Year in Review”, 2016. Available: [www.Cisco.com](http://www.Cisco.com).

[3]. Agiwal, M., Roy, A., & Saxena, N. 2016. Next generation 5G wireless networks: A comprehensive survey. *IEEE Communications Surveys & Tutorials*, 18(3), 1617-1655.

[4]. Yang, Y., Xu, J., Shi, G., & Wang, C. X. 5G Wireless Systems. Springer International Publishing, 2018; pp 2-7.

[5]. Demirci M., 5G Haberleşme Teknolojisi için Mikroşerit Yama Anten Tasarımı, Master's Thesis, Osmaniye Korkut Ata Üniversitesi, Osmaniye, 2020.

[6]. Internet: Aselsan, “Yeni Nesil Geniş Bantlı Haberleşme Teknolojileri, 5G Nedir?”, ISSN 1300-2473, 35(111), 2022; pp 26-30. Available: [www.aselsan.com.tr](http://www.aselsan.com.tr)

[7]. Parchin, N. O., Mohamed, H. G., Moussa, K. H., See, C. H., Abd-Alhameed, R. A., Alwadai, N. M., & Amar, A. S. 2023. An efficient antenna system with improved radiation for multi-standard/multi-mode 5G cellular communications. *Scientific Reports*, 13(1), 4179.

[8]. Raj, T., Mishra, R., Kumar, P., & Kapoor, A. 2023. Advances in MIMO antenna design for 5G: A comprehensive review. *Sensors*, 23(14), 6329.

[9]. Krishnamoorthy, R., Kumar, U. S., Swathi, G., Begum, M. A., Nancharaiyah, B., & Sagar, K. D. 2023. Metamaterial inspired quad-port multi-antenna system for millimeter wave 5G applications. *Journal of Infrared, Millimeter, and Terahertz Waves*, 44(5), 346-364.

[10]. Al-Azzawi, Z. F., AbdulSattar, R. K., Muhsin, M. Y., Azeez, M. A., Salim, A. J., & Ali, J. K. 2023. Designing eight-port antenna array for multi-band MIMO applications in 5G smartphones. *Journal of Telecommunications and Information Technology*, (4).

[11]. Chbeine, M., Azmani, M., & Astito, A. Advanced UWB MIMO Antenna with Wide Bandwidth and High-Efficiency Performance for

5G. 11th International Conference on Signal Processing and Integrated Networks (SPIN), IEEE. 2024, March, pp. 227-232.

[12]. Ibrahim, S. K., Singh, M. J., Al-Bawri, S. S., Ibrahim, H. H., Islam, M. T., Islam, M. S. & Abdulkawi, W. M. 2023. Design, challenges and developments for 5G massive MIMO antenna systems at sub 6-GHz band: a review. *Nanomaterials*, 13(3), 520.

[13]. Cao, T. N., Nguyen, M. T., Phan, H. L., Nguyen, D. D., Vu, D. L., Nguyen, T. Q. H., & Kim, J. M. 2023. Millimeter-wave broadband MIMO antenna using metasurfaces for 5G cellular networks. *International Journal of RF and Microwave Computer-Aided Engineering*, 2023(1), Article ID 9938824. <https://doi.org/10.1155/2023/9938824>

[14]. Sharaf, M. H., Zaki, A. I., Hamad, R. K., & Omar, M. M. (2020). A novel dual-band (38/60 GHz) patch antenna for 5G mobile handsets. *Sensors*, 20(9), 2541.

[15]. Demirci, M., Ermiş, S. 2021. 5G teknolojisi için çift bantlı (28/38 GHz) dikdörtgen mikroşerit anten tasarımı. *Bilişim Teknolojileri Dergisi*, 14(2), 171-181.

[16]. Haneef, S. R., Selvaperumal, S. K., & Jayapal, V. 2020. High gain rectangular single patch antenna at mmwave band. *International Journal of Advanced Science and Technology*, 29(1), pp. 1311- 1325.

[17]. Ramli, N., Noor, S. K., Khalifa, T., & Abd Rahman, N. H. 2020. Design and performance analysis of different dielectric substrate based microstrip patch antenna for 5G applications. *International Journal of Advanced Computer Science and Applications*, 11(8).

[18]. Ahmad, I., Sun, H., Zhang Y. & Samad, A. High Gain Rectangular Slot Microstrip Patch Antenna for 5G mm-Wave Wireless Communication, 5th International Conference on Computer and Communication Systems (ICCCS), Shanghai, China, 2020, pp. 723-727, doi: [10.1109/ICCCS49078.2020.9118602](https://doi.org/10.1109/ICCCS49078.2020.9118602).

[19]. Sree, M. F. A., Abd Elazeem, M. H., & Swelam, W. Dual Band Patch Antenna Based on Letter Slotted DGS for 5G Sub-6GHz Application. In *Journal of Physics: Conference Series*, IOP Publishing, Vol. 2128, No. 1, 2021, December, p. 012008.

[20]. Marasco, I., Niro, G., Mastronardi, V. M., Rizzi, F., D’Orazio, A., De Vittorio, M., & Grande, M. 2022. A compact evolved antenna for 5G communications. *Scientific reports*, 12(1), 10327.

[21]. Yadav, J., Sharma, S., & Arora, M. 2022. A paper on microstrip patch antenna for 5G applications. *Materials Today: Proceedings*, 66, 3430-3437.

[22]. Ermiş, S., & Demirci, M. 2023. Improving the performance of patch antenna by applying bandwidth enhancement techniques for 5G applications. *Tehnički glasnik*, 17(3), 305-312.

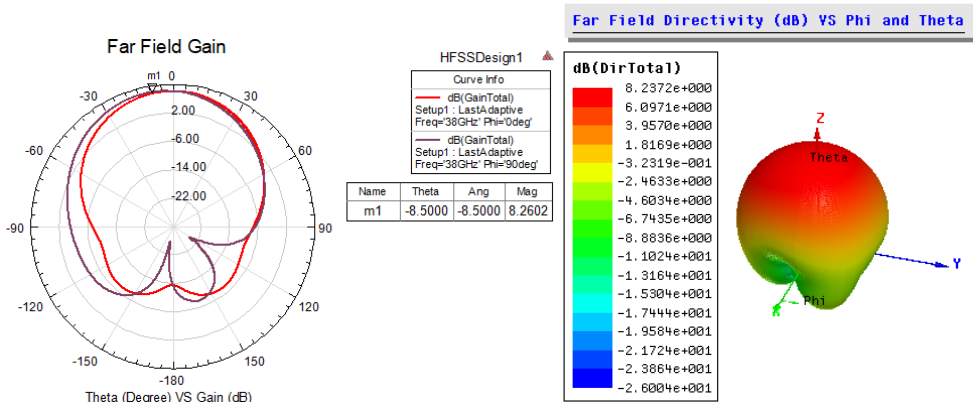
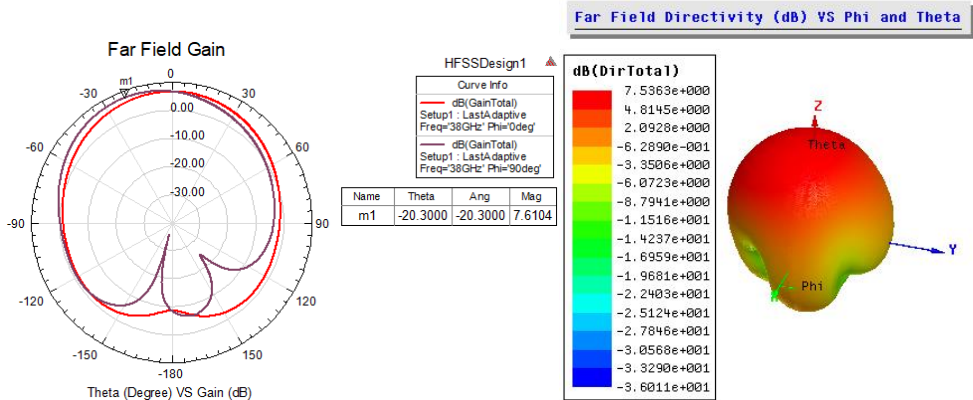
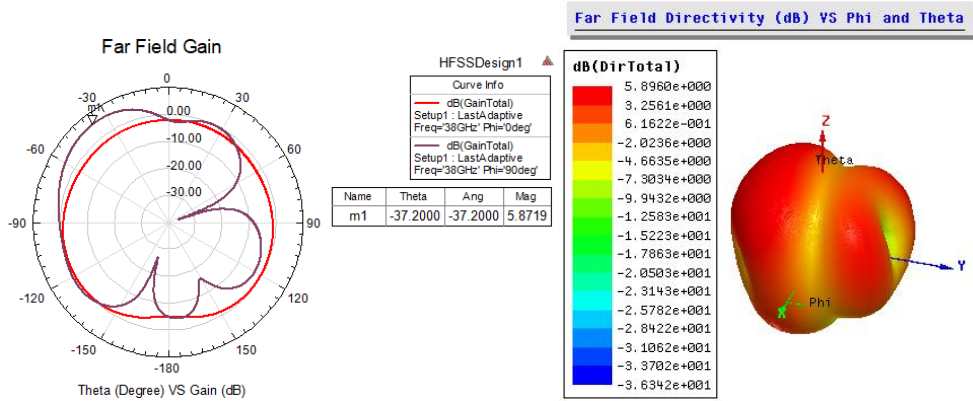
[23]. Kumar, L., Nath, V., & Reddy, B. V. R. 2023. Triple-band stub loaded patch antenna with high gain for 5G Sub-6 GHz, WLAN and WIMAX applications using DGS. *Facta Universitatis, Series: Electronics and Energetics*, 36(2), 171-188.

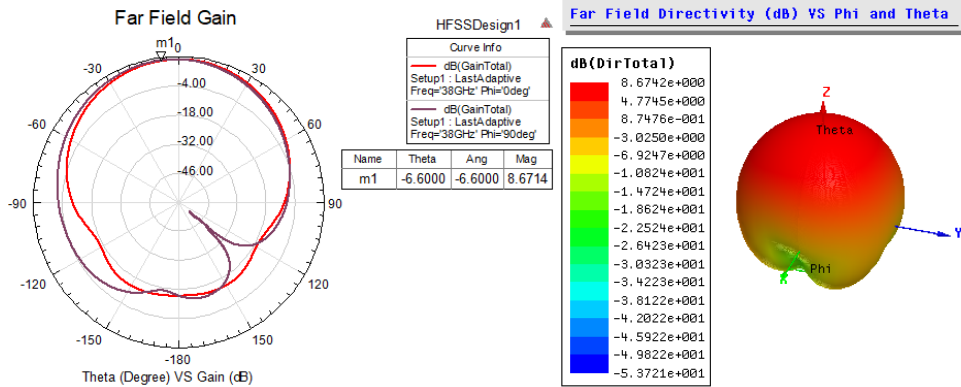
[24]. Es-saleh, A., Bendaoued, M., Lakrit, S., Das, S., Atounti, M., & Faize, A. 2023. A novel fractal patch antenna using Defected Ground Structure (DGS) with high isolation for 5G applications. *Journal of Nano- and Electronic Physics*, 15(3), 03012(4pp).

[25]. Balanis, C. A. *Antenna Theory: Analysis and Design*. Second Edition, John Wiley & Sons, 2016, pp 722-784.

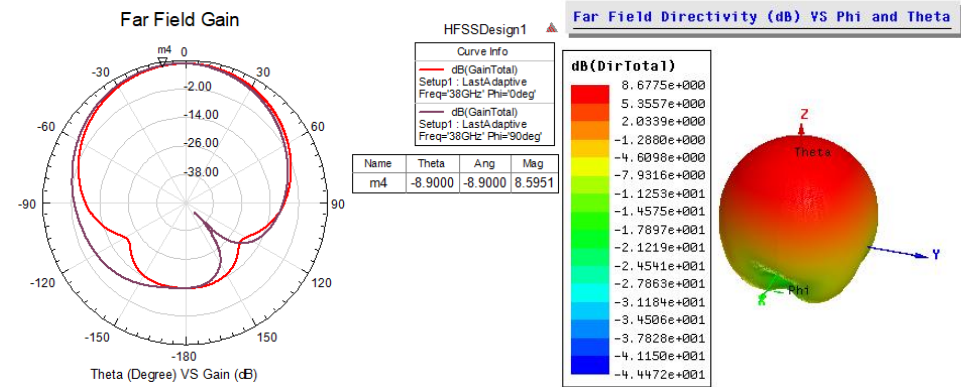
[26]. Garg, R. *Microstrip Antenna Design Handbook*. Artech House, 2001, pp 253-314.

### Appendix 1.



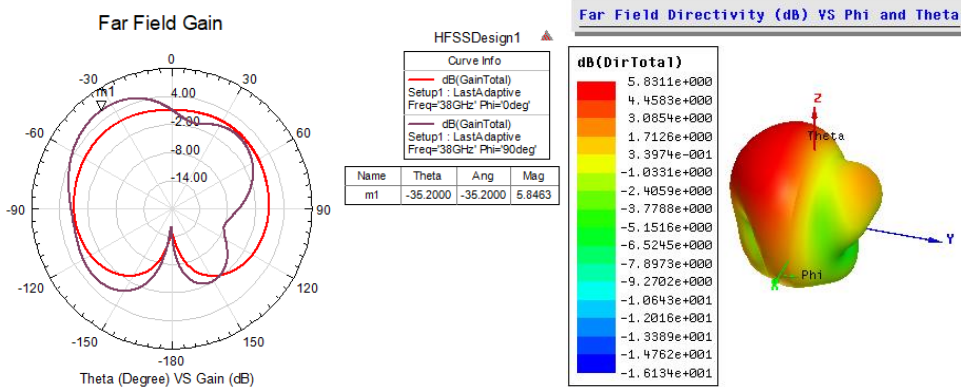


(d)

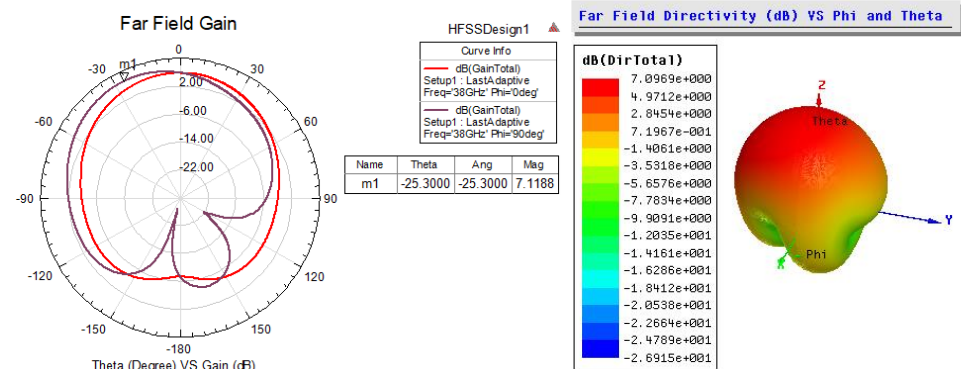


(e)

**Figure A1.** Far field gain and 3D directivity patterns for Test Group#1 ( $\epsilon_r = 2.2$ ) with varying substrate thicknesses;  $h=1.57\text{mm}$  (a),  $h=0.787\text{mm}$  (b),  $h=0.508\text{mm}$  (c),  $h=0.254\text{mm}$  (d) and  $h=0.127\text{mm}$  (e)



(a)



(b)



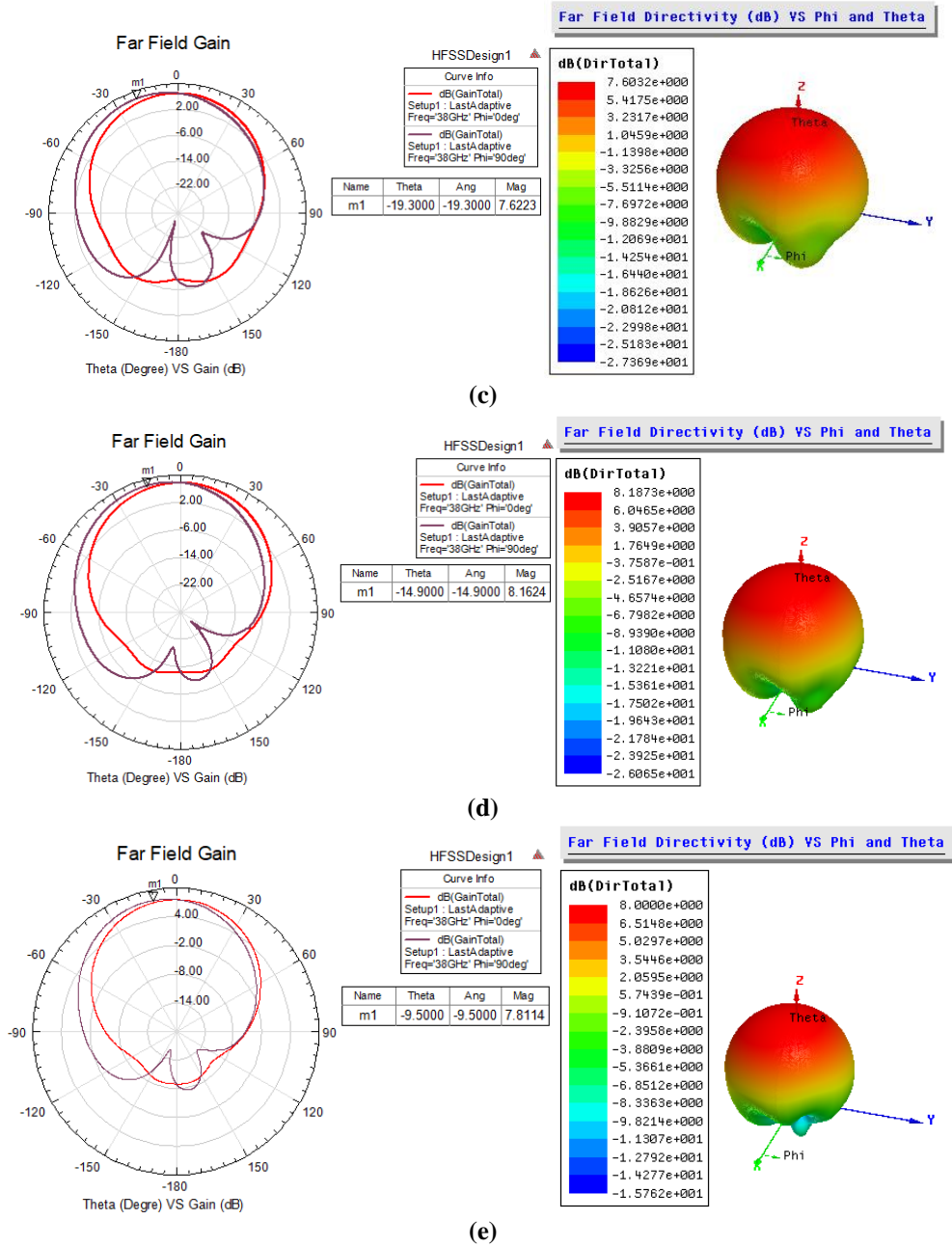


**Figure A2.** Far field gain and 3D directivity patterns for Test Group#2 ( $\epsilon_r = 3$ ) with varying substrate thicknesses;  $h = 1.57\text{mm}$  (a),  $h = 0.787\text{mm}$  (b),  $h = 0.508\text{mm}$  (c),  $h = 0.254\text{mm}$  (d) and  $h = 0.127\text{mm}$  (e)

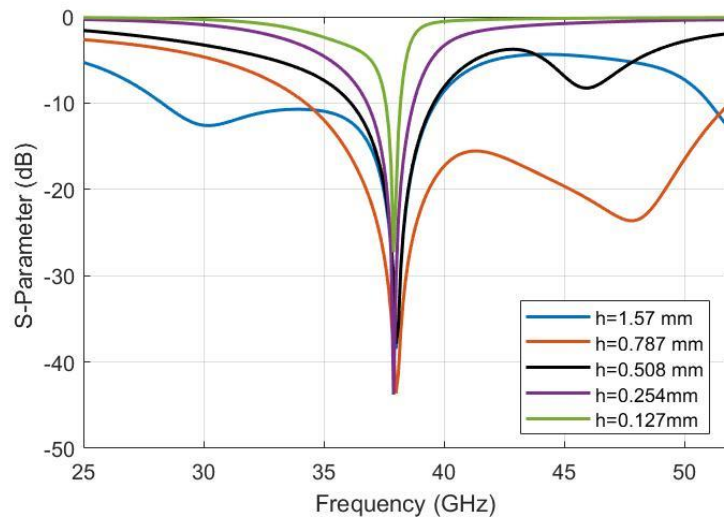
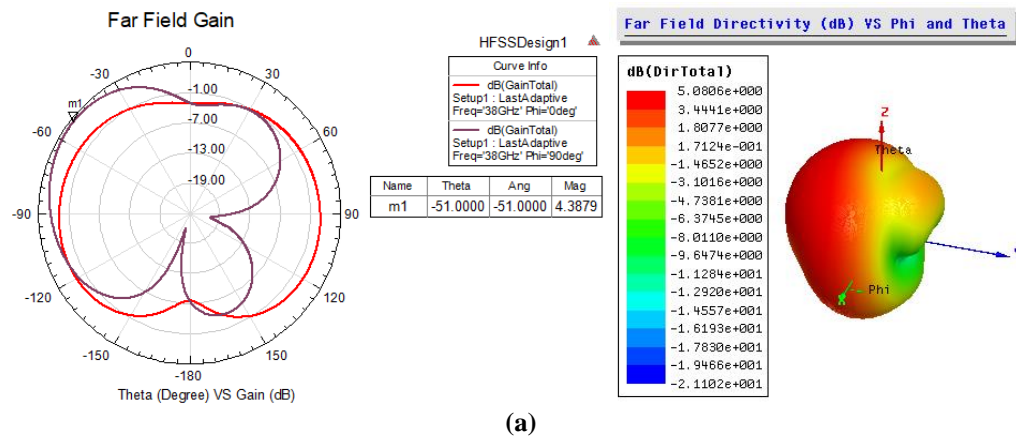
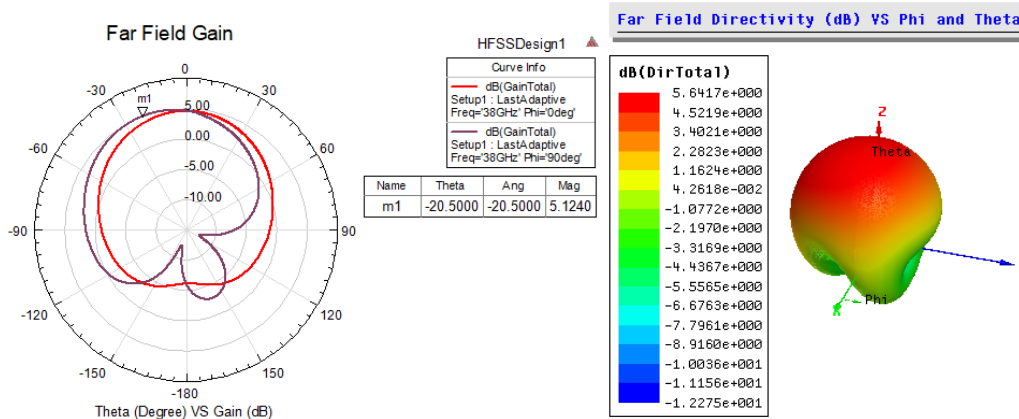


**Figure A3.** Comparison of Return loss (S11) graphs for Test Group#2 ( $\epsilon_r = 3$ ) across various thicknesses



(a)



(b)

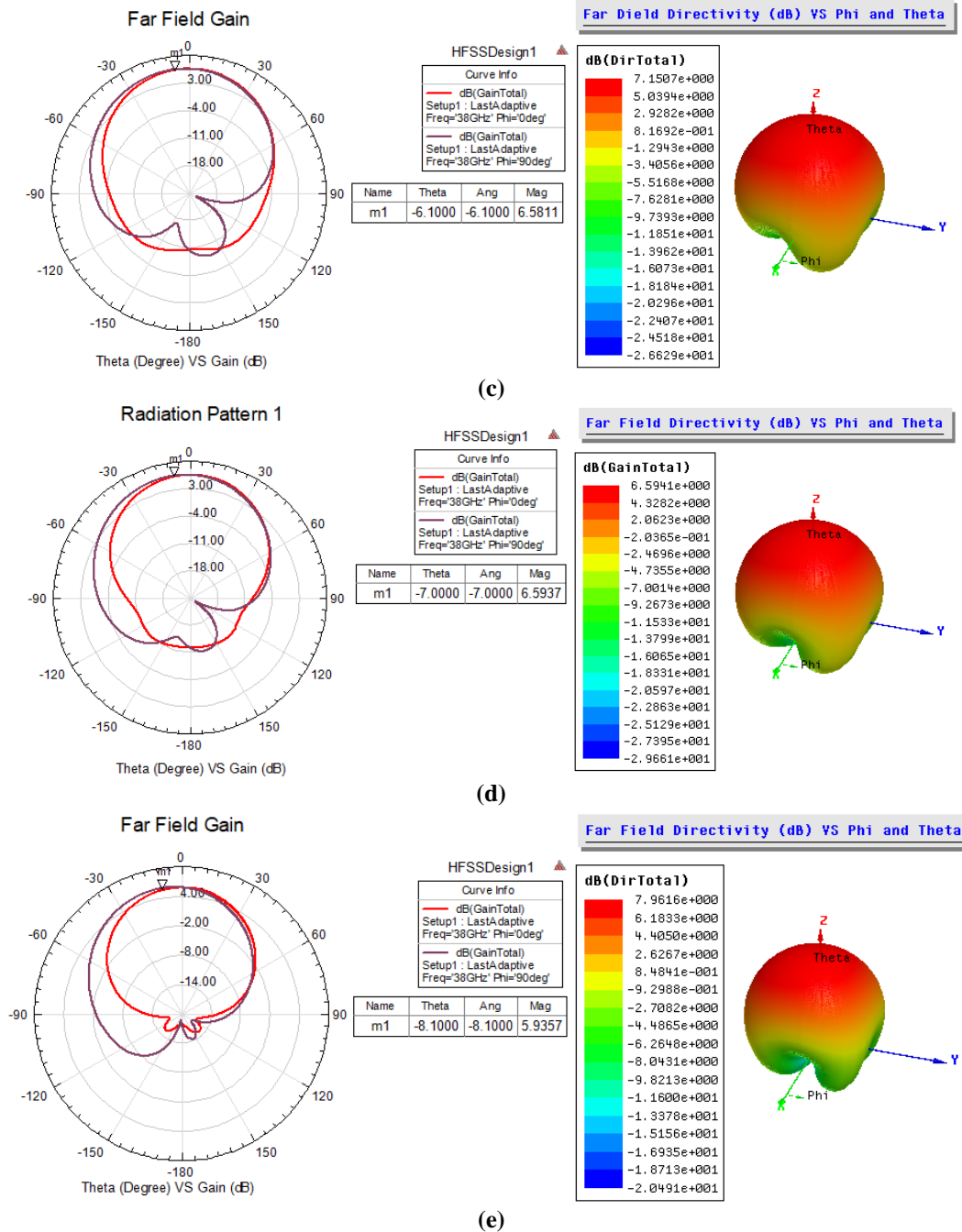


**Figure A4.** Far field gain and 3D directivity patterns for Test Group#3 ( $\epsilon_r = 4.4$ ) with varying substrate thicknesses;  $h=1.57\text{mm}$  (a),  $h=0.787\text{mm}$  (b),  $h=0.508\text{mm}$  (c),  $h=0.254\text{mm}$  (d) and  $h=0.127\text{mm}$  (e)

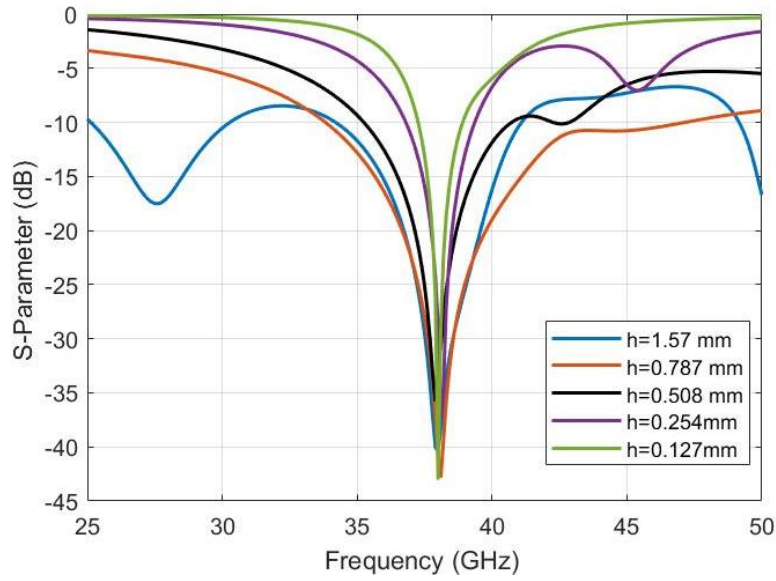
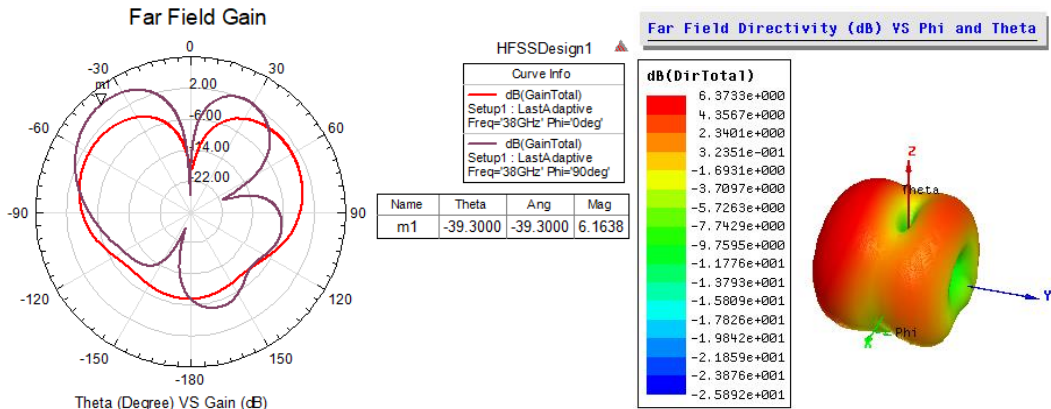
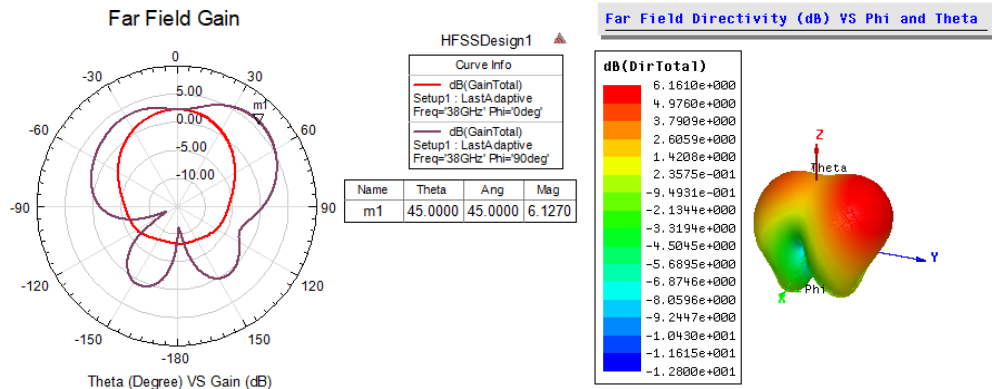


Figure A5. Comparison of Return loss (S11) graphs for Test Group#3 ( $\epsilon_r = 4.4$ ) across various thicknesses



(a)



(b)

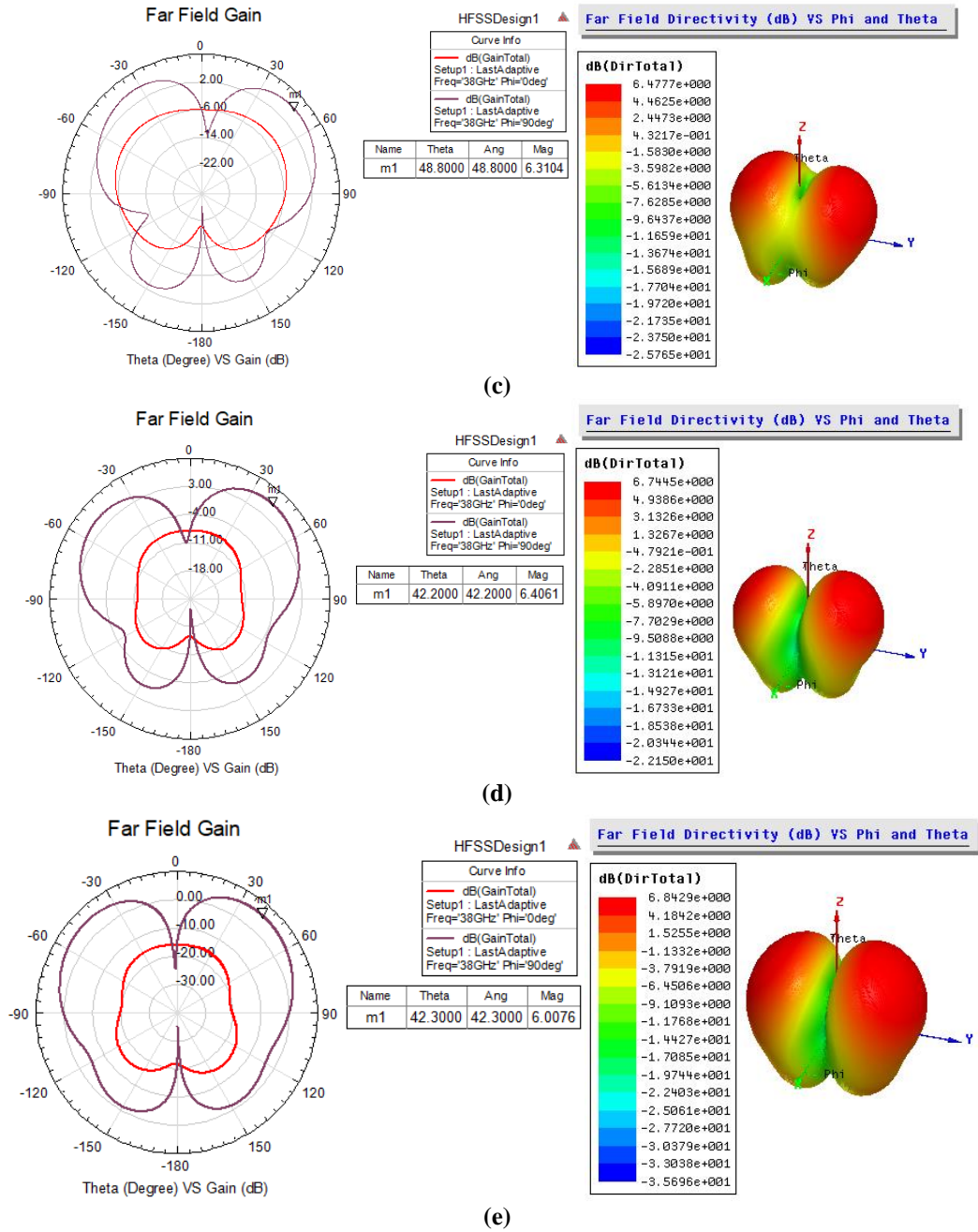


**Figure A6.** Far field gain and 3D directivity patterns for Test Group#4 ( $\epsilon_r = 6.15$ ) with varying substrate thicknesses;  $h=1.57\text{mm}$  (a),  $h=0.787\text{mm}$  (b),  $h=0.508\text{mm}$  (c),  $h=0.254\text{mm}$  (d) and  $h=0.127\text{mm}$  (e)



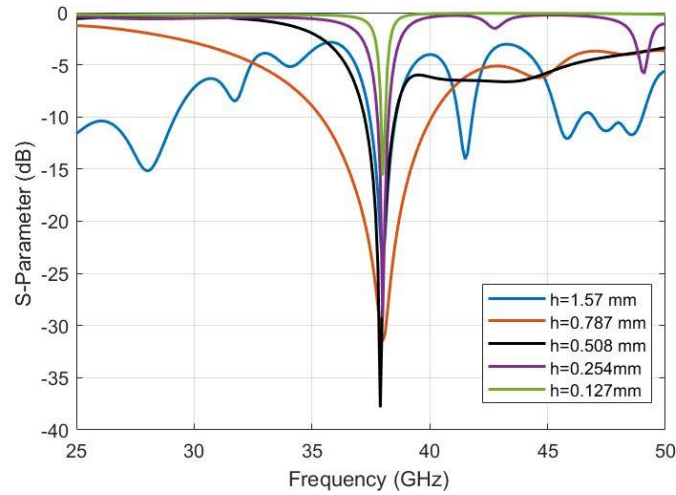
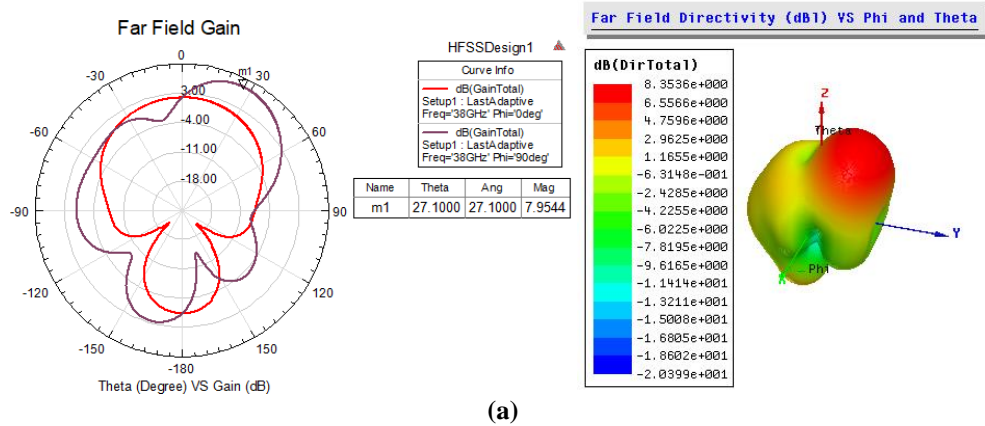
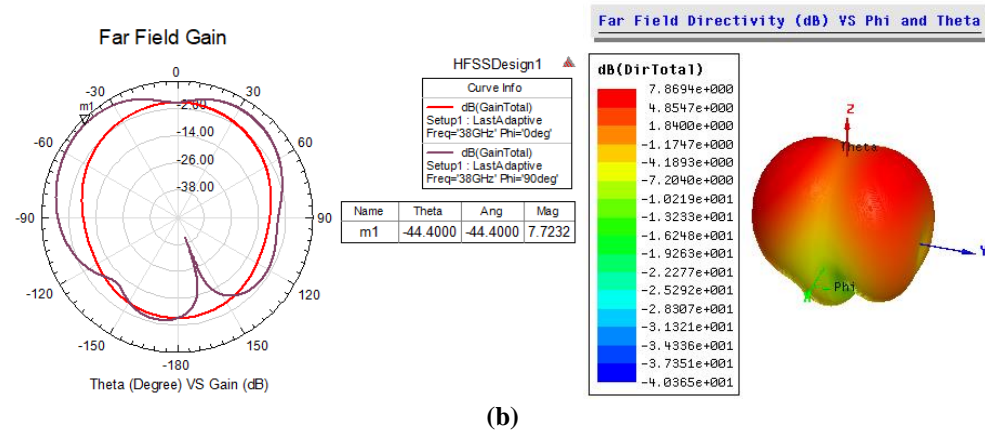


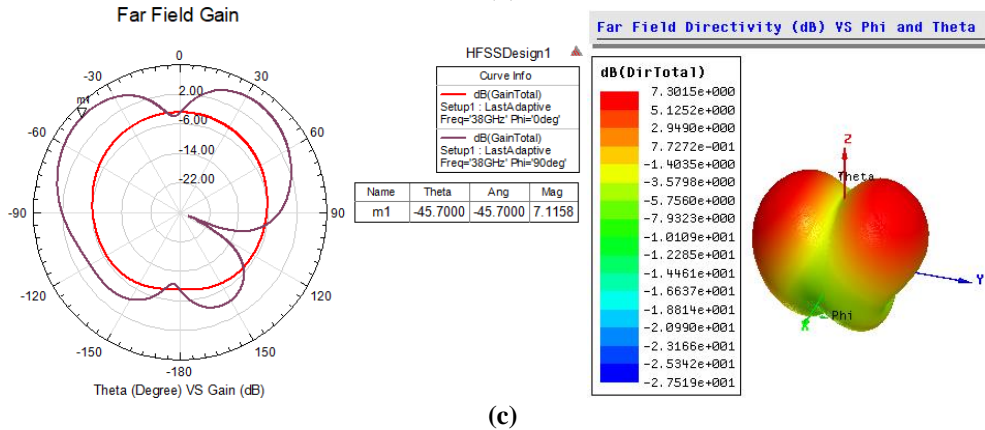
**Figure A7.** Comparison of Return loss (S11) graphs for Test Group#4 ( $\epsilon_r = 6.15$ ) across various thicknesses



(a)



(b)



(c)

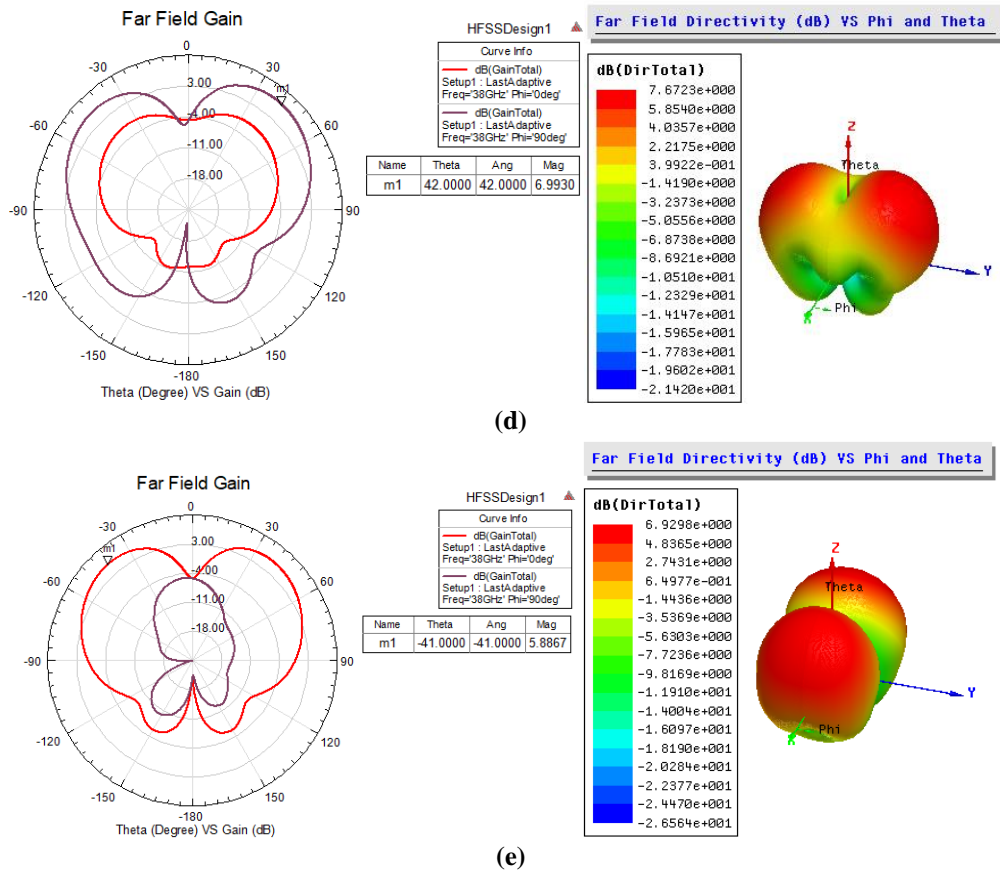


**Figure A8.** Far field gain and 3D directivity patterns for Test Group#5 ( $\epsilon_r = 10.2$ ) with varying substrate thicknesses;  $h=1.57\text{mm}$  (a),  $h=0.787\text{mm}$  (b),  $h=0.508\text{mm}$  (c),  $h=0.254\text{mm}$  (d) and  $h=0.127\text{mm}$  (e)

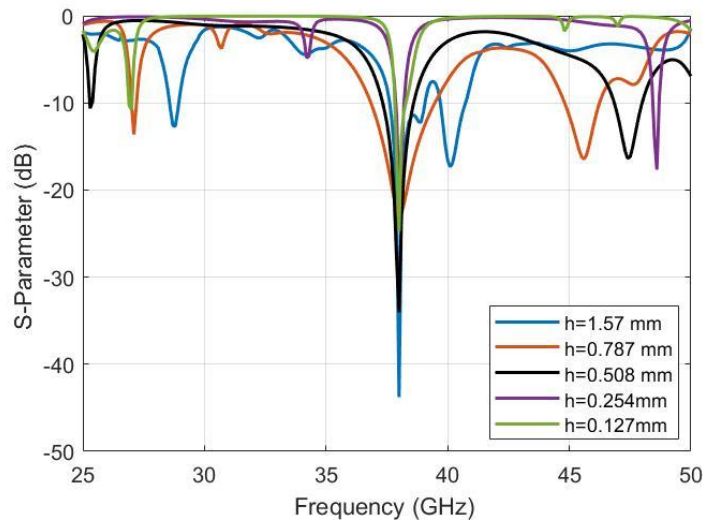


**Figure A9.** Comparison of Return loss (S11) graphs for Test Group#5 ( $\epsilon_r = 10.2$ ) across various thicknesses

# Use of Active Carbon Produced by Hydrothermal Method from Agricultural Waste in Methylene Blue Removal

Mustafa Boyrazlı<sup>1</sup> , Elif Arancı Öztürk<sup>2\*</sup> , Emrah Çelik<sup>1</sup> , Mehmet Ali Yashlı<sup>1</sup> 

<sup>1</sup>Firat University, Faculty of Engineering, Department of Metallurgical and Materials Engineering, Elazığ, Türkiye

<sup>2</sup>Balıkesir University, Balıkesir Vocational School, Department of Machine and Metal Technologies, Balıkesir, Türkiye

\* [elif.ozturk@balikesir.edu.tr](mailto:elif.ozturk@balikesir.edu.tr)

\* Orcid No: 0000-0001-8362-7332

Received: 16 July 2024

Accepted: 12 October 2024

DOI: 10.18466/cbayarfbe.1517079

## Abstract

In this study, the use of activated carbon produced from agricultural waste via the hydrothermal method for the removal of methylene blue from solution was examined. Pistachio roasting facility waste was selected as the agricultural waste. For activated carbon production, carbonized products were treated in a hydrothermal device in the presence of an activator for various durations. During processes conducted at a constant temperature, high pressure was achieved, allowing the activated carbon to attain a high adsorption capacity. The results showed that the sample with a KOH impregnation ratio of 1:1, treated in a hydrothermal device for 480 minutes at 160 °C, was able to remove methylene blue with a 99.85% extraction yield in a solution with a 350 ppm methylene blue concentration.

**Keywords:** Activated Carbon, Adsorption, Hydrothermal Carbonization, Methylene Blue, Organic Waste, Pistachio.

## 1. Introduction

Activated carbon (AC) is carbonaceous material with a highly developed internal surface area and porosity. The large surface area gives a high capacity for adsorbing chemicals from gases or liquids. The specific surface areas of ACs vary widely, with reported values ranging from 250 m<sup>2</sup>/g to over 2000 m<sup>2</sup>/g, making them versatile adsorbents with a wide range of applications [1]. However, production and regeneration of commercial activated carbons are still expensive and so the importance of activated carbon production by using low-cost raw materials and methods are still up to date [2].

Synthesis of activated carbon from waste biomass is of current interest towards sustainability. The properties of biomass derived activated carbon largely depends on the carbonization process [3]. Biomass being recyclable and abundantly present across the planet has been allotted numerous roles to play for sustainable development. In addition to being a food source and renewable raw material, it can be used for energy production, carbon sequestration and, as an essential element for the production of hydrochars and activated carbons [4]. In

response to rising costs associated with waste disposal and increasing environmental demands, the sustainable conversion of wastes into useful products is becoming increasingly important [1].

The world consumption of activated carbons is steadily increasing and new applications are always emerging, particularly those concerning environmental pollution remediation, which should help to sustain demand for them. Important applications are related to their use in water treatment for the removal of flavor, color, odor and other undesirable organic impurities from water. Activated carbon is also used in industrial wastewater and gas treatment due to the necessity for environment protection and also for material recovery purposes. The food and pharmaceutical industries are also a major consumer of activated carbon. Activated carbon is defined as a carbonaceous material with a large internal surface area and highly developed porous structure resulting from the processing of raw materials under high temperature reactions. It is composed of 87% to 97% carbon but also contains other elements depending on the processing method used and raw material it is derived from. Activated carbon's porous structure allows it to adsorb materials from the liquid and gas

phase [1]. Its pore volume typically ranges from 0.20 to 0.60 cm<sup>3</sup>/g, and has been found to be as large as 1 cm<sup>3</sup>/g. Its surface area ranges typically from 800 to 1500 m<sup>2</sup>/g [2] but has been found to be in excess of 3,000 m<sup>2</sup>/g.

Since the hetero atoms that may be present in the activated carbon structure cannot fully fill the strong valences surrounding the carbon atoms, they are bonded to the ends and corners of the crystal structure. If there is an incorrect arrangement of carbon atoms in the crystal lattice, these atoms react with oxygen, hydrogen and other atoms to reduce their energy. High-energy carbon atoms fill their valence by bonding to a neighboring simple crystal or by bonding to thermal decomposition products during carbonization [5-7].

Many studies can be found in the literature examining the production and characterization of activated carbon from a wide variety of carbon-containing materials and its potential to remove various organic and inorganic pollutants from aqueous solution. Hameed et al. in the study conducted on rattan sawdust by, the capacity of activated carbon was found to be 294.14 mg g<sup>-1</sup> [8].

Duman et al. produced activated carbon from pine cones by chemical activation using H<sub>3</sub>PO<sub>4</sub> and ZnCl<sub>2</sub> and after characterizing it, they reported the surface area as 1823 m<sup>2</sup> g<sup>-1</sup> [9].

In the literature, sugar beet molasses [10], rice hulls [11], maize stalks [12], sunflower oil cake [13], peanut shells [14], green alga [15], date pits [16], lignite coal [17], bagasse, hard shells of apricot stones, almond, walnut and hazelnut shells [18] has been used for the production of activated carbon. It is possible to come across studies using organic materials.

The USA ranks first in world pistachio production with 523.900 tons in the 2023/24 production season. In the same production season, Iran follows the USA with 135.000 tons and Turkey with 119.355 tons. Turkey provides 12% of the world pistachio production [19].

In this study, the methylene blue adsorption ability of activated carbon produced by hydrothermal carbonization method was examined. It is aimed to evaluate these shells, which are left to the environment as waste after pistachio production, especially in the South Eastern Anatolia Region of Turkey.

## 2. Materials and Methods

### 2.1. Material

For the experiments, pistachio processing plant waste (PPPW) collected from the waste areas of three different pistachio processing facilities in Birecik district of Şanlıurfa were used. These wastes are materials that are

not used in pistachio facilities and are generally thrown into the environment (Figure 1).



**Figure 1.** PPPW released into the environment after being processed in facilities

PPPW consists of the pistachio paddy located on the upper part of the pistachio fruit, known as the soft shell layer. It is a material consisting of pistachio paddy, pistachio resin and leaves.

Merck 1.05033.1000 cas number 85% purity potassium hydroxide, Merck 1.00317.2500 cas number 37% purity hydrochloric acid, Merck 1.00063.2511 cas number 100% purity acetic acid and Merck 106268.1000 cas number 99% purity sodium acetate were used in the experiments. Chem Bio, 61734 methylene blue with 99% purity was used as dye.

### 2.2. Equipment and Analysis

In the experiments, a domestic Vommak brand ball mill and a sieve manufactured by Yüksel Kaya Makina were used. Electro-Mag M5040P brand oven was used to evaporate the moisture in the PPPW.

For the hydrothermal treatment of PPPW samples, the Fytronix brand hydrothermal device shown in Figure 2 was used.



**Figure 2.** Hydrothermal device used in experiments

This device; it consists of a temperature and time controlled control panel, a hydrothermal reactor and a



magnetic stirrer. The hydrothermal reactor is made of stainless steel. The interior of the reactor is designed to accommodate a 100 ml teflon container. There are two valves and a digital pressure gauge on the cover of the reactor to ensure gas inlet and outlet. The mixing process of the reactor is carried out by rotating the magnetic fish placed in the teflon container by the magnetic stirrer.

The activation process was carried out in a Nevada 160/7 brand muffle furnace with an 8-liter capacity, capable of reaching 1600 °C, and programmable in 30 different steps for time and temperature.

Shimadzu UVmini-1240 spectrophotometer device in the Metallurgical and Materials Engineering laboratories of Fırat University was used in the analyses. In the spectrophotometer with a single measuring cell, absorbance correction was made with distilled water (solvent) before the analyses. Thus, the absorbance of the solvent was subtracted during the analysis and the absorbance value of the sample was recorded directly.

Scanning electron microscope (SEM) analysis was carried out with Zeiss - EVO MA10 device in Fırat University Central Laboratory.

BET analyses were carried out using Micromeritics 3Flex device in Atatürk University DAYTAM laboratory and surface area and pore size analyser were determined. Adsorbed nitrogen gas with 99.999% purity was used in the measurements.

### 2.3. Method

In the literature, many studies have indicated that by increasing the surface area through grinding, higher efficiencies can be achieved in both activation and carbonization processes within shorter time periods. Additionally, grinding is necessary due to the small capacity of the HTC device's chamber [20-22].

In addition, in a study by Şentorun-Shalaby et al. (2006) investigating the production of activated carbon from apricot pits of similar sizes, it was reported that smaller particles were more easily activated to produce activated carbons with relatively higher surface area [23].

In a study conducted by Yener et al. (2008), the use of commercially purchased granular and powdered activated carbons for the removal of methylene blue was investigated. This study found that the absorption capacity and rate were significantly higher in powdered activated carbons [24]. For these reasons, the raw material (PPPW) was ground before use.

PPPW samples were ground in a ball mill for 15 minutes, sieved through a 150 µm sieve and dried in an oven at 80 °C for 1440 minutes. Dried PPPW was placed in the teflon chamber of the hydrothermal device at the ratio of PPPW/Water = 1/10. It was processed in a hydrothermal device (HTC) at 160 °C for 240 min, 480 min and 720 min. During the operations carried out in the HTC chamber, the mixture was continuously stirred by a magnetic fish. During the process, it was observed that the pressure in the chamber varied between 6 and 7.2 bars. After the mixture taken out from the HTC chamber was filtered on filter paper, the solid material remaining on the upper part of the filter paper was called hydrochar. After the hydrochar was dried in the oven at 80 °C for 1440 minutes, mixtures were prepared for the activation process, with hydrochar/KOH=1/1 and hydrochar/KOH=1/0.5.

These mixtures were placed in a muffle furnace in steel crucibles with lids and the activation process of hydrochar was carried out by keeping them at temperatures of 600 °C, 700 °C, 800 °C and for 30 minutes, 60 minutes and 120 minutes for each temperature. The temperature of the muffle furnace was programmed to rise at 10 °C per minute. The product taken from the oven was placed in a beaker with a ratio of Carbonized Product / HCl solution = 1/10, and this beaker was swashed in a vortex device at the lowest speed (100 rpm) for 60 minutes. After the vortex process, the mixtures were filtered, and the sample remaining on the filter paper was washed repeatedly with pure water until pH = 6.5-7. The washed samples were dried in an oven at 80 °C for 1440 minutes and stored in zip lock bags for analysis.

The adsorption capacities of activated carbon samples produced from PPPW were determined using methylene blue (MB). For this purpose, 1000 mg/L MB stock solution was prepared. The stock MB solution was diluted to a concentration of 350 mg/L using 0.03 M acetic acid - 0.07 M sodium acetate solution (pH = 4.85). 50 ml of MB solutions together with 0.05 g adsorbent (activated carbon) were transferred to 250 ml conical flasks, and shaken at 150 rpm for 24 hours. Sodium acetate-acetic acid buffer solution, containing the same amount of adsorbent but without MB, was used as a blank solution. At the end of 24 hours, the samples taken from the shaker were filtered on blue banded filter paper, and the MB concentrations remaining in the filtered solution were determined by analysing them with a UV spectrophotometer at a wavelength of 664 nm after diluting with sodium acetate-acetic acid buffer solution at the appropriate ratio. To determine the amount of MB in absorbance values, the calibration curve created from the absorbance values of standard MB solutions at a concentration between 2-10 mg/L was used. The amount of MB adsorbed per unit amount of adsorbent at equilibrium ( $q_e$ , mg/g) was calculated using equation



(2.1.) based on the MB concentration values of the solutions before ( $c_0$ , mg/L) and after ( $c_e$ ) adsorption [25].

$$q_e = \frac{(C_0 - C_e)V}{M_S} \quad (2.1.)$$

Here,

V: MB solution volume (L),

$M_S$ : indicates the amount of adsorbent (g) used in adsorption.

Then, according to the Langmuir adsorption equation (2.2.) given below for each concentration, the calculated  $c_e/q_e$  values against the equilibrium concentration values ( $c_e$ ) were plotted and Langmuir adsorption capacities ( $q_m$ , mg/g) were calculated from the slope of the obtained line. Thus, the MB adsorption capacities of each carbonized product were determined.

$$\frac{C_e}{q_e} = \frac{C_e}{q_m} + \frac{1}{bq_m} \quad (2.2.)$$

Here,

b is the constant related to the adsorption energy.

After the process in HTC, the experimental conditions and sample codes of activated carbon production carried out with an activator in the furnace are given in Table 1.

**Table 1.** Experimental conditions of carbonization processes

Hydrochar/KOH= 1/1 (N Series)				
		HTC Time (160 °C)		
Muffle Furnace		240 min	480 min	720 min
600 °C	30 min.	N1	N2	N3
	60 min.	N4	N5	N6
	120 min.	N7	N8	N9
700 °C	30 min.	N10	N11	N12
	60 min.	N13	N14	N15
	120 min.	N16	N17	N18
800 °C	30 min.	N19	N20	N21
	60 min.	N22	N23	N24
	120 min.	N25	N26	N27
Hydrochar/KOH= 1/0.5 (A Series)				
		HTC Time (160 °C)		
Muffle Furnace		240 min	480 min	720 min
600 °C	30 min.	A1	A2	A3
	60 min.	A4	A5	A6
	120 min.	A7	A8	A9
700 °C	30 min.	A10	A11	A12
	60 min.	A13	A14	A15
	120 min.	A16	A17	A18
800 °C	30 min.	A19	A20	A21
	60 min.	A22	A23	A24
	120 min.	A25	A26	A27

### 3. Results and Discussion

The samples, which were processed for 240, 480 and 720 minutes in the HTC device, were then activated for different periods of time in the muffle furnace at 600 °C and the MB removal efficiencies were examined (Figure 3 (a) and (b)).

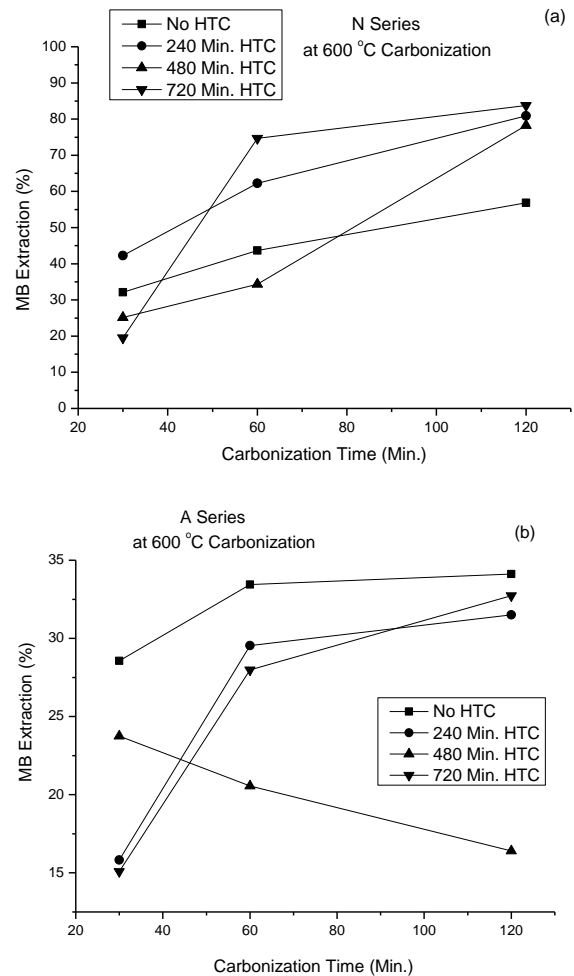


**Figure 3.** Methylene blue adsorption capacities of samples activated for 30, 60 and 120 min at 600 °C, (a) N Series: Hydrochar/KOH=1/1 (b) A Series: Hydrochar/KOH=1/0.5

While the MB extraction yield of the activated carbon obtained from the sample carbonized for 120 minutes at 600 °C with Hydrochar/KOH=1/1 (N Series) without treatment in the HTC device was 56.83%, after being processed in the HTC for 720 minutes, the sample which was activated at the same conditions of carbonization, the extraction yield of the was calculated as 83.75%.

As a result of examining the graphs, it was observed that the best performance was obtained with the sample coded N20, which was subjected to the process in the HTC device for 480 minutes, then prepared with a Hydrochar/KOH ratio of 1/1, and subsequently

activated in a muffle furnace at 800 °C for 30 minutes. The MB removal yield of this sample was calculated as 99.85%.

Figure 4 (a) shows the image of the solution containing 350 mg/L methylene blue, and Figure 4 (b) shows the image of this solution after being treated with the N20 coded sample for 24 hours.

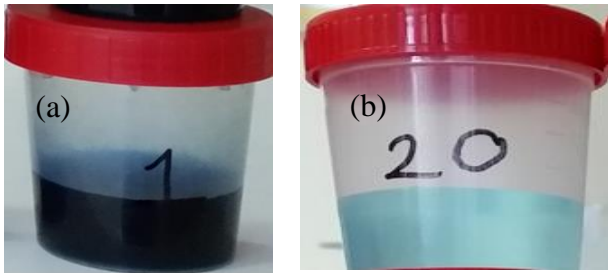


**Figure 4.** a) 350 mg/L MB solution b) the solution in which was removed MB with the sample of N20

The time for adsorption to reach equilibrium is known as the contact time. If the contact between the adsorbent and the adsorbed is achieved by shaking or mixing, the adsorption rate also increases due to the increase in the number of intermolecular collisions. With the mixing and shaking processes, the number of collisions of the molecules increased, and the MB removal yield in the solution reached up to 99.85%.

The SEM image of the sample coded N20 is given in Figure 5. When Figure 5 is examined, the honeycomb structure, which is the distinctive feature of activated carbon, is clearly seen in this sample.

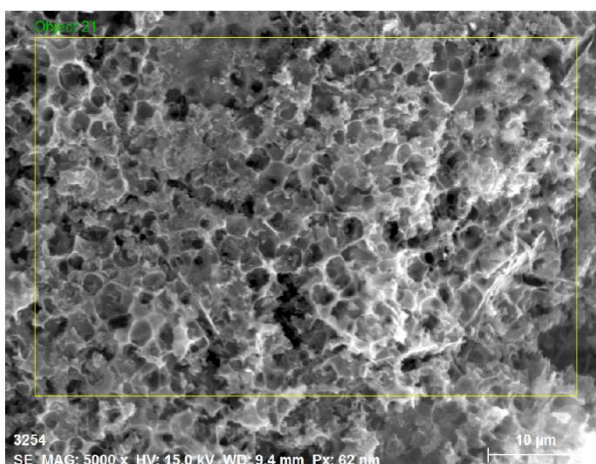


**Figure 5.** SEM image (5000X) of the N20 coded sample

According to SEM images, it can be said that the activation method applied with KOH is effective in pore formation. First, dehydration reactions took place within the PPPW, which was taken from the hydrothermal

device and mixed with potassium hydroxide and placed in the oven. Potassium hydroxide acted as a catalyst and accelerated the degradation of lignin and hemicellulose molecules that form the cell wall. Cellulose molecules, which consist of carbon, hydrogen and oxygen, which are resistant to chemical degradation, have undergone thermal degradation during the carbonization stage.

Surface area measurements of carbonized products obtained by hydrothermal carbonization were carried out with the Surface Area Measurement Device (BET). Accordingly, the highest BET surface area was determined as 1,094.34 m<sup>2</sup>/g in sample A27, while the surface area of sample number N20, which had the highest methylene blue extraction efficiency, was determined as 1,035.74 m<sup>2</sup>/g.

In the literature, it is stated that the impregnation ratio strongly influences the properties of activated carbon, and selecting the appropriate impregnation ratio is crucial for producing activated carbons with the highest surface area and pore volume. It has been noted that the composition of lignocellulosic materials affects the structure of activated carbons in terms of porosity, and if they contain a relatively high amount of lignin, the BET surface area of the activated carbons will increase [13].

In commercial products, the BET surface area values are stated to be ≥800 m<sup>2</sup>/g for Merck [26], <1000 m<sup>2</sup>/g for APC Pure [27], and between 500-1000 m<sup>2</sup>/g for Sigma Aldrich [28]. In the literature, the BET surface area values for activated carbon samples produced from various organic sources are reported as ranging from 1368.5 to 792.2 m<sup>2</sup>/g for sugar beet molasses [10], 1684 m<sup>2</sup>/g for maize stalks [12], 726 m<sup>2</sup>/g for peanut shells [14], 1000 m<sup>2</sup>/g for Tunçbilek lignite coal [17], and 1387.30 m<sup>2</sup>/g for apricot stones [18].

#### 4. Conclusion

In this study, activated carbon was produced by hydrothermal method using pistachio processing plant waste (PPPW), which are grown abundantly in our country, especially in the eastern and South Eastern Anatolia regions, and which cause environmental pollution after harvesting. For activated carbon production, carbonized products were processed in a hydrothermal device (HTC) in the presence of an activator for various periods of time. In the processes carried out at constant temperature, high pressure values were reached, enabling activated carbon to reach a high

adsorption capacity. As a result of the studies, it was determined that the sample held in the HTC at 160 °C for 480 minutes, then impregnated with KOH at a 1:1 ratio, and subsequently activated in a muffle furnace at 800 °C for 30 minutes, was able to remove MB from a solution with a concentration of 350 ppm with a 99.85% extraction efficiency.

### Acknowledgement

This study was supported by Firat University Scientific Research Projects Coordination Unit (FÜBAP) under the Rectorate of Firat University within the scope of the project titled “Activated carbon production by hydrothermal method from pistachio roasting plant wastes” with the code number MF.19.02.

### Author’s Contributions

**Mustafa BOYRAZLI:** Supervised manuscript writing, performed the result analysis.

**Elif ARANCI ÖZTÜRK:** Drafted and wrote the manuscript, assisted in analytical analysis on the structure.

**Emrah ÇELİK:** Supervised the experiment’s progress, helped in manuscript preparation.

**Mehmet Ali YASLI:** The experimenter is a graduate student.

### Ethics

There are no ethical issues after the publication of this manuscript.

### References

- [1]. Ntuli, V., Hapazari, I., 2013, Sustainable waste management by production of activated carbon from agroforestry residues. *South African Journal of Science*. 2013;109(1/2), Art. #1077, 6 pages. <http://dx.doi.org/10.1590/sajs.2013/1077>
- [2]. Açikyıldız, M., Gürses, A., Karaca, S., 2014, Preparation and characterization of activated carbon from plant wastes with chemical activation, *Microporous and Mesoporous Materials*, 198 (2014) 45–49
- [3]. Hossain, M.Z., Wu, W., Xu, W.Z., Chowdhury, M.B.I., Jhavar, A.K., Machin, D., Charpentier, P.A., 2018, High Surface Area Mesoporous Activated Carbon from Hemp Bast Fibre Using Hydrothermal Processing, *Journal of Carbon Research*. doi:10.20944/preprints201804.0372.v1
- [4]. Jain, A., Balasubramanian, R., Srinivasan, M.P., 2015, Hydrothermal conversion of biomass waste to activated carbon with

high porosity: A review, *Chemical Engineering Journal* 283 (2016) 789–805

[5]. Hayashi, J., Kazehaya, A., Muroyama, K., Watkinson, A. P., 2000. Preparation of Activated Carbon From Lignin By Chemical Activation, *Carbon*, 38, 1873-1878.

[6]. Hendawy, A.N., 2003. Influence of HNO<sub>3</sub> Oxidation on the Structure and Adsorptive Properties of Corn-cob-Based Activated Carbon, *Carbon*, 41, 713-722

[7]. Pradhan, B.K., Sandle, N.K., 1999. Effect Of Different Oxidizing Agent Treatments On The Surface Properties Of Activated Carbons, *Carbon*, 37, 1323-1332

[8]. Hameed, B.H., Ahmad, A.L., Latiff, K.N.A., 2007. Adsorption of basic dye (methylene blue) onto activated carbon prepared from rattan sawdust, *Dyes and Pigments*, 75, 143-149

[9]. Duman, G., Onal, Y., Okutucu, C., Onenc, S., Yanik, J., 2009. Production of Activated Carbon from Pine Cone and Evaluation of Its Physical, Chemical, and Adsorption Properties, *Energy & Fuels*, 23, 2197-2204.

[10]. Aci, F., Nebioglu, M., Arslan, M., Imamoglu, M., Zengin, M., Küçükislamoglu, M., 2008. Preparation of Activated Carbon from Sugar Beet Molasses and Adsorption of Methylene Blue, *Fresenius Environmental Bulletin*, 17, 997-1001. ([https://www.prt-parlar.de/download\\_list/?c=FEB\\_2008\\_FEB\\_08a\\_2008](https://www.prt-parlar.de/download_list/?c=FEB_2008_FEB_08a_2008))

[11]. Teker, M., Imamoglu, M., Bocek, N., 2009. Adsorption of Some Textile Dyes on Activated Carbon Prepared from Rice Hulls, *Fresenius Environmental Bulletin*, 18, 709-714. ([https://www.prt-parlar.de/download\\_list/?c=FEB\\_2009\\_FEB\\_05a\\_2009](https://www.prt-parlar.de/download_list/?c=FEB_2009_FEB_05a_2009))

[12]. El-Hendawy, A.-N.A., 2009. An Insight into the KOH Activation Mechanism Through the Production of Microporous Activated Carbon for the Removal of Pb<sup>2+</sup> Cations, *Applied Surface Science*, 255, 3723-3730.

[13]. Karagöz, S., Tay, T., Ucar, S., Erdem, M., 2008. Activated Carbons from Waste Biomass by Sulfuric Acid Activation and Their Use on Methylene Blue Adsorption, *Bioresource Technology*, 99, 6214-6222.

[14]. Wilson, K., Yang, H., Seo, C.W., Marshall, W.E., 2006. Select Metal Adsorption by Activated Carbon Made from Peanut Shells, *Bioresource Technology*, 97, 2266–2270.

[15]. El-Sikaily, A., El Nemr, A., Khaled, A., Abdelwehab, O., 2007. Removal of Toxic Chromium from Wastewater Using Green Alga *Ulva lactuca* and Its Activated Carbon, *Journal of Hazardous Materials*, 148, 216-228.

[16]. Banat, F., Al-Asheh, S., Al-Makhadmeh, L., 2004. Utilization of Raw and Activated Date Pits for the Removal of Phenol from Aqueous Solutions, *Chemical Engineering and Technology*, 24, 80-86.


[17]. Önal, Y., Akmil-Başar, C., Eren, D., Sarıcı-Özdemir, Ç., Depci, T., 2006. Adsorption Kinetics of Malachite Green onto Activated Carbon Prepared from Tunçbilek Lignite, *Journal of Hazardous Materials*, 128, 150-157.

[18]. Soleimani, M., Kaghazchi, T., 2007, Agricultural Waste Conversion to Activated Carbon by Chemical Activation with Phosphoric Acid, *Chemical Engineering & Technology*, Volume 30, Issue5, May, 2007, Pages 649-654.

[19]. Pistachio production amounts of countries. <https://atlasbig.com.tr/ulkelerin-antepfistigi-uretimi>. (accessed at 20.04.2024)

- [20]. Apaydın, A., Altuntaş, E., Şamil, A. 2023. Hidrotermal Ön İşlemlili Okaliptüs Kök Odunlarından Piroliz Yöntemiyle Aktif Karbon Üretimi. *Kahramanmaraş Sütçü İmam Üniversitesi Mühendislik Bilimleri Dergisi*, 26(3), 653-662.
- [21]. Guo, Q., Qiao, S., Zhang, D., Zhang, Z., Yu, F., Ma, Z., Hu, Y. 2023. A comparison of hydrothermal carbonization versus pyrolysis-activation for sludge-derived carbon materials on physiochemical properties and electrochemical performance. *Biomass and Bioenergy* 182 (2024) 107079.
- [22]. Boyrazlı, M., Süner, M., Çelik, E. Dere, A., Canbay, C.A., Karip, E. 2023. Çay Tesisi Atıklarından Hidrotermal Yöntemle Aktif Karbon Üretimi. *Fırat Üniv. Fen. Bil. Dergisi* 35(2), 119-129, 2023
- [23]. Şentorun-Shalaby, Ç., Uçak-Astarlıoğlu, M. G., Artok, L., & Sarıcı, Ç. 2006. Preparation and characterization of activated carbons by one-step steam pyrolysis/activation from apricot stones. *Microporous and mesoporous materials*, 88(1-3), 126-134.
- [24]. Yener, J., Kopac, T., Dogu, G., Doğu, T. 2008. Dynamic analysis of sorption of Methylene Blue dye on granular and powdered activated carbon. *Chemical Engineering Journal* 144 (2008) 400-406
- [25]. Çakmak, L., 2019. Şeker Pancarı Melası ve Küspesinden Hidrotermal Yöntemle Manyetik Nanopartikül Destekli Karbon (MNPDK) Üretimi, Fırat Üniversitesi, Biyomühendislik Anabilim Dalı, Yüksek Lisans Tezi.
- [26]. [https://www.merckmillipore.com/TR/tr/product/Charcoal-activated.MDA\\_CHEM-102216?ReferrerURL=https%3A%2F%2Fwww.google.com.tr%2F](https://www.merckmillipore.com/TR/tr/product/Charcoal-activated.MDA_CHEM-102216?ReferrerURL=https%3A%2F%2Fwww.google.com.tr%2F) (accessed at 28.08.2024)
- [27]. <https://apcpure.com/product/charcoal-activated-powder-dc1320/> (accessed at 28.08.2024)
- [28]. <https://www.sigmaaldrich.com/TR/en/product/sigald/242276> (accessed at 28.08.2024)

# The Concept of Parafree Zinbiel Algebras

Zekiye Çiloğlu Şahin<sup>1\*</sup> 

<sup>1</sup> Department of Mathematics, Süleyman Demirel University Doğu Yerleşkesi, 32100-Çünür, Isparta, Türkiye

\* [zekiyeciloglu@sdu.edu.tr](mailto:zekiyeciloglu@sdu.edu.tr)

\* Orcid No: 0000-0002-3711-4621

Received: 19 March 2024

Accepted: 18 October 2024

DOI: 10.18466/cbayarfbe.1455387

## Abstract

Pf (parafree) Zinbiel (PfZin) algebras, a generalization of Leibniz algebras, share various traits with free Zinbiel algebras. This article delves into the intricacies of PfZin algebras, presenting their structure and exploring significant findings analogous to those in parafree Leibniz algebras. The focus extends to properties of subalgebras and quotient algebras within the realm of PfZin algebras. Additionally, the direct sum of these algebras is examined, demonstrating that the amalgamation of two PfZin algebras yields a Zinbiel algebra. A new connection between weak Hopf algebras and PfZin algebras is constructed. Moreover, from the direct sum of PfZin algebras weak Hopf algebra is handled and construction of weak Hopf algebra using PfZin algebra is showed.

**Keywords:** Zinbiel algebra, Subalgebras, Division algebras, Direct sum, Weak Hopf algebra

## 1. Introduction

Zinbiel algebras, the Koszul dual of Leibniz algebras, were first presented by Loday in [13]. The term "Zinbiel" was coined by Lemaire [14], by reversing the word "Leibniz". In [15] Loday defined Leibniz algebras as a non-associative extensions of Lie algebras with the property that the right-multiplication operator is a derivation. Key results from Leibniz algebras also hold for Zinbiel algebras in [1,6,8,16,18,19]. Some papers [2,4,5,13] delve into the cohomological and structural aspects of Leibniz algebras. Ginzburg and Kapranov [12] introduced Koszul dual operads, and it was shown that the dual of the Leibniz algebra category is determined by the Zinbiel identity. Our motivation in this article is to see how the parafree algebras considered in Lie algebras and Leibniz algebras work in Zinbiel algebras. In [3,9,10,17,20] parafree Lie and Leibniz algebras were discussed and the studies were expanded and advanced. In addition, it is discussed in the article [11] that this type of algebra is Hopfian. In this paper, in the light of the above mentioned studies we construct parafree Zinbiel algebras. Which we will briefly denote as PfZin (Parafree Zinbiel). We concentrate on PfZin algebras and review key findings in this field derived from prior studies. Next, we will focus on examining the subalgebra structure in PfZin algebras. Our objective is to explore intrinsic characteristics of subalgebras and division algebras in the

context of PfZin algebras. Additionally, we demonstrate a key result that shows how combining two PfZin algebras creates a new Zinbiel algebra while preserving the Pf property. The connection between PfZin algebras and weak Hopf algebras is investigated. The connection lies in their construction and properties, such as for a given PfZin algebra  $P$ , we can construct a weak Hopf algebra  $H(P)$  using the direct sum of the algebra structures on  $P$  and its dual  $P^*$ . The antipode on  $H(P)$  is defined as the linear map that satisfies the required conditions.

The construction of a weak Hopf algebra using a PfZin algebra demonstrates the connection between these two concepts. The weak Hopf algebra  $H(P)$  inherits properties from the PfZin algebra  $P$ , such as the self-dual property. This relationship highlights the importance of considering weaker axioms in certain situations, as seen in the context of weak Hopf algebras in [7].

## 2. Notations and Definitions

In this part, we review important founding crucial for ours objectives as mentioned in references [10,11,12,15], using standart inscription. During this discussion,  $F$  demonstrates a characteristic zero field. A Zinbiel algebra  $Z$  is defined as an algebra that satisfies the identity:



$$[x, y, z] = [x, [y, z]] + [x, [z, y]] \quad (2.1)$$

for all  $x, y, z \in Z$ . We introduce a series of ideals

$$Z^1 \supseteq Z^2 \supseteq \dots \supseteq Z^k \supseteq \dots$$

where  $Z^1 = Z$ ,  $Z^2 = [Z, Z]$ , ...,  $Z^{k+1} = [Z^k, Z]$  for  $k \geq 1$ , termed the lower central series of  $Z$ .

A Zinbiel algebra  $Z$  is classified as nilpotent if there exists an integer  $k \geq 1$  such that  $Z^k = \{0\}$ . If  $Z_1/Z_1^n \cong Z_2/Z_2^n$ . Then we propose that,  $Z_1$  and  $Z_2$  have an identical lower central series. Let  $X$  be a set and  $A(X)$  be the free non-associative algebra over  $F$  generated by  $X$ . We define  $I$  as the two-sided ideal in  $A(X)$  generated by elements of the form

$$[[x, y], z] - [x, [y, z]] - [x, [z, y]] \quad (2.2)$$

for all  $x, y, z \in A(X)$ . As a result, the algebra

$Z(X) = A(X)/I$  is established as a free Zinbiel algebra. In addition, we provide definitions for Zinbiel algebras that resemble those commonly associated with Lie and Leibniz algebras.

**Definition 2.1.** A Zinbiel algebra is deemed "Hopfian" if it satisfies the following equivalent conditions:

- (i) It is isomorphic to any of its proper quotients.
- (ii) Each endomorphism that maps onto it is an automorphism.

**Definition 2.2.** If  $Z$  is a Zinbiel algebra, it is considered residually nilpotent (has residual nilpotency) if the intersection of its ascending powers from  $n$  equals 1 to infinity, represented as  $\bigcap_{n=1}^{\infty} Z^n$  is equal to  $\{0\}$ .

**Definition 2.3.** The free Zinbiel algebra generated by  $X$  is denoted as  $Z(X)$ . A Zinbiel algebra  $P$  is considered Pf over  $X$  if it satisfies the following conditions:

- (i)  $P$  has a residual nilpotency,
- (ii)  $Z(X)/Z(X)^n = P/P^n$ , for all  $n \geq 1$  indicating that  $P$  and  $X$  have the same lower central series.

The number of elements in  $X$  is referred to as the rank of  $P$ .

**Example 2.4.** Now, let's construct a Zinbiel algebra example that satisfies the definitions. Consider the Zinbiel algebra  $Z = \langle x, y \rangle$  where  $x$  and  $y$  are generators, and the bilinear product is defined as:

$$[x, x] = x, [x, y] = y, [y, x] = 0, [y, y] = 0$$

This is a Zinbiel algebra satisfies the following properties:

Hopfian:

Proving the First Condition:

To prove that  $Z$  is isomorphic to any of its proper quotients, we need to show that for any proper quotient  $Z/I$ , there exists an isomorphism  $\varphi: Z \rightarrow Z/I$ .

Let  $I$  be a proper ideal of  $Z$ . Then,  $I$  is a subspace of  $Z$  that is closed under the bilinear product. Since  $Z$  is generated by  $x$  and  $y$ ,  $I$  must be generated by some subset of  $\{x, y\}$ .

Case 1:  $I = \langle 0 \rangle$ . In case 1,  $Z/I = Z$  and the identity map is an isomorphism.

Case 2:  $I = \langle x \rangle$ . In case 2,  $Z/I = \langle y \rangle$ , and the map  $\varphi: Z \rightarrow Z/I$  defined by  $\varphi(x) = 0$  and  $\varphi(y) = y$  is an isomorphism.

Case 3:  $I = \langle y \rangle$ . In case 3,  $Z/I = \langle x \rangle$  and the map  $\varphi: Z \rightarrow Z/I$  defined by  $\varphi(x) = x$  and  $\varphi(y) = 0$  is an isomorphism.

Case 4:  $I = \langle x, y \rangle$ . In this case,  $Z/I = \{0\}$ , and the zero map is an isomorphism.

In all cases, we have shown that  $Z$  is isomorphic to any of its proper quotients.

Proving the Second Condition:

To prove that each endomorphism that maps onto  $Z$  is an automorphism, we need to show that for any endomorphism  $f: Z \rightarrow Z$ , if  $f$  is surjective, then  $f$  is injective.

Let  $f: Z \rightarrow Z$  be a surjective endomorphism. Then,  $f(x)$  and  $f(y)$  generate  $Z$ . Since  $Z$  is generated by  $x$  and  $y$ , we can write:

$$f(x) = ax + by, f(y) = cx + dy$$

for some  $a, b, c, d \in F$ , where  $F$  is the underlying field of characteristic zero. Since  $f$  is surjective, we know that  $f(x)$  and  $f(y)$  are linearly independent. This implies that the matrix:

$$\begin{bmatrix} a & b \\ c & d \end{bmatrix}$$

Has non-zero determinant. Therefore, the matrix is invertible, and we can write:

$$x = a'f(x) + b'f(y) \quad y = c'f(x) + d'f(y)$$

for some  $a', b', c', d' \in F$ .

Now, define  $g: Z \rightarrow Z$  by  $g(f(x)) = x$  and  $g(f(y)) = y$ :

Then,  $g$  is an endomorphism of  $Z$ , and we have

$$g \circ f = id(Z).$$

This implies that  $f$  is injective, and therefore,  $f$  is an automorphism. We have proven that our example  $Z = \langle x, y \rangle$  satisfies Hopfian conditions. Specifically, we have shown that  $Z$  is isomorphic to any of its proper quotients and that each endomorphism that maps onto  $Z$  is an automorphism.

Residually Nilpotent: The ascending powers of  $Z$  are:

$$Z^1 = \langle x, y \rangle, Z^2 = \langle x \rangle, Z^3 = \langle 0 \rangle, \dots$$

The intersection of these ascending powers is  $\bigcap_{n=1}^{\infty} Z^n$  is equal to  $\{0\}$ , making  $Z$  residually nilpotent.

**Free Zinbiel Algebra and Pf:** Let  $X = \{x, y\}$  and consider the free Zinbiel algebra  $Z(X)$  generated by  $X$ . The Zinbiel algebra  $Z(X)$  is the vector space spanned by all possible words in  $X$ , with the bilinear bracket product. We can construct a Zinbiel algebra  $P = \langle x, y \rangle$ , which is Pf over  $X$ , it is freely generated by  $X$  i.e., it has a residual nilpotency, meaning that the intersection of its ascending powers is  $\{0\}$  and it has a lower central series, which is a sequence of ideals that satisfy certain properties.

Summary, we've successfully constructed a PfZin algebra example that satisfies the given definitions.

### 3. Sub and Division algebras of PfZin Algebras

The proofs of our key results on division algebras and subalgebras in the space of PfZin algebras are presented here. Contrary to the analogous case in parafree Lie algebras, as stated in [3], where a subalgebra remains parafree, this assertion doesn't hold for PfZin algebras. Notably, due to the non-freeness of every subalgebra of a free Zinbiel algebra, a subalgebra of a PfZin algebra may not retain the Pf property. However, our theorem demonstrates that any free subalgebra within a PfZin algebra indeed remains Pf.

**Theorem 3.1** A free subalgebra of PfZin algebra is Pf.

*Proof.* Suppose with the same lower central series as the free Zinbiel algebra  $Z(X)$ , let  $S$  be the PfZin algebra. We can establish isomorphisms

$$\varphi_n: S / S^n \rightarrow Z(X) / Z(X)^n,$$

by using the canonical mapping  $\varphi: S \rightarrow Z(X)$ , where  $n \geq 2$ . Next, let  $H$  be a free subalgebra of  $P$  such that  $H \cap S^n = H^n$ . Therefore, we have  $\bigcap_{i=1}^{\infty} H^i \subset \bigcap_{i=1}^{\infty} S^i$ . Since  $S$  is Pf, we know that  $\bigcap_{i=1}^{\infty} S^i = \{0\}$ . From this, it follows that  $\bigcap_{i=1}^{\infty} H^i = \{0\}$ , which establishes the residual nilpotency of  $H$ . Therefore  $H$  is a free Zinbiel subalgebra and shares the identical lower central series as a free Zinbiel algebra, we conclude that  $H$  is also Pf. Furthermore, we can utilize a theorem that applies to PfZin algebras. This theorem has a straightforward proof and leverages the analogous result established for parafree Leibniz algebras as detailed in [17].

**Example 3.2.** In example 2.4 we have shown that  $P = \langle x, y \rangle$ , which is Pf. Now, let's construct a free subalgebra  $Q$  of  $P$  generated by a single element  $x$ . We define the bilinear product on  $Q$  as:  $[x, x] = x$ . This free subalgebra  $Q$  is a PfZin algebra in its own right satisfying the conditions:

$Q$  has a residual nilpotency, as it is a subalgebra of  $P$ .  $Z(X) / Z(X)^n = Q / Q^n$ , for all  $n \geq 1$ , which can be verified

by directly. In conclusion, a free subalgebra of PfZin algebra is Pf.

**Theorem 3.3.** A PfZin algebra's quotient algebra is Pf.

*Proof.* Consider  $P$  as a PfZin algebra with  $I$  as its ideal. Finding the residual nilpotency of the quotient algebra  $S/I$  is our first objective.

Assume  $x \in \bigcap_{n=1}^{\infty} (S/I)^n$ . Thus, for all  $n$ ,

$x \in (S/I)^n = (S^n + I)/I$  implying  $x = y + I$  where  $y \in S^n + I$ . Leveraging the residual nilpotency of  $S$ , we conclude that  $S/I$  is residually nilpotent. Now let's demonstrate that  $S/I$  shares the identical lower central series as a free Zinbiel algebra. Take into account  $(S/I) / (S/I)^n$ .

Since  $(S^n + I)/I$  isomorphic to  $S^n/I$ , we have

$$\begin{aligned} (S/I) / (S/I)^n &\cong (S/I) / ((S^n + I)/I) \\ &\cong (S/I) / (S^n/I) \cong S/S^n. \end{aligned}$$

This demonstrates that  $(S/I) / (S/I)^n$  has the identical lower central series as a free Zinbiel algebra. Whence,

$$(S/I) / (S/I)^n \cong Z(X) / Z(X)^n.$$

Consequently,  $S/I$  is Pf.

**Example 3.4.** Consider the PfZin algebra  $P = \langle x, y \rangle$  which is explained in example 2.4. We want to construct an ideal  $I$  of  $P$  generated by the element  $y$ . Of course  $I$  contains all possible products of  $y$  with elements of  $P$ . The ideal  $I$  is generated by taking the span of these elements. We define the quotient algebra  $P/I$  as the set of equivalence classes of elements of  $P$ , where two elements are considered equivalent if their difference lies in  $I$ . Then the quotient algebra  $P/I$  is a PfZin algebra in its own right, satisfying the aforementioned conditions.

**Lemma 3.5.** Consider  $S$ , PfZin algebra with finite rank and  $I$  be an ideal of  $S$ . If  $S$  and  $S/I$  have the identical rank, then it follows that  $I = \{0\}$ .

*Proof.* Presumably, the ranks of  $S$  and  $S/I$  are equal. For any positive number  $n$ ,

$$S/I \cong (S/I) / (S/I)^n \cong (S/I) / I \cong S / (S^n + I).$$

According to the Theorem 3.3,  $S/I$  has residual nilpotency. Subsequently by [10],  $S/I$  remains Hopfian. Moreover,

$$S / (S^n + I) \subseteq S / S^n$$

and

$$S / S^n \cong S / (S^n + I).$$

Given that  $S/I$  is Hopfian, a contradiction. Therefore for each  $n$ ,  $I \subseteq S^n$ , then  $I = \{0\}$ .

### 4. PfZin algebra Direct Sum

Presume  $Z_1, Z_2, \dots, Z_n$  be Zinbiel algebras. We define the direct sum  $Z = Z_1 \oplus Z_2 \oplus \dots \oplus Z_n$  as the vector space

direct sum of the  $Z_i$  with the Zinbiel product  $[\sum_{i=1}^n x_i, \sum_{i=1}^n y_i] = \sum_{i=1}^n [x_i, y_i]$ , where  $[x_i, y_i] \in Z_i \cap Z_j = \{0\}$  for  $i \neq j, x_i \in Z_i, y_j \in Z_j$ . The following theorems can be viewed as obvious consequences of direct sums:

**Lemma 4.1.** Let  $Z_1, Z_2$  be Zinbiel algebras. The direct sum  $Z = Z_1 \oplus Z_2$  is a Zinbiel algebra with the product  $[x_1 + x_2, y_1 + y_2] = [x_1, y_1] + [x_2, y_2]$  for  $x_1, y_1 \in Z_1, x_2, y_2 \in Z_2$ .

**Theorem 4.2.** Let  $F_1$  and  $F_2$  be free Zinbiel algebras. Then  $F_1 \oplus F_2$  is again free.

**Theorem 4.3.** Let  $S_1$  and  $S_2$  be PfZin algebras and  $S = S_1 \oplus S_2$ . Then  $S$  is PfZin algebra.

Now we will present an example showing that the direct sum of two PfZin algebras is also a PfZin algebra, we will take the example we discussed in the article one step further and build an example on direct sum.:

**Example 4.4.** Consider two PfZin algebras  $P = \langle x, y \rangle$ , and  $Q = \langle z, w \rangle$ , where  $x, y$  and  $z, w$  are generators, and the bilinear products are defined as:

$$\begin{aligned} [x, x] &= x, [x, y] = y, [y, x] = 0, [y, y] = 0 \\ [z, z] &= z, [z, w] = w, [w, z] = 0, [w, w] = 0 \end{aligned}$$

The direct sum  $P \oplus Q$  is a PfZin algebra.

**Theorem 4.3.** The direct sum of two parafree Zinbiel algebras is a weak Hopf algebra.

**Proof.** Let  $P$  and  $Q$  are two parafree Zinbiel algebras. We can construct their direct sum  $P \oplus Q$  as a Zinbiel algebra with the bilinear product defined component-wise.

Using the definition of a weak Hopf algebra from [7], we can show that  $P \oplus Q$  satisfies the required axioms.

**Multiplication:** The direct sum  $P \oplus Q$  has well-defined multiplication, as it is a Zinbiel algebra.

**Comultiplication:** The comultiplication on  $P \oplus Q$  can be defined component-wise, using the comultiplications on  $P$  and  $Q$ .

**Counit:** The counit on  $P \oplus Q$  can be defined as the direct sum of the counits on  $P$  and  $Q$ . However, this counit does not satisfy the usual counit axiom. Instead, it satisfies the weaker axiom required for a weak Hopf algebra. Therefore, the direct sum  $P \oplus Q$  is a weak Hopf algebra.

**Corollary 4.4.** The direct sum of two PfZin algebras is not necessarily a Hopf algebra, but it is a weak Hopf algebra.

**Theorem 4.5** Let  $P$  be a parafree Zinbiel algebra. Then, the weak Hopf algebra  $H(P)$  constructed above is a weak Hopf algebra that satisfies the following properties:

(i)  $H(P)$  is a self-dual weak Hopf algebra, meaning that its dual  $H(P)^*$  is also a weak Hopf algebra.

(ii) The regular representation of  $H(P)$  is a left  $H(P)$ -module that satisfies the equation:

$$H(P) \cong \sum_j \text{End}_F(V_j)$$

Where  $V_j$ 's are the irreducible representations of  $H(P)$  and  $\text{End}_k(V)$  denotes the set of endomorphisms of a vector space  $V$  over a field  $F$ .

**Proof.**

Using the definition of a weak Hopf algebra [7], and the construction of  $H(P)$  above, we can show that  $H(P)$  satisfies the required axioms:

**Multiplication:** The direct sum of the algebra structures on  $P$  and its dual  $P^*$  defines a well-behaved multiplication on  $H(P)$ .

**Comultiplication:** The direct sum of the coalgebra structures on  $P$  and its dual  $P^*$  defines a well-behaved comultiplication on  $H(P)$ .

**Antipode:** The linear map defined above satisfies the required conditions for an antipode.

Using the results from [7], we can show that the regular representation of  $H(P)$  satisfies the equation:

$$H(P) \cong \sum_j \text{End}_F(V_j)$$

In conclusion, we've provided the weak Hopf algebra  $H(P)$  constructed from a parafree Zinbiel algebra  $P$ .

**Corollary 4.6.** Let  $P$  and  $Q$  be two Zinbiel algebras, and  $R$  be a parafree quotient algebra of  $P \oplus Q$  then,  $R$  is a weak Hopf algebra that satisfies the following properties:

(i)  $R$  is a self-dual weak Hopf algebra, meaning that its dual  $R^*$  is also a weak Hopf algebra.

(ii) The regular representation of  $R$  is a left  $R$ -module that satisfies the equation:

$$R \cong \sum_j \text{End}_F(V_j)$$

Where  $V_j$ 's are the irreducible representations of  $R$  and  $\text{End}_F(V)$  denotes the set of endomorphisms of a vector space  $V$  over a field  $F$ .

## 5. Conclusion

The study of PfZin algebras and related concepts offers a rich landscape for future research. Exploring the connections between PfZin algebras and other algebraic structures, such as category theory and homotopy theory, can lead to a deeper understanding of the underlying principles of algebra and its applications.

In conclusion, PfZin algebras are an important area of research that offers a unique perspective on algebraic structures and their properties.



## References

- [1]. Aissaoui, R., Makhlof, A., & Silvestrov, S. (2014). Hom-Lie coalgebras, Hom-Zinbiel algebras and Hom-Hopf algebras. *Frontiers in Mathematics*, 1(1), 89-111.
- [2]. Bahturin, Y. I. 1987. Density relations in Lie algebras, *VNU Science Press, Utrecht*.
- [3]. Baur, H. 1980. A note on parafree Lie algebras, *Commun. in Alg.*; 8(10): 953-960.
- [4]. Baur, H. 1978. Parafreie Lie algebren and homologie, *Diss. Eth Nr.*; 6126: 60 pp.
- [5]. Bloh, A.M. 1965. A generalization of the concept of Lie algebra, *Dokl. Akad. Nauk SSSR*; 165: 471-473.
- [6]. Bloh, A.M. 1971. A certain generalization of the concept of Lie algebra, *Algebra and Number Theory, Moskow. Gos. Ped. Inst. U`cen*; 375: 9-20.
- [7]. Böhm, Gabriella; Nill, Florian; Szlachányi, Kornel (1999). "Weak Hopf algebras. I. Integral theory and C-structure". *Journal of Algebra*. 221 (2): 385–438. doi:10.1006/jabr.1999.7984.
- [8]. Elduque, A., & Makhlof, A. 2020. Super Zinbiel algebras. Symmetry, Integrability and Geometry: *Methods and Applications*, 16, 017.
- [9]. Ekici, N, Velioglu, Z. 2014. Unions of Parafree Lie algebras, *Algebra*; Article ID 385397.
- [10]. Ekici N, Velioglu Z. 2015. Direct Limit of Parafree Lie algebras, *Journal of Lie Theory*; 25(2): 477-484.
- [11]. Evans, T. 1969. Finitely presented loops, lattices, etc. are Hopfian, *J. London Math. Soc.*; 44: 551-552.
- [12]. Gunzburg, V. & Kapranov, M. 1994. Koszul duality for operads, *Duke Math. J.* 76, 203-273.
- [13]. Loday, J. L. 1995. Cup-product for Leibniz cohomology and dual Leibniz algebras, *Math Scand.* 77 (2), 189-196.
- [14]. Loday, J. L. 2001. Dialgebras, In *J.L. Loday, F. Chapoton, A. Frabetti and F. Goichot: Dialgebras and Related Operads. Lecture Notes in Mathematics, Springer, Berlin, Heidelberg vol 1763*.
- [15]. Loday, J. L., Pirashvili, T. 1993. Universal enveloping algebras of Leibniz algebras and (co)homology, *Math. Ann.*; 269(1): 139-158.
- [16]. Makhlof, A., & Goze, M. 2010. Zinbiel algebras and the Wajnryb homomorphism. *Journal of Algebra*, 324(3), 874-890.
- [17]. Mansuroglu, N. 2022. On parafree Leibniz algebras. *Celal Bayar University of Science*, 18,3, 275-278.
- [18]. Poland, A. 2015. Zinbiel Algebras: *From Foundations to Applications*. Springer.
- [19]. Silvestrov, S., & Makhlof, A. 2014. Deformations of Zinbiel algebras and higher homotopy algebras. *Journal of Noncommutative Geometry*, 8(2), 421-47.
- [20]. Velioglu, Z. 2013. Subalgebras and Quotient algebras of Parafree Lie algebras, *I. Journal Pure and Applied Maths.*; 83(3) 507-514.

# Thermal Performance Analysis of a Liquid Cooling Plate for Power Electronics

Mehmet Bahattin AKGÜL<sup>1\*</sup> , Furkan Sinan ERÇEL<sup>2</sup> 

<sup>1</sup> Department of Mechanical Engineering, Manisa Celal Bayar University, 45140 Muradiye, Manisa, Türkiye

<sup>2</sup> R&D Department, Coşkunöz Kalıp Makine, 16000 Nilüfer, Bursa, Türkiye

\* [mbakgul@gmail.com](mailto:mbakgul@gmail.com)

\* Orcid No: 0000-0002-8916-1171

Received: 6 August 2024

Accepted: 16 September 2024

DOI: 10.18466/cbayarfbe.1528939

## Abstract

The need for effective cooling methods has become very critical because of the miniaturization and increasing heat flux density in power electronics equipment. The power electronics systems must have good thermal management engineering for efficiency and safe operation. Due to increasing heat loads, liquid cooling options are more preferred than the air cooling solutions. In this study, thermal performance of a liquid cooling plate is investigated by using computational fluid dynamics (CFD) tools. Different flow path configurations are examined for homogeneous and effective cooling of power electronics equipments with high power density. The pressure losses, surface temperatures and thermal resistances at different coolant flow rates are computed and compared together. Moreover, the influence of the cooling channel height and width on the thermal thermal performance is analyzed.

**Keywords:** Liquid Cooling, Cold Plate, CFD, IGBTs

## 1. Introduction

The insulated-gate bipolar transistors (IGBTs) are widely used as voltage-controlled switching element in power electronic applications. IGBTs can dissipate significant amount of heat during operation despite their small size. The junction temperatures of IGBTs must be kept at certain levels for operating safely at high performance. Taking into consideration the criteria such as size and weight, liquid cooling of IGBTs modules is more preferred than air cooled systems. IGBTs are generally mounted on a cold plate and junction temperatures are kept at the desired values by means of coolant circulation in liquid cooling applications. The cold plate studies which provide homogeneous cooling at low pressure losses have been the subject of many studies in the literature [1-18]. İlikan and Yayli [19] numerically investigated performances of three liquid cold plates with different flow configurations for li-ion battery cells in electric vehicle applications. Hetsroni et al. [20] studied the steady-state heat transfer for different types of microchannels for electronics cooling. They obtained a significant enhancement of heat transfer under the conditions of flow boiling in microchannels. Özbektaş et al. [21] numerically investigated the effect of flow

circulation pattern and velocity on the performance of water-cooled heat sink. They showed that pressure difference, outlet temperature, power consumption, and heat transfer rate to air increased by increasing Reynolds number. Jayarajan and Azimov [22] proposed a novel cold plate design featuring a zig-zag serpentine flow pattern within a rectangular profile channel. Their study found that the increases in mass flow rate reduced the maximum temperature, and improved surface standard temperature and heat transfer rate but increases the pressure drop by nearly 49% Akbarzadeh et al. [23] conducted a new cold plate study for liquid cooling of lithium-ion batteries. They reduced the pump power by 30% and achieved more homogeneous cooling with their newly developed cold plate. Huo et al. [24] designed a mini-channel cold plate for prismatic battery cells. They examined the effects of coolant flow rate, flow direction and ambient temperature in their studies. Jin et al. [25] developed a new cold plate with an oblique fin structure. They indicated that oblique finned cold plates were able to maintain the average temperature of the battery surface below 50 °C for a heat load of 1240 W at a flow rate of less than 0.9 l/min. Jassem and Salem [26] carried out experimental and numerical investigations of a finned cold plate under different conditions. They significantly increased the cold plate performance in their study. Pan



et al. [27] examined the performance of IGBT modules by way of integrating a vapor chamber into the cold plate utilized for cooling. They indicated that the performance of the cold plate integrated with the vapor chamber improved. Reeves et al. [28] examined the cooling performance by adding a novel fin pattern to the cold plate utilized in power electronics applications. They indicated that novel fin structure improved heat transfer without significant pressure loss. Zhang et al. [29] investigated cold plates with linear, S and helix type flow configurations for cooling IGBT modules. They found that the cold plate of S-type with guide plates possess the favorable thermal performance. Zhang et al. [30] carried out CFD investigation of two novel designs of variable cross-section overflow channels of manifold cold plates for lithium-ion batteries. They reported that the average temperature of the cooling plate surface of the novel manifold design decreased by 3.65 K compared to the conventional manifold unit. Chu et al. [31] found that the heat transfer coefficient of hybrid nanofluid drastically enhances compared to distilled water for varying the inlet velocity. Nada et al. [32] reported that the nanofluid provides an enhancement of the heat transfer rate compared to water due to the higher thermal conductivity of the nanoparticles.

In this study, the performance analysis of a cold plate integrated with two IGBT modules used in power electronics applications is carried out for different flow

configurations and coolant flow rates. The cooling performance is investigated for series, parallel and series-parallel flow configurations. The temperature distributions and thermal resistances of the cold plate with pressure losses are determined at different flow rates and presented graphically. The effects of the cooling channel height and width on the thermal performance are examined. The proposed series-parallel flow configuration contributes to the effective cooling of IGBTs modules.

## 2. Methodologies

### 2.1. Physical Model of Cold Plate

Fig.1 (a) shows IGBTs mounted cold plate. The cold plate consists of a main metal block, cover and coolant inlet/outlet adapters as given in Fig.1 (b). Generally, high thermal conductivity metals such as aluminum are used for producing cold plates. In this study, main metal block material is chosen AL 6063 alloy and cover is Al 1050. Two PrimePack3 IGBT modules are mounted on the cold plate. The modules are cooled by coolant which circulates within the machined flow channels inside the main block. A mixture of 50% ethylene glycol in 50% water is used as the coolant. The thermophysical properties of the coolant and solid materials are given in Table 1.

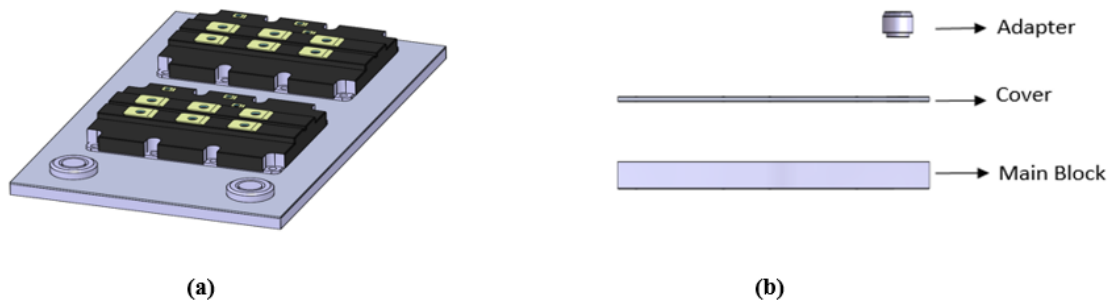


**Figure 1.** (a) IGBT mounted cold plate; (b) Assembly of subcomponents of the cold plate.

**Table 1.** Material Properties

Material	Density ( $\text{kg}\cdot\text{m}^{-3}$ )	Specific Heat ( $\text{J}/(\text{kgK})$ )	Dynamic Viscosity ( $\text{Pa}\cdot\text{s}$ )	Thermal Conductivity ( $\text{W}/\text{mK}$ )
Al 1050	2705	900	-	227
Al 6063	2700	900	-	200
Coolant	1045	3425	0.002	0.41

Three flow configurations are considered in order to examine thermal performance of cold plate. Coolant flow paths such as serial, parallel and serial/parallel are

machined inside the cold plate and shown in Fig.2. Cross-sectional dimensions of the flow channels are the same for all configurations.

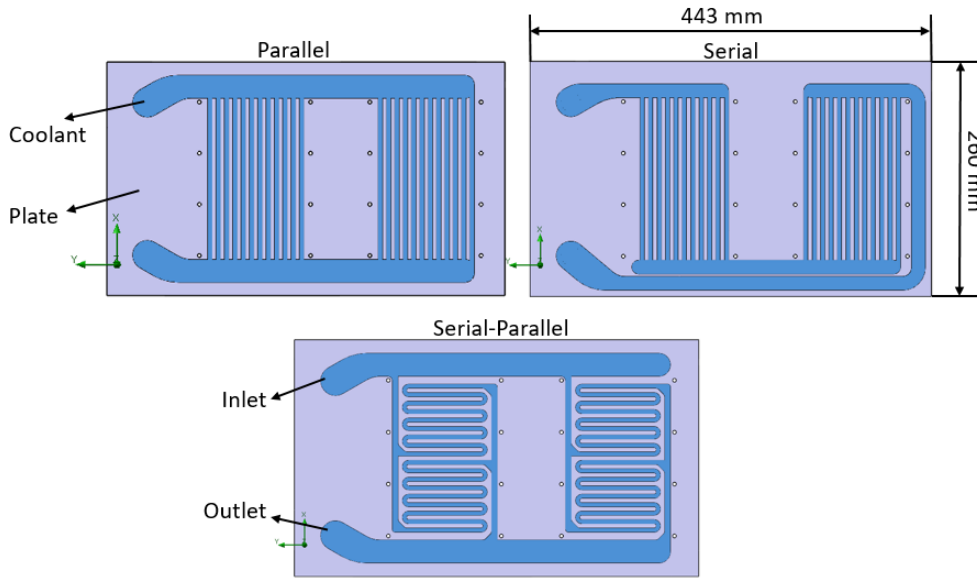


**Figure 2.** Flow configurations of the cold plate

## 2.2. Numerical Model and Grid Dependence Verification

The Simcenter FLOEFD [33] is used to perform numerical analysis and this commercial software is based on a 3D finite volume solver for the Navier-Stokes and energy equations. The computational domain consists of solid and fluid regions. Solid regions represent the cold plate body and fluid regions indicate the coolant. Incompressible flow and steady state conditions are assumed for the analysis. The governing equations are expressed as follows:

Continuity equation:

$$\nabla \cdot \vec{V} = 0 \quad (1)$$

Momentum equation:

$$\rho(\vec{V} \cdot \nabla \vec{V}) = -\nabla p + \mu \cdot \nabla^2 \vec{V} \quad (2)$$

Energy equations for fluid and solid domains are respectively given as:

$$\rho c_p (\vec{V} \cdot \nabla T) = k_f \nabla^2 T \quad (3)$$

$$k_s \nabla^2 T = 0 \quad (4)$$

In these equations,  $\rho$  is the coolant density,  $\mu$ ,  $k$  and  $c_p$  are the dynamic viscosity, thermal conductivity and specific heat, respectively.  $P$  is the pressure,  $V$  is the mean velocity vector and  $T$  is the temperature.

The coolant inlet temperature of 55 °C is used for all the simulations. Flow rates are defined as 10, 15 and 20 l/min, respectively. The standard k- $\epsilon$  turbulent model is used to model turbulent flow. Pressure at the cold plate outlet is set to 100 kPa. In the analysis, each IGBT's module is assumed to dissipate heat a rate of 2 kW. The effective heat dissipation region of IGBT elements is generally in the middle region, which comprises about 50% of the contact surface. The constant heat flux is applied to the 50% of the IGBTs total contact area. The other surfaces of the cold plate is considered as adiabatic. The schematic presentation of the boundary conditions is given in Fig.3 and summarized in Table 2.

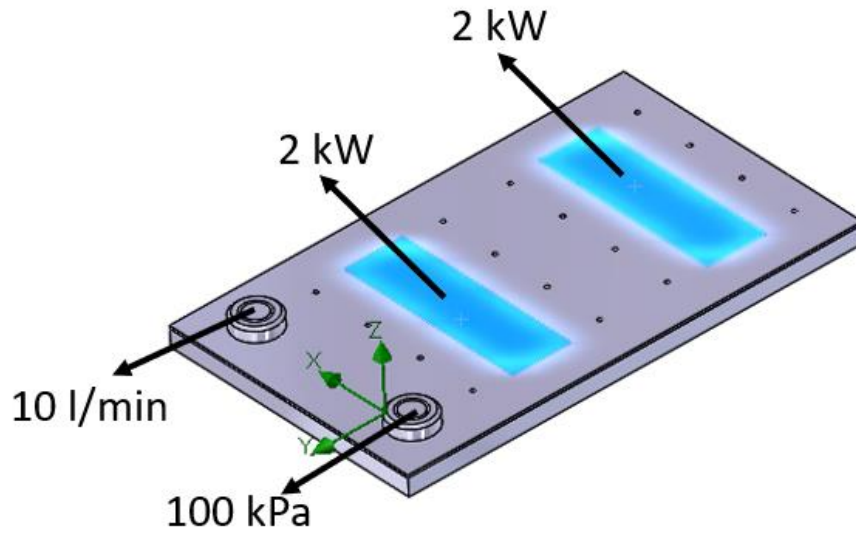


**Figure 3.** Boundary conditions

**Table 2.** Details of the boundary conditions

Inlet	Volume flow inlet
Outlet	Pressure outlet
Fluid-solid interface surface	Coupled wall
IGBTs mounting surfaces	Constant heat flux
Other surface	Adiabatic

In order to evaluate thermal performance of the cold plate, some performance parameters need to be defined. Maximum surface temperature ( $T_{s,max}$ ), pressure drop of the coolant ( $\Delta P$ ) across the cold plate, thermal resistance ( $R_{th}$ ) and the effectiveness ( $\varepsilon$ ) of the cold plate are considered as main parameters. Thermal resistance and effectiveness equations are given as follows:

$$R_{th} = \frac{T_{s,max} - T_{c,in}}{Q}, \quad \left( \frac{^{\circ}C}{kW} \right) \quad (5)$$

$$\varepsilon = \frac{T_{c,o} - T_{c,in}}{T_{s,max} - T_{c,in}} \quad (6)$$

where  $T_{s,max}$  is the maximum surface temperature of the cold plate,  $Q$  is the total heat load of the IGBTs,  $T_{c,in}$  and  $T_{c,o}$  are the coolant inlet and outlet temperatures, respectively.

A grid is created by the hexahedral elements in the computational domain. High-resolution mesh is adopted in the vicinity of the boundary layer region for the simulation accuracy. Fig. 4 presents the created grid structure. The total number of grids of 0.7, 1.1, 1.3 and 1.75 million are applied for the grid dependence test in the computational domain. The purpose of the grid dependence study is to obtain precision solution with smaller number of elements. The results of the grid dependence study are given in Fig. 5. The results of the surface temperature and pressure drop indicate about 0.1% variation for more than 1.39 million grid elements.

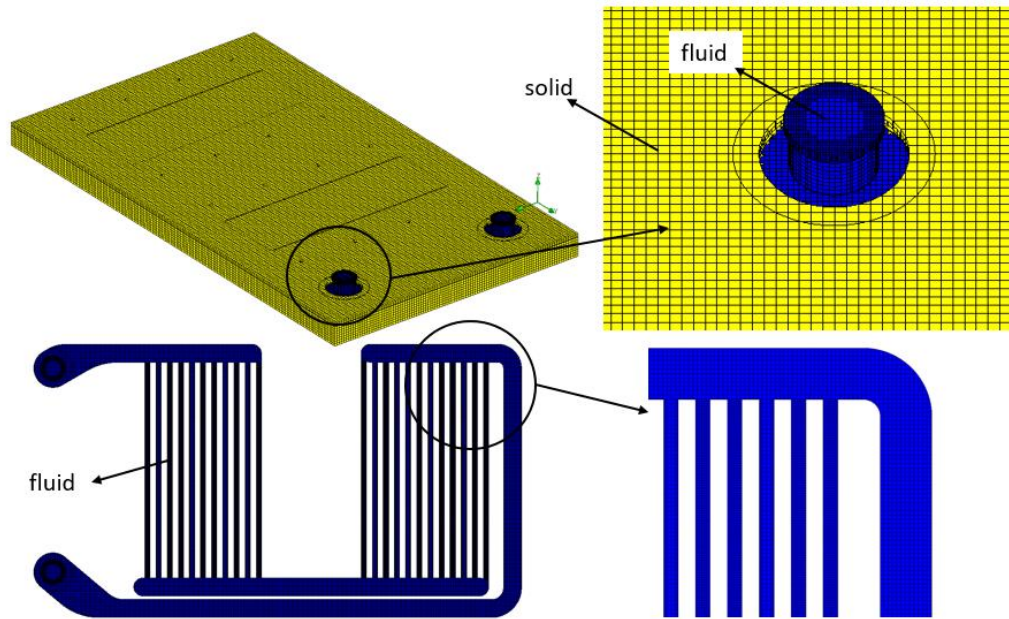


Figure 4. Grid structure

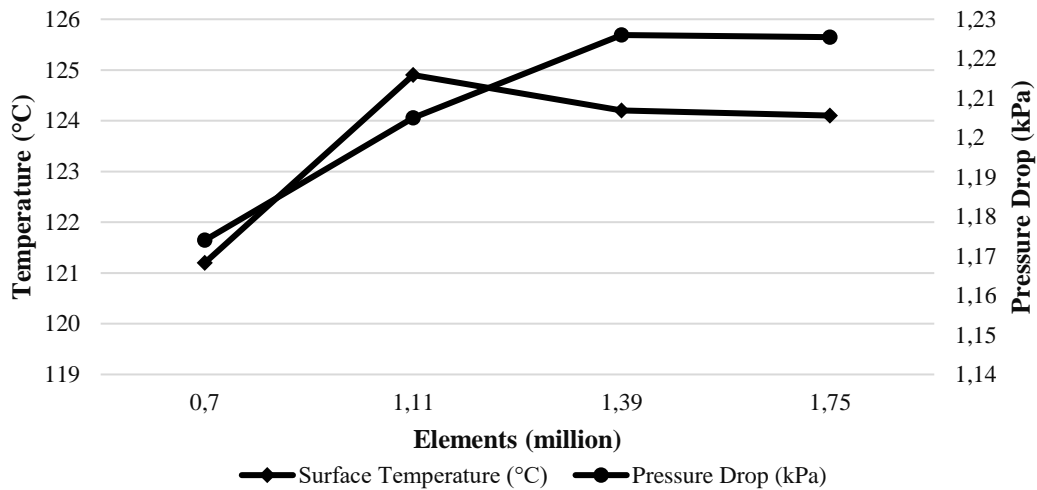


Figure 5. Effects of grid number on the pressure drop and surface temperature.

### 3. Results and Discussion

#### 3.1. Effects of Flow Channel Configuration

The thermal analysis of a cold plate with three different flow channel structure is conducted for various flow rates. The velocity, pressure and temperature distributions are compared for the three flow channel

configuration. Surface temperatures of the cold plate are given in Fig. 6 for different flow rates. The lowest surface temperature is observed on the serial-parallel channel configuration. In addition to this, the maximum surface temperature of the parallel channel is higher than that of serial. Also, it is observed that the temperature distribution in the serial-parallel channel configuration is more homogeneous on the IGBTs mounting surfaces

compared with the other configurations. It is apparent that as the flow rate increases, the maximum and average

surface temperatures of the cold plate decreases due to strong convection effects.

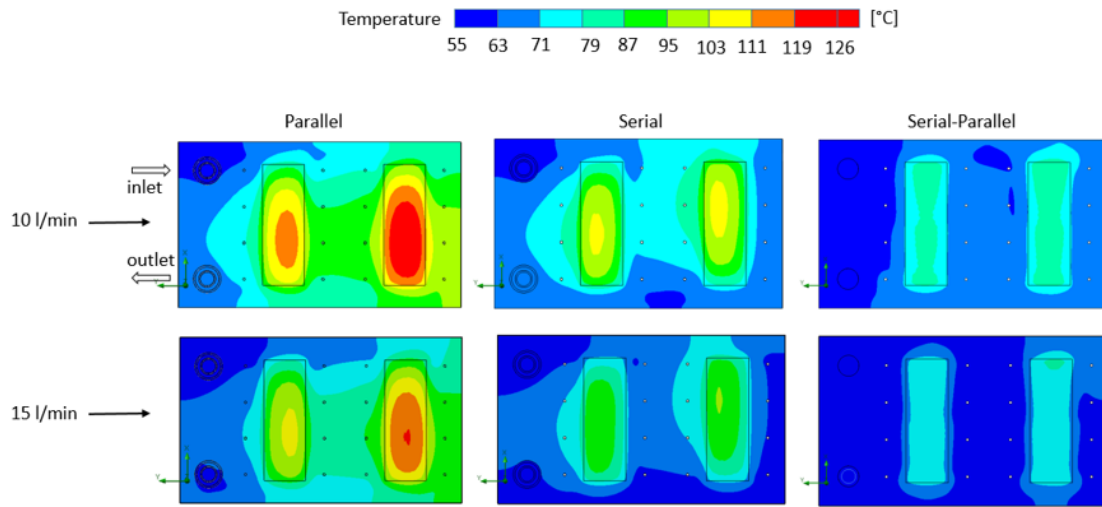


**Figure 6.** Temperature distribution on the cold plate for different flow rates

**Table 3.** Effectiveness and thermal resistance values of cold plate for flow rate of 10 l/min

Channel Type	$\epsilon$	$R_{th}$
Parallel Channel	0.0968	17.3
Serial Channel	0.1233	12.15
Serial-Parallel Channel	0.2272	7.33

The computed thermal resistance and effectiveness values are presented in Table 3 for flow rate of 10 l/min. The low thermal resistance implies that the plate transfers the more heat from the IGBT module. To make a comparison of the thermal resistances, the lowest thermal resistance occurs in the series-parallel channel, while the highest thermal resistance occurs in the parallel channel cooling plate. On the contrary of the thermal resistance, effectiveness value is the highest for the case of serial-parallel configuration. This is because decrease in the maximum surface temperature and improved the temperature uniformity.

Fig. 7 shows the velocity distributions in the mid-height plane for different flow rates. It can be seen that, the velocity of the coolant in the parallel channels is significantly slower than other configurations. The low flow velocity values cause high surface temperature and poor temperature uniformity on the cold plate surface. A more uniform velocity distribution is achieved in the serial-parallel configuration compared to the serial flow channels. In addition to this, the flow velocity values increase by the flow rate.



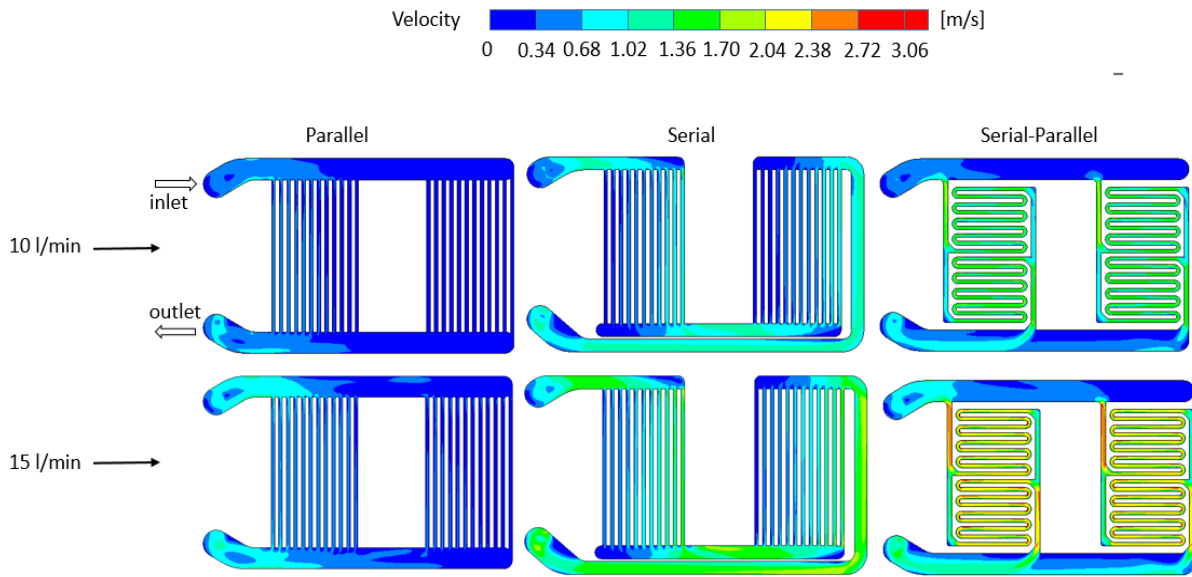


**Figure 7.** Velocity distribution on the cold plate for different flow rates

The thermal resistance and pressure drop values are presented in Fig. 8 and 9 for various flow rates. The cooling performance of the cold plate is significantly enhanced for serial-parallel flow configuration for each flow rate. The thermal resistance decreases for all flow configurations with the increase of flow rate due to strengthening of

convection effects. Pressure drop values increase with the increase of the flow rate. This increase is much more evident for the case of serial-parallel flow configuration due to high coolant velocity in the flow channels and extra minor losses arising from the channel structure.

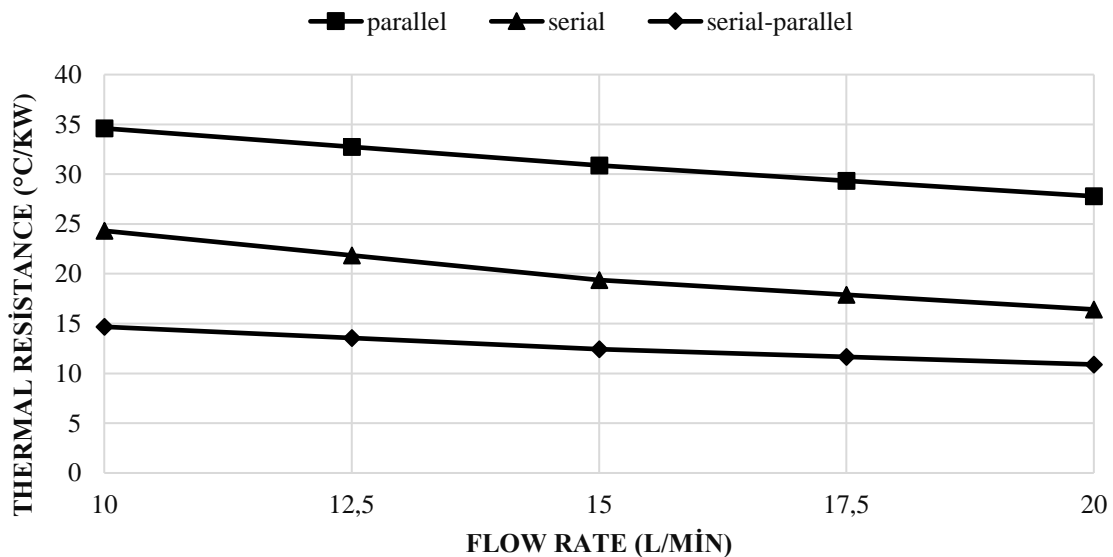


**Figure 8.** Variation of thermal resistance for different flow rate values

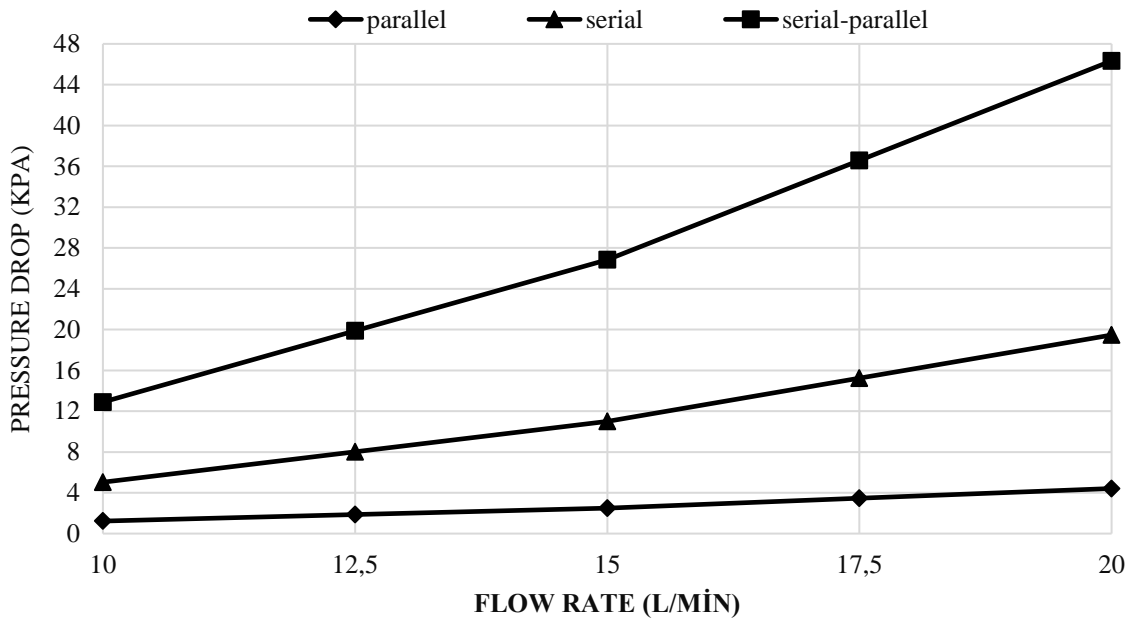


**Figure 9.** Variation of pressure drop for different flow rate values

### 3.2. Effects of Channel Aspect Ratio

The flow channel dimensions play a vital role for effective heat removal with optimum pumping power for the cold plate applications. The presentation of the flow

channels is given in Fig. 10. The effect of the aspect ratio (defined as the ratio of channel height to the channel width) on the cooling performance is analyzed in this section for the serial-parallel configuration.

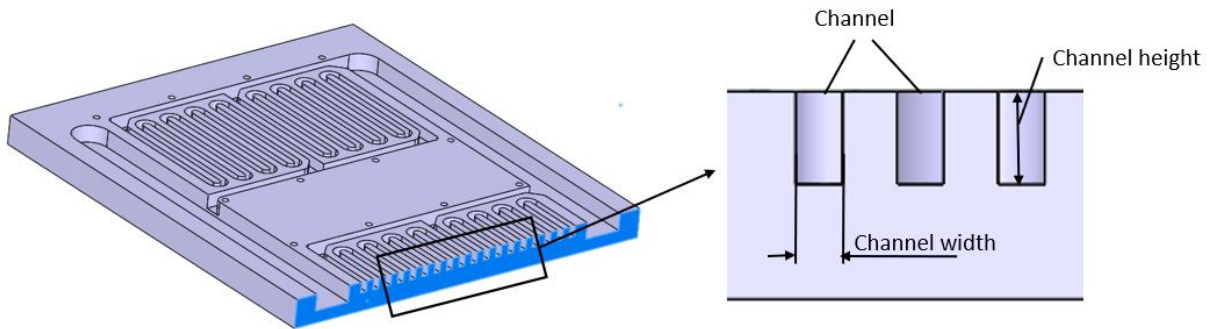


**Figure 10.** Schematic diagram of channel layout

The surface temperature distribution of the cold plate for flow rate of 10 l/min is shown in Fig. 11. It is obvious that the surface temperature of the cold plate with aspect ratio of 1.1 is lesser than other two cases. For fixed flow rate, the coolant velocity increases with the decrease of the aspect ratio. Larger coolant velocities indicate more powerful convective heat transfer. As shown in Table 4,

the aspect ratio plays dominant role in the cold plate pressure drop. The pressure drop increases about two-fold when the aspect ratio decreases to 1.1 from 1.7. Also, it is observed that the effect of the aspect ratio on the thermal resistance is lower compared to the pressure drop.

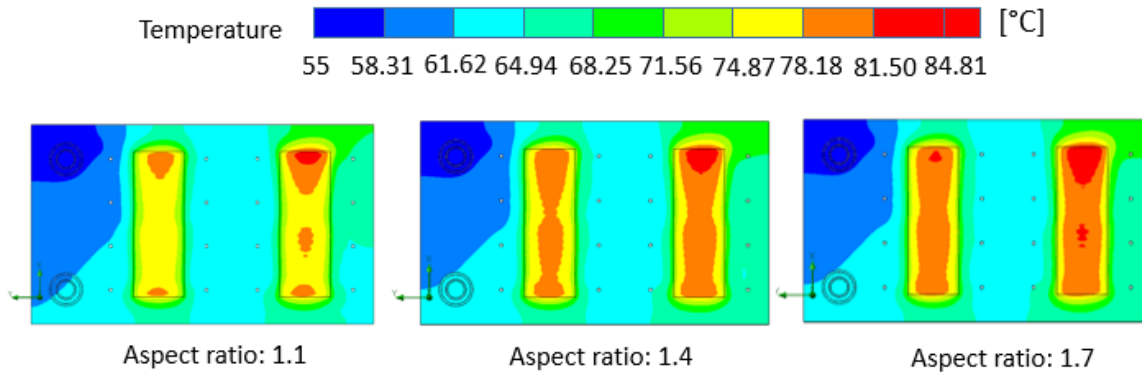


**Figure 11.** Surface temperature distributions for various aspect ratios

**Table 4.** Thermal resistance, pressure drop and maximum surface temperature values for various aspect ratios

Aspect Ratio	1.1	1.4	1.7
$R_{th}$ ( $^{\circ}\text{C}/\text{kW}$ )	7.10	7.33	7.47
$\Delta P$ (kPa)	19.69	12.83	10.13
$T_{max}$ ( $^{\circ}\text{C}$ )	83.41	84.35	84.88

#### 4. Conclusion

In this study, the performance analysis of a cold plate containing two IGBTs utilized in the rail system applications is carried out for different flow configurations and coolant flow rates. Three different flow configurations are studied namely series, parallel and series-parallel. Temperature distributions, thermal resistance and pressure drops in the cold plate for different flow rates are obtained by using commercial software. According to the analysis results, the maximum temperature decreases significantly for series-parallel flow configuration. The thermal resistance decreases about 60% in the case of serial-parallel configuration comparing with the parallel flow channels. Moreover, despite the improvement in the thermal resistance, pressure drop values for serial parallel configuration are a 10 times higher than in parallel configuration. In addition to this with the increase of the channel aspect ratio, pressure drop decreases by 48.5% while the thermal resistance increases by only %5. The serial-parallel channel configuration can provide a significant performance improvement in electronic cooling applications with proper aspect ratio optimization.

#### Author's Contributions

**Mehmet Bahattin Akgül:** Drafted and wrote the manuscript, performed the analytical analysis and result.

**Furkan Sinan Erçel:** Assisted in analytical analysis on the structure, supervised the experiment's progress, result interpretation and helped in manuscript preparation.

#### Ethics

There are no ethical issues after the publication of this manuscript.

#### References

- [1]. Kandlikar, S.G. and Hayner, C.N. 2009. Liquid cooled cold plates for industrial high-power electronic devices thermal design and manufacturing considerations. *Heat Transfer Engineering*; 30(12), 918–930.
- [2]. Teng H., Yeow, K. 2012. Design of direct and indirect liquid cooling systems for high- capacity, high-power lithium-ion battery packs. *SAE International Journal of Alternative Powertrains*; 1(2), 525-536.
- [3]. Jarrett A, Kim IY. 2011. Design optimization of electric vehicle battery cooling plates for thermal performance. *Journal of Power Sources*; 196(23):10359–68
- [4]. Maddipati, U. R., Rajendran, P., & Laxminarayana, P. 2013. Thermal design and analysis of cold plate with various proportions of ethyl glycol water solutions. *International Journal of Advanced Trends in Computer Science and Engineering*; 2(6), 22-25.
- [5]. Lu, Z., Zhang, K. 2021. Study on the performance of a Y-shaped liquid cooling heat sink based on constructal law for electronic chip cooling. *Journal of Thermal Science and Engineering Applications*; 13(3), 034501.
- [6]. Datta, A.B., Majumdar, A.K. 1980. Flow distribution in parallel and reverse flow manifolds, *International Journal of Heat and Fluid Flow*; 2(4), 253-262

- [7]. Chen, D., Jiang J., Kim, G., Yang, C., Pesaran, A. 2016. Comparison of different cooling methods for lithium ion battery cells, *Applied Thermal Engineering*; 94(1), 846-854.
- [8]. Panchal, S., Mathewson, S., Fraser, R., Culham, R., Fowler, M. 2015. Thermal management of lithium-ion pouch cell with indirect liquid cooling using dual cold plates approach, *SAE International Journal of Alternative Powertrains*; 4(2), 293-307.
- [9]. Teng, H., Ma, Y., Yeow, K., Thelliez, M. 2011. Thermal characterization of a li-ion battery module cooled through aluminum heat-sink plates, *SAE International Journal of Passenger Cars—Mechanical Systems*; 4(3), 1331-1342.
- [10]. Yeow, K., Teng, H., Thelliez, M., Tan, E. 2012. Thermal analysis of a li-ion battery system with indirect liquid cooling using finite element analysis approach, *SAE International Journal of Alternative Powertrains*; 1(1), 65-78.
- [11]. Yeow, K., Teng, H. 2013. Reducing temperature gradients in high-power, large-capacity lithium-ion cells through ultra-high thermal conductivity heat spreaders embedded in cooling plates for battery systems with indirect liquid cooling, *SAE World Congress & Exhibition*; Detroit, USA, 1(0234), 1-11.
- [12]. Ming-Chang, L., Chi-Chuan, W. 2006. Effect of the inlet location on the performance of parallel-channel cold-plate, *IEEE Transactions on Components and Packaging Technologies*; 29, 30–38.
- [13]. Hetsroni G., Mosyak A., Segal Z. 2001. Nonuniform temperature distribution in electronic devices cooled by flow in parallel microchannels, *IEEE Transactions on Components and Packaging Technologies*; 24, 16–22.
- [14]. Muratçobanoğlu, B., Mandev, E., Ceviz, M. A., Manay, E., & Afshari, F. 2024. CFD simulation and experimental analysis of cooling performance for thermoelectric cooler with liquid cooling heat sink. *Journal of Thermal Analysis and Calorimetry*; 149(1), 359-377.
- [15]. Zhang, F., Huang, Z., Li, S., Sun, S., & Zhao, H. 2024. Design and thermal performance analysis of a new micro-fin liquid cooling plate based on liquid cooling channel finning and bionic limulus-like fins. *Applied Thermal Engineering*; 237, 121597.
- [16]. Chu, Y. M., Farooq, U., Mishra, N. K., Ahmad, Z., Zulfıqar, F., Yasmin, S., & Khan, S. A. 2023. CFD analysis of hybrid nanofluid-based microchannel heat sink for electronic chips cooling: applications in nano-energy thermal devices. *Case Studies in Thermal Engineering*; 44, 102818.
- [17]. Li, W., Garg, A., Wang, N., Gao, L., Le Phung, M. L., & Tran, V. M. 2022. Computational fluid dynamics-based numerical analysis for studying the effect of mini-channel cooling plate, flow characteristics, and battery arrangement for cylindrical lithium-ion battery pack. *Journal of Electrochemical Energy Conversion and Storage*; 19(4), 041003.
- [18]. Zhang, F., Tao, Y., He, Y., & Qiu, S. 2024. Optimization and thermal characterization of a new liquid-cooled plate with branching channels of fractal geometry. *Applied Thermal Engineering*; 123881.
- [19]. İlikan A. N., Yaylı, A. 2022. Performance comparison of parallel and series channel cold plates used in electric vehicles by means of CFD simulations. *Eskişehir Osmangazi Üniversitesi Mühendislik ve Mimarlık Fakültesi Dergisi*; 30(3), 397-404.
- [20]. Jafari, R. 2021. Dimensional optimization of two-phase flow boiling in microchannel heat sinks. *International Advanced Researches and Engineering Journal*; 5(3), 475-483.
- [21]. Özbektaş S., Sungur B., and Topaloğlu B. 2022. Numerical investigation of the effect of flow circulation pattern and velocity on the performance of water-cooled heat sink. *Gümüşhane Üniversitesi Fen Bilimleri Dergisi*; 12(1), 151-163.
- [22]. Jayarajan, S. A., & Azimov, U. 2023. CFD Modeling and Thermal Analysis of a Cold Plate Design with a Zig-Zag Serpentine Flow Pattern for Li-Ion Batteries. *Energies*; 16(14), 5243.
- [23]. Akbarzadeh, M., Jaguemont, J., Kalogiannis, T., Karimi, D., He, J., Jin, L., et al., 2021. A novel liquid cooling plate concept for thermal management of lithium-ion batteries in electric vehicles. *Energy Conversion. Management*; 231, 113862.
- [24]. Huo Y, Rao Z, Liu X, Zhao J. 2015. Investigation of power battery thermal management by using mini-channel cold plate. *Energy Conversion Management*; 89:387–95.
- [25]. Jin LW, Lee PS, Kong XX, Fan Y, Chou SK. 2014. Ultra-thin minichannel LCP for EV battery thermal management. *Applied Energy*; 113:1786–94.
- [26]. Jassem, R. R., & Salem, T. K. 2016. An experimental and Numerical study the performance of finned Liquid cold-plate with different operating conditions. *International Journal of Current Research and Review*; 9(3), 41-46.
- [27]. Pan, M. 2021. Study of the performance of an integrated liquid cooling heat sink for high-power IGBTs. *Applied Thermal Engineering*; 190, 116827..
- [28]. Reeves, M., Moreno, J., Beucher, P., Loong, S. J., & Brown, D. 2011. Investigation on the impact on thermal performances of new pin and fin geometries applied to liquid cooling of power electronics. In *PCIM Europe* ; 772-778.
- [29]. Zhang, Y. P., Yu, X. L., Feng, Q. K., & Zhang, R. T. 2009. Thermal performance study of integrated cold plate with power module. *Applied Thermal Engineering*; 29(17-18), 3568-3573.
- [30]. Zhang, H., Ganesan, P., Sharma, R. K., Zubir, M. N. B. M., Badruddin, I. A., & Chong, W. T. 2024. A novel overflow channel design of manifold cold plate for lithium-ion battery: A CFD study. *Process Safety and Environmental Protection*; 189, 648-663.
- [31]. Chu, Y. M., Farooq, U., Mishra, N. K., Ahmad, Z., Zulfıqar, F., Yasmin, S., & Khan, S. A. 2023. CFD analysis of hybrid nanofluid-based microchannel heat sink for electronic chips cooling: applications in nano-energy thermal devices. *Case Studies in Thermal Engineering*; 44, 102818.
- [32]. Nada, S. A., El-Zoheiry, R. M., Elsharnoby, M., & Osman, O. S. 2022. Enhancing the thermal performance of different flow configuration minichannel heat sink using Al<sub>2</sub>O<sub>3</sub> and CuO-water nanofluids for electronic cooling: An experimental assessment. *International Journal of Thermal Sciences*; 181, 107767.
- [33]. User manual of software FloEFD.

# Using Deep Learning Architectures for Skin Cancer Classification

Bafreen Mohammed<sup>1\*</sup> , Özkan İnik<sup>2</sup> 

<sup>1</sup>Department of Computer Engineering , Tokat Gaziosmanpaşa University, Türkiye

<sup>2</sup>Department of Computer Engineering , Tokat Gaziosmanpaşa University, Türkiye

\* [bafreen771@gmail.com](mailto:bafreen771@gmail.com)

\* Orcid No: 0009-0008-1137-9307

Received: 10 July 2024

Accepted: 3 November 2024

DOI: 10.18466/cbayarfbe.1513945

## Abstract

Since skin cancer is one of the most common types of cancer, prompt diagnosis is essential to successful treatment. Impressive performance in image-based classification tasks has been demonstrated by convolutional neural networks (CNNs), particularly in recent years. In this study, the proposed CNN model was applied to the ISIC skin cancer classification challenge. A proposed deep learning model and four popular deep CNN models (ResNet, GoogleNet, AlexNet, and VGG16) were used to classify the skin cancer images. High levels of accuracy on test data from the ISIC dataset were achieved by the proposed CNN model, according to experimental results. Preprocessing was performed on images with sizes of 64x64, 100x100, 224x224, and 128x128 pixels. The experimental results show that the proposed CNN model achieved the highest accuracy rate of 86.76% on 128x128 size images.

**Keywords:** Classification, Convolutional neural network (CNN), Deep learning (DL), Skin Cancer, ISIC dataset

## 1. Introduction

Skin cancer is a prevalent type of cancer that originates in the skin's epidermal layer. It accounts for one in three cancer cases globally[1]. At about 90.0%, exposure to ultraviolet light is one of the main causes of skin cancer[2]. It was one of the five illnesses that were prevalent in the US, particularly in an area with intense sunlight. 2019 saw almost 2490 females and 4740 males lose their lives to melanoma, translating to nearly 20 deaths per day in the US alone[3, 4]. In contrast, an estimated 6850 novel fatalities associated with melanoma were documented in 2020, comprising 2240 females and 4610 males[5]. Dermatologists most commonly use dermoscopic images, also known as epiluminescence light microscopy, to analyze pigmented skin lesions. Because of the similarities between the lesions and healthy tissues, a visual examination performed with the naked eye may contain errors in recognition [6-9]. Dermatologists' manual inspection is often difficult, subjective, and time-consuming, resulting in varied recognition accuracy depending on their workload and skill[9-12]. A deep-learning convolutional neural network (CNN) image classifier that outperformed 21 board-certified dermatologists in recognizing photos with malignant

lesions was initially reported by Esteva et al. [13] in 2017. During training, the CNN dissected digital photos of skin lesions and created its own diagnostic standards for melanoma identification. Deep neural networks (CNN) have been used to demonstrate dermatologist-level skin cancer categorization in a number of follow-up articles [14-17].

In this work, we trained a skin cancer convolutional neural network by using open source ISIC dataset. The classification results of the proposed CNN were compared with the four-pretrained models. To avoid bias in the creation of the data set, we implemented the ImageDataGenerator object with the desired transformations, which balanced the overall dataset images to 2500 for each class of (actinic keratosis, basal cell carcinoma, dermatofibroma, melanoma, nevus, pigmented benign keratosis, seborrheic keratosis, squamous cell carcinoma, and vascular lesion) images divided into training, validation, and testing.



## 2. Materials and Methods

The materials and procedures used in this article to carry out the experiments are the main topics of this section. Section 2.1 describes ISIC datasets, whereas Section 2.2 explains the proposed Methodology. In Section 2.3, model performance and evaluation are presented.

### 2.1. Dataset

A dataset consisting of 2357 photographs of both benign and malignant oncological conditions, provided by the International Skin Imaging Collaboration (ISIC), was utilized. All photographs, except for melanomas and moles which are more prevalent in the photos, were categorized according to the ISIC classification. Each subgroup was then divided into an equal number of images[13]. Figure 1. displays a sample from the ISIC dataset .

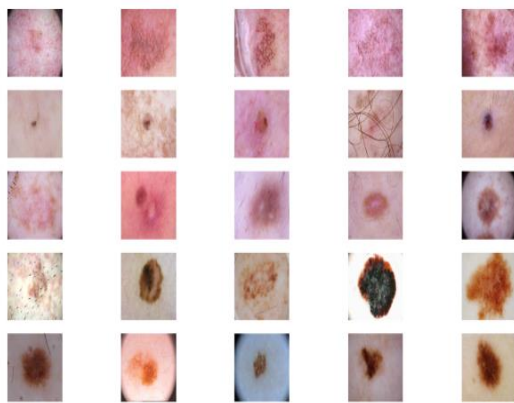


Figure 1. ISIC dataset sample

Table 1. Class-distribution of the ISIC Dataset

Class Name	Number of Images
actinic keratosis	130
basal cell carcinoma	392
Dermatofibroma	111
Melanoma	454
Nevus	373
Pigmented benign keratosis	478
seborrheic keratosis	80
Squamous cell carcinoma	197
vascular lesion	142
<b>Total Number of Images</b>	<b>2357</b>

### 2.2. Methodology

Deep neural networks can be understood mathematically as functions with millions of freely variable parameters, or weights. The intensities of the

pixels in an input image are transferred to a probability of a class label when these weights are modified for a specific image classification task. Training these functions necessitates a large number of images for which the class is known due to the enormous number of free parameters. The function's output is computed for each image, compared to the specified class label, and then the weights are gently adjusted to lower the error. With only the pixel intensities of each image as input, the function "learns" how to accurately predict the class labels through numerous repetitions of this method for every image in the training set. The function shows considerable generality in predicting the class labels for unknown images, thanks to the use of training data that accurately describe the potential input space. CNNs, which have a particular architecture, were used in this work. In normal neural networks, all pixel dependencies influence all weights, with the exception of the first layers. CNNs, on the other hand, first combine nearby local pixels to identify local features before combining them to create global features. Faster training and less complex models are the outcomes of this restriction on local connections. For this reason, CNNs have been successfully applied to many different problems [18-20] because they create different representations at different layers.

The proposed convolutional neural network (CNN) model, which is intended for image classification tasks, was presented in this paper. The model begins with an input layer that requires images to have three color channels and four different resolutions, those of 64x64, 100x100, 128x128 and 224x224 pixels. The next three convolutional layers use max-pooling to decrease spatial dimensions and progressively increase filter depth (32, 64, and 128). After every convolutional layer, batch normalization is used to speed up and stabilize training. After that, a global average pooling layer is used to further reduce spatial dimensions. Dropout layers for regularization are then added after two dense layers with 128 and 64 units, respectively, and rectified linear unit (ReLU) activation functions. The last layer uses softmax activation for multi-class output probabilities and is a dense layer with nine units, which correspond to the number of classes in the classification problem. For optimization, the Adam optimizer is selected, having an epsilon of 1e-07 and a learning rate of 0.001. Accuracy is the evaluation metric, and the model is created using the categorical crossentropy loss function. With the help of regularization approaches, this architecture seeks to extract hierarchical features from input images for efficient classification, improving generalization performance.

The methodology of the proposed method is given in Table 2. As can be seen in the table, the imbalance between the classes in the dataset is eliminated in the first stage. Data augmentation methods were used to eliminate data imbalance. After balancing the dataset,

the dataset is divided into three parts: training, testing and validation. The CNN models run on the training and validation data were then tested with the test data and the final result was obtained. Four different state-of-the-art models and an original new model were developed and used as CNN models.

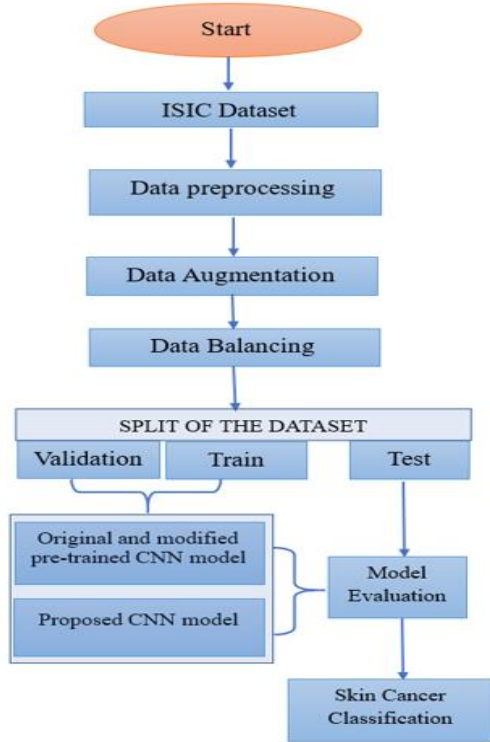


Figure 2. Proposed methodology diagram

### 2.2.1. Data balancing

Three techniques were employed by early machine learning researchers to address the classification problem with imbalanced data: class weight balancing [21, 22], under sampling [23, 24], and oversampling [25, 26]. Oversampling [25, 26] causes the data for categories with fewer photos to be duplicated. Oversampling does have one drawback, though: the duplicate image is identical to the original, making it useless for feature learning. Second, under sampling [23] eliminates data in categories with a higher number of photographs; however, this has the drawback of potentially removing a large number of images with useful attributes. The final step in the class weight balancing process is to multiply the loss weights by constants, each of which has an inverse relationship to the quantity of data in each category. The learning rate step may get too big to converge as a result of the class weight balancing; this is more noticeable in highly unbalanced data [27]. As a result, the suggestion in this article is to provide data for categories with fewer images. In order to enable the learning process to converge, the image generation approach [28] not only preserves the original data's features, but also adds random vectors to prevent overfitting. As shown in Figure 3. The original image data was resized to 64, 100, 128, and 224 dimensions, and the resized images were used after the dataset was balanced using augmentation techniques. Finally, the diversity of created images is increased by employing data augmentation [36] approaches.

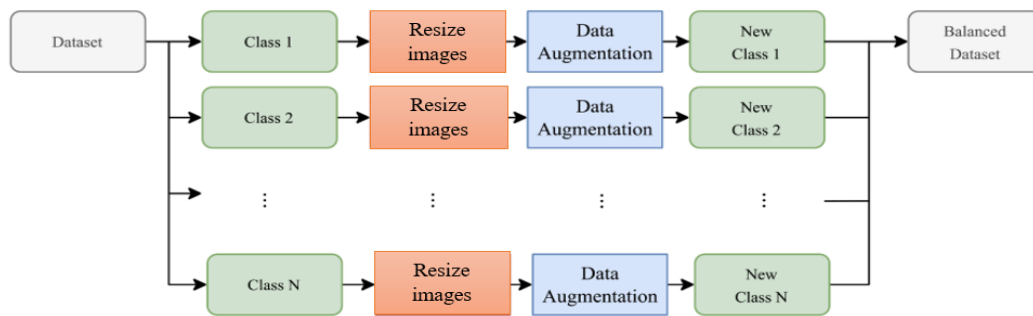


Figure 3. Flowchart of the dataset balancing

### 2.2.2. Data Augmentation

More and more diverse training data sets are known to enhance the performance of deep learning neural networks [29]. The process of creating artificially altered copies of images from training data is known as data augmentation, which also enlarges the training dataset by combining the original training data with the altered versions of the images. In this work, we employed rotation, flipping, shearing, and zooming as the augmentation functions. The angle of random

rotation was between 0 and 20 degrees. There was a 0.2 random zooming range. The shearing range was 0.2, meaning that one axis would lengthen by 20% while the other would remain intact. It is extremely improbable that the lesion will disappear from the image due to this slight degree of rotation, shearing, and zooming because it is located in the center of the image in both datasets. A few arbitrary enhanced pictures were taken from the

training dataset as shown in Table 2. ISIC Dataset Summary after augmentation

**Table 2.** ISIC Dataset Summary after augmentation

ISIC	Train images	Validation images	Test images	Total images
actinic keratosis	631	167	202	1000
basal cell carcinoma	631	167	202	1000
dermatofibroma	634	163	203	1000
melanoma	649	149	202	1000
nevus	633	164	203	1000
pigmented benign keratosis	647	153	200	1000
seborrheic keratosis	660	153	187	1000
squamous cell carcinoma	645	164	191	1000
vascular lesion	645	164	204	1000

## 2.3 Model Performance and Evaluation

This parameter is a measure of the statistical correctness of the prediction as defined in Equation-1[30]. Relying on this parameter alone can be sometimes misleading in evaluating the performance of a predictor because of its dependence on both the FP and FN. This means that two models can have the same accuracy, while one has high FP and low FN, and the other one has the opposite, i.e., low FP and high FN. Thus, the first model can be preferred to the other one, due to having a low FN for the sensitive medical scenario, which may not be decided only from the accuracy values of the models.

**True Positives (TP):** Occurrences where a positive outcome was predicted, and the actual result was also positive.

**True Negatives (TN):** Occurrences where a negative outcome was predicted, and the actual result was also negative.

**False Positives (FP):** Occurrences where a positive outcome was predicted, but the actual result was negative.

**False Negatives (FN):** Occurrences where a negative outcome was predicted, but the actual result was positive. [31].

Accuracy is defined as the ratio of the total number of input samples to the number of right predictions[31].

$$\text{Accuracy} = \frac{TP+TN}{TP+TN+FP+FN} \quad \text{Eq (1)}$$

Precision is defined as the number of correct positive results divided by the total number of positive outcomes that the classifier predicted[31].

Precision and recall are measured with the statistical correctness of the final prediction as defined in Equation-2 and Equation-3, respectively. Precision measures among the predicted images for a particular class and how many of them are actually of that class. On the other hand, recall measures the total number of images from a particular class and what fraction of that are correctly classified as images from that class.

Recall is the number of correct sure results divided by the total number of conjugate samples—that is, all the samples that should have been classified as sure[31].

$$\text{Precision} = \frac{TP}{TP+FP} \quad \text{Eq (2)}$$

$$\text{Recall} = \frac{TP}{TP+FN} \quad \text{Eq (3)}$$

**F1-score,** It also goes by the name "harmonic mean," which seeks to strike a balance between recall and precision. It works well on an unbalanced dataset and requires both false positives and false negatives for computation[31]. F1-score, defined in Equation-4 is known as weighted average of recall and precision.

$$F1 = \frac{2 \times \text{Precision} \times \text{Recall}}{\text{Precision} + \text{Recall}} \quad \text{Eq (4)}$$

Additionally, we observe that the precision, recall, and F1 score range in values from 0 to 1. A model performs better for a certain classification job the greater its precision, recall, and F1 score values [32].

## 3. Results and Discussion

### 3.1. Result of proposed CNN model with image size 224x224

For the purpose of the performance analysis, the dataset is split into three sets, one of which is the training set that is used to train the model. To prevent overfitting, the model's hyperparameters are adjusted using the validation set. And lastly, the testing set, which is used to evaluate the overall performance of the model. The training loss and validation loss gradually decreasing across the epochs indicates that the model is learning and generalising successfully. After epoch 50, the validation loss stops decreasing, suggesting that the model has reached its peak performance. It is important to keep in mind that the appropriate number of epochs can vary depending on the size of the dataset and the complexity of the model. **Error! Reference source not found.** shows the proposed model's with image size

(224x224) training and validation accuracy over a range of epochs, and Figure 5. shows the model's loss analyses over the same number of epochs. Figure 6.

show the confusion matrix of proposed model with the same image size.

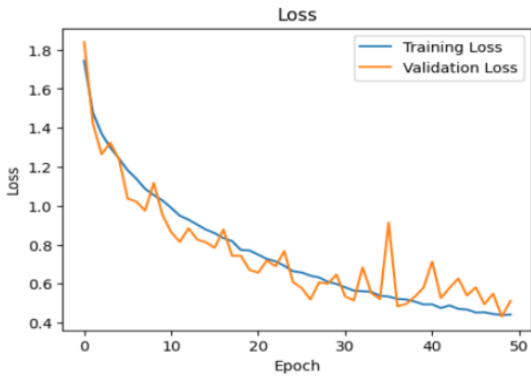


**Figure 4.** Convergence graph of the training and accuracy loss values obtained by the proposed CNN model in the training phase on the 224x224 image size dataset.

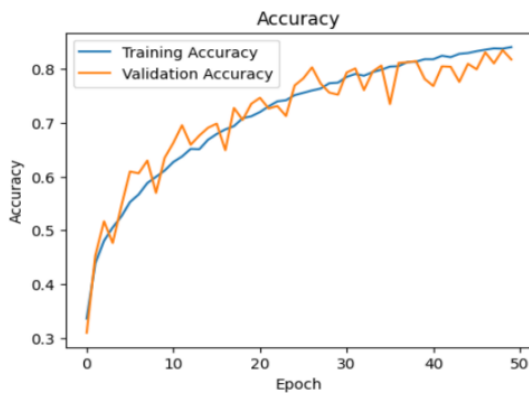


**Figure 5.** Convergence graph of the training and validation accuracy values obtained by the proposed CNN model in the training phase on the 224x224 image size dataset.

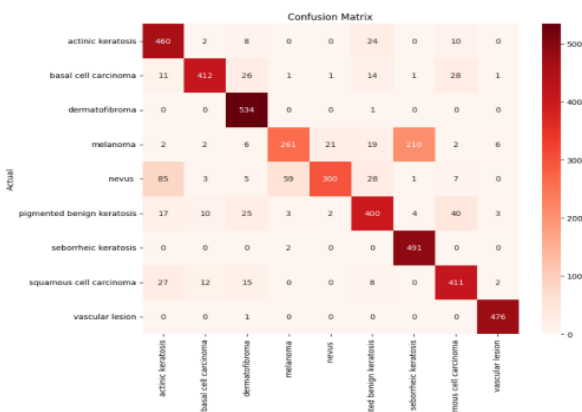


**Figure 6.** The confusion matrix obtained by the proposed CNN model on the 224x224 test dataset.

### 3.2. Result proposed CNN model with image size 128x128

After reducing the image to 128x128 pixels, the proposed CNN model result increased the accuracy of our model. Following this stage, our accuracy was 86.76%. Figure 7 shows the loss convergence graph obtained by the model during the training phase, and Figure 8 shows the accuracy convergence graph. Figure 9 shows the confusion matrix obtained by the model on the test data. When looking at the confusion matrix, it was seen that the model incorrectly labeled the “melanoma” class the most.

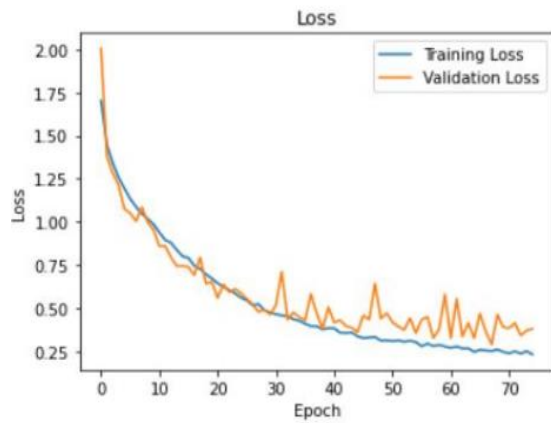


**Figure 7.** Convergence graph of the training and accuracy loss values obtained by the proposed CNN model in the training phase on the 128x128 image size dataset.

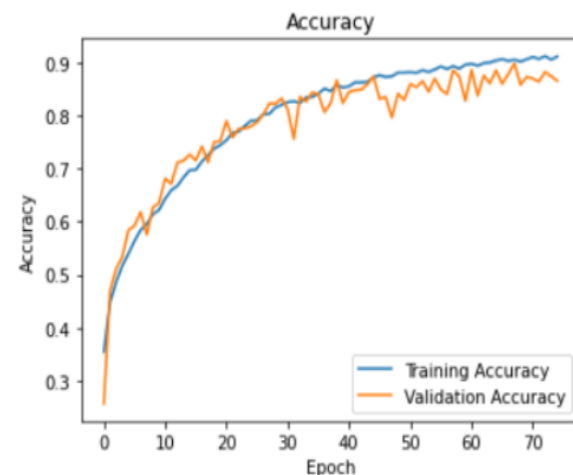


**Figure 8.** Convergence graph of the training and validation accuracy values obtained by the proposed

CNN model in the training phase on the 128x128 image size dataset.

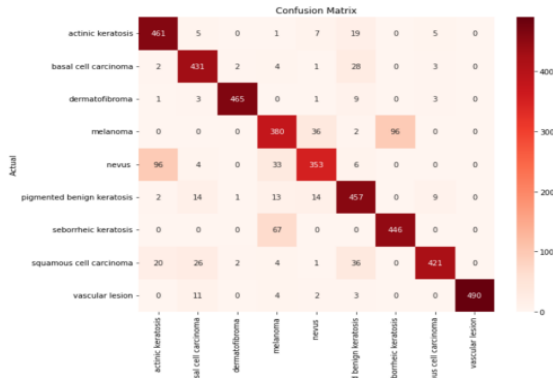


**Figure 9.** The confusion matrix obtained by the proposed CNN model on the 128x128 test dataset.

### 3.3. Result proposed CNN model with image size 64x64

The proposed CNN model was trained on a 64x64 dataset. The loss convergence graph in the training phase is given in Figure 10, and the accuracy convergence graph is given in Figure 11. When looking at the convergence graphs, the model showed its best performance approximately from the 35th epoch, and its success continued horizontally after this epoch. The confusion matrix obtained by the model on the test data is given in Figure 12. When looking at the confusion matrix, it was seen that the model incorrectly labeled the “actinic keratosis” class the most.

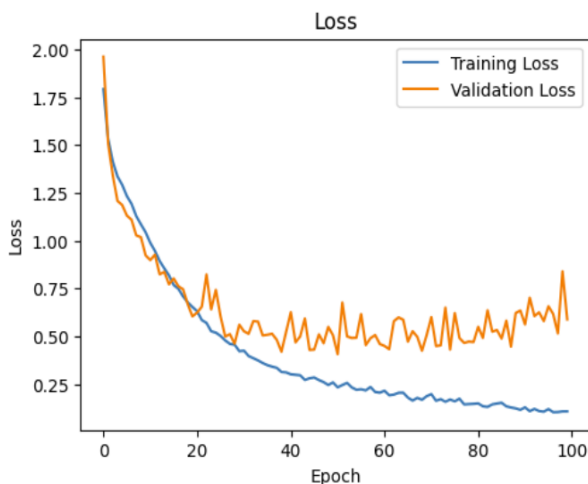


**Figure 10.** Convergence graph of the training loss and validation loss values obtained by the proposed CNN model in the training phase on the 64x64 image size dataset.

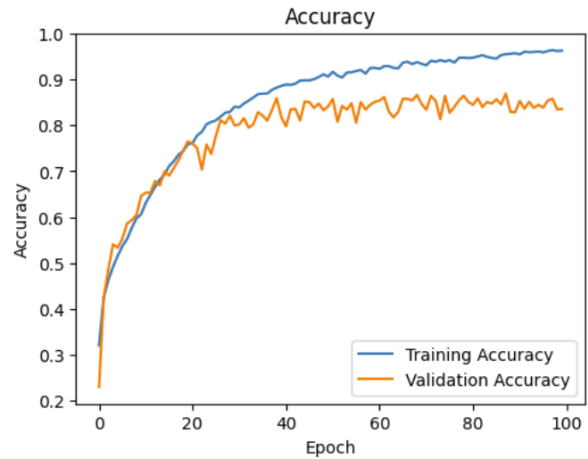


**Figure 11.** Convergence graph of the training and validation accuracy values obtained by the proposed CNN model in the training phase on the 64x64 image size dataset

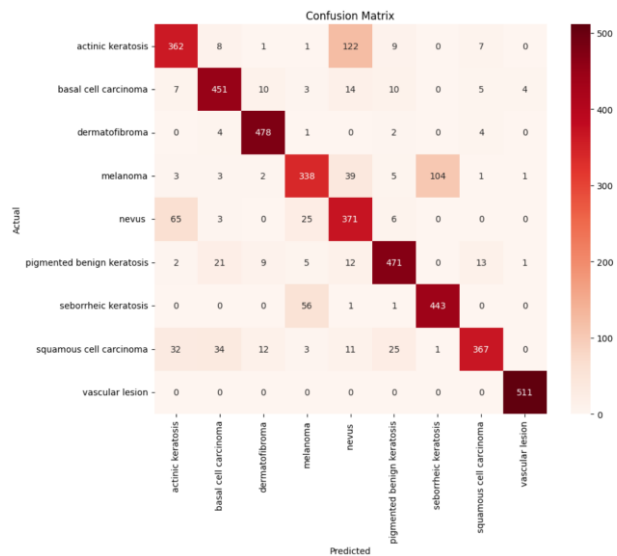


**Figure 12.** The confusion matrix obtained by the proposed CNN model on the 64x64 test dataset.

### 3.4. Result proposed CNN model with image size 100x100

The loss convergence graph of the CNN model trained on the 100x100 dataset in the training phase is given in Figure 13, and the accuracy convergence graph is given in Figure 14. When the convergence graphs are examined, the model showed its best performance approximately from the 36th epoch, and its success continued horizontally after this epoch. The confusion matrix obtained by the model on the test data is given in Figure 15. When looking at the confusion matrix, it was seen that the model incorrectly labeled the “melanoma” class the most.



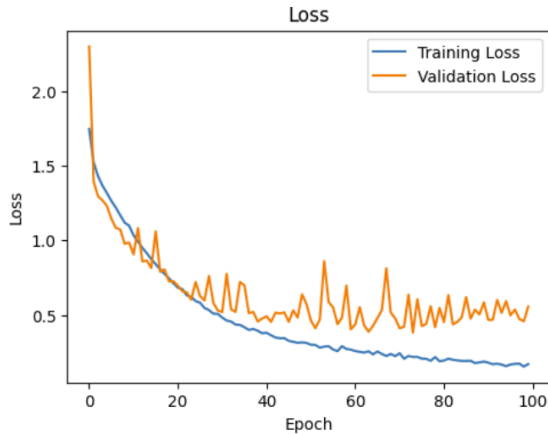


**Figure 13.** Convergence graph of the training and validation loss values obtained by the proposed CNN model in the training phase on the 100x100 image

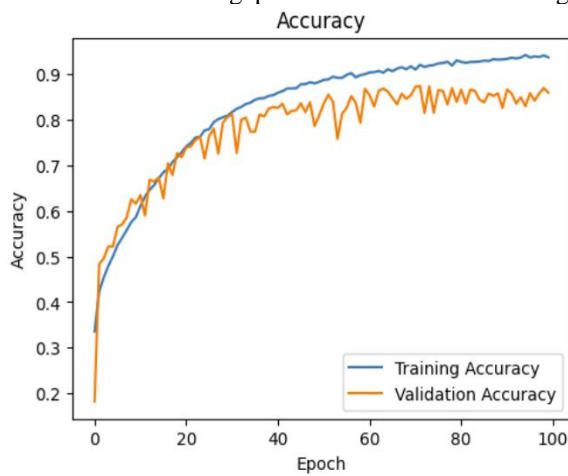


**Figure 14.** Convergence graph of the training and validation accuracy values obtained by the proposed CNN model in the training phase on the 100x100 image size.

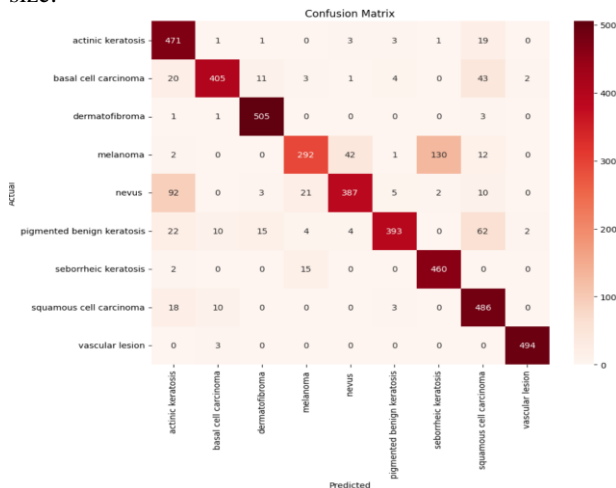


**Figure 15.** The confusion matrix obtained by the proposed CNN model on the 100x100 test dataset.

### 3.5. Result of Used Original Popular CNN Model

We first trained a number of well-known Convolutional Neural Network (CNN) models, including InceptionV3, AlexNet, ResNet, and InceptionV3, on the ImageNet

dataset in order to tackle our classification task. For our 9-class challenge, the early findings did not yield great accuracy, even with their outstanding feature extraction skills. In order to address this, we modified each of these models before using them again for our classification task. Specifically, we added more thick layers and dropout layers to enhance performance and avoid overfitting.

During preprocessing, we used data augmentation approaches to improve the model's generalization capabilities across various skin conditions and reduce class imbalances within the ISIC dataset. Applying a number of transformations, such as rotation, shifting the width and height, shearing, zooming, and horizontal flipping, was required for this. By enhancing the existing photos, these methods guaranteed that each class was adequately represented in addition to adding diversity to the training data. Next, we made sure the dataset was carefully balanced by limiting the number of images to 1000 for each class. After that, several models were trained and assessed using the balanced and expanded dataset. The accuracy comparison of these models is shown in Table, which also highlights how well they classify various skin disorders.

The parameter numbers of the models in the study are given in Table 3. When the table is examined, it is seen that the proposed CNN model has fewer parameters than all other models.

**Table 3.** Parameter comparison of the proposed CNN model and the state-of-the-art CNN models.

Models	Number of Parameters	Model Size
Modified AlexNet	46803035	178.54 MB
Modified VGG16	8266761	31.54 MB
Modified ResNet50	24756644	94.44 MB
Modified InceptionV3	48250537	184.06 MB
Original AlexNet	71988013	274.61 MB
Original VGG16	136362825	520.18 MB
Original ResNet50	25695113	98.02 MB
Original InceptionV3	23910185	91.21 MB
<b>Proposed CNN Model (64, 100, 128,224)</b>	<b>764041</b>	<b>465.04 KB</b>

The comparison of the results obtained in this study with the competitor studies is given in Table 4. The table shows the references of the studies on the ISIC dataset and the accuracy rates obtained in these studies. It is seen that some studies have achieved a higher success rate than the proposed method. However, since the training and test datasets used in the studies are not known, the accuracy values are not an absolute measure of success. Another parameter of model success is model computational complexity. In this context, the proposed CNN model obtained an accuracy value close to other models with a very low number of parameters.

**Table 4.** Review of the studies performed on the ISIC dataset and comparison of the results of these studies with the proposed method.

Reference	Model	Accuracy (%)
Albahar [33]	CNN and Novel Regularizer	97.49
Sanketh et al. [34]	CNN	98
Daghrir, Tlig et al. [35]	Hybrid approach	85.5
Vipin, Nath et al. [36]	U-Net	88.7
Rahi, Khan et al. [37]	CNN network with CGG16, RESNET50, DENSNET50	90
Jojoa Acosta et al. [38]	CNN combined with pretrained ResNet152	90.4
Rahi et al. [37]	CNN	76
Yu et al. [39]	CNN	94.9
Majtner et al. [40]	HCF+CNN	82.6
Li and Shen [41]	CNN	85.7
Mahbod et al. [42]	CNN	90.5
Zhang et al. [43]	CNN	87.4
Amin et al. [44]	CNN	99.0
Mahbod et al. [45]	CNN	96.6
Kwasigroch et al. [46]	HCF+CNN	77.0
Hameed et al. [47]	HCF+CNN	96.5
Khan et al. [48]	CNN	93.4
Mporas et al. [49]	ML+ANN	74.3
Khan et al. [50]	CNN	92.8
Pereira et al. [51]	HCF	90.0
Khan et al. [52]	CNN	90.7
	Proposed CNN Model_64	84.27
	Proposed CNN Model_100	86.5
	Proposed CNN Model_128	86.76
	Proposed CNN Model_224	83.22
	Modified AlexNet	89.56
	Original AlexNet	73
Proposed Work	Modified VGG16	86.50
	Original VGG16	64
	Modified ResNet50	88.94
	Original ResNet50	53
	Modified InceptionV3	90.56
	Original InceptionV3	64

#### 4. Conclusion

In this paper, a novel CNN model working on RGB images for skin cancer classification is presented. In addition, ResNet, GoogleNet, AlexNet, and VGG16 deep learning models are used by reorganizing them by changing some of their layers. The models are tested using ISIC datasets, with image enhancement in pre-processing utilizing the Image class from the PIL or Pillow library to open and resize images, and np.asarray to translate the resized images into NumPy arrays. Data augmentation techniques are also used. The proposed novel CNN model achieved 84.27%, 86.51%, 86.76%, and 83.22% accuracy rates for different resolutions of 64x64, 100x100, 128x128, and 224x 224 pixel image sizes, respectively. The proposed model has very few parameters and its success metrics are comparable to other studies.

Furthermore, in this study compared a set of pre-trained modified CNN models using both original and customized models to compare their parameters and performance. After doing a comparative analysis, updated VGG16 achieved 86.50%, AlexNet 89.56%, ResNet 88.94%, and InceptionV3 90.56%. In future work, we would like to add more different images and revisions to the training dataset in order to improve the model's ability to generalize to varying skin tones and appearance changes. Optimizing the current model, attempting more complex architectures, or experimenting with different transfer learning algorithms or pre-trained models will all yield better results.

## References

1. Leiter, U., U. Keim, and C. Garbe, *Epidemiology of skin cancer: update 2019*. Sunlight, Vitamin D and Skin Cancer, 2020: p. 123-139.
2. Narayanamurthy, V., et al., *Skin cancer detection using non-invasive techniques*. RSC advances, 2018. **8**(49): p. 28095-28130.
3. Singer, S., et al., *Gender identity and lifetime prevalence of skin cancer in the United States*. JAMA dermatology, 2020. **156**(4): p. 458-460.
4. Trager, M.H., et al., *Biomarkers in melanoma and non-melanoma skin cancer prevention and risk stratification*. Experimental dermatology, 2022. **31**(1): p. 4-12.
5. Siegel, R.L., K.D. Miller, and A. Jemal, *Cancer statistics, 2018*. CA: a cancer journal for clinicians, 2018. **68**(1): p. 7-30.
6. Jones, O., et al., *Dermoscopy for melanoma detection and triage in primary care: a systematic review*. BMJ open, 2019. **9**(8): p. e027529.
7. Phillips, M., et al., *Detection of malignant melanoma using artificial intelligence: an observational study of diagnostic accuracy*. Dermatology practical & conceptual, 2020. **10**(1).
8. Vestergaard, M., et al., *Dermoscopy compared with naked eye examination for the diagnosis of primary melanoma: a meta-analysis of studies performed in a clinical setting*. British Journal of Dermatology, 2008. **159**(3): p. 669-676.
9. Carli, P., et al., *Addition of dermoscopy to conventional naked-eye examination in melanoma screening: a randomized study*. Journal of the American Academy of Dermatology, 2004. **50**(5): p. 683-689.
10. Al-Masni, M.A., D.-H. Kim, and T.-S. Kim, *Multiple skin lesions diagnostics via integrated deep convolutional networks for segmentation and classification*. Computer methods and programs in biomedicine, 2020. **190**: p. 105351.
11. Hasan, M.K., et al., *Dermo-DOCTOR: A framework for concurrent skin lesion detection and recognition using a deep convolutional neural network with end-to-end dual encoders*. Biomedical Signal Processing and Control, 2021. **68**: p. 102661.
12. Hasan, M.K., et al., *DSNet: Automatic dermoscopic skin lesion segmentation*. Computers in biology and medicine, 2020. **120**: p. 103738.
13. Esteva, A., et al., *Dermatologist-level classification of skin cancer with deep neural networks*. nature, 2017. **542**(7639): p. 115-118.
14. Marchetti, M.A., et al., *Results of the 2016 International Skin Imaging Collaboration International Symposium on Biomedical Imaging challenge: Comparison of the accuracy of computer algorithms to dermatologists for the diagnosis of melanoma from dermoscopic images*. Journal of the American Academy of Dermatology, 2018. **78**(2): p. 270-277. e1.
15. Haenssle, H.A., et al., *Man against machine: diagnostic performance of a deep learning convolutional neural network for dermoscopic melanoma recognition in comparison to 58 dermatologists*. Annals of oncology, 2018. **29**(8): p. 1836-1842.
16. Brinker, T.J., et al., *A convolutional neural network trained with dermoscopic images performed on par with 145 dermatologists in a clinical melanoma image classification task*. European Journal of Cancer, 2019. **111**: p. 148-154.
17. Brinker, T.J., et al., *Skin cancer classification using convolutional neural networks: systematic review*. Journal of medical Internet research, 2018. **20**(10): p. e11936.
18. İnik, Ö., et al., *A new method for automatic counting of ovarian follicles on whole slide histological images based on convolutional neural network*. Computers in biology and medicine, 2019. **112**: p. 103350.
19. Celik, M. and O. Inik, *Development of hybrid models based on deep learning and optimized machine learning algorithms for brain tumor Multi-Classification*. Expert Systems with Applications, 2024. **238**: p. 122159.
20. Inik, O., et al., *Prediction of Soil Organic Matter with Deep Learning*. Arabian Journal for Science and Engineering, 2023. **48**(8): p. 10227-10247.
21. King, G. and L. Zeng, *Logistic regression in rare events data*. Political analysis, 2001. **9**(2): p. 137-163.
22. Zhu, M., et al., *Class weights random forest algorithm for processing class imbalanced medical data*. IEEE Access, 2018. **6**: p. 4641-4652.
23. Han, H., W.-Y. Wang, and B.-H. Mao. *Borderline-SMOTE: a new over-sampling method in imbalanced data sets learning*. in *International conference on intelligent computing*. 2005. Springer.
24. He, H. and E.A. Garcia, *Learning from imbalanced data*. IEEE Transactions on knowledge and data engineering, 2009. **21**(9): p. 1263-1284.
25. Lemažžtre, G., F. Nogueira, and C.K. Aridas, *Imbalanced-learn: A python toolbox to tackle the curse of imbalanced datasets in machine learning*. Journal of machine learning research, 2017. **18**(17): p. 1-5.
26. Ramentol, E., et al., *Smote-rs b\*: a hybrid preprocessing approach based on oversampling and undersampling for high imbalanced data-sets using smote and rough sets theory*. Knowledge and information systems, 2012. **33**: p. 245-265.
27. Dong, Q., S. Gong, and X. Zhu, *Imbalanced deep learning by minority class incremental rectification*. IEEE transactions on pattern analysis and machine intelligence, 2018. **41**(6): p. 1367-1381.
28. Mariani, G., et al., *Bagan: Data augmentation with balancing gan*. arXiv preprint arXiv:1803.09655, 2018.
29. Cubuk, E.D., et al. *Autoaugment: Learning augmentation strategies from data*. in *Proceedings of the IEEE/CVF conference on computer vision and pattern recognition*. 2019.
30. Çelik, M. and Ö. İnik, *Detection of monkeypox among different pox diseases with different pre-trained deep learning models*. Journal of the Institute of Science and Technology. **13**(1): p. 10-21.
31. Ali, M.S., et al., *An enhanced technique of skin cancer classification using deep convolutional neural network with transfer learning models*. Machine Learning with Applications, 2021. **5**: p. 100036.
32. Chanda, D., et al., *DCENSnet: A new deep convolutional ensemble network for skin cancer classification*. Biomedical Signal Processing and Control, 2024. **89**: p. 105757.
33. Albahar, M.A., *Skin lesion classification using convolutional neural network with novel regularizer*. IEEE Access, 2019. **7**: p. 38306-38313.
34. Sanketh, R.S., et al. *Melanoma disease detection using convolutional neural networks*. in *2020 4th International Conference on Intelligent Computing and Control Systems (ICICCS)*. 2020. IEEE.
35. Daghbir, J., et al. *Melanoma skin cancer detection using deep learning and classical machine learning techniques: A hybrid approach*. in *2020 5th international conference on advanced technologies for signal and image processing (ATSIP)*. 2020. IEEE.

36. Vipin, V., et al. *Detection of melanoma using deep learning techniques: A review*. in *2021 international conference on communication, control and information sciences (ICCISc)*. 2021. IEEE.
37. Rahi, M.M.I., et al. *Detection of skin cancer using deep neural networks*. in *2019 IEEE Asia-Pacific Conference on Computer Science and Data Engineering (CSDE)*. 2019. IEEE.
38. Jojoa Acosta, M.F., et al., *Melanoma diagnosis using deep learning techniques on dermatoscopic images*. *BMC Medical Imaging*, 2021. **21**: p. 1-11.
39. Yu, L., et al., *Automated melanoma recognition in dermoscopy images via very deep residual networks*. *IEEE transactions on medical imaging*, 2016. **36**(4): p. 994-1004.
40. Majtner, T., S. Yildirim-Yayilgan, and J.Y. Hardeberg. *Combining deep learning and hand-crafted features for skin lesion classification*. in *2016 Sixth International Conference on Image Processing Theory, Tools and Applications (IPTA)*. 2016. IEEE.
41. Li, Y. and L. Shen, *Skin lesion analysis towards melanoma detection using deep learning network*. *Sensors*, 2018. **18**(2): p. 556.
42. Mahbod, A., et al., *Fusing fine-tuned deep features for skin lesion classification*. *Computerized Medical Imaging and Graphics*, 2019. **71**: p. 19-29.
43. Zhang, J., et al., *Attention residual learning for skin lesion classification*. *IEEE transactions on medical imaging*, 2019. **38**(9): p. 2092-2103.
44. Amin, J., et al., *Integrated design of deep features fusion for localization and classification of skin cancer*. *Pattern Recognition Letters*, 2020. **131**: p. 63-70.
45. Mahbod, A., et al., *Transfer learning using a multi-scale and multi-network ensemble for skin lesion classification*. *Computer methods and programs in biomedicine*, 2020. **193**: p. 105475.
46. Kwasigroch, A., M. Grochowski, and A. Mikołajczyk, *Neural architecture search for skin lesion classification*. *IEEE Access*, 2020. **8**: p. 9061-9071.
47. Hameed, N., et al., *Multi-class multi-level classification algorithm for skin lesions classification using machine learning techniques*. *Expert Systems with Applications*, 2020. **141**: p. 112961.
48. Khan, M.A., et al., *Developed Newton-Raphson based deep features selection framework for skin lesion recognition*. *Pattern Recognition Letters*, 2020. **129**: p. 293-303.
49. Mporas, I., I. Perikos, and M. Paraskevas. *Color models for skin lesion classification from dermatoscopic images*. in *Advances in Integrations of Intelligent Methods: Post-workshop volume of the 8th International Workshop CIMA 2018, Volos, Greece, November 2018 (in conjunction with IEEE ICTAI 2018)*. 2020. Springer.
50. Khan, M.A., et al., *Pixels to classes: intelligent learning framework for multiclass skin lesion localization and classification*. *Computers & Electrical Engineering*, 2021. **90**: p. 106956.
51. Pereira, P.M., et al., *Skin lesion classification enhancement using border-line features—The melanoma vs nevus problem*. *Biomedical Signal Processing and Control*, 2020. **57**: p. 101765.
52. Khan, M.A., et al., *Skin lesion segmentation and multiclass classification using deep learning features and improved moth flame optimization*. *Diagnostics*, 2021. **11**(5): p. 811.

# A study on chaotic dynamics of deep artificial neural network activated by biological neuron model

Erdem Erkan<sup>1\*</sup> 

<sup>1</sup> Computer Engineering Department, Bartın University, 74110 Bartın, Türkiye

\* [eerkan@bartin.edu.tr](mailto:eerkan@bartin.edu.tr)

\* Orcid No: 0000-0002-2386-1271

Received: 25 August 2024

Accepted: 11 November 2024

DOI: 10.18466/cbayarfbe.1538362

## Abstract

This paper analyzes the effects of the chaotic signals used by the brain to perform some cognitive functions on the Spiking Neural Network (SNN), defined as the third-generation Artificial Neural Network (ANN) that best represents the biological neuron. In the first phase of the paper, neural networks with different layers are designed to perform classifications like ANN and SNN. Classification performances of these deep networks using the Rectified Linear Unit activation function in ANN mode and the Izhikevich Neuron model in SNN mode are presented comparatively. It is observed that SNNs perform at least as well as ANNs under normal conditions. In the second stage of the study, the classification performances of these deep networks in the SNN mode were analyzed in different chaotic environments, and the findings were reported. In light of the findings, it is seen that SNNs can exhibit a classification success similar to ANNs and maintain this success rate up to a certain chaotic current intensity. Moreover, some levels of chaotic current contribute to the network's classification performance. This is the first study to investigate the chaotic environment behavior of SNNs.

**Keywords:** SNN, Izhikevich neuron, Chaotic environment, EEG-Image Classification

## 1. Introduction

The Artificial Neural Network (ANN) is created by placing units, also called artificial neurons, which are the mathematical representations of the biological neuron in one or more layers. These units use non-linear activation functions such as hyperbolic tangent, sigmoid, and Rectified Linear Unit (ReLU) that make it possible to learn by iteratively changing the weight of each neuron in the network. Since the ANN emerged with Rosenblatt's Perceptron in 1958, ANN has been used in many studies [1]. Although it lost its popularity from time to time, ANNs regained their popularity with two studies conducted in 2009 and 2012. The first is a back propagation ANN study developed for the speech recognition problem [2] and the other is an image classification study AlexNet [3] for estimating the dominant object in the given image. Apart from these, ANNs have been used in pattern recognition, two or multi-class seizure classification, and human-robot interaction systems. It has been reported that the classification performance of ANNs is better than other classification methods in many studies [4]

Although ANNs developed with inspiration from the brain, they do not have an information transmission mechanism that has the firing pattern of a real biological neuron. This mechanism is defined by the Spiking Neural Network (SNN), which is considered to be the third generation ANN and is thought to revolutionize the field in the future [5] SNNs use neuron models expressed with differential equations such as Integrated and Fire [6], Hudking-Huxley [7], Izhikevich [8], FitzHugh-Nagumo [9], Morris-Lecar Neurons [10]. These models frequently used in the field of computational neuroscience are the mathematical equations that best express the biological neuron today. In recent years, more realistic, energy-efficient, and physically applicable machine learning studies have been carried out by the use of these models with machine learning. For example, [11] has presented a state-of-the-art review of the development of spiking neurons and SNNs, and it has provided insight into their evolution through their article [12], introduced a new class of SNN, dynamic eSNN, that utilizes both rank-order learning and dynamic synapses to learn spatial and spectro-temporal data in a fast, on-line mode with their study. Although most of the SNN-based studies are based on image classification [13], there are also studies



on electroencephalography (EEG) classification. In a study, it was compared spiking Neurons with other traditional classifiers commonly used in the recognition of motor imagery tasks [14]. [15] presented brain-inspired SNN architecture to explore the modeling of neural networks underlying the tinnitus symptom by using EEG. In another study, [16] proposed a novel method of using the SNNs and the EEG processing techniques to recognize emotion states. [17] introduced a biologically plausible speech recognition approach by using an unsupervised self-organizing map (SOM) for feature representation and event-driven SNN for spatiotemporal pattern classification. SNNs were also used for acoustic modeling and evaluated their performance in a few vocabulary recognition tasks [18].

In ANNs, the number of layers of the network expresses the depth of the network. For example, AlexNet is known as a deep network consisting of 8 layers and millions of parameters. Equipped with trainable parameters in multiple layers, the deep learning architecture has shown outstanding performance in ANN [19]. The same architecture can be adaptable to SNN. Realizing a deep SNN comparable to traditional Deep Neural Networks (DNN) is a challenge due to hardware constraints. Therefore, the classification performance of SNNs is not as good as the classification performance of DNNs [20].

On the other hand, chaotic regimes induced by the environmental influences in the firing activity of neurons have recently attracted the attention of researchers [21]. In a study, it has been shown that sleep is governed by stable self-sustaining oscillations whereas the silent wake state and active wakefulness state are governed by both disordered oscillations and chaotic dynamics [22]. In [23], it has been noted that the Onchidium Pacemaker neuron exhibits chaotic spiking behavior when exposed to certain periodic signals. With the emergence of chaotic firings in neurons, studies have been conducted in computational neuroscience examining the dynamics of neurons responding to stimuli in a chaotic environment [24]. It has been shown that some cognitive functions in the brain can be performed in the presence of optimal chaotic current. For instance, [25] showed that a bistable system can be steadily designed to certain logic gate operations at the ideal chaotic signal intensity in computational neuroscience. As far as it is known, the chaotic environment behaviors of deep SNNs have not been examined yet. With this motivation, in the first phase of this study, which is carried out in two stages, neural networks with different layers that can classify in ANN and SNN modes are introduced to classify images and brain signals separately. The classification results of these networks are analyzed comparatively in both modes. In the second stage of the study, the classification performances of designed networks activated by Izhikevich neurons in SNN mode were

tested in chaotic environments with different chaotic current intensities. The results are compared in both modes of the networks with the same layer structure and the number of neurons. According to the author's best knowledge, this is the first study that investigated the classification success of brain and image signals by using deep SNNs in a chaotic environment.

The remainder of this paper is organized as follows: Section 2 introduces the mathematical structure of the feature extraction method, neuron, and network models. Section 3 includes the comparison of the ANN and SNN modes of the neural networks are designed and gives the classification results of deep biologically capable SNNs in a chaotic environment. Conclusions are drawn in Section 4.

## 2. Materials and Methods

### 2.1. Datasets

The methods proposed in this study are tested on two different datasets containing EEG and image data.

#### 2.1.1. ECoG Dataset

The electrocorticography (ECoG) dataset consisting of brain signals was recorded with 64 channels in BCI competition III. During the recording phase, the subject made imaginary movements with his left little finger or tongue. ECoG signals were acquired with electrodes on the contralateral (right) motor cortex, with a 3-second time series and 1000 Hz sampling rate, and amplified to microvolt levels. Every trial consisted of either an imagined tongue or finger movement. The training dataset contains 139 tongue and 139 finger class labeled data [26]. The performances of proposed neural networks were evaluated on the ECoG dataset for motor imaginary tasks.

#### 2.1.2. MNIST Dataset

It is also tested the performance of the neural networks in a digit recognition task. For this reason, data samples were used from the MNIST database, which contains centered, grayscale, 28x28 pixel images of handwritten numbers 0-9 [27]. The training dataset contains 10000 samples, and the test dataset contains 60000 samples. It trained the system with 400 samples of the MNIST dataset in 200 iterations for the 4-digit classification task. MNIST is a numeric character database popularly used for machine learning research. The classes used in the MNIST dataset are given in Figure 1 as a representation.



Figure 1. MNIST dataset sample for 4 class

## 2.2. Continuous Wavelet Transform

Feature extraction of the ECoG dataset is based on Continuous Wavelet Transform (CWT), which is a technique that allows to model variations of an entire signal, within the scale-time domain [28]. Continuous wavelet transform (CWT) is often used in the analysis of time-frequency information for engineering and real-life problems. It is preferred in signal analysis because it preserves time-frequency information. A basis function, named the mother wavelet ( $\psi(t)$ ) is formulated in Equation 2.1. The  $s$  and  $n$  represent the scale and position of the signal respectively. Using scaled and dilated forms of the  $\psi(t)$ , the Continuous Wavelet Transform (CWT) decomposes a finite-energy signal,  $x(t)$ . The CWT coefficients obtained by decomposing  $x(t)$ , are given in Equation 2.2.  $\psi_{s,n}^*(t)$  denotes the complex conjugate of the mother wavelet function. The  $x(t)$  is a finite-energy function, that is,  $x(t) \in L^2(\mathbb{R})$ . Low-frequency information is obtained at larger scales while high-frequency information is obtained at smaller scales [28].

$$\psi_{s,n}(t) = s^{-1/2} \psi\left(\frac{t-n}{s}\right) \quad (2.1)$$

$$CWT_x(s, n; \psi) = \int_{-\infty}^{+\infty} x(t) \psi_{s,n}^*(t) dt \quad (2.2)$$

CWT is used for feature extraction for the ECoG dataset. EEG signals are converted to image format with this method. 2-D time-frequency images called a scalogram, represent the square of CWT. The time-frequency images are used as input for the proposed model.

## 2.3. Neuron Model (Izhikevich)

The change of the cell membrane potential of the Izhikevich neuron with time is given by Equation 2.3 [8].

$$\frac{dV}{dt} = \frac{k(V - V_r)(V - V_t) - U + pI + \epsilon I_{chaos}}{C} \quad (2.3)$$

$$\frac{dU}{dt} = a(b(V - V_r) - U)$$

$$\text{If } V \geq V_{peak}, \text{ then } V \leftarrow c, U \leftarrow U + d \quad (2.4)$$

The  $V$ ,  $C = 100 \mu\text{F}/\text{cm}^2$ ,  $V_t$ ,  $V_r$ ,  $I$ ,  $U$  express the membrane potential, the membrane capacitance, the instantaneous threshold potential, the resting membrane potential, the input current, and the recovery current respectively. The model's  $a$ ,  $b$ ,  $c$ , and  $d$  parameters in

Equation 2.4 are also expressed as recovery position constant, resistance for input, voltage reset parameter, and the downstroke current during the spike. The  $I_{chaos} = \epsilon x$  represents chaotic current. The  $\epsilon$  is the level of chaotic activity and  $x$  is a chaotic signal source [29]:

$$\frac{dx}{dt} = \sigma(y - x), \frac{dy}{dt} = px - y, \frac{dz}{dt} = xz - \lambda z \quad (2.5)$$

The time series of chaotic signal  $x$  generated by the Lorenz system and  $x - z$  phase plane diagram of the chaotic Lorenz system are given in Figure 2 a and b respectively. It can be seen in Figure 2 that the  $x$  signal is in a chaotic oscillation state.

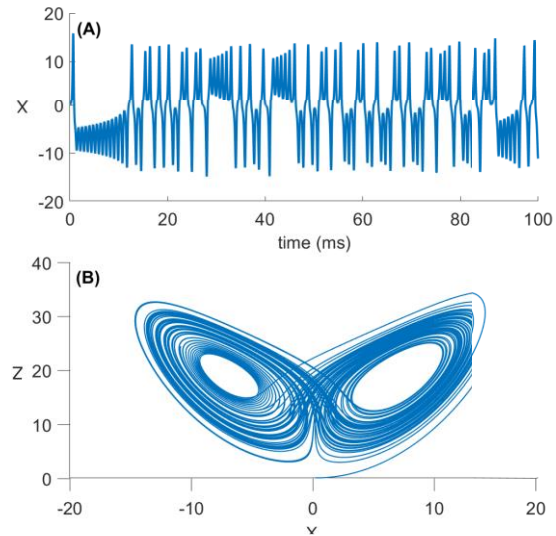
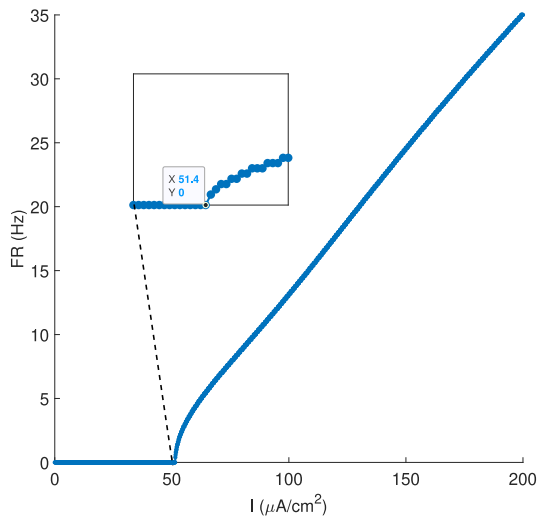
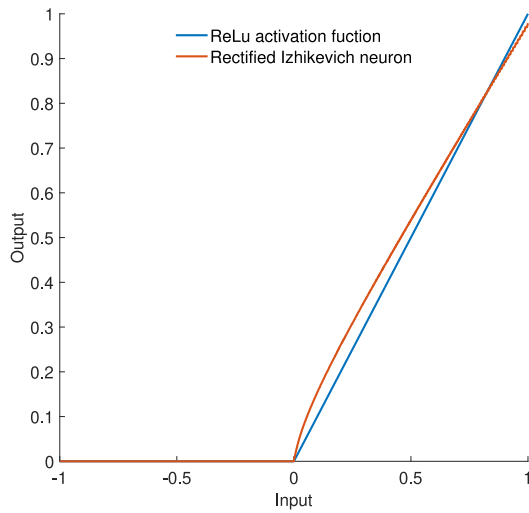


Figure 2. (A) Time series of chaotic signal  $x$ ; (B) Phase diagram of chaotic Lorenz system.

The Izhikevich neuron model exhibits different firing patterns at different parameter values. In this study, Class 1 excitable type Izhikevich neuron is used. The firing rates (FR) produced by the neuron in response to different input currents are given in Figure 3. In the inset of Figure 3, it is seen that the neuron can produce spikes when currents above approximately  $51.4 \mu\text{A}$  are applied. To make the model more similar to the ReLu, an external current ( $51.4 \mu\text{A}$ ) is applied to the model. Additionally, the model is moved to a more appropriate input output space by multiplying the input current  $I$  and the firing rate FR by the coefficients  $p$  and  $q$ , respectively. A similar modulation process has also been shown in the brain in an experimental study with mice [30].



**Figure 3.** Firing rates of the model



**Figure 4.** The output of Rectified Izhikevich neuron.

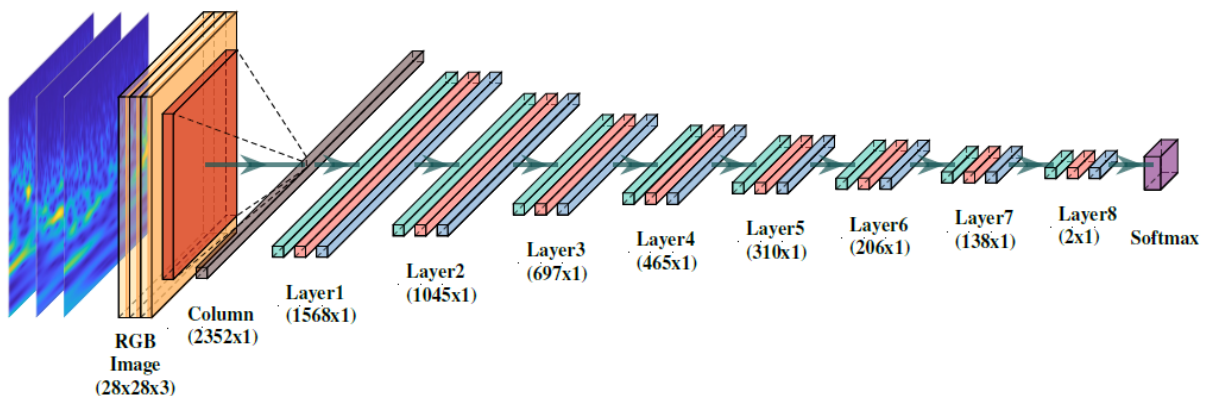


**Figure 5.** The proposed deep neural network model with 8 layers.

In the study, this model revised with  $p$  and  $q$  coefficients is called the corrected Izhikevich model. Figure 4 is shown the normalized input and output of the corrected Izhikevich neuron by choosing the  $p$  and  $q$  values as  $10^4$  and  $10^{-3}$ , respectively. The FR of the neuron is obtained by calculating the number of spikes produced by the neuron membrane potential in response to the  $I$  for 1000 ms using the Euler method.

#### 2.4. Deep Neural Networks

Figure 5 and Figure 6 show the structure of 8 and 4-layer deep neural networks which exhibit ANN or SNN behavior according to the activation mechanism. The neurons that make up the network are activated by ReLu or rectified Izhikevich neurons depending on the mode of the network. In SNN mode, the rectified Izhikevich neuron produces FR as output in response to input, the rectified Izhikevich neuron produces FR as output in response to input  $I$ . The data given as a column matrix at the input of the network express the current  $I$ . At each layer of the network, the current  $I$  from the previous layer is multiplied by the weight  $w$  of the network represented by green prisms, normalized by pink prisms, and transformed into a nonlinear form by the activation function represented by blue prisms. The classification result is gained at the softmax output, which is the last layer of the network.

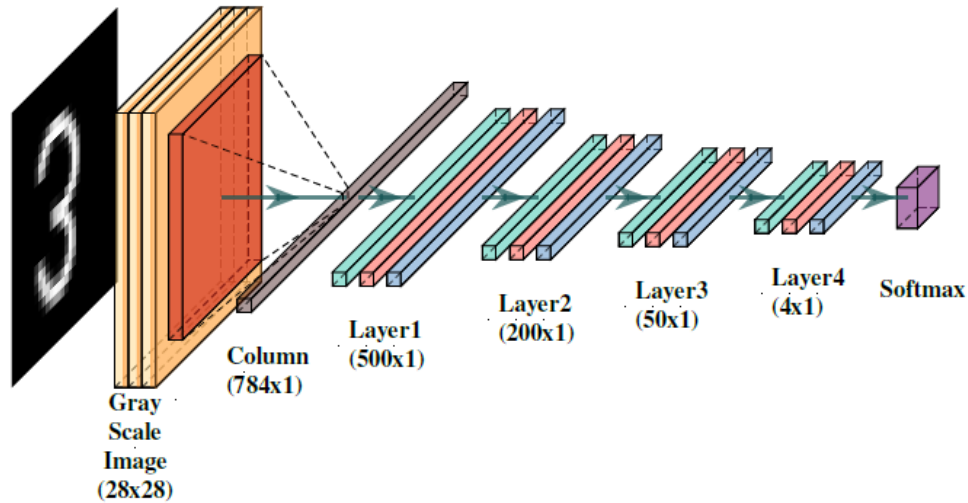


**Figure 6.** The proposed deep neural network model with 4 layers..

### 3. Experimental Results

The ECoG and MNIST datasets are classified by using proposed neural networks that can classify in both modes. For the ECoG dataset, the image feature vectors of  $28 \times 28 \times 3$  are created from the Wavelet scalogram of each trial for the three channels (channel numbers 12, 38, and 29) determined in a previous study [31]. The weights represented by  $w$  of the network layers are initially assigned randomly and updated according to the error rate after each iteration. The learning rate  $\alpha$  is chosen as  $1 \times 10^{-6}$  and  $5 \times 10^{-4}$  for ECoG and MNIST datasets, respectively. Experiments are carried out with different learning rates in both types of networks and experiments are continued with the learning rates that achieved optimum classification success. The determined learning rates can be considered as constraints for the study. Experiments are performed in MATLAB 2021b.

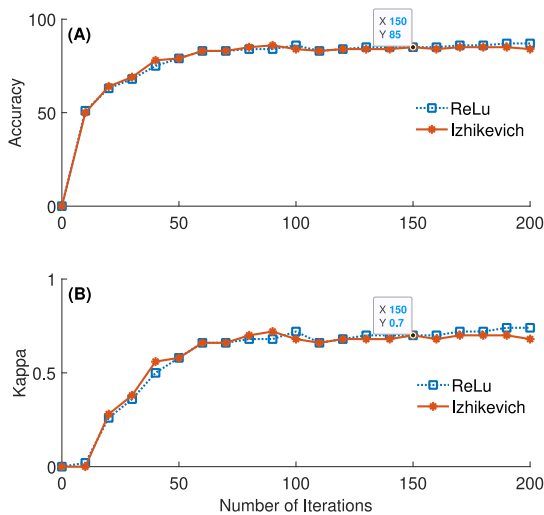


**Figure 7.** The classification results of the ECoG dataset, (A) accuracies for ANN and SNN modes, (B) Kappa values for ANN and SNN modes ( $\alpha = 1 \times 10^{-6}$ ).

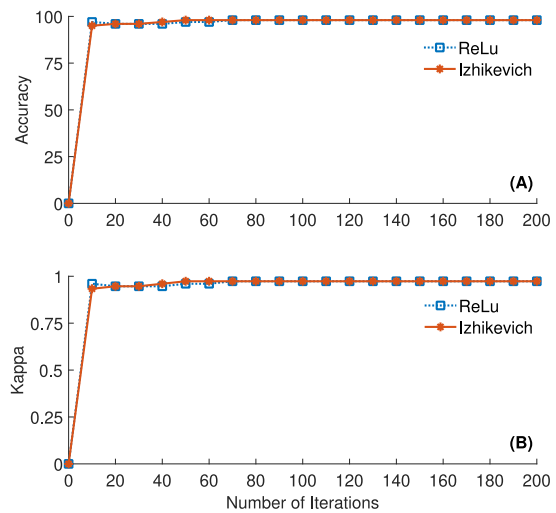


**Figure 8.** The classification results of the MNIST dataset, (A) accuracies for ANN and SNN modes, (B) Kappa values for ANN and SNN modes. ( $\alpha = 5 \times 10^{-4}$ )

The classification results are given in Figure 7 A and B, for the ECoG dataset. Figure 7A is shown that the network exhibits similar classification results in SNN and ANN mode. These classification results are supported by Kappa values of 0.70 and above that represent significant classification harmony given in Figure 7 B. Similarly, the MNIST dataset with 4 classes is classified by the ANN mode of the deep neural network given in Figure 6. The high classification result ( 98%) supported by Kappa value (0.97) is obtained and presented in Figure 8. Classification accuracies and Kappa values for 200 iterations are shown in Figure 8 A and B.

In the first phase of the study, it is seen that 8 and 4-layer deep neural networks are exhibited similar classification results for both modes. One of these parameters is the chaotic current, which is thought to be used in the execution of some cognitive functions in the

brain [32]. In line with this idea, in the second stage of the study, 4 different intensities of chaos currents were applied to the rectified Izhikevich neurons in these neural networks to analyze the classification results of the deep SNNs with biological capability in a chaotic environment. The chaotic current applied to the Rectified Izhikevich neuron is demonstrated in Figure 9.

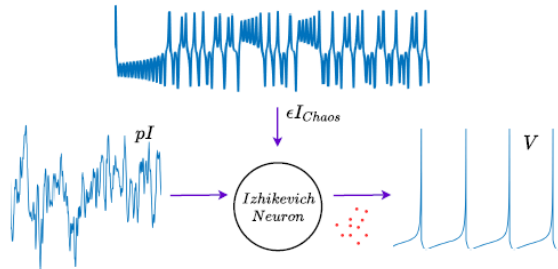


**Figure 9.** The demonstration of chaotic current on rectified Izhikevich neuron.

This section, it is aimed to investigate the effects of the chaotic environment on the classification performance of the designed SNNs. The average FRs of the rectified Izhikevich neuron as a result of chaotic currents of varying intensity acting on it are shown in Figure 10 in the range  $[-1, 1]$ . As seen in Figure 10, the consistency of the firing pattern decreases inversely with the chaotic current intensity applied to the neuron. While this consistency is highest with chaos level  $\epsilon = 0.001$ , it is lowest with chaos level  $\epsilon = 0.1$  which represents the highest chaotic current intensity.

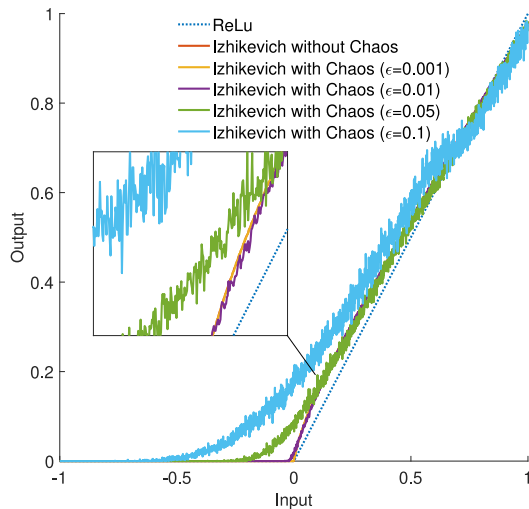


**Figure 10.** Firing patterns of rectified Izhikevich neuron exposed to different chaotic signal levels.

The classification accuracies, Kappa values, and their average classification accuracies of the SNN consisting of Izhikevich neurons exposed to these different levels of chaotic currents are given in detail in Figure 11, Figure 12, and Table 1, respectively for the ECoG dataset. When both figures and Table 1 are examined, it

is seen that the SNNs perform almost the same or even more successful classification compared to an ANN with the same structure activated with the ReLu function, with the selected classification features. More importantly, it has been observed that this classification result is maintained and slightly increased at the optimal chaotic environment level ( $\epsilon = 0.01$ ). It is seen that the classification performance decreases considerably at chaotic current intensities above the optimal level.

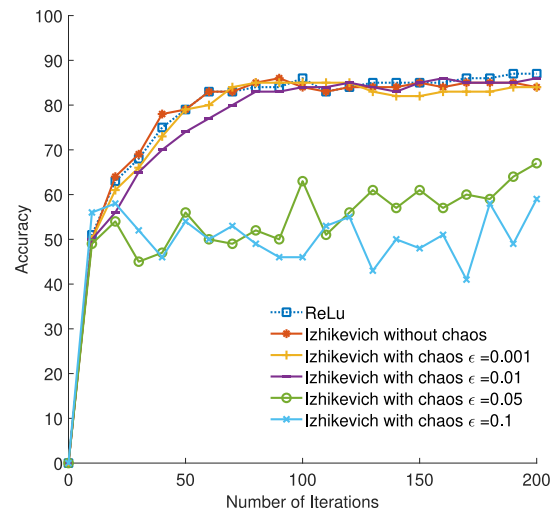


**Figure 11.** The classification accuracies of the neuron model with ECoG dataset in different level chaos mediums. ( $\alpha = 1 \times 10^{-6}$ )

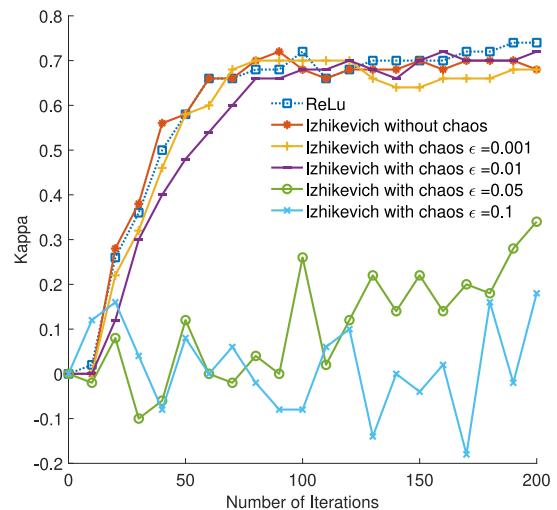


**Figure 12.** The classification Kappas of the neuron model with ECoG dataset in different level chaos mediums. ( $\alpha = 1 \times 10^{-6}$ )



**Table 1.** Comparison of overall accuracy for ECoG dataset in different chaotic mediums.

Neuron Type*	Mean Accuracy%	Mean Kappa
ReLu	86.00	0.72
Izhikevich without chaos	84.67	0.69
Izhikevich with chaos $\epsilon = 0.001$	83.17	0.66
Izhikevich with chaos $\epsilon = 0.01$	85.33	0.71
Izhikevich with chaos $\epsilon = 0.05$	61.33	0.23
Izhikevich with chaos $\epsilon = 0.1$	51.00	0.02

Similarly, the classification accuracies, Kappa values, and their average classification accuracies of the SNN consisting of Izhikevich neurons exposed to different levels of chaotic currents are given in detail in Figure 13, Figure 14, and Table 2, respectively for the MNIST dataset. When both figures and Table 2 are examined, results that are in line with the results achieved from the ECoG dataset are obtained. The 4-layer deep neural network given in Figure 6 produced successful results like ANN mode, up to a certain chaotic signal level ( $\epsilon = 0.01$ ) in SNN mode but it could not maintain the classification performance at chaotic levels above  $\epsilon = 0.05$ . These results are confirmed by the Kappa values given in Figure 14 and the averages given in Table 2.

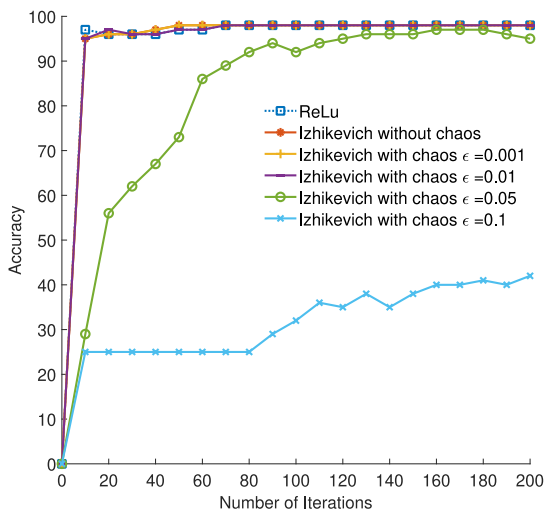


**Figure 13.** The classification accuracies of the neuron model with MNIST dataset in different level chaos mediums. ( $\alpha = 5 \times 10^{-4}$ )

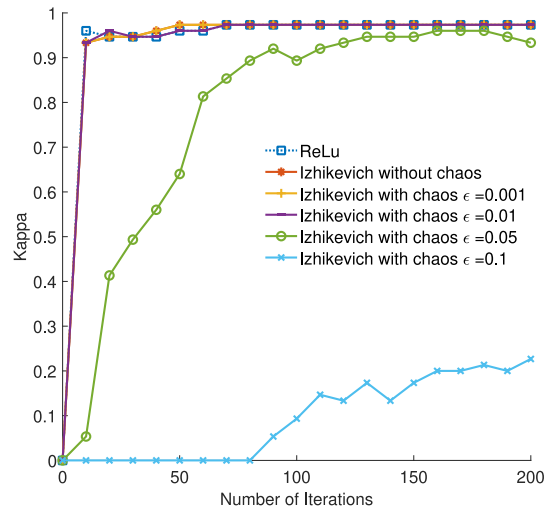


**Figure 14.** The classification Kappas of the neuron model with MNIST dataset in different level chaos mediums. ( $\alpha = 5 \times 10^{-4}$ )

**Table 2.** Comparison of overall accuracy for MNIST dataset in different chaotic mediums

Neuron Type	Mean Accuracy%	Mean Kappa
ReLu	98.00	0.97
Izhikevich without chaos	98.00	0.97
Izhikevich with chaos $\epsilon = 0.001$	98.00	0.97
Izhikevich with chaos $\epsilon = 0.01$	98.00	0.97
Izhikevich with chaos $\epsilon = 0.05$	96.33	0.95
Izhikevich with chaos $\epsilon = 0.1$	40.17	0.20

In Figure 14, classification accuracies of 8 and 4-layer SNNs that classify ECoG and MNIST datasets are given according to the chaotic current levels applied to the neurons in the network. When Figure 15 is examined, it is seen that at a certain chaotic current level ( $\epsilon = 0.01$ ), the classification performance increases slightly, at least the classification performance is preserved. The chaotic current effect is seen more clearly in the classification results of the ECoG dataset. The classification success of the SNN is lower in regions outside the detected chaotic current level ( $\epsilon = 0.01$ ).

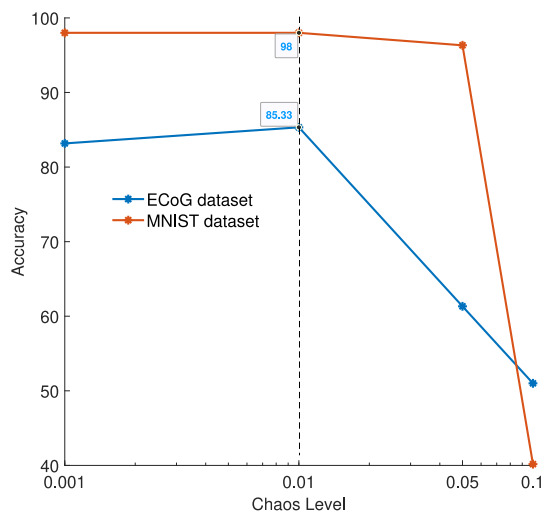


**Figure 15.** Classification accuracies according to chaotic levels.

#### 4. Conclusion

In the first phase of the paper, neural networks with different layers are designed to perform classifications like ANN and SNN. These neural networks are successfully tested on motor imagery and image datasets. In the first phase of the study, a classification success similar to that of the ANN mode is observed in the SNN mode. In the second stage of the study, starting from the idea that some cognitive brain functions are realized via irregular chaotic neuronal firings [32], the classification performance of the deep SNNs consisted rectified Izhikevich neurons is investigated in different chaotic environments. To the best of our knowledge, the present study is the first to analyze the classification performance of a deep SNN in a chaotic medium. In light of the results obtained, it is seen that the chaotic current applied to the neurons in the network significantly reduces the information processing capability of the network, and this situation is inversely proportional to the intensity of the applied chaotic current. It is noticed that deep SNNs can tolerate the negative effects of chaotic current up to a certain level and even increase the classification performance at some chaotic current levels ( $\epsilon = 0.01$ ). The highest classification accuracies are achieved at this chaotic signal level in both of the data sets used in the study. However, the information processing ability of the SNNs exhibits rapid declines above this value. It is also predicted that a reasonable level of chaotic current will contribute to preventing the overfitting of neural networks. Since the SNNs can express the biological neuron more realistically, these designed SNNs offer the opportunity to investigate the effect of different parameters such as chaotic signals on the neuron. In future studies, it is aimed to investigate similar effects with different data sets on complex neuron models such as Hodgkin Huxley, which better represent the biological neuron.

#### Author's Contributions

**Erdem Erkan:** Drafted and wrote the manuscript, performed the experiment and result analysis.

#### Ethics

There are no ethical issues after the publication of this manuscript.

#### References

- [1]. Rosenblatt, F., 1958. The perceptron: a probabilistic model for information storage and organization in the brain. *Psychological review* 65, 386.
- [2]. Abdel-rahman M., George D., Geoffrey H., et al. 2009 Deep belief networks for phone recognition. *In Nips workshop on deep learning for speech recognition and related applications*, volume 1, page 39.
- [3]. Krizhevsky A., Sutskever I, and Hinton G.X. 2012 Imagenet classification with deep convolutional neural networks. *Curran Associates, Inc.*, volume 25.
- [4]. M. Alfaro-Ponce, A. Argüelles, and I. Chairez. 2016 Pattern recognition for electroencephalographic signals based on continuous neural networks. *Neural Networks*, 79(11):88–96.
- [5]. Maass W. 1997 Networks of spiking neurons: the third generation of neural network models. *Neural networks*, 10(9):1659–1671.
- [6]. Abbott L.F. 1999 Lapicque's introduction of the integrate-and-fire model neuron (1907). *Brain research bulletin*, 50(5-6):303–304.
- [7]. Hodgkin A.L. and Huxley A.F. 1952 A quantitative description of membrane current and its application to conduction and excitation in nerve. *The Journal of physiology*, 117(4):500.
- [8]. Izhikevich. E.M. 2004 Which model to use for cortical spiking neurons? *IEEE Transactions on Neural Networks*, 15(5):1063–1070.
- [9]. FitzHugh R. 1961 Impulses and physiological states in theoretical models of nerve membrane. *Biophysical journal*, 1(6):445–466.
- [10]. Koch C. and Segev I. 1998 Methods in neuronal modeling: from ions to networks. *MIT press*.
- [11]. Ghosh-Dastidar S. and Adeli H. 2009 Spiking neural networks. *International journal of neural systems*, 19(04):295–308.
- [12]. Kasabov N., Dhoble K., Nuntalid N., and Indiveri G. 2013 Dynamic evolving spiking neural networks for on-line spatio-and spectro-temporal pattern recognition. *Neural Networks*, 41:188–201.
- [13]. Dermot Kerr, Sonya Coleman, and Thomas Martin McGinnity. 2018 Biologically inspired intensity and depth image edge extraction. *IEEE Transactions on Neural Networks and Learning Systems*, 29(11):5356–5365
- [14]. Carlos D. Virgilio G., Juan H. Sossa A., Javier M. Antelis, and Luis E. Falcón. 2020 Spiking neural networks applied to the classification of motor tasks in eeg signals. *Neural networks*, 122:130–143.
- [15]. Sanders P.J., Doborjeh Z.G., Doborjeh M.G., Kasabov N.K., and Searchfield G.D. 2021 Prediction of acoustic residual inhibition of tinnitus using a brain-inspired spiking neural network model. *Brain Sciences*, 11(1):52.



- [16]. Luo Y., Fu Q., Xie J., Qin J., Wu G., Liu J., Jiang F., Cao Y., and Ding X. 2020 Eeg-based emotion classification using spiking neural networks. *IEEE Access*, 8:46007–46016.
- [17]. Wu J., Chua Y., and Li H. A biologically plausible speech recognition framework based on spiking neural networks. International Joint Conference on Neural Networks (IJCNN), 2018, pages 1–8. IEEE.
- [18]. Wu J., Yılmaz E., Zhang M., Li H., and Tan. C. K 2020 Deep spiking neural networks for large vocabulary automatic speech recognition. *Frontiers in neuroscience*, 14:199.
- [19]. Schmidhuber J. 2015 Deep learning in neural networks: An overview. *Neural networks*, 61:85–117.
- [20]. Tavanaei A., Ghodrati M., Kheradpisheh S.R., Masquelier, and Anthony T. 2019 Deep learning in spiking neural networks. *Neural networks*, 111:47–63.
- [21]. Stiefel K.M., Englitz B., and Sejnowski T.J. 2013 Origin of intrinsic irregular firing in cortical interneurons. *Proceedings of the National Academy of Sciences*, 110(19):7886–7891.
- [22]. Rasmussen R., Jensen M.H., and Heltberg M.L. 2017 Chaotic dynamics mediate brain state transitions, driven by changes in extracellular ion concentrations. *Cell systems*, 5(6):591–603.
- [23]. Hayashi H., Ishizuka S., and Hirakawa K. 1985 Chaotic response of the pacemaker neuron. *Journal of the Physical Society of Japan*, 54(6):2337–2346.
- [24]. Yao Y., Ma J., Gui R, and Cheng G. 2021 Enhanced logical chaotic resonance. *Chaos: An Interdisciplinary Journal of Nonlinear Science*, 31(2):023103.
- [25]. Yao Y. and Ma J. 2020 Logical chaotic resonance in a bistable system. *International Journal of Bifurcation and Chaos*, 30(13):2050196.
- [26]. Lal T., Hinterberger G., Widman T., Schrder G., Hill J., Rosenstiel W., Elger C., Schlkopf B., and Birbaumer B. 2005 Methods Towards Invasive Human Brain Computer Interfaces. *The MIT Press*,.
- [27]. LeCun Y., Bottou L., Bengio Y., and Haffner P. Gradient-based learning applied to document recognition. *Proceedings of the IEEE*, 1998 86(11):2278–2324.
- [28]. Peng Z., Chu F., and He Y. 2002 Vibration signal analysis and feature extraction based on reassigned wavelet scalogram. *Journal of Sound and Vibration*, 253(5):1087–1100.
- [29]. Ma J., Ying H., and Pu Z. 2005 An anti-control scheme for spiral under lorenz chaotic signals. *Chinese Physics Letters*, 22(5):1065–1068.
- [30]. Beppu K., Kubo N., and Matsui K. 2021 Glial amplification of synaptic signals. *The Journal of Physiology*, 599(7):2085–2102.
- [31]. Erkan E. and Kurnaz I. 2017 A study on the effect of psychophysiological signal features on classification methods. *Measurement*, 101:45.-52.
- [32]. Hansel D. and Mato G. 2013 Short-term plasticity explains irregular persistent activity in working memory tasks. *Journal of Neuroscience*, 33(1):133–149.

# Synthesis and Characterization of Schiff Base Compounds Containing Mono and Disulfonic Groups

İsmet Kaya<sup>1\*</sup> , Feyza Kolcu<sup>1,2</sup> , Sude Süel<sup>1</sup> 

<sup>1</sup> Çanakkale Onsekiz Mart University, Faculty of Science, Department of Chemistry, Polymer Synthesis and Analysis Laboratory, Çanakkale, Türkiye

<sup>2</sup> Çanakkale Onsekiz Mart University, Lapseki Vocational School, Department of Chemistry and Chemical Processing Technologies, 17800, Çanakkale, Türkiye

\* [ikaya@comu.edu.tr](mailto:ikaya@comu.edu.tr)

\* Orcid No: 0000-0002-9813-2962

Received: 8 August 2024

Accepted: 11 November 2024

DOI: 10.18466/cbayarfbe.1529884

## Abstract

Aromatic mono- or diamine compounds containing sulfonic groups are extensively utilized in the production of textiles, dyes, and polymers. Schiff base compounds are synthesized through the condensation reactions of these types of compounds with aromatic aldehydes or ketones. Due to their multifunctional nature, these Schiff base compounds serve as precursors in the synthesis of poly(ester)s, poly(ether)s, poly(urethane)s, and poly(azomethine)s. The Schiff base compounds were 2,5-bis((E)-(2-hydroxybenzylidene)amino)benzene sulfonic acid (SCH1) and 4,4'-bis((E)-(2-hydroxybenzylidene)amino)-[1,1'-biphenyl]-2,2'-disulfonic acid (SCH2). The yields of SCH1 and SCH2 were calculated to be 85% and 80%, respectively. Structural confirmation was achieved using FT-IR, UV-Vis, <sup>1</sup>H NMR and <sup>13</sup>C NMR measurements. Further characterization through fluorescence spectroscopy (PL), thermogravimetric analysis (TGA) and cyclic voltammetry (CV) revealed high thermal stability of the compounds, attributed to the phenyl groups in their structures. TGA measurements indicated the initial decomposition temperatures for SCH1 and SCH2 at 298°C and 347 °C, respectively, with the residual masses of 34.64% and 41.24% at 1000 °C.

**Keywords:** Schiff base, Sulfo Group, Thermal properties, Optical properties, LOI

## 1. Introduction

Schiff base compounds were first synthesized by German chemist Hugo Schiff in 1864. Imines have been extensively studied for over a century due to their unique reactivity and physical properties. Monomers containing imine (-C=N-) bonds, which result from the condensation reaction between an active carbonyl group and a primary amine, are known as Schiff bases. Azomethines, with the general formula of RCH=NR, are produced through the condensation reactions between primary aliphatic or aromatic amines (R-NH<sub>2</sub>) and aldehydes or ketones [1]. The synthesis of Schiff base monomers involves two main steps: first, an addition reaction occurs, resulting in the formation of an unstable intermediate compound called 'carbonyl amine' through the condensation of a carbonyl group with primary amines. In the second step, a dehydration reaction transforms the unstable carbonyl

amine into the Schiff base [2]. Additionally, compounds containing sulfo groups and imine bonds are employed in textile dyeing and the production of conductive textile materials [3].

Imine compounds are extensively utilized in various fields, including biological systems, chemical catalysis reactions, medicine, pharmacy, chemical analysis, and technology. Due to their high chelating capacity, these compounds are also used for the removal of heavy metal ions in wastewater. The presence of a phenyl ring in their main chain contributes to their high thermal stability.

In this study, Schiff base monomer compounds incorporating mono and di sulfo groups were synthesized. The structural characterization of the compounds was conducted using FT-IR, UV-Vis, <sup>1</sup>H NMR and <sup>13</sup>C NMR spectroscopy. The electrochemical, optical, and thermal properties of SCH1 and SCH2 were

investigated using CV, UV-Vis, and TG-DTA measurements, respectively. Analysis of the optical and electrochemical band gap values were calculated from the UV-Vis and CV measurements, respectively.

## 2. Materials and Methods

### 2.1. Materials

2-Hydroxybenzaldehyde, 2,5-diamino benzene sulfonic acid, 4,4'-diamino-2,2'-biphenyl sulfonic acid, N, N'-dimethylformamide (DMF), dimethylsulfoxide (DMSO), ethanol (Et-OH), tetrahydrofuran, methanol, hexane, acetonitrile, toluene, dichloromethane, chloroform, were procured from Merck Chemical Co. (Germany). Tetrabutylammoniumhexafluorophosphate ( $\text{Bu}_4\text{AF}_6\text{P}$ , 98%) was sourced from Sigma-Aldrich Chem. Co. (Germany). All reagents were used without further purification.

### 2.2. Synthesis of Schiff bases

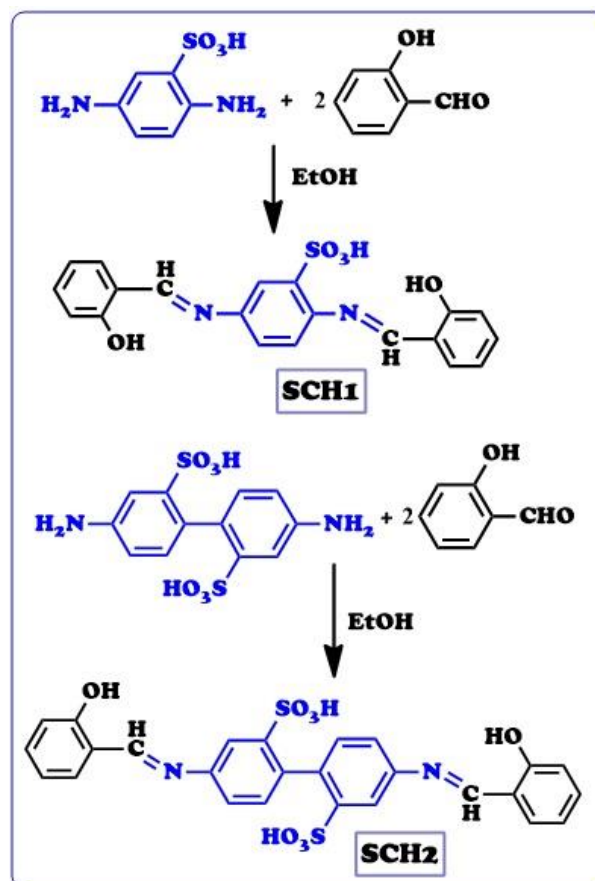
2,5-bis((E)-(2-hydroxybenzylidene)amino)benzene sulfonic acid (SCH1) was synthesized using 2-hydroxybenzaldehyde (2.0 mmol) dissolved in 5 mL of ethanol, followed by the addition of 2,5-diamino benzene sulfonic acid (1.0 mmol) to this solution. The mixture was refluxed at 70 °C for 5 h.

4,4'-bis((E)-(2-hydroxybenzylidene)amino)-[1,1'-biphenyl]-2,2'-disulfonic acid (SCH2) was synthesized using 2-hydroxybenzaldehyde (2.0 mmol) dissolved in ethanol (5 mL), and then 4,4'-diamino-2,2'-biphenyl sulfonic acid (1.0 mmol) was added to this solution. The mixture was refluxed at 70 °C for 5 h [4]. The products (SCH1 and SCH2) were purified via crystallization in ethanol. The yields of SCH1 and SCH2 were calculated to be 85% and 80%, respectively. The synthesis pathways of SCH1 and SCH2 are given in **Scheme 1**.

### 2.3. Characterization Methods

The infrared spectra of SCH1 and SCH2 compounds were recorded using a PerkinElmer Frontier FT-IR-FIR Spectrometer. Functional groups analysis of the compounds was conducted through FT-IR spectroscopy, employing a PIKE technologies GladiATR sampling accessory ( $4000\text{-}400\text{ cm}^{-1}$ ).  $^1\text{H}$  and  $^{13}\text{C}$  NMR spectra were obtained using an Agilent 600 MHz and 150 MHz Premium COMPACT NMR Magnet, with  $\text{DMSO-}d_6$  as the solvent and TMS as the internal standard at room temperature. Analytikjena Specord 210 spectrometer was utilized to assess the optical properties of SCH1 and SCH2 in the range of 250-700 nm, using DMSO as the solvent. PerkinElmer Diamond Thermal Analyzer was employed to perform TG-DTA analyses from 20 °C to 1000 °C at a heating rate of 10 °C  $\text{min}^{-1}$  under  $\text{N}_2$  atmosphere (200 mL  $\text{min}^{-1}$ ). CHI 660C Electrochemical Analyzer was employed to process cyclic voltammetry analyses at a scan rate of 25 mV  $\text{s}^{-1}$ , to investigate the

electrochemical features of SCH1 and SCH2. The electrochemical study utilized, a cell comprising a reference electrode (silver wire), a working electrode (glassy carbon electrode; GCE;  $d = 0.3\text{ cm}$  in diameter) and an auxiliary electrode (platinum wire), in a 0.1 M  $\text{NBu}_4\text{PF}_6$  in acetonitrile solution as the supporting electrolyte. The system was purged with argon for five minutes before measurements taken at room temperature. The electrochemical HOMO-LUMO energy levels and the electrochemical band gaps ( $E'_g$ ) were estimated from the onset values of oxidation ( $E_{ox}$ ) and the reduction ( $E_{red}$ ) [5].



**Scheme 1.** Mechanism of the Schiff base synthesis

## 3. Results and Discussion

FT-IR spectra of SCH1 and SCH2 compounds are given in Figure 1. As shown in Figure 1A, the stretching vibration bands of  $\text{-C=N-}$ ,  $\text{-C=C-}$  and  $\text{-C-O}$  of SCH1 were observed at  $1639$ ,  $1608$  and  $1246\text{ cm}^{-1}$ , respectively. As seen in Figure 1B, the stretching vibration bands of  $\text{-C=N-}$ ,  $\text{-C=C-}$  and  $\text{-C-O}$  of SCH2 were observed at  $1639$ ,  $1608$  and  $1234\text{ cm}^{-1}$ , respectively. The vibrations observed at  $3354\text{ cm}^{-1}$  and  $3353\text{ cm}^{-1}$  are attributed to O-H stretching, while those at  $3053\text{ cm}^{-1}$  and  $3081\text{ cm}^{-1}$  are attributed to aromatic C-H stretching for SCH1 and SCH2, respectively. The asymmetric and symmetric  $\text{O=S=O}$  stretching vibrations of the sulfonic acid group are assigned to the peaks at  $1380\text{ cm}^{-1}$  and  $1161\text{ cm}^{-1}$  for



SCH1, and at 1382  $\text{cm}^{-1}$  and 1164  $\text{cm}^{-1}$  for SCH2, respectively [6].

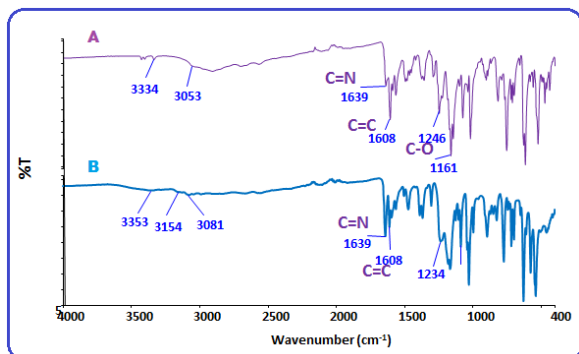


**Figure 1.** FT-IR spectra of SCH1 (A) and SCH2 (B).

As illustrated in Figure 2, the maximum absorption wavelength corresponding to the  $\pi \rightarrow \pi^*$  transitions induced by phenyl rings in SCH1 and SCH2 were observed at 320 and 326 nm, respectively. Additionally, transitions associated with  $n \rightarrow \pi^*$  involving electron pairs on oxygen atoms and imine bonds appeared at 360 and 385 nm, respectively. The optical band gap values ( $E_g$ ) of SCH1 and SCH2 compounds were calculated by the following equation:

$$E_g = \frac{1242}{\lambda_{onset}} \quad (1)$$

where  $\lambda_{onset}$  represents the onset wavelength for the electronic transition which can be obtained from the absorption edges of the UV-Vis spectra [7]. The  $\lambda_{onset}$  values for SCH1 and SCH2, derived from their UV-Vis absorption bands, were found to be 438 nm and 400 nm, respectively. The optical band gap ( $E_g$ ) values for the SCH1 and SCH2 compounds were determined from their  $\lambda_{onset}$  values, yielding 2.84 eV and 3.11 eV, respectively.

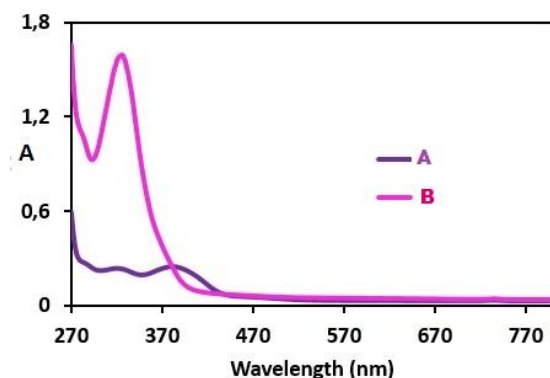


**Figure 2.** UV-Vis spectra of SCH1 (A) and SCH2 (B).

As illustrated in the  $^1\text{H}$  NMR spectrum of the SCH1 compound shown in Figure 3A, the proton signals of  $-\text{CH}=\text{N}-$ ,  $-\text{OH}$ , and  $-\text{SO}_3\text{H}$  groups were observed at 10.67, 10.22, and 8.98 ppm, respectively. For SCH1, the aromatic protons appeared between 6.84 and 7.91 ppm. In the case of SCH2, the proton signals of  $-\text{CH}=\text{N}-$ ,  $-\text{OH}$ ,

and  $-\text{SO}_3\text{H}$  groups were observed at 10.69, 10.22 and 9.09 ppm, respectively, with aromatic protons appearing between 6.92 and 7.92 ppm. Observation of signals of imine protons at 10.22 ppm in the  $^1\text{H}$  NMR spectra of SCH1 and SCH2 compounds confirms the formation of Schiff base structure.

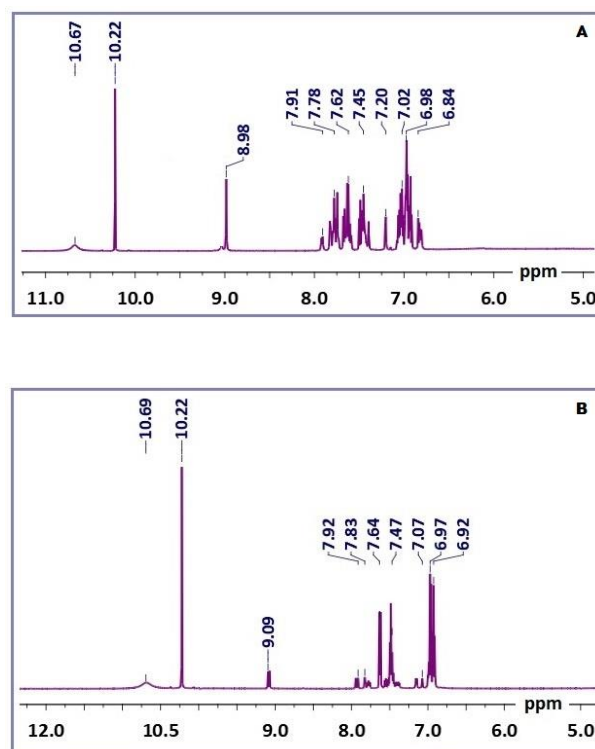


**Figure 3.**  $^1\text{H}$  NMR spectra of SCH1 (A) and SCH2 (B).

As depicted in the  $^{13}\text{C}$  NMR spectrum of the SCH1 compound in Figure 4A, the carbon atoms of  $-\text{CH}=\text{N}-$  and  $-\text{C}-\text{OH}$  were observed at 162.20 and 161.12 ppm, respectively. The aromatic carbon atoms in SCH1 were detected between 117.00 and 141.44 ppm. For SCH2, the  $-\text{CH}=\text{N}-$  and  $-\text{C}-\text{OH}$  carbon signals were observed at 163.24 and 161.13 ppm, respectively, while the aromatic carbon signals were detected between 117.24 and 146.33 ppm in Figure 4B. The detection of imine carbon signals at 162.20 and 163.24 ppm in the  $^{13}\text{C}$  NMR spectra of SCH1 and SCH2 compounds confirms the successful formation of these compounds.

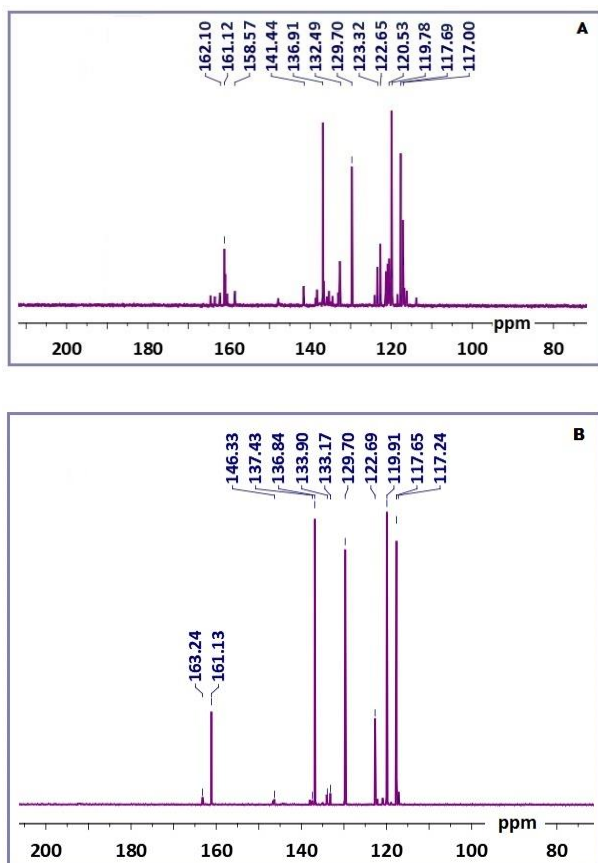


**Figure 4.**  $^{13}\text{C}$  NMR spectra of SCH1 (A) and SCH2 (B).

Figure 5 presents the cyclic voltammograms (CVs) of the synthesized compounds, used to calculate their HOMO and LUMO energies as well as the electrochemical band gap ( $E'_g$ ) depending on the following equations [8]:

$$E_{\text{HOMO}} = -(4.39 + E_{\text{ox}}) \quad (2)$$

$$E_{\text{LUMO}} = -(4.39 + E_{\text{red}}) \quad (3)$$

$$E'_g = E_{\text{LUMO}} - E_{\text{HOMO}} \quad (4)$$

$E_{\text{HOMO}}$  and  $E_{\text{LUMO}}$  represent the energies of the HOMO and LUMO levels of the compounds, respectively. According to Figure 5, two cathodic peak potentials signify the oxidation of two phenolic -OH groups, leading to the formation of a phenoxy polaron structures for SCH1 and SCH2 [9]. The anodic reduction peak potentials were related to the imine bond for the compounds. The electrochemical  $E_g$  values of SCH1 and SCH2 were calculated as 2.28 eV and 2.42 eV, respectively, which were consistent with the optically measured energy gap ( $E_g$ ) values.

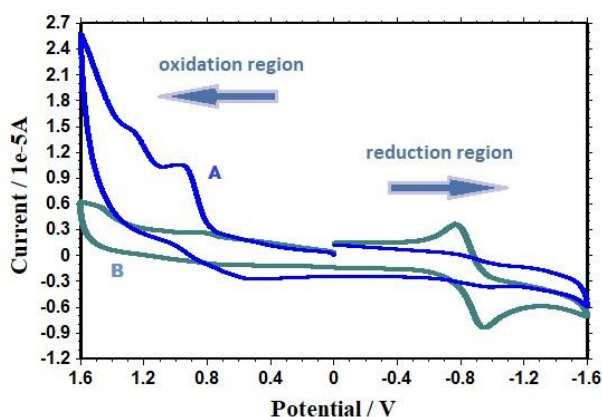


**Figure 5.** CV voltammograms of SCH1 (A) and SCH2 (B).

Figure 6 displays the thermal analysis curves for the Schiff bases. The initial degradation temperatures ( $T_{\text{on}}$ ) for SCH1 and SCH2 were recorded at 298 °C and 347 °C, respectively. The  $T_{\text{max}}$  values, obtained from the DTG curves, were 330 °C and 716 °C for SCH1, and 368 °C and 732 °C for SCH2. Based on TG curves, the temperatures corresponding to 5%, 10%, 20%, 30%, and 50% weight losses for SCH1 and SCH2 were calculated to be 306 °C, 317 °C, 340 °C, 381 °C, and 721 °C, and 354 °C, 363 °C, 375 °C, 410 °C, and 807 °C, respectively. The  $T_{\text{on}}$  values suggest that the compound containing a phenyl group exhibits higher thermal stability. This enhanced stability is attributed to the presence of multiple phenyl groups in the main chain, which contribute to increased thermal resistance. The residual amounts of SCH1 and SCH2 at 1000 °C were calculated to be 34.64% and 41.24%, respectively.

Both compounds underwent degradation in two steps. For SCH1, the mass loss values were 39.37% in the temperature range of 261-513 °C and 25.98% in the range of 513-1000 °C. For SCH2, the mass loss values were 39.54% between 260 °C and 527 °C and 19.22% in the temperature range of 527-1000 °C. As displayed in Figure 6B, a 7% loss due to water and organic solvent was observed up to 150 °C. Additionally, endothermic peaks were observed in the DTA curves of SCH1 and SCH2 at 296 and 365 °C, respectively.

The flame retardancy values of the synthesized Schiff bases can be obtained by following the Van Krevelen's calculation, utilizing the percentage of residue at 1000 °C. The formation of carbon residue during thermal decomposition restricts the emission of organic volatile compounds. This carbonaceous layer, produced in the process, impedes the propagation of flammable gases by diminishing heat transfer to the material. In this regard, Van Krevelen proposed a formula of  $LOI = 17.5 + 0.4(s)$  where  $LOI$  represents the limiting oxygen index and ( $s$ ) denotes the percentage of residue in the organic compounds, respectively [10]. According to Van Krevelen's theory, an increase in residue formation correlates with the flammability of organic compounds.

For compounds to be self-extinguishing, their *LOI* values must be at least 26 or higher [11]. The *LOI* values for SCH1 and SCH2 were calculated as 31.36 and 34.00, respectively, concluding with the fact that high *LOI* values render them self-extinguishing and qualify them for various applications requiring good flame resistance [12]. SCH2 includes an additional aromatic ring, resulting in increased material flammability.

Additionally, the Heat Resistance Index ( $T_{HRI}$ ) was calculated following the method outlined in the literature [13] using the temperatures corresponding to 5% and 30% weight loss. The calculated  $T_{HRI}$  values for SCH1 and SCH2 were 171.99 °C and 189.92 °C, respectively. The incorporation of an additional aromatic ring as in SCH2 is evident in the enhanced *LOI* and  $T_{HRI}$ , indicating a significant improvement in both the thermal stability and flame retardancy of SCH2. Therefore, SCH1 and SCH2, characterized by high thermal stability and substantial char yield, show potential for use in the fabrication of heat-resistant materials.

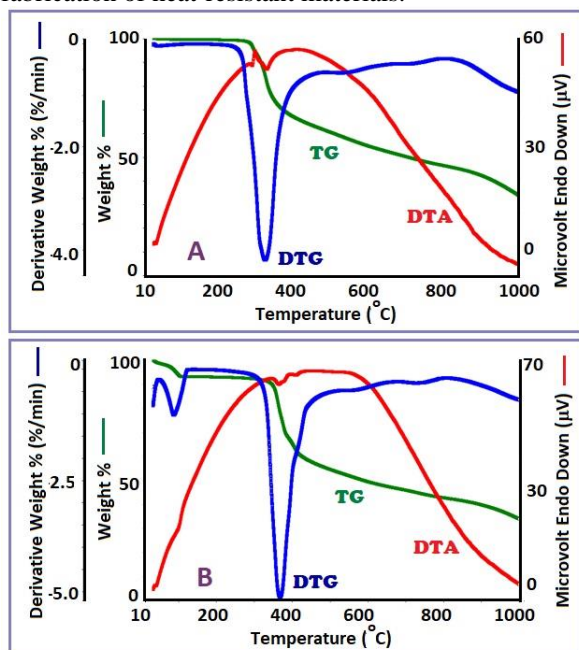


**Figure 6.** TG-DTA-DTG curves of SCH1 (A) and SCH2 (B).

#### 4. Conclusion

Two Schiff bases were synthesized through the reactions of aromatic diamine compounds containing mono and di sulfo units in their structure with salicylaldehyde. The yields of the compounds were obtained to be high. The structures of the synthesized Schiff bases were confirmed using FT-IR, UV-Vis,  $^1\text{H}$  and  $^{13}\text{C}$  NMR spectroscopy. The synthesized compounds exhibited significant thermal stability, with initial decomposition temperatures for SCH1 and SCH2 determined to be 298 °C and 347 °C, respectively, based on the TG measurements. The optical band gap values ( $E_g$ ) of SCH1 and SCH2 were

calculated to be 2.84 eV and 3.11 eV, respectively. The onset degradation temperatures of SCH1 and SCH2 were recorded at 298 °C and 347 °C, respectively. The thermal stability of these compounds was notably influenced by an additional aromatic ring, enhancing thermal stability and increasing the onset degradation temperature  $T_{on}$ .

The presence of dihydroxy groups in the synthesized Schiff bases facilitates the synthesis and characterization of poly(ether) and poly(urethane) macromolecules. This investigation will provide valuable insights for future research in this field.

#### Author's Contributions

**İsmet Kaya:** He performed FT-IR, TG and NMR measurements and data analysis of the compounds.

**Feyza Kolcu:** She performed UV-Vis, CV and Fluorescence measurements and data analyses of the compounds.

**Sude Süel:** She synthesized the Schiff base compounds.

#### Ethics

There are no ethical issues after the publication of this manuscript.

#### References

- [1]. Park, S., Mathur, V.K., Planalp, R.P. 1998. Synthesis, solubilities and oxygen absorption properties of new Cobalt (II) Schiff base complexes, *Polyhedron*, 17 (2-3): 325-330.
- [2]. Tüzün, C. 1996. Organic chemistry, 9<sup>th</sup> press, Palme publisher, pp. 545-547, Ankara, Türkiye.
- [3]. Zhang, T., Bai, R., Shen, J., Wang, O., Wang, P., Yuan, J., Fan, X. 2018. Laccase-catalyzed polymerization of diamino-benzene sulfonic acid for pH-responsive color-changing and conductive wool fabrics, *Textile Research Journal*; 88 (19): 2258-2266.
- [4]. Kaya, İ., Akyüz, B., Kolcu, F., Söyüt, H. 2022. Facile one-pot synthesis of water-soluble conjugated polymers derived from 7-amino-4-hydroxy-2-naphthalenesulfonic acid: Synthesis and photoluminescence properties, *Reactive and Functional Polymers*; 175: Article Nu.105281.
- [5]. Kaya, İ., Kolcu, F., Satılmış, S., Yazıcıoğlu, Z. 2018. Synthesis and characterization of fluorescent polyphenols anchored Schiff bases via oxidative polycondensation, *Materials Science-Poland*; 36 (4), 584-596.
- [6]. Yang, J.C., Jablonsky, M.J., Mays, J. 2002. NMR and FT-IR studies of sulfonated styrene-based homopolymers and copolymers, *Polymer*, 43, 5125-5132.
- [7]. Burns, M., Wagenknecht, U., Kretzschmar, B., Focke, W.W. 2008. Effect of hydrated fillers and red phosphorus on the limiting oxygen index of poly(ethylene-co-vinyl acetate)-poly(vinyl butyral) and low density polyethylene-poly(ethylene-co-vinyl alcohol) blends, *Journal of Vinyl and Additive Technology*, 14 (3), 113-119.



[8]. Kolcu F, Kaya İ. 2024. Oligomerization of dibrominated aminophenol on the basis of the chemical and HRP-catalyzed oxidative processes: Characterization and photoluminescence properties, *Dyes and Pigments*, 227, Article Nu.112185.

[9]. Liu, W., Lee, S., Yang, S., Bian, S., Lia, L., Samuelson, L.A., Kumar, J., Tripathy, S.K. 2001. Biologically derived photoactive macromolecular azodyes. *Journal of Macromolecular Science - Pure and Applied Chemistry*, 38 A (12) 1355-1370.

[10]. Bredas, J.L., Street, G.B. 1985. Polarons, bipolarons, and solitons in conducting polymers, *Accounts of Chemical Research Journal*, 18, 309-315.

[11]. van Krevelen, D.W. 1975. Some basic aspects of flame resistance of polymeric materials. *Polymer*, 16, 615-620.

[12]. van Krevelen, D.W. *Properties of Polymers*, 3rd ed.; Elsevier, New York, 1972.

[13]. Arora, S., Mestry, S., Naik, D., Mhaske, S. 2020. o-phenylenediamine-derived phosphorus-based cyclic flame retardant for epoxy and polyurethane systems. *Polymer Bulletin*, 77, 3185-3205.

# Unveiling the antioxidant secrets: Phytochemical profiling and bioactive potential of water extracts from Muğla propolis samples

Cengiz Sarıkürkcü<sup>1\*</sup> 

<sup>1</sup> Faculty of Pharmacy, Afyonkarahisar Health Sciences University, TR-03100, Afyonkarahisar, Türkiye

\* [sarikurkc@gmail.com](mailto:sarikurkc@gmail.com)

\* Orcid No: 0000-0001-5094-2520

Received: 13 October 2025

Accepted: 15 November 2025

DOI: 10.18466/cbayarfbe.1566363

## Abstract

Propolis, a resinous substance collected by bees, is known for its diverse biological activities, including antioxidant properties, which are largely attributed to its phenolic and flavonoid content. This study aimed to investigate the chemical composition and antioxidant activities of water extracts from propolis samples collected from different locations in Muğla, Turkey. Total phenolic and flavonoid contents were quantified, and antioxidant activities were evaluated using various assays, including  $\beta$ -carotene bleaching, superoxide anion radical scavenging, DPPH radical scavenging, reducing power, and ferrous ion chelation. The total phenolic content of the samples ranged from 27.72 to 91.57 mg PEs/g extract, with Arpacık showing the highest phenolic content (91.57 mg PEs/g). In contrast, flavonoid content ranged from 9.33 to 25.78 mg QEs/g extract, with Fethiye exhibiting the highest value (25.78 mg QEs/g). The antioxidant assays revealed that the Fethiye extract consistently demonstrated the strongest activity, with a  $\beta$ -carotene inhibition rate of 96.73% and an IC<sub>50</sub> of 49.50  $\mu$ g/mL in the DPPH assay. Arpacık also showed considerable antioxidant capacity, albeit slightly lower than Fethiye, while the Dalaman and Döğüşbelen samples exhibited weaker activities. Correlation analysis indicated that total phenolic content had a strong positive correlation with DPPH scavenging ( $r = 0.994$ ) and reducing power ( $r = 0.986$ ), while flavonoid content was significantly correlated with superoxide anion scavenging ( $r = 0.931$ ) and ferrous ion chelation ( $r = 0.894$ ). These results suggest that phenolic and flavonoid compounds are key contributors to the antioxidant mechanisms in propolis. Future studies should explore the effects of different extraction methods and expand the geographical scope to better understand the factors influencing the bioactive composition of propolis.

**Keywords:** Propolis, Antioxidant activity, Muğla, Phenolic content.

## 1. Introduction

Propolis, a natural resinous substance that honeybees collect from the buds and secretions of specific plants and trees, is believed to serve as a defensive shield in the hive against potential threats. Traditionally, it has been employed in folk medicine across various cultures [1]. Numerous studies have reported its wide range of biological activities, including antibacterial [2], antiviral [3], anti-inflammatory [4], and anticancer [5,6] effects. Consequently, propolis is frequently incorporated into foods and beverages as a functional ingredient, aiming to promote health and help prevent conditions like inflammation, cardiovascular diseases, diabetes, and cancer [7].

Propolis typically comprises an array of chemical constituents, including polyphenols (such as flavonoids,

phenolic acids, and their esters), terpenoids, steroids, and amino acids. The specific composition of propolis is largely influenced by the local plant life in the area from which it is collected [7]. Due to these geographical variations, the chemical makeup of propolis differs between samples from Europe, South America, and Asia [8]. European and Chinese propolis are rich in flavonoids and phenolic acid esters [9], whereas Brazilian propolis predominantly contains terpenoids and prenylated derivatives of *p*-coumaric acids [10,11]. These compositional differences result in varying biological activities depending on the region of origin. For instance, Miyataka et al. [12] found significant differences in the ability of Brazilian and Chinese propolis to inhibit hyaluronidase and release histamine from rat peritoneal mast cells when stimulated by compound 48/80 or concanavalin A [13]. In another study, Hegazi et al. [14] demonstrated that German propolis exhibited strong



antimicrobial effects against *Staphylococcus aureus* and *Escherichia coli*, while Austrian propolis was highly effective against *Candida albicans*. Additionally, Banskota et al. [15] reported that methanol extracts from Dutch and Chinese propolis showed potent cytotoxic effects on murine colon 26-L5 carcinoma cells, whereas the activity of Brazilian propolis varied between samples.

Propolis has been widely recognized for its antioxidant properties, as highlighted by numerous studies. In this study, we aim to assess the antioxidant potential of water extracts of propolis from different geographic regions of Muğla-Türkiye using *in vitro* methods. We employed assays such as superoxide anion and 1,1-diphenyl-2-picrylhydrazyl (DPPH) radical scavenging,  $\beta$ -carotene bleaching, ferrous ion chelation, and reducing power assays to evaluate antioxidant performance. Additionally, total phenolic and flavonoid contents of the extracts were determined spectrophotometrically and the relationship between phenolic/flavonoid compounds contained in the extracts and antioxidant activity tests was revealed using statistical methods.

## 2. Materials and Methods

### 2.1. Sample collection and preparation of water extracts

Propolis samples were collected from four distinct locations in Muğla, Turkey: Arpacık, Dalaman, Döğüşbelen, and Fethiye. A 25 g sample of propolis was extracted in 250 mL of boiling deionized water for 30 minutes. Following extraction, each sample was centrifuged at 4000 rpm for 10 minutes. The resulting extracts were then filtered through filter paper. The water extracts of propolis from Arpacık, Dalaman, Döğüşbelen, and Fethiye were subsequently dried using a freeze-dryer, yielding extract percentages of 5.90%, 3.11%, 5.18%, and 5.79% (w/w), respectively.

### 2.2. Assay for total phenolics and flavonoids

Total phenolic constituent of the extracts were determined by employing the methods given in the literature [16]. Pyrocatechol was used as a standard agent and the results were calculated as pyrocatechol equivalents (mg PEs/g extract). Total flavonoid constituent was determined using the Dowd method as adapted by Zengin et al. [17]. The results were given as quercetin equivalents (mg QEs/g extract). Both test conditions were provided in the supplementary file.

### 2.3. Antioxidant Activity

The antioxidant activity of propolis extracts was evaluated using five different test systems: superoxide anion and 1,1-diphenyl-2-picrylhydrazyl (DPPH) radical scavenging,  $\beta$ -carotene bleaching, ferrous ion chelation, and reducing power.

The antioxidant capacity is assessed by quantifying the inhibition of volatile organic compounds and conjugated diene hydroperoxides generated during the oxidation of linoleic acid [18]. The reducing power was assessed using the method described by Oyaizu [19]. Radical scavenging activities were measured using two different assays including DPPH radical [17] and superoxide anion radical [20] according to the procedure in literature. Ferrous ion chelating activity was determined by the method described by Aktumsek et al. [21].

The results are given as inhibition at 2 mg/mL and 0.2 mg/mL concentration for  $\beta$ -carotene/linoleic acid test and superoxide anion radical scavenging, and as  $IC_{50}$  (mg/mL) for DPPH radical scavenging, ferrous ion chelation, and reducing power. All antioxidant activity test conditions were conducted as detailed in the supplementary file.

### 2.4. Statistical Analysis

Detailed information on the Relative Antioxidant Capacity Index (RACI) [22] and the statistical analyses performed is available in the supplementary file.

## 3. Results and Discussion

### 3.1. Chemical composition of the propolis samples

The total phenolic and flavonoid contents of the water extracts from propolis samples collected from different locations in Muğla (Turkey) exhibited considerable variation (Figure 1). The total phenolic content ranged from 27.72 mg PEs/g extract to 91.57 mg PEs/g extract, with statistically significant differences observed among the samples ( $p < 0.05$ ). The Arpacık sample displayed the highest total phenolic content at 91.57 mg PEs/g extract, significantly different from all other samples. Fethiye followed with 85.18 mg PEs/g extract, also distinct from the others but lower than Arpacık. The Dalaman and Döğüşbelen samples showed similar phenolic contents, at 27.72 mg PEs/g extract and 28.20 mg PEs/g extract respectively and were statistically grouped together.

For total flavonoid content, Fethiye had the highest value at 25.78 mg QEs/g extract, significantly differing from the other samples. The Arpacık sample, although showing lower flavonoid content at 16.81 mg QEs/g extract, was still statistically different from the remaining locations. Döğüşbelen exhibited a total flavonoid content of 14.90 mg QEs/g extract, which was not significantly different from Arpacık, but it was distinct from Dalaman, which had the lowest flavonoid content at 9.33 mg QEs/g extract (Figure 2).

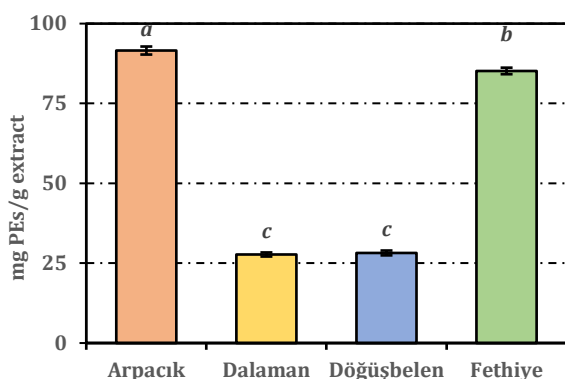


**Figure 1.** Total phenolic contents of propolis water extracts. PEs: Pyrocatechol equivalents. Values indicated by the same superscripts are not different from the honestly significant difference after Tukey's hoc test at 5% significance level.

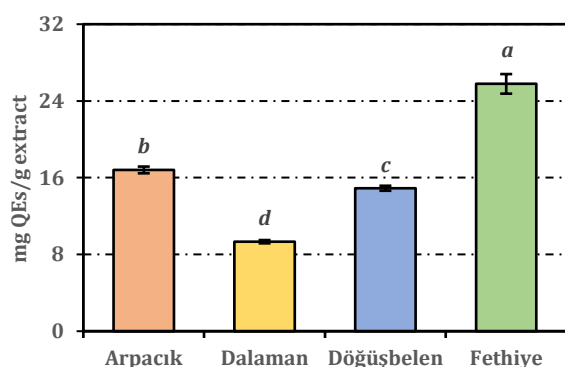


**Figure 2.** Total flavonoid contents of propolis water extracts. QEs: Quercetin equivalents. Values indicated by the same superscripts are not different from the honestly significant difference after Tukey's hoc test at 5% significance level.

When comparing the two groups of compounds, the Fethiye sample consistently showed high levels of both total phenolics and flavonoids, suggesting that this sample may have a more balanced and rich composition of bioactive compounds. In contrast, the Arpacık sample had the highest phenolic content but a comparatively lower flavonoid content, which may indicate a phenolic-dominant profile. On the other hand, both the Dalaman and Döğüşbelen samples exhibited low phenolic contents, but Döğüşbelen contained a relatively higher amount of flavonoids, showing a different bioactive profile compared to Dalaman.

The statistical analysis reveals that the phenolic and flavonoid compositions of these propolis samples vary significantly across locations, indicating that geographical factors might influence the biosynthesis of these compounds in propolis. Furthermore, the distinct statistical groupings in phenolic and flavonoid contents highlight the diversity in the chemical makeup of the samples, which may reflect different ecological and botanical conditions influencing the resin sources for the bees. Such variations in phenolic and flavonoid profiles could lead to differing biological activities, which

warrants further investigation into the bioactivity of these regionally diverse propolis samples.

The present study demonstrated significant variation in the total phenolic and flavonoid contents of water extracts from propolis samples collected from different locations in Muğla, Turkey. These variations are consistent with previous findings in the literature, where the phenolic and flavonoid profiles of propolis have been shown to depend on geographic, botanical, and climatic factors [23,24]. For instance, the total phenolic content in this study ranged from 27.72 mg PEs/g extract (Dalaman) to 91.57 mg PEs/g extract (Arpacık), with Fethiye showing a similarly high phenolic content (85.18 mg PEs/g extract). These values align with studies such as those by Bouchelaghem et al. [25] and Sulaeman et al. [26], where propolis samples from different regions displayed total phenolic contents ranging from 20 to 100 mg PEs/g, depending on their geographical origins.

The total flavonoid content in this study also exhibited location-based variability, ranging from 9.33 mg QEs/g extract (Dalaman) to 25.78 mg QEs/g extract (Fethiye). The high flavonoid content in the Fethiye sample is comparable to results from Indonesian and Malaysian propolis, which showed flavonoid concentrations between 10 and 30 mg QEs/g extract [23,26]. In the present study, while Arpacık exhibited the highest phenolic content, its flavonoid content was lower compared to Fethiye, which suggests a phenolic-dominant composition. This phenolic-flavonoid distribution is in line with the observation by Wang et al. [24], where distinct propolis profiles were observed depending on regional and botanical diversity.

The differences in phenolic and flavonoid compositions across the Muğla samples are likely influenced by the local flora that bees source for resin collection. As noted by Wang et al. [24], environmental factors such as altitude, vegetation, and climate significantly impact the chemical makeup of propolis. The present data showing that Arpacık, with its higher altitude and distinct flora, yielded the highest phenolic content, while Fethiye's sample was more balanced in both phenolics and flavonoids, support this hypothesis. Such botanical influences have been widely documented, with similar trends observed in Indonesian and South Korean propolis samples [24,26].

### 3.2. Antioxidant activity of the propolis samples

The antioxidant activity of water extracts from propolis samples collected in various regions of Muğla (Turkey) was evaluated using multiple assays, revealing distinct variations in their efficacy. These assays provide insight into the capacity of the extracts to inhibit lipid peroxidation, scavenge reactive oxygen species, and reduce or chelate ions, which together give a comprehensive view of their antioxidant potential.

The  $\beta$ -carotene bleaching assay showed that all propolis extracts exhibited considerable antioxidant activity, with Fethiye extract demonstrating the highest inhibition at 96.73%, statistically comparable to the positive control, BHT (97.44%) (Figure 3). Arpacık and Dalaman extracts also showed high inhibition rates, 92.19% and 92.44% respectively, with no significant difference between them ( $p > 0.05$ ). Döğüşbelen, however, showed a lower activity at 86.10%, significantly different from the other samples ( $p < 0.05$ ). The superior performance of the Fethiye extract in this assay suggests its strong capability in preventing oxidative degradation of  $\beta$ -carotene.

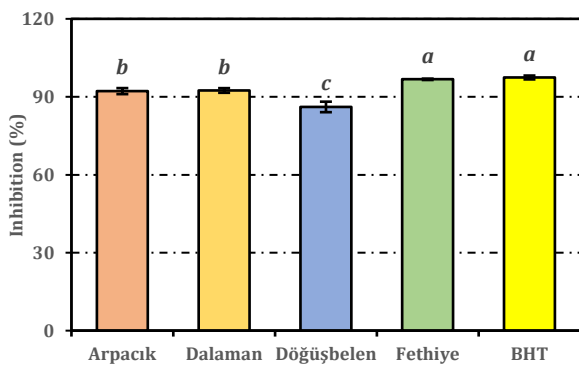


**Figure 3.** Antioxidant activity (%) of propolis water extracts at 2 mg/mL concentration measured by  $\beta$ -carotene bleaching method. Values indicated by the same superscripts are not different from the honestly significant difference after Tukey's hoc test at 5% significance level.

When evaluating the scavenging effect on superoxide anion radicals, Fethiye extract again outperformed the others, with a high inhibition rate of 72.59%, significantly surpassing even the reference compound quercetin (68.22%) (Figure 4). Arpacık exhibited moderate activity at 44.21%, which was significantly higher than both Dalaman (38.03%) and Döğüşbelen (38.42%), which displayed similar and lower scavenging effects ( $p < 0.05$ ). This data indicates that the Fethiye extract has a much stronger capacity for neutralizing superoxide radicals, a key reactive species involved in oxidative stress.

The DPPH assay showed Fethiye and Arpacık extracts as the most effective scavengers, with  $IC_{50}$  values of 49.50  $\mu$ g/mL and 51.30  $\mu$ g/mL respectively, which are not statistically different ( $p > 0.05$ ) (Figure 5). These values are also significantly lower than those for the other two samples, Dalaman (145.50  $\mu$ g/mL) and Döğüşbelen (151.40  $\mu$ g/mL), indicating their inferior ability to neutralize DPPH radicals. Fethiye's performance was even stronger than BHT ( $IC_{50} = 73.00$   $\mu$ g/mL), suggesting that this extract may possess potent free radical scavenging properties.

In the reducing power assay, Fethiye and Arpacık samples again demonstrated strong activity with  $IC_{50}$  values of 10.59  $\mu$ g/mL and 11.01  $\mu$ g/mL, respectively,

both significantly better than the Dalaman and Döğüşbelen extracts, which showed higher  $IC_{50}$  values of 28.97  $\mu$ g/mL and 42.15  $\mu$ g/mL ( $p < 0.05$ ) (Figure 6). However, BHT displayed the best performance with an  $IC_{50}$  of 9.82  $\mu$ g/mL, although the difference between Fethiye, Arpacık, and BHT was not statistically significant (Figure 6).

The ferrous ion chelating ability test revealed a significant difference among the samples (Figure 7). The Fethiye extract showed the strongest chelating activity with an  $IC_{50}$  of 413  $\mu$ g/mL, outperforming even BHT ( $IC_{50} = 866$   $\mu$ g/mL). Arpacık ( $IC_{50} = 887$   $\mu$ g/mL) showed moderate chelating activity, similar to BHT ( $p > 0.05$ ). On the other hand, Dalaman ( $IC_{50} = 1960$   $\mu$ g/mL) and Döğüşbelen ( $IC_{50} = 4651$   $\mu$ g/mL) exhibited much weaker chelating capacities, significantly different from the other samples ( $p < 0.05$ ).

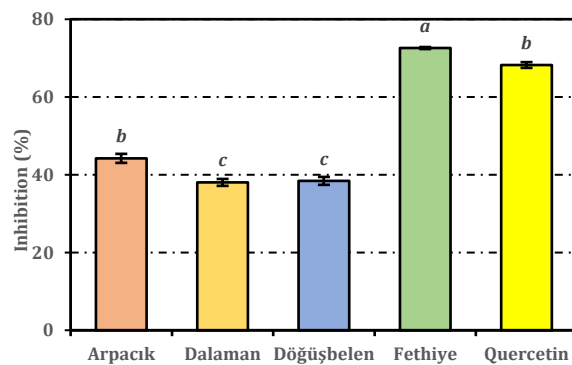


**Figure 4.** Scavenging effect (%) on superoxide anion radicals of propolis water extracts at 0.2 mg/mL concentration. Values indicated by the same superscripts are not different from the honestly significant difference after Tukey's hoc test at 5% significance level.

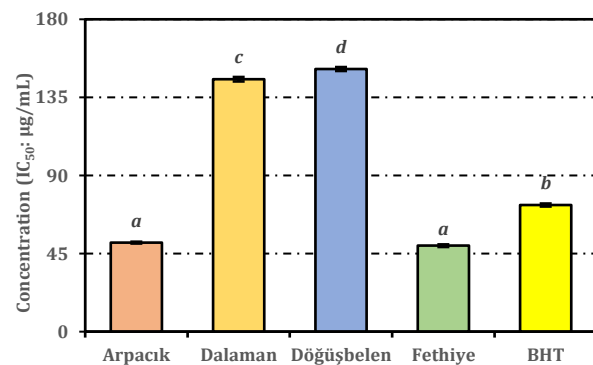


**Figure 5.** Scavenging effect on DPPH radicals of propolis water extracts. Values indicated by the same superscripts are not different from the honestly significant difference after Tukey's hoc test at 5% significance level.

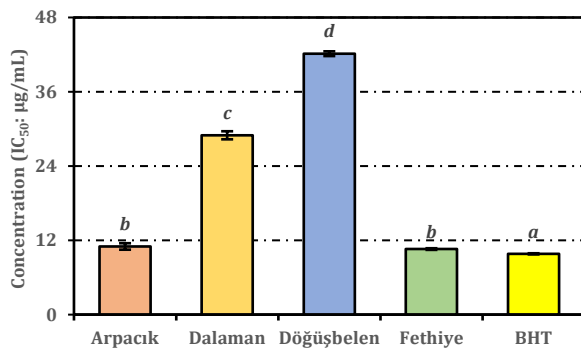


**Figure 6.** Reducing power of propolis water extracts. Values indicated by the same superscripts are not different from the honestly significant difference after Tukey's hoc test at 5% significance level.

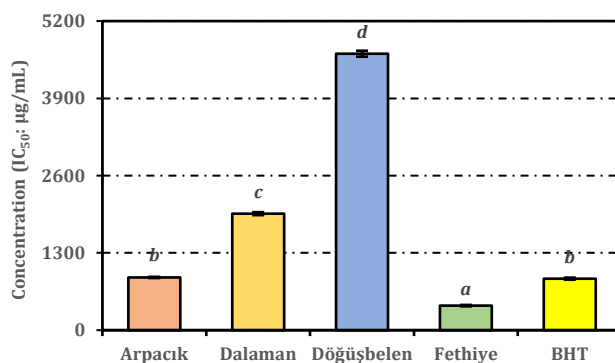


**Figure 7.** Ferrous ion chelating activity of propolis water extracts. Values indicated by the same superscripts are not different from the honestly significant difference after Tukey's hoc test at 5% significance level.

Fethiye consistently showed the highest antioxidant activity across all assays, which correlates with its high total phenolic (85.18 mg PEs/g) and flavonoid content (25.78 mg QEs/g). The rich phenolic and flavonoid composition likely contributes to its superior radical scavenging, reducing, and chelating abilities. In contrast, Arpacık, which also exhibited strong antioxidant performance in most assays, had the highest phenolic content (91.57 mg PEs/g) but a lower flavonoid concentration (16.81 mg QEs/g), suggesting that phenolics may be the primary contributors to its antioxidant activity.

Dalaman and Döğüşbelen extracts, which consistently displayed lower antioxidant capacities, also contained lower levels of both phenolics and flavonoids. These results reinforce the role of phenolic and flavonoid compounds in driving the antioxidant activity of propolis. In particular, the correlation between phenolic content and reducing power, as well as flavonoid content and radical scavenging capacity, is evident in these findings.

The relative antioxidant capacity index (RACI) was calculated for each water extract of propolis from

different locations in Muğla (Turkey), allowing for a comparative assessment of their overall antioxidant potential across the various assays (Figure 8). RACI, by standardizing the results from distinct antioxidant assays, provides a more holistic evaluation of each extract's antioxidant capacity, making it possible to rank them even though individual tests measure different mechanisms of action.

The RACI values suggest that the Fethiye extract possesses the highest overall antioxidant capacity, with a score of 1.13, significantly outperforming the other samples. This finding aligns well with the earlier assay results, where Fethiye consistently demonstrated superior antioxidant activity across the  $\beta$ -carotene bleaching, superoxide anion radical scavenging, DPPH radical scavenging, and reducing power tests. Its higher phenolic and flavonoid content further supports this elevated activity, as these compounds are well-established contributors to antioxidant defense mechanisms.

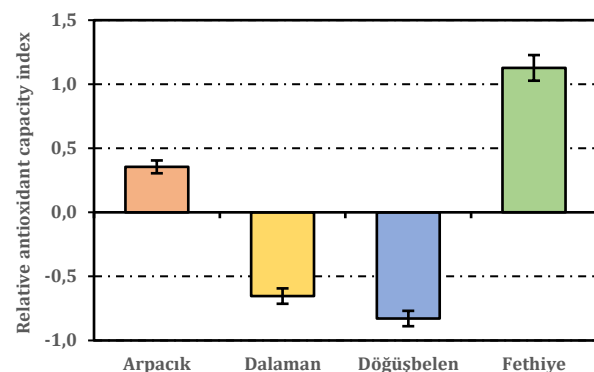


**Figure 8.** Relative antioxidant capacity index of propolis water extracts

The Arpacık extract follows with a positive RACI value of 0.35, indicating a relatively high antioxidant capacity. This is consistent with the individual assay data, where Arpacık exhibited strong performance, particularly in  $\beta$ -carotene bleaching and reducing power assays. Although its superoxide anion scavenging and DPPH radical scavenging activities were moderate, the overall RACI score reflects its generally good antioxidant profile. This is in accordance with its rich phenolic content, which likely contributes to its substantial antioxidant activity.

In contrast, both Dalaman and Döğüşbelen samples show negative RACI values of -0.65 and -0.83, respectively, indicating lower overall antioxidant capacities. These results also correspond with the previous findings, where both extracts displayed comparatively weaker antioxidant activities across all assays. Their lower phenolic and flavonoid contents provide a plausible explanation for this diminished antioxidant potential. Specifically, their limited ability to scavenge radicals and reduce ions, as shown in the DPPH, reducing power, and



ferrous ion chelating assays, is reflected in their negative RACI values.

In summary, the RACI values provide a comprehensive ranking of the antioxidant capacity of the propolis extracts, with Fethiye and Arpacık demonstrating stronger antioxidant activities, while Dalaman and Döğüşbelen exhibit significantly weaker performances. These results are consistent with the chemical composition data, suggesting that higher phenolic and flavonoid concentrations are closely associated with enhanced antioxidant activity in the propolis extracts.

The correlation analysis between the chemical composition and antioxidant activities of water extracts from propolis samples collected from various locations in Muğla (Turkey) reveals several significant relationships, indicating that the phenolic and flavonoid content plays a crucial role in influencing the antioxidant potential of these extracts (Table 1).

Notably, total phenolic content demonstrates a very strong positive correlation with the DPPH radical scavenging activity ( $r = 0.994$ ) and reducing power ( $r = 0.986$ ). This suggests that phenolic compounds are major contributors to these specific antioxidant mechanisms. The strong correlation with both assays implies that the phenolics present in the extracts are highly effective in neutralizing free radicals and promoting electron transfer processes, which are critical to antioxidant defenses.

Similarly, a substantial positive correlation is observed between total flavonoid content and superoxide anion radical scavenging activity ( $r = 0.931$ ), highlighting the significant role of flavonoids in mitigating oxidative stress caused by superoxide radicals. This finding suggests that the flavonoid-rich extracts, such as those from Fethiye and Arpacık, possess enhanced capacity to counteract reactive oxygen species, which aligns with their higher overall antioxidant performance in the superoxide anion radical assay.

Furthermore, the correlation between total flavonoid content and ferrous ion chelation ( $r = 0.894$ ) is also

strong, indicating that flavonoids contribute meaningfully to the metal-chelating properties of the extracts. This relationship is critical, as metal chelation can inhibit the generation of reactive species via Fenton reactions, thus protecting against oxidative damage.

The  $\beta$ -carotene bleaching assay also shows moderate correlations with both phenolic ( $r = 0.649$ ) and flavonoid ( $r = 0.562$ ) content, suggesting that these compounds play a role in protecting against lipid peroxidation, though not as strongly as in other assays. The moderate correlation indicates that while phenolics and flavonoids contribute to this mechanism, other compounds in the extracts may also be involved in inhibiting the oxidation of linoleic acid in this specific test.

Ferrous ion chelation exhibits strong correlations with both phenolic ( $r = 0.790$ ) and flavonoid content ( $r = 0.894$ ), reinforcing the notion that these compounds are key players in the extracts' ability to bind and neutralize metal ions, which could otherwise catalyze the formation of harmful radicals.

Overall, the correlation data indicate that both phenolic and flavonoid compounds are essential to the antioxidant activity of the propolis extracts, with phenolics more strongly influencing DPPH radical scavenging and reducing power, while flavonoids exhibit a more pronounced effect on superoxide anion scavenging and ferrous ion chelation. These findings highlight the multifaceted nature of the antioxidant mechanisms in propolis extracts, wherein different phytochemicals contribute to distinct antioxidant pathways.

The antioxidant activity of propolis water extracts from different locations in Muğla (Turkey) revealed substantial variability across multiple assays, demonstrating that the chemical composition, particularly phenolic and flavonoid contents, significantly influences their bioactivity. These findings are consistent with existing literature, which supports the strong correlation between the phenolic and flavonoid profiles of propolis and its antioxidant properties [23,27].

**Table 1.** Correlations among phenolic compounds and assays

	$\beta$ -Carotene bleaching	Superoxide anion radical	DPPH radical	Reducing power	Ferrous ion chelation
Superoxide anion radical	0.779				
DPPH radical	0.709	0.735			
Reducing power	0.767	0.730	0.994		
Ferrous ion chelation	0.873	0.970	0.854	0.862	
Total phenolic	0.649	0.654	0.994	0.986	0.790
Total flavonoid	0.562	0.931	0.791	0.751	0.894



In the current study, the Fethiye sample consistently exhibited the highest antioxidant activity, which aligns with its rich chemical composition, including a high total phenolic content and the highest flavonoid content. The superior performance of this sample across various assays, such as  $\beta$ -carotene bleaching and superoxide radical scavenging, highlights the critical role these compounds play in its bioactivity. This trend is supported by research conducted by Gregoris and Stevanato [28], who found a strong correlation between polyphenolic content and antioxidant activity in Venetian propolis, emphasizing that high phenolic concentrations contribute to enhanced radical scavenging and lipid peroxidation inhibition.

The relationship between phenolic content and antioxidant capacity was particularly evident in the Arpacık sample, which showed the highest total phenolic content and performed strongly in assays such as DPPH and reducing power. However, despite its lower flavonoid content compared to Fethiye, Arpacık's performance suggests that phenolics are the primary contributors to its antioxidant efficacy, a conclusion also reached by da Silva et al. [27], who reported that phenolic acids significantly drive the antioxidant activity in Brazilian propolis.

On the other hand, the Dalaman and Döğüşbelen samples, which consistently displayed lower antioxidant activities, also contained lower levels of both phenolics and flavonoids, indicating their limited ability to neutralize free radicals. This observation is in line with studies like those by Fathi Hafshejani et al. [29] and Narimane et al. [30], who demonstrated that samples with reduced phenolic and flavonoid contents generally exhibit weaker antioxidant properties. Furthermore, the chelating activity of these extracts was also significantly lower, which again underscores the importance of a rich phenolic and flavonoid composition for robust antioxidant potential.

The overall findings from this study strongly support the established view that the antioxidant activity of propolis is largely determined by its phenolic and flavonoid composition. In particular, Fethiye's balanced high levels of both compounds correlate with its superior performance across all antioxidant assays. This mirrors the work of Asem et al. [23], who found that Malaysian propolis with high phenolic and flavonoid contents exhibited enhanced radical scavenging and lipid peroxidation inhibition. Similarly, Gregoris and Stevanato [28] concluded that high phenolic content enhances the reducing power and radical scavenging activity of propolis, a pattern clearly evident in the current data.

In conclusion, the variations in antioxidant activity among the Muğla propolis samples are closely tied to their chemical compositions, particularly their phenolic

and flavonoid profiles. Samples with higher concentrations of these compounds, like Fethiye and Arpacık, exhibited stronger antioxidant activity, underscoring the critical role of these bioactive compounds. The present findings are consistent with literature, which consistently highlights the contribution of phenolics and flavonoids to the antioxidant properties of propolis from various regions [23,27,28]. Future studies may benefit from further exploring the specific phenolic compounds responsible for the observed activities, as well as expanding the geographical scope to examine how environmental factors influence the bioactivity of propolis.

#### 4. Conclusion

This study provides compelling evidence that the antioxidant activities of water extracts from propolis samples collected across different locations in Muğla (Turkey) are strongly influenced by their phenolic and flavonoid contents. The Fethiye and Arpacık samples consistently exhibited the highest antioxidant capacities across multiple assays, which correlates with their rich phenolic and flavonoid compositions. Particularly, the Fethiye extract, with its high levels of both phenolics and flavonoids, demonstrated superior radical scavenging, reducing, and chelating abilities, surpassing even standard antioxidant compounds in certain assays. Arpacık, while phenolic-dominant, also showed significant antioxidant performance, although its lower flavonoid content may have limited its activity in assays like superoxide radical scavenging.

The observed correlations between total phenolic and flavonoid content and various antioxidant mechanisms underscore the central role these compounds play in determining the bioactivity of propolis extracts. Phenolics were more closely associated with DPPH radical scavenging and reducing power, while flavonoids demonstrated a stronger influence on superoxide radical scavenging and ferrous ion chelation, indicating distinct contributions of these compounds to different antioxidant pathways.

Despite these promising findings, the study also highlights several limitations. First, the focus on water extracts may not fully capture the antioxidant potential of propolis, as different solvents could extract varying bioactive compounds. Future studies should include a broader range of extraction methods to provide a more comprehensive understanding of propolis' antioxidant capacity. Additionally, while the phenolic and flavonoid content appears to be key drivers of antioxidant activity, other bioactive compounds, such as terpenes and polysaccharides, may also contribute. Further research using advanced analytical techniques like mass spectrometry and nuclear magnetic resonance (NMR)

could identify these additional components and their potential synergies.

Another limitation lies in the geographical scope of the study. While significant variation was observed across the Muğla region, expanding the sampling to include other regions could reveal broader trends and provide insights into how different environmental factors influence the bioactive composition of propolis. Moreover, the ecological and botanical factors driving the observed variations were not fully explored. Detailed studies on the floral sources of the propolis and their seasonal variations could provide critical context for understanding these chemical differences.

In conclusion, this study confirms the significant impact of phenolic and flavonoid compounds on the antioxidant activity of propolis extracts and opens the door for future investigations into the broader chemical composition and ecological influences affecting propolis bioactivity. Further research addressing the noted limitations will help to solidify our understanding of propolis as a potent natural antioxidant and its potential applications in food, pharmaceutical, and cosmetic industries. The main conclusions of the study should be presented, not to summarize information already presented in the results and discussion section.

### Acknowledgement

This study was supported by Afyonkarahisar Health Sciences University Scientific Research Projects Coordination Unit project number 24.KARİYER.001.

### Author's Contributions

**Cengiz Sarikurkcu:** Conceptualization, Methodology, Data curation, Software, Visualization, Investigation, Validation, Writing- original draft, Supervision, Writing-review and editing.

### Ethics

There are no ethical issues after the publication of this manuscript.

### References

[1]. Hashemi, J. M. 2016. Biological effect of bee propolis: a review. *European Journal of Applied Sciences*; 8: 311-318.

[2]. Kujumgiev, A.; Tsvetkova, I.; Serkedjieva, Y.; Bankova, V.; Christov, R.; Popov, S. 1999. Antibacterial, antifungal and antiviral activity of propolis of different geographic origin. *J. Ethnopharmacol.*; 64(3): 235-240.

[3]. Amoros, M.; Lurton, E.; Boustie, J.; Girre, L.; Sauvager, F.; Cormier, M. 1994. Comparison of the anti-herpes simplex virus activities of propolis and 3-methyl-but-2-enyl caffeate. *J. Nat. Prod.*; 57(5): 644-647.

[4]. Wang, L. 1993. Antiinflammatory effect of propolis. *Japanese Pharmacology & Therapeutics*; 24: 223-224.

[5]. Kimoto, T.; Aga, M.; Hino, K.; Koya-Miyata, S.; Yamamoto, Y.; Micallef, M. J. et al. 2001. Apoptosis of human leukemia cells induced by Artepillin C, an active ingredient of Brazilian propolis. *Anticancer Res.*; 21(1A): 221-228.

[6]. Matsuno, T. 1995. A new clerodane diterpenoid isolated from propolis. *Zeitschrift für Naturforschung C*; 50(1-2): 93-97.

[7]. Kumazawa, S.; Hamasaka, T.; Nakayama, T. 2004. Antioxidant activity of propolis of various geographic origins. *Food Chem.*; 84(3): 329-339.

[8]. Marcucci, M. C. 1995. Propolis: chemical composition, biological properties and therapeutic activity. *Apidologie*; 26(2): 83-99.

[9]. Bankova, V. S.; de Castro, S. L.; Marcucci, M. C. 2000. Propolis: recent advances in chemistry and plant origin. *Apidologie*; 31(1): 3-15.

[10]. Marcucci, M. C. 1999. Chemical composition, plant origin and biological activity of Brazilian propolis. *Current Topics in Phytochemistry*; 2: 115-123.

[11]. Tazawa, S.; Warashina, T.; Noro, T. 1999. Studies on the constituents of Brazilian propolis. II. *Chemical and Pharmaceutical Bulletin*; 47(10): 1388-1392.

[12]. Miyataka, H.; Nishiki, M.; Matsumoto, H.; Fujimoto, T.; Matsuka, M.; SATOH, T. 1997. Evaluation of propolis. I. Evaluation of Brazilian and Chinese propolis by enzymatic and physico-chemical methods. *Biological and Pharmaceutical Bulletin*; 20(5): 496-501.

[13]. Miyataka, H.; Nishiki, M.; Matsumoto, H.; Fujimoto, T.; Matsuka, M.; Isobe, A. et al. 1998. Evaluation of propolis (II): effects of Brazilian and Chinese propolis on histamine release from rat peritoneal mast cells induced by compound 48/80 and concanavalin A. *Biological and Pharmaceutical Bulletin*; 21(7): 723-729.

[14]. Hegazi, A. G.; Abd El Hady, F. K.; Abd Allah, F. A. 2000. Chemical composition and antimicrobial activity of European propolis. *Zeitschrift für Naturforschung C*; 55(1-2): 70-75.

[15]. Banskota, A. H.; Tezuka, Y.; Adnyana, I. K.; Midorikawa, K.; Matsushige, K.; Message, D. et al. 2000. Cytotoxic, hepatoprotective and free radical scavenging effects of propolis from Brazil, Peru, the Netherlands and China. *J. Ethnopharmacol.*; 72(1-2): 239-246.

[16]. Slinkard, K.; Singleton, V. L. 1977. Total phenol analysis: automation and comparison with manual methods. *Am. J. Enol. Vitic.*; 28(1): 49-55.

[17]. Zengin, G.; Sarikurkcu, C.; Aktumsek, A.; Ceylan, R.; Ceylan, O. 2014. A comprehensive study on phytochemical characterization of *Haplophyllum myrtifolium* Boiss. endemic to Turkey and its inhibitory potential against key enzymes involved in Alzheimer, skin diseases and type II diabetes. *Ind. Crops Prod.*; 53: 244-251.

[18]. Sarikurkcu, C.; Eryigit, F.; Cengiz, M.; Tepe, B.; Cakir, A.; Mete, E. 2012. Screening of the antioxidant activity of the essential oil and methanol extract of *Mentha pulegium* L. from Turkey. *Spectrosc. Lett.*; 45: 352-358.

[19]. Oyaizu, M. 1986. Studies on products of browning reactions: antioxidative activities of browning reaction prepared from glucosamine. *Japanese Journal of Nutrition*; 44: 307-315.

[20]. Dasgupta, N.; De, B. 2004. Antioxidant activity of *Piper betle* L. leaf extract in vitro. *Food Chem.*; 88(2): 219-224.

- [21]. Aktumsek, A.; Zengin, G.; Guler, G. O.; Cakmak, Y. S.; Duran, A. 2013. Antioxidant potentials and anticholinesterase activities of methanolic and aqueous extracts of three endemic *Centaurea* L. species. *Food Chem. Toxicol.*; 55: 290-296.
- [22]. Sun, T.; Tanumihardjo, S. A. 2007. An integrated approach to evaluate food antioxidant capacity. *J. Food Sci.*; 72(9): R159-R165.
- [23]. Asem, N.; Abdul Gapar, N. A.; Abd Hapit, N. H.; Omar, E. A. 2020. Correlation between total phenolic and flavonoid contents with antioxidant activity of Malaysian stingless bee propolis extract. *J. Apic. Res.*; 59(4): 437-442.
- [24]. Wang, X.; Sankarapandian, K.; Cheng, Y.; Woo, S. O.; Kwon, H. W.; Perumalsamy, H. et al. 2016. Relationship between total phenolic contents and biological properties of propolis from 20 different regions in South Korea. *BMC Complementary and Alternative Medicine*; 16: 1-12.
- [25]. Bouchelaghem, S.; Das, S.; Naorem, R. S.; Czuni, L.; Papp, G.; Kocsis, M. 2022. Evaluation of total phenolic and flavonoid contents, antibacterial and antibiofilm activities of Hungarian Propolis ethanolic extract against *Staphylococcus aureus*. *Molecules*; 27(2): 574.
- [26]. Sulaeman, A.; Marliyati, S. A.; Fahrudin, M. 2019. Antioxidant activity and total phenolic content of stingless bee propolis from Indonesia. *Journal of Apicultural Science*; 63(1): 139-147.
- [27]. da Silva, J. F. M.; de Souza, M. C.; Matta, S. R.; de Andrade, M. R.; Vidal, F. V. N. 2006. Correlation analysis between phenolic levels of Brazilian propolis extracts and their antimicrobial and antioxidant activities. *Food Chem.*; 99(3): 431-435.
- [28]. Gregoris, E.; Stevanato, R. 2010. Correlations between polyphenolic composition and antioxidant activity of Venetian propolis. *Food Chem. Toxicol.*; 48(1): 76-82.
- [29]. Fathi Hafshejani, S.; Lotfi, S.; Rezvannejad, E.; Mortazavi, M.; Riahi-Madvar, A. 2023. Correlation between total phenolic and flavonoid contents and biological activities of 12 ethanolic extracts of Iranian propolis. *Food Sci. Nutr.*; 11(7): 4308-4325.
- [30]. Narimane, S.; Demircan, E.; Salah, A.; Salah, R. 2017. Correlation between antioxidant activity and phenolic acids profile and content of Algerian propolis: Influence of solvent. *Pak. J. Pharm. Sci.*; 30: 1417-1423.

# The Determination of Molecular Electrostatic Potential and Anticancer Properties of Eugenol: A Theoretical Study

Bilge Bıçak<sup>1\*</sup> 

<sup>1</sup> Physics Department, Science Faculty, Istanbul University, 34134, Istanbul, Türkiye

\* [bbicak@istanbul.edu.tr](mailto:bbicak@istanbul.edu.tr)

\* Orcid No: 0000-0003-1147-006X

Received: 29 May 2024

Accepted: 9 December 2024

DOI: 10.18466/cbayarfbe.1490879

## Abstract

Cancer is one of the deadliest diseases worldwide, and for this reason, it is a prominent field of study in drug development. It has been reported in various studies that some of the plants and essential oils obtained from plants have high anticancer activities. This situation is related to the compound groups found in plants and essential oils. Studies on using essential oils in combination with synthetic drugs or aromatherapy are ongoing. Essential oils show cytotoxic properties and may play a role in the death of cancer cells. Eugenol is an important compound found in clove, laurel, and cinnamon essential oils that has anticancer activity in various types of cancer. Eugenol has the ability to reduce cyclooxygenase-2 (COX-2) activity and to inhibit cell proliferation through NF- $\kappa$ B suppression in various types of cancer. In this study, the binding profiles of eugenol with COX-2 and Human inhibitor of nuclear transcription factor  $\kappa$ B (I $\kappa$ B) kinase beta, which plays a crucial role in the NF- $\kappa$ B signaling pathway, were examined by molecular docking study, which is one of the methods used in computer-aided drug design. A supporting study was performed to understand the electrostatic complementarity between ligand and receptor by molecular electrostatic potential (MEP) analysis. As a result of the study, it was comparatively presented that eugenol has similar interaction profiles with reference compounds.

**Keywords:** MEP, Molecular docking, Anticancer, Essential Oil

## 1. Introduction

Cancer is one of the world's deadliest diseases, known as uncontrolled cell proliferation caused by genetic and/or environmental factors. There are also plant-based studies in cancer treatment development studies, which have extensive scientific literature and are still being studied. Studies conducted with plants have reported anticancer effects [1-3]. It has been observed in the results of the study that various compounds in plants have properties that inhibit the growth of cancer cells and promote the apoptosis of cells. Since essential oils (EOs) have multiple effects such as antibacterial, antioxidant, and anticancer, their use with different treatment options has been reported to be popular in literature studies [4]. Plant essential oils have also been evaluated in cancer-related studies and have been reported to have cytotoxic effects on various cancer cell lines. For example, in a study conducted on Caco-2 colorectal cancer cell lines with EO of *Eucalyptus camaldulensis* Dehnh., it was reported that EO induced programmed cell death [5]. In a study conducted on

breast cancer cell lines (MCF-7) with thyme and clove oils, it was reported that both essential oils inhibited the growth of cancer cell lines in a concentration-dependent manner [6]. However, more studies and results are needed for more reliable information about the cell target specificity of essential oils and their use in drug delivery systems [4]. Because various risks such as hydrophobicity, high volatility, and instability bring some limitations on their use. The encapsulation method is used to minimize these limitations [7]. In a study conducted by Ercin et al., encapsulation of *Laurus nobilis* L. EO was performed, and it was evaluated that it could be used as a phytotherapeutic agent-based controlled release system in cancer treatment [8].

Eugenol is a phenylpropanoid found in many essential oils (clove, laurel, cinnamon, etc.) and has been reported to have anticancer properties against many types of cancer, from lung cancer to prostate cancer, from breast cancer to leukemia [9-11]. The anticancer effect of eugenol can occur through different mechanisms, such as inducing cell death, cell cycle arrest, and metastasis [9,12,13]. Eugenol has the ability to reduce

cyclooxygenase-2 activity and inhibit NF- $\kappa$ B in various types of cancer [9]. COX-2 enzymes are important biological structures that provide the production of prostaglandins that are associated with inflammation. COX-2 inhibitors generally have inflammation-blocking properties [14]. Additionally, the increase in cyclooxygenase (COX-2) level due to chronic inflammation is associated with different stages such as tumor formation and proliferation. This is why the COX-2 enzyme is tried to be suppressed in cancer treatment studies [15]. It was reported by Jaganathan and Supriyanto that Eugenol may play a role in the inhibition of COX-2 expression [16]. The increase in NF- $\kappa$ B activity in tumor tissues is directly proportional to the release of factors such as pro-inflammatory cytokines, and this may cause the cancerous area to spread [17]. Human I $\kappa$ B kinase beta plays a crucial role in the NF- $\kappa$ B signaling pathway [18,19]. Some of the studies reported that eugenol potentiates the effect of cisplatin on cancer stem-like cells by targeting the NF- $\kappa$ B pathway [20], and that eugenol exhibits inhibitory properties on cell proliferation through NF- $\kappa$ B suppression in the rat gastric carcinogenesis model induced by N-methyl-N'-nitro-N-nitrosoguanidine [21].

Molecular docking and molecular electrostatic potential (MEP) analysis, which are molecular modeling methods, are used in drug design studies. With the molecular docking method, the interactions of the drug candidate, that is, the ligand, with the macromolecules, that is, the receptors, targeted for the disease are examined [22]. Molecular electrostatic potential (MEP) analysis is related to the charge distribution of the molecule. The charge distribution of the molecule is also an significant indicator of intermolecular interactions [23-25]. For example, the capability of a ligand to bind to the target receptor is determined through molecular electrostatic interactions. Both molecular docking and molecular electrostatic potential analyses are two important methods used to study interactions at the molecular level.

In this study, molecular electrostatic potential analysis of eugenol, one of the essential oil compounds known to have anticancer properties, and molecular docking studies with COX-2 and Human I $\kappa$ B kinase beta, which are important targets, were carried out.

## 2. Materials and Methods

Eugenol structure was obtained from Pubchem (CID: 3314) (<https://pubchem.ncbi.nlm.nih.gov/compound/Eugenol>). Eugenol was optimized at Gaussian09 package program [26] with DFT/B3LYP/6-311++G(d,p). For molecular docking studies, eugenol was prepared as ligand with AutoDock Tools. COX-2 (PDB: 5IKR) and human I $\kappa$ B kinase beta (PDB: 4KIK) structures were downloaded from PDB DataBank (<https://www.rcsb.org/>). Receptors

were cleared of solutions and ions and added polar hydrogens. Grid boxes were adjusted as 30x30x30 Å, and molecular docking studies were carried out via AutoDock Vina program [27].

## 3. Results and Discussion

### 3.1 Molecular Docking

As a predictive tool for whether or not an effect will occur experimentally, molecular docking is an important method used in computer-aided drug design. It has been reported in literature studies that Eugenol may play a role in the inhibition of COX-2 expression and suppression of NF- $\kappa$ B [16,21]. In this study, considering that the mechanisms of action are active, the binding profiles and binding types that may occur in the event of the experimental effect were evaluated.

The first molecular docking study was performed with COX-2. The binding affinity of eugenol was calculated as -6.0 kcal/mol, in this study. When the RMSD values were examined, it was observed that they did not exceed values around 2 Å and gave values within an acceptable range (see Table 1). The interactions between eugenol and COX-2 were provided by amide- $\pi$  stacked,  $\pi$ -alkyl, alkyl, and van der Waals (vdW) interactions (see Figure 1). Eugenol had an amide- $\pi$  stacked interaction with Gly-526.  $\pi$ -alkyl interactions of eugenol occurred with Val-523, Tyr-355, Val-349, Leu-352 and Ala-527 residues of COX-2. Additionally, there was another alkyl interaction with Ala-527. vdW interactions of eugenol occurred with Ser-353, Arg-120, Phe-518, Trp-387, Met-522, Phe-381 and Ser-530 residues of COX-2.

Considering the literature studies, the fact that similar amino acid residues play a role in the interaction is evidence that eugenol is in the active site. While it was observed in the literature that 4-Nitro-5-O-benzoylpinostrubin, 5-O-Benzoylpinostrubin, and flavanone interact with Arg-120 through different interaction types such as hydrogen bonding and  $\pi$ -interaction [28], eugenol also interacted with Arg-120 in this study. While 4-Nitro-5-O-benzoylpinostrubin, flavonol, and chrysin molecules interacted with amide- $\pi$  stacked interaction with residue Gly-526 [28,29], eugenol also made the same interaction with the same residue in this study. In the study conducted with COX-2, quercetin, a potential anticancer agent [30], was reported to have  $\pi$  interactions with Val-523, Val-349, and Leu-352 residues [31]. In this study conducted with eugenol, it was determined that Tyr-355 and Ala-527 residues were also involved in  $\pi$  interactions in addition to these residues. Tyr-355 is an important amino acid residue involved in interactions. In another study, interactions in the active site of COX-2 were presented with the binding affinity value of eugenol. While there were interactions with residues similar to the results in



this study, it was determined that the binding affinity value in our study gave a better value [32].

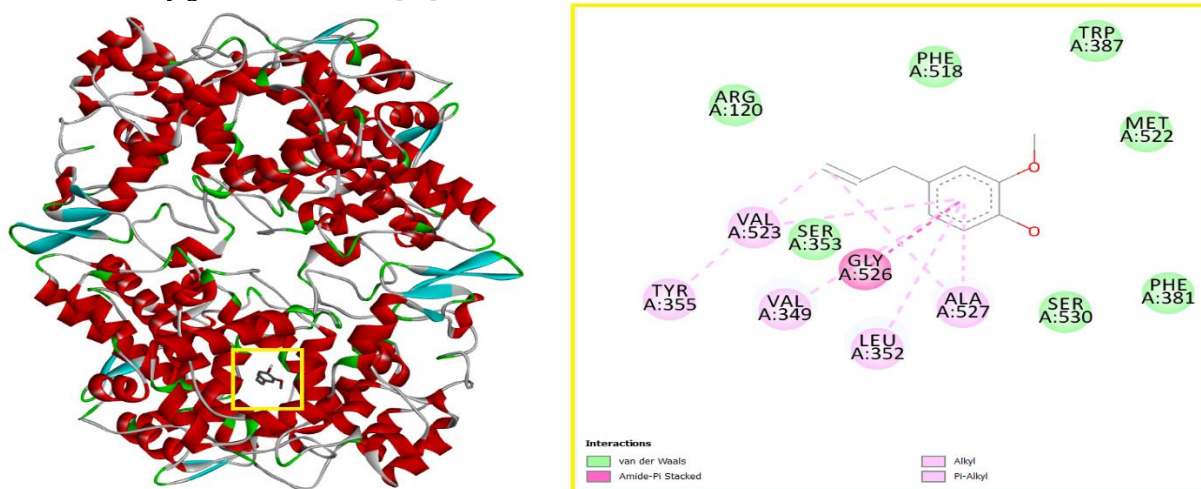


**Figure 1.** The binding profile of eugenol and COX-2.

**Table 1.** Binding affinities and RMSD values obtained from molecular docking study of Eugenol and COX-2.

Mode	Affinity (kcal/mol)	dist from best mode	
		rmsd l.b.	rmsd u.b.
1	-6.0	0.000	0.000
2	-5.9	1.326	1.782
3	-5.9	2.592	5.061
4	-5.9	1.440	2.761
5	-5.9	1.687	2.893
6	-5.6	2.443	4.660
7	-5.5	2.989	4.900
8	-5.4	2.518	4.685
9	-5.4	1.482	2.715

In the second part of the molecular docking study, eugenol was docked with human I $\kappa$ B kinase beta, and the binding energy was calculated as -6.3 kcal/mol. When the RMSD values were examined, it was observed that they gave values within the acceptable range in terms of suitability of the molecular docking study (see Table 2). The interactions between eugenol and human I $\kappa$ B kinase beta were provided by hydrogen bond, pi-sulfur, pi-sigma, pi-alkyl, alkyl, and vdW interactions (see Figure 2). Eugenol made hydrogen bond and pi-sulfur interactions with Cys-99 residue.

Additionally, eugenol made pi-sigma interaction with Val-152 residue of human I $\kappa$ B kinase beta. Pi interactions were very active in the binding region. Another pi interaction (pi-alkyl) occurred with residues Ile-165, Val-29, and Leu-21. Ile-165, and Val-29 also made alkyl interactions. Met-96 was also observed as another residue participating in alkyl interactions. Considering the vdW interactions, it was determined that Val-74, Asp-166, Asp-103, Gly-102, and Tyr-98 residues interact with eugenol.

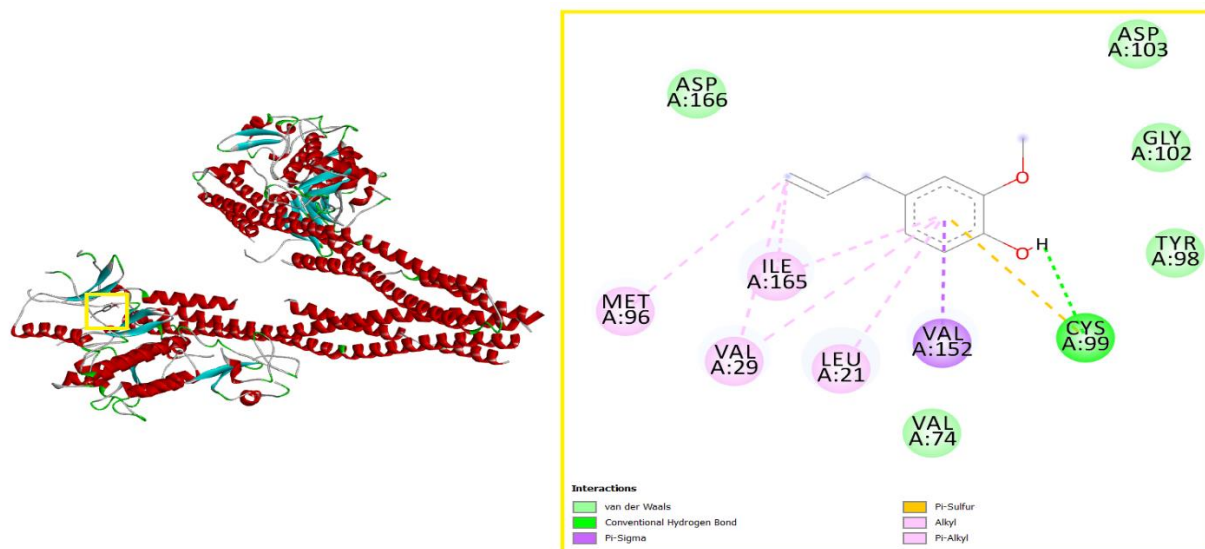


**Figure 2.** The binding profile of eugenol and human Ikb kinase beta.

**Table 2.** Binding affinities and RMSD values obtained from molecular docking study of Eugenol and human Ikb kinase beta.

Mode	Affinity (kcal/mol)	dist from best mode	
		rmsd l.b.	rmsd u.b.
1	-6.3	0.000	0.000
2	-6.2	1.231	1.602
3	-6.0	2.480	3.527
4	-5.8	2.032	3.597
5	-5.8	2.147	4.861
6	-5.8	2.586	4.542
7	-5.7	1.702	2.768
8	-5.7	1.116	2.618
9	-5.5	3.207	5.069

It has been determined that the prominent residues in the docking studies performed with human Ikb kinase beta are quite compatible with the residues with which eugenol interacts in the active site of the receptor. In most of the literature studies, hydrogen bonding or hydrophobic interactions with Cys-99 have been observed [33,34]. In this study, eugenol made both hydrogen bond and pi-sulfur interaction with Cys-99. Terpenoids are plant defense molecules known to have anticancer effects [35]. In the docking study carried out with terpenoid plant components, it was reported that Asp-103 and Gly-102 came to the fore in hydrogen bond interactions or hydrophobic interactions [34]. Eugenol also had a van der Waals interaction with these residues. Leu-21, Val-152, Ile-165, and Val-29 residues are other important residues that are at the forefront in molecular interactions [33,34]. In this study, these amino acid residues were especially involved in pi interactions. Hematein is a molecular structure that has the role of preventing the proliferation of cancer cells and initiating cell apoptosis [36]. As a result of the molecular docking study of hematein, it was reported that this molecule makes hydrogen bonds with Cys-99,

and also interacts closely with Leu-21, Val-152, Ile-165, and Val-29 [33]. Eugenol also interacted with these residues, making hydrogen bonds and pi-sulfur interactions with Cys-99. It was also determined that it made pi interactions with Leu-21, Val-152, Ile-165, and Val-29 residues. Genistein, which is reported to play a role in blocking NF-kB pathways [37-39], and apigenin, which targets pathways such as NF-kB [40], also interacted with similar residues with the eugenol molecule [41]. The Cys-99 residue, which is the most prominent and important indicator in all these literature studies, is observed in the foreground in this study.

### 3.2 MEP Analysis

Molecular electrostatic potential (MEP) is an important determinant of hydrogen bond interactions and is related to the charge distribution of the molecule. In studies such as molecular docking, the most appropriate interactions between drug candidates and target receptors begin with the existence of electrostatic potentials [42-44].

MEP analysis of eugenol was carried out in a vacuum environment using the Gaussian09 program. In the study carried out in a vacuum environment for the eugenol molecule, it was determined that the energy values of the red region, which is rich in electrons, and the blue region, which is poor in electrons, were between  $-0.06302$  au and  $+0.06302$  au, respectively (see Figure 3).

In the MEP map obtained for the vacuum environment, it was observed that the region where the O1 ( $-0.0445078$  au) atom is located is the electrophilic region. When looking at the nucleophilic regions, the region with H22 bonded to the O2 atom stands out ( $+0.0626075$  au). In both docking studies, it was

observed that hydrophobic interactions were dominant, especially in regions where the electrostatic potential was close to neutral. In the study conducted with human I $\kappa$ B kinase beta, it was observed that the nucleophilic region played a role in the hydrogen bond interaction with the Cys-99 residue. In another molecular docking study of eugenol, it was observed that electrophilic and nucleophilic regions take part in hydrogen bond interactions, while other regions make hydrophobic interactions [45]. These types of interactions are formed as a result of the amino acid residues in the active site of the targeted receptor and eugenol having the most suitable pose in the active site (key-lock compatibility).

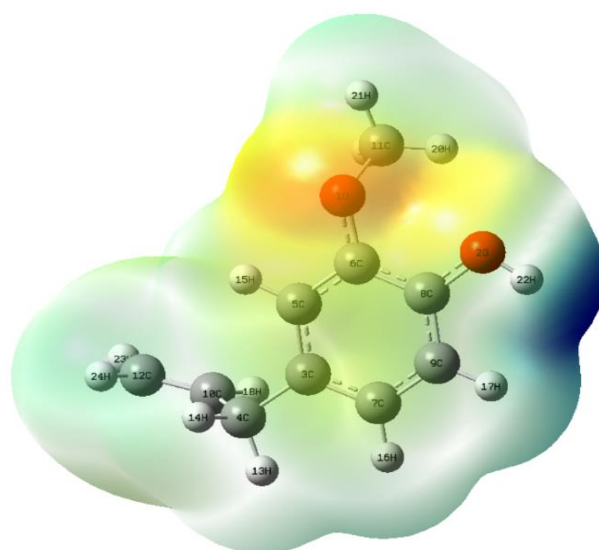


**Figure 3.** Molecular electrostatic potential (MEP) map of eugenol.

#### 4. Conclusion

An attempt was made to elucidate how eugenol, which has been found to be effective in various types of cancer and is among the major compounds in the essential oils of plants such as clove and cinnamon, interacts with certain targets used in cancer studies at the molecular level. Considering that eugenol reduces COX-2 activation and inhibits NF- $\kappa$ B, molecular docking studies were performed. The study determined that eugenol had a similar interaction profile with potential therapeutic compounds in the literature. In addition, the electrophilic and nucleophilic regions of eugenol and the electrostatic potential values of these regions were determined by molecular electrostatic potential analysis. When molecular docking study and MEP analysis were evaluated together, it was observed that the regions where the electrostatic potential was close to neutral played a role in hydrophobic interactions. It was evaluated in this study that hydrophobic interactions

may play a role in the therapeutic effect of eugenol. It is anticipated that the role of eugenol in the cancer mechanism will be elucidated in more detail in future experimental studies.

#### Author's Contributions

**Bilge Bıçak:** Drafted and wrote the manuscript, performed the all analysis.

#### Ethics

There are no ethical issues after the publication of this manuscript.

#### References

[1]. Solowey, E, Lichtenstein, M, Sallon, S, Paavilainen, H, Solowey, E, Lorberboum-Galski, H. 2014. Evaluating medicinal plants for anticancer activity. *The Scientific World Journal*, 2014.

- [2]. Ohiagu, FO, Chikezie, PC, Chikezie, CM, Enyoh, CE. 2021. Anticancer activity of Nigerian medicinal plants: a review. *Future Journal of Pharmaceutical Sciences*, 7: 1-21.
- [3]. Aboul-Enein, AM, El-Ela, FA, Shalaby, EA, El-Shemy, HA. 2012. Traditional medicinal plants research in Egypt: Studies of antioxidant and anticancer activities. *J Med Plants Res*, 6(5): 689-703.
- [4]. Sharma, M, Grewal, K, Jandrotia, R, Batish, DR, Singh, HP, Kohli, RK. 2022. Essential oils as anticancer agents: Potential role in malignancies, drug delivery mechanisms, and immune system enhancement. *Biomedicine & Pharmacotherapy*, 146: 112514.
- [5]. Taheri, E, Ghorbani, S, Safi, M, Sani, NS, Amodizaj, FF, Heidari, M, ... & Heidari, M. 2020. Inhibition of colorectal cancer cell line CaCo-2 by essential oil of eucalyptus camaldulensis through induction of apoptosis. *Acta Medica Iranica*, 260-265.
- [6]. El-Darier, SM, El-Ahwany, AM, Elkenany, ET, Abdeldaim, AA. 2018. An in vitro study on antimicrobial and anticancer potentiality of thyme and clove oils. *Rendiconti Lincei. Scienze Fisiche e Naturali*, 29: 131-139.
- [7]. Cimino, C, Maurel, OM, Musumeci, T, Bonaccorso, A, Drago, F, Souto, EMB, ... & Carbone, C. 2021. Essential oils: Pharmaceutical applications and encapsulation strategies into lipid-based delivery systems. *Pharmaceutics*, 13(3): 327.
- [8]. Ercin, E, Kecel-Gunduz, S, Gok, B, Aydin, T, Budama-Kilinc, Y, Kartal, M. 2022. *Laurus nobilis* L. essential oil-loaded PLGA as a nanoformulation candidate for cancer treatment. *Molecules*, 27(6): 1899.
- [9]. Zari, AT, Zari, TA, Hakeem, KR. 2021. Anticancer properties of eugenol: A review. *Molecules*, 26(23): 7407.
- [10]. Nisar, MF, Khadim, M, Rafiq, M, Chen, J, Yang, Y, Wan, CC. 2021. Pharmacological properties and health benefits of eugenol: A comprehensive review. *Oxidative medicine and cellular longevity*, 2021.
- [11]. Ulanowska, M, Olas, B. 2021. Biological properties and prospects for the application of eugenol—a review. *International journal of molecular sciences*, 22(7): 3671.
- [12]. TR, DP, Haykal, MN. 2021. Eugenol Nanoparticle Encapsulated Chitosan Enhances Cell Cycle Arrest in HeLa Human Cervical Cancer Cells. *Systematic Reviews in Pharmacy*, 12(2).
- [13]. Liu, H, Schmitz, JC, Wei, J, Cao, S, Beumer, JH, Strychor, S, ... & Lin, X. 2014. Clove extract inhibits tumor growth and promotes cell cycle arrest and apoptosis. *Oncology research*, 21(5): 247.
- [14]. Fuertes-Agudo, M, Luque-Tévar, M, Cucarella, C, Martín-Sanz, P, Casado, M. 2023. Advances in understanding the role of NRF2 in liver pathophysiology and its relationship with hepatic-specific Cyclooxygenase-2 expression. *Antioxidants*, 12(8): 1491.
- [15]. Méric, JB, Rottey, S, Olausson, K, Soria, JC, Khayat, D, Rixe, O, Spano, JP. 2006. Cyclooxygenase-2 as a target for anticancer drug development. *Critical reviews in oncology/hematology*, 59(1): 51-64.
- [16]. Jaganathan, SK, Supriyanto, E. 2012. Antiproliferative and molecular mechanism of eugenol-induced apoptosis in cancer cells. *Molecules*, 17(6):6290-6304.
- [17]. Xia, Y, Shen, S, Verma, IM. 2014. NF- $\kappa$ B, an active player in human cancers. *Cancer immunology research*, 2(9): 823-830.
- [18]. Schmid, JA, Birbach, A. 2008. I $\kappa$ B kinase  $\beta$  (IKK $\beta$ /IKK2/IKBKB)—A key molecule in signaling to the transcription factor NF- $\kappa$ B. *Cytokine & growth factor reviews*, 19(2): 157-165.
- [19]. Yadav, D, Mishra, BN, Khan, F. 2018. 3D-QSAR and docking studies on ursolic acid derivatives for anticancer activity based on bladder cell line T24 targeting NF- $\kappa$ B pathway inhibition. *Journal of Biomolecular Structure and Dynamics*, 37(14): 3822-3837.
- [20]. Islam, SS, Ibtehaj, AS, Ahlam, S, Aboussekhra, A. 2016. Eugenol potentiates the effect of cisplatin on cancer stem-like cells through targeting the NF- $\kappa$ B pathway. *Cancer Research*, 76(14\_Supplement): 2907-2907.
- [21]. Manikandan, P, Vinothini, G, Vidya Priyadarsini, R, Prathiba, D, Nagini, S. 2011. Eugenol inhibits cell proliferation via NF- $\kappa$ B suppression in a rat model of gastric carcinogenesis induced by MNNG. *Investigational new drugs*, 29: 110-117.
- [22]. Ferreira, LG, Dos Santos, RN, Oliva, G, Andricopulo, AD. 2015. Molecular docking and structure-based drug design strategies. *Molecules*, 20(7): 13384-13421.
- [23]. Pepe, G, Siri, D, Reboul, JP. 1992. The molecular electrostatic potential and drug design. *Journal of Molecular Structure: THEOCHEM*, 256: 175-185.
- [24]. Carpio-Martínez, P, Cortés-Guzmán, F. 2023. Structural and bond evolutions during a chemical reaction. In *Advances in Quantum Chemical Topology Beyond QTAIM*, 53-71.
- [25]. Murray, JS, Sen, K. (Eds.). 1996. Molecular electrostatic potentials: concepts and applications.
- [26]. Frisch, MJ, Trucks, GW, Schlegel, HB, Scuseria, GE, Robb, MA, Cheeseman, JR, et.al. 2003. *Revision B. Gaussian. Inc.*, Pittsburgh PA.
- [27]. Trott, O, Olson, AJ. 2010. AutoDock Vina: improving the speed and accuracy of docking with a new scoring function, efficient optimization, and multithreading. *Journal of computational chemistry*, 31(2): 455-461.
- [28]. Wiyono, AS, Diyah, NW. 2023. Molecular docking of 5-o-benzoylpinostrubin derivatives from *Boesenbergia pandurata* roxb. as anti-inflammatory. *Journal of Public Health in Africa*, 14(Suppl 1).
- [29]. Nadia, L, Mouna, C, Djadi, N. 2024. Exploring the Interactions of Natural Flavonoids with COX-2: Insights from Molecular Docking, DFT Analysis, and ADME Calculations. *Physical Chemistry Research*, 12(3): 675-691.
- [30]. Panthi, VK, Kaushal, S, Adhikari, B, Basnet, N, Chaudhary, D, Pajaruli, RR, Pokhrel, P. 2020. A Review of Quercetin: Anti-Cancer Activity. *International Journal of Innovative Research and Reviews*, 4(1): 1-7.
- [31]. Artos, RIH, Avila, GAA. 2023. Theoretical Analysis of Potential Selective Cyclooxygenase (Cox)-2 Inhibitors in Active Ingredients of Medicinal Plants by Molecular Docking. *International Journal of Latest Research in Humanities and Social Science*, 6(4): 21-30.
- [32]. Das Chagas Pereira de Andrade, F, Mendes, AN. 2020. Computational analysis of eugenol inhibitory activity in lipoxygenase and cyclooxygenase pathways. *Scientific reports*, 10(1): 16204.
- [33]. Cho, YW, Lim, HJ, Han, MH, Kim, BC, Han, S. 2020. Small molecule inhibitors of I $\kappa$ B kinase  $\beta$ : a chip-based screening and molecular docking simulation. *Bioorganic & Medicinal Chemistry*, 28(9): 115440.
- [34]. Raju, SK, Kumar, S, Sekar, P, Sundhararajan, N, Nagalingam, Y. 2023. Ligand Based Multi-Targeted Molecular Docking Analysis of Terpenoid Phytoconstituents as Potential Chemotherapeutic Agents Against Breast Cancer: An In Silico Approach. *prevention*, 22(2):55-62.

- [35]. Kłos, P, Chlubek, D. 2022. Plant-derived terpenoids: a promising tool in the fight against melanoma. *Cancers*, 14(3): 502.
- [36]. Wang, R, Wang, J, Ding, N, He, S, Zhao, Y, Gao, P. 2019. Effects of okadaic acid and hematein on human lung adenocarcinoma A549 cells and responses of mitochondria and endoplasmic reticulum apoptosis pathways. *Translational Cancer Research*, 8(3): 968.
- [37]. Konstantinou, EK, Gioxari, A, Dimitriou, M, Panoutsopoulos, GI, Panagiotopoulos, AA. 2024. Molecular Pathways of Genistein Activity in Breast Cancer Cells. *International Journal of Molecular Sciences*, 25(10): 5556.
- [38]. Chae, HS, Xu, R, Won, JY, Chin, YW, Yim, H. 2019. Molecular targets of genistein and its related flavonoids to exert anticancer effects. *International Journal of Molecular Sciences*, 20(10): 2420.
- [39]. Pavese, JM, Farmer, RL, Bergan, RC. 2010. Inhibition of cancer cell invasion and metastasis by genistein. *Cancer and Metastasis Reviews*, 29: 465-482.
- [40]. Fossatelli, L, Maroccia, Z, Fiorentini, C, Bonucci, M. 2023. Resources for Human Health from the Plant Kingdom: The Potential Role of the Flavonoid Apigenin in Cancer Counteraction. *International journal of molecular sciences*, 25(1): 251.
- [41]. Peanlikhit, T, Aryal, U, Welsh, J, Shroyer, K, Rithidech, K. 2024. In silico comparison of apigenin and related compounds with diverse pharmacological activities using AutoDock 4.2. 6.
- [42]. Bağlan, M, Gören, K, Yıldiko, Ü. 2023. HOMO–LUMO, NBO, NLO, MEP analysis and molecular docking using DFT calculations in DFPA molecule. *International Journal of Chemistry and Technology*, 7(1): 38-47.
- [43]. Buvanewari, M, Santhakumari, R, Usha, C, Jayasree, R, Sagadevan, S. 2021. Synthesis, growth, structural, spectroscopic, optical, thermal, DFT, HOMO–LUMO, MEP, NBO analysis and thermodynamic properties of vanillin isonicotinic hydrazide single crystal. *Journal of Molecular Structure*, 1243: 130856.
- [44]. Saravanan, RR, Seshadri, S, Gunasekaran, S, Mendoza-Meroño, R, García-Granda, S. 2015. Conformational analysis, X-ray crystallographic, FT-IR, FT-Raman, DFT, MEP and molecular docking studies on 1-(1-(3-methoxyphenyl) ethylidene) thiosemicarbazide. *Spectrochimica Acta Part A: Molecular and Biomolecular Spectroscopy*, 139: 321-328.
- [45]. Alminderej, F, Bakari, S, Almundarij, TI, Snoussi, M, Aouadi, K, Kadri, A. 2020. Antioxidant activities of a new chemotype of Piper cubeba L. fruit essential oil (Methyleugenol/Eugenol): In Silico molecular docking and ADMET studies. *Plants*, 9(11): 1534.





## Correction / Erratum Article

### Correction Note

This erratum has been published at the request of the authors. Due to a technical error in the layout process, the volume and issue numbers were displayed as "X" in the article titled "*Preparation of ECH-PCCB for the Pre-concentration and Determination of Cadmium (II) Ions Prior to FAAS by FIA*". The publication date, volume, and issue number have been corrected to **Volume 19, Issue 3, Year 2023**.

The editorial board sincerely apologizes to the authors and readers of the journal for this technical error.

Best regards.

### The first version of the article:



Celal Bayar University Journal of Science  
Volume x, Issue x, 2023, p 237-242  
Doi: 10.18466/cbayarfbe.1280291

V.N. Tirtom

## Preparation of ECH-PCCB for the Pre-concentration and Determination of Cadmium (II) Ions Prior to FAAS by FIA

Vedia Nüket Tirtom<sup>1</sup>\*, Fatma Özkafalı<sup>1</sup> 

<sup>1</sup> Manisa Celal Bayar University, Faculty of Science and Arts, Chemistry Department, Manisa, Türkiye  
[\\*nuket.tirtom@cbu.edu.tr](mailto:nuket.tirtom@cbu.edu.tr)  
\*Orcid No:0000-0002-2490-2741

Received: 10 April 2023

Accepted: 15 June 2023

DOI: 10.18466/cbayarfbe.1280291



### The corrected version of the article:



Celal Bayar University Journal of Science  
Volume 19, Issue 3, 2023, p 237-242  
Doi: 10.18466/cbayarfbe.1280291

V.N. Tirtom

## Preparation of ECH-PCCB for the Pre-concentration and Determination of Cadmium (II) Ions Prior to FAAS by FIA

Vedia Nüket Tirtom<sup>1</sup>\*, Fatma Özkafalı<sup>1</sup> 

<sup>1</sup> Manisa Celal Bayar University, Faculty of Science and Arts, Chemistry Department, Manisa, Türkiye  
[\\*nuket.tirtom@cbu.edu.tr](mailto:nuket.tirtom@cbu.edu.tr)  
\*Orcid No:0000-0002-2490-2741

Received: 10 April 2023

Accepted: 15 June 2023

DOI: 10.18466/cbayarfbe.1280291